Processes and Dynamics of Global to Regional Ocean Heat Uptake and Variability

Author:
Huguenin-Virchaux, Maurice

Publication Date:
2023

DOI:
https://doi.org/10.26190/unsworks/25224

Climate Change Research Centre

School of Biological, Earth and Environmental Sciences

Processes and Dynamics of Global to Regional Ocean Heat Uptake and Variability

A thesis submitted in fulfilment of the requirements for the degree of

Doctor of Philosophy

Maurice F. Huguenin

supervised by

Prof. Dr. Matthew H. England and Dr. Ryan M. Holmes

23rd May 2023

Declarations

ORIGINALITY STATEMENT

> ☑ I hereby declare that this submission is my own work and to the best of my knowledge it contains no materials previously published or written by another person, or substantial proportions of material which have been accepted for the award of any other degree or diploma at UNSW or any other educational institution, except where due acknowledgement is made in the thesis. Any contribution made to the research by others, with whom I have worked at UNSW or elsewhere, is explicitly acknowledged in the thesis. I also declare that the intellectual content of this thesis is the product of my own work, except to the extent that assistance from others in the project's design and conception or in style, presentation and linguistic expression is acknowledged.

COPYRIGHT STATEMENT

> ☑ I hereby grant the University of New South Wales or its agents a non-exclusive licence to archive and to make available (including to members of the public) my thesis or dissertation in whole or part in the University libraries in all forms of media, now or here after known. I acknowledge that I retain all intellectual property rights which subsist in my thesis or dissertation, such as copyright and patent rights, subject to applicable law. I also retain the right to use all or part of my thesis or dissertation in future works (such as articles or books).
>
> For any substantial portions of copyright material used in this thesis, written permission for use has been obtained, or the copyright material is removed from the final public version of the thesis.

AUTHENTICITY STATEMENT

> ☑ I certify that the Library deposit digital copy is a direct equivalent of the final officially approved version of my thesis.

Publications Statement

UNSW is supportive of candidates publishing their research results during their candidature as detailed in the UNSW Thesis Examination Procedure.

Publications can be used in the candidate's thesis in lieu of a Chapter provided:

- The candidate contributed **greater than 50%** of the content in the publication and are the "primary author", i.e. they were responsible primarily for the planning, execution and preparation of the work for publication.
- The candidate has obtained approval to include the publication in their thesis in lieu of a Chapter from their Supervisor and Postgraduate Coordinator.
- The publication is not subject to any obligations or contractual agreements with a third party that would constrain its inclusion in the thesis.

☑ The candidate has declared that **their thesis has publications - either published or submitted for publication - incorporated into it in lieu of a Chapter/s. Details of these publications are provided below.**.

Publication Details #1

Full Title:	Drivers and distribution of global ocean heat uptake over the last half century
Authors:	Maurice F. Huguenin, Ryan M. Holmes and Matthew H. England
Journal or Book Name:	Nature Communications
Volume/Page Numbers:	13, 4921
Date Accepted/Published:	7. September 2022
Status:	published
The Candidate's Contribution to the Work:	M. F. H. performed the analyses and wrote the initial draft of the paper in discussion with R. M. H. and M. H. E. All authors formulated the experimental design, contributed to interpreting the results and refinement of the paper.
Location of the work in the thesis and/or how the work is incorporated in the thesis:	This work has been reproduced with copyright permission as Part 1 of the thesis.

Publication Details #2

Full Title:	Key Role of Diabatic Processes in Regulating Warm Water Volume Variability over ENSO Events
Authors:	Maurice F. Huguenin, Ryan M. Holmes and Matthew H. England
Journal or Book Name:	Journal of Climate
Volume/Page Numbers:	33, 9945–9964
Date Accepted/Published:	15. November 2020
Status:	published
The Candidate's Contribution to the Work:	M. F. H. completed the simulations and wrote the initial manuscript together with input from R. M. H. and M. H. E. All authors formulated the experimental design, contributed to interpreting the results and refinement of the paper.
Location of the work in the thesis and/or how the work is incorporated in the thesis:	This work has been reproduced with copyright permission as Part 2 of the thesis.

Publication Details #3

Full Title:	Subsurface warming of the West Antarctic continental shelf linked to El Niño-Southern Oscillation
Authors:	Maurice F. Huguenin, Ryan M. Holmes, Paul Spence and Matthew H. England
Journal or Book Name:	Geophysical Research Letters
Volume/Page Numbers:	-
Date Accepted/Published:	-
Status:	submitted
The Candidate's Contribution to the Work:	M. F. H. completed the simulations and wrote the initial manuscript together with input from R. M. H., P. S. and M. H. E. All authors formulated the experimental design, contributed to interpreting the results and refinement of the paper.
Location of the work in the thesis and/or how the work is incorporated in the thesis:	The submitted manuscript has been included as Part 3 of the thesis.

Candidate's Declaration

I confirm that where I have used a publication in lieu of a chapter, the listed publication(s) above meet(s) the requirements to be included in the thesis. I also declare that I have complied with the Thesis Examination Procedure.

"It seems to me that the natural world is the greatest source of excitement; the greatest source of visual beauty; the greatest source of intellectual interest. It is the greatest source of so much in life that makes life worth living."

— David Attenborough, English broadcaster, natural scientist and author.

Abstract

Since the 1970s, the ocean has absorbed over 90% of the excess heat trapped in the Earth system due to increasing greenhouse gases. However, sparse observations limit our understanding of the processes driving this heat uptake and its regional patterns. In this thesis, three numerical modelling projects demonstrate how ocean warming has played out over the last 50 years, including how it is affected by El Niño-Southern Oscillation (ENSO), the Earth's dominant mode of interannual climate variability.

Part 1 of this thesis investigates recent multi-decadal ocean heat content trends basin-by-basin, including what proportion of the total trend is forced by atmospheric surface warming, surface wind changes or both. The analysis reveals that Southern Ocean heat uptake accounts for almost all the planet's ocean warming since the 1970s, thereby controlling the rate of climate change. This heat uptake is facilitated in almost equal parts by both warming of the atmosphere and changes in the surface winds.

An integral part of forecasting ENSO is the analysis of the Pacific warm water volume (WWV), the volume of water above 20°C between 5°S and 5°N of the equator. This is because WWV variations lead ENSO events by 6-8 months. WWV variability is thought to be dominated by adiabatic advection of warm water into and out of the equatorial latitude band. Part 2 uses a complete heat budget to illustrate that WWV changes associated with diabatic processes (surface heat fluxes and vertical mixing) are also important.

ENSO impacts remote regions around the globe, including West Antarctica through its atmospheric teleconnections to the Amundsen Sea. Subsurface warming associated with ENSO in this region has the potential to affect basal melting of West Antarctic ice shelves, yet our knowledge of the oceanic ENSO response remains limited. Part

3 reveals that during El Niño, the Amundsen Sea Low and coastal easterlies in West Antarctica weaken and reduce the poleward Ekman transport of cold waters across the shelf break. Consequently, warm Circumpolar Deep Water (CDW) flows onto the continental shelf to balance this mass deficit. The La Niña shelf circulation response is largely opposite and inhibits cross-shelf upwelling of CDW. This has implications for global sea level rise as basal melting can reduce the buttressing of the ice sheets behind the West Antarctic ice shelves.

Acknowledgments

I would like to show my respects and acknowledge the **Bedegal people**, the Traditional Custodians who have cared for this land, sea and water that I live and work on across Australia. I acknowledge that sovereignty of this land has never been ceded and that climate justice has to include justice for First Nations people.

My heartfelt thank you goes to my PhD supervisors, **Dr. Ryan Holmes** and **Prof. Dr. Matthew England**, without their support this thesis would not have been possible. Thank you for your insights, your encouragement and patience, especially when things did not quite go as planned (for example when I permanently deleted all 12 TB of my Part 1 model data). I honestly could not have asked for better supervisors.

Thank you **Matt** for the very valuable input in our meetings, for always coming up with new ideas and perspectives when I got stuck, for joining the Friday frisbees, for the countless coffees during our Wednesday group catch-ups, the late night SMS during our ocean heat study embargo times and for choosing me as a Postdoctoral research associate. Thank you **Ryan** for reading through so many drafts of my manuscripts I stopped counting, for answering what must have been hundreds of technical modelling questions on slack, for the many impromptu meetings even when you were overseas, for allowing me to visit the University of Sydney every now and then, and for continuing to be my PhD supervisor despite two job changes. Thank you also to **Paul Spence** for the foundational work for Part 3, for your constant encouragement in the many zoom meetings, and most of all your relaxed attitude and humour which brightened so many of my days over the last four years.

I also thank the many members of CCRC who have accompanied me in this PhD journey. Many thanks especially to my PhD colleagues, **Julia Neme** for being an awesome friend, for the conversations about the Gadi supercomputer not working (again) and for the fun times we spent at EGU in Vienna, **Hannah Dawson** for being such a wonderful friend and colleague, for always being keen to go grab a coffee wherever we were, for the countless laughs we shared about random things and for playing (and always beating me) at chess, **Jon Page** for organising the Friday frisbees, for being the best student rep during lockdowns and for allowing me to join the Mount Kosciuzsko camping trip, **Ellie Ong** for joining me on a sightseeing tour through Vienna during EGU, for always being there to listen to my many questions about all things related to Gadi and for the Stroopwafels during the final writing stages of this thesis, **Rishav Goyal** for the good times we shared during many conferences and workshops, and for your continuous encouragement during my Master's thesis and now also during my PhD, **Zhi Li** for our discussions about travelling, our families overseas, TV series, ocean heat content and for always being there just on the other side of my cubicle when I had questions, **Christina Schmidt** for often coming to my desk to talk in German and for looking after my office oak tree (*Quercus ilex*) I planted in April 2022, **Lina Teckentrup** for allowing me to vent in German about my PhD way too many times, **Katie Quail** for the many discussions during lunch breaks and for only setting a hat on fire when it could have been more, **Valentina Ortiz** for the daily discussions at our desks, **Tanya Singh** and **Rachael Isphording** for the many chats in the CCRC seminar room, and **Shannon Bengtson** and **Charuni Pathmeswaran** for the Thursday morning runs in and around Centennial Park.

Thank you **Jan Zika** and **Joey Bisits** for allowing me to join and be part of the UNSW Climate Data & Dynamics Lab, **Bronwen Smith** for buying countless coffee beans and milk jugs for the CCRC coffee machine and for stocking up the cookie cupboard for the regular Afternoon Teas, **Katrin Meissner** for the motivating messages during the COVID-19 pandemic and all the hard work in the background to keep CCRC up and running, **Dipayan Choudhury** for introducing me to the Star Wars franchise between COVID-19 lockdowns, **Saurabh Rathore** and **Fabio Boeira Dias** for the helpful tips about my upcoming Postdoc position, **Martin Jucker** for our conversations in Swiss-German and for your humour which made me laugh so many times,

Alvin Stone for helping me write the CLEX newsletter articles, **Ariaan Purich** for the support and motivation when I deleted all my data, **Melissa Hart** for being a fantastic CLEX graduate director and for helping me out with the many questions I had over the last four years, **Pedro Colombo** for being the best Argentinian working from home :-), **Iain Suthers** and **Amandine Schaeffer** for allowing me to join the research cruise on board the *RV Investigator*, and **Iain** especially for inviting me to your traditional Canadian Christmas dinner, **Alex Sen Gupta** for reading through my Postdoc applications, **Philipp Aglas** for the good times we spent chatting at CCRC and over zoom, **Tim Raupach** for the many memories we shared about living in Switzerland, **Anna Ukkola** and **Chiara Holgate** for coming to the ice hockey with me during AGU, **Stephen Gray** for sending out the insightful and often funny Hump Day Tips on Wednesdays, **Amélie Meyer** for the many discussions about PhD topics during the workshops and conferences we both attended and for organising the Best Tasmanian Honey for me, **Sanaa Hobeichi** for always asking me in the kitchen how I felt on a particular day and for the many Za'atar pizza you brought to CCRC, **Diana Zhang** for the many Thursday morning coffee catch-ups during our PhD journey, and **Jules Kajtar** for running the board games group I enjoyed on countless evenings.

I thank **Joel Lüthi** and **Fabio Steffen**, my friends from high school, for the many 'Avengers Assemble!' zoom calls on weekends and for sharing the many COVID-19 related PhD struggles we all went through together, **Sandra Hauswirth** for the good times we shared during EGU, during the train ride from Vienna to Zurich and during the AGU Fall meeting in Chicago, my friends from my Master's back in Switzerland with whom I managed to stay in contact despite living on the other side of the planet: **Verena Bessenbacher**, **Manuel Bussmann**, **Anna Ehrler**, **Monika Feldmann**, **Raphael Aellig**, **Marc Schwärzel**, **Elisabeth Tschudi**, **Inne Vanderkelen**, **Sandro Vattioni** and **Joel Zeder**.

Thank you **Hiroyuki Tsujino** and **Hakase Hayashida** for providing access to the OMIP-2 model output, **Damien Irving** and **Taimoor Sohail** for calculating the CMIP6 time series and thanks to the hugely important **CMIP** and **Argo** projects for

providing access to their data sets that were used in Part 1 of the thesis. Many thanks to **Iselin Medhaug**, **Reto Knutti**, **Nicola Maher** and **Shayne McGregor** for the valuable discussions and input during the manuscript writing for Part 2. Thank you **Simon Scherrer**, **Cornelia Schwierz** and **Sven Kotlarski** for the great input during the final writing stages and the review period of our MeteoSwiss study. Further thanks goes to **NOAA's GFDL**, **ESRL**, **NODC** and the **TAO Project Office of NOAA/PMEL**, the **Japanese Meteorological Agency** and **ECMWF** for making their data sets which I used in Part 2 publicly available. Thank you **Adele Morrison** for sending me the script to analyse the observational seal data, **Georgina Harmer** for the graphics design input to the ENSO-Antarctica summary schematic, and the International **MEOP Consortium** for making the marine mammal data freely available for me to use in Part 3 of the thesis. This thesis would not have been possible without these many observational and modelling products that were made freely available online.

Thank you also to **Ivana Cerovečki** for organising my stay at Scripps and **Erich Fischer** for our discussions about Postdoc positions at AGU in Chicago, and for welcoming me back to ETH during my 2022/23 Christmas break in Zurich. My thanks also go out to my two thesis examiners, **Shang-Ping Xie** and **John Fasullo**, for their constructive and very motivating feedback.

I thank the Consortium for Ocean-Sea Ice Modelling in Australia (**COSIMA**) and their many members who helped me out during my PhD studies, especially **Andrew Kiss** and **Aidan Heerdegen**, who have helped me with many modelling issues. I am very grateful to have been and continue to be part of such a welcoming and motivating community. The simulations in this thesis were conducted with resources and services from the National Computational Infrastructure (**NCI**) which is supported by the Australian Government. I am still baffled by the computational power I was allowed to use during my research; isn't it awesome to conduct experiments on a supercomputer using more than 5000 CPUs simultaneously, with 34 GB memory per node?!

My research has been supported by a Scientia PhD scholarship from the **University of New South Wales** (Program code 1476) and by both the **ARC Centre of Excellence for Climate Extremes** (CLEX; ARC Grant No. CE170100023) and the **ARC Australian Centre for Excellence in Antarctic Science** (ACEAS; ARC Grant No. SR200100008). I am grateful for the funding I received that allowed me to accomplish so much during my PhD thesis.

And lastly, my most important thanks go out to my parents and my siblings in Switzerland. **Mum** and **Dad**, this thesis would not have been possible without your unconditional support, not only throughout the last four years but since my very first day in school. **Catherine**, **Felix**, **Nicolas** and **Louis**, thank you for always being there when I had questions about (or when I was questioning) life Down Under. Thank you for sending me photo and video updates of my nephews and niece growing up. Your support made all the difference when I was stuck in lockdown limbo during the COVID-19 pandemic.

Contents

List of Figures

List of Tables

Nomenclature

General Abbreviations

AABW	Antarctic Bottom Water
ACC	Antarctic Circumpolar Current
ACEAS	ARC Australian Centre for Excellence in Antarctic Science
AGU	American Geophysical Union
AMOC	Atlantic Meridional Overturning Circulation
AMOS	Australian Meteorological and Oceanographic Society
AR5 SPM	Summary for Policy Makers in the Fifth Assessment Report of IPCC
ARC	Australian Research Council
ASL	Amundsen Sea Low
CDW	Circumpolar Deep Water
CLEX	ARC Centre of Excellence for Climate Extremes
COSIMA	Consortium for Ocean-Sea Ice Modelling in Australia
CPU	Central Processing Unit
C-SHOR	Centre for Southern Hemisphere Oceans Research
DSW	Dense Shelf Water
ECMWF	European Centre for Mid-range Weather Forecasting
EGU	European Geophysical Union
ENSO	El Niño-Southern Oscillation
EOF	Empirical Orthogonal Function
EQ	Equator
ESRL	Earth System Research Laboratory
ETH	Swiss Federal Institute of Technology
EUC	Equatorial Undercurrent
GB	Gigabyte

GFDL	Geophysical Fluid Dynamics Laboratory
GMSST	Global Mean Sea Surface Temperature
IAC	Institute for Atmospheric and Climate Science
IPCC	Intergovernmental Panel for Climate Change
IPO	Interdecadal Pacific Oscillation
ITF	Indonesian Throughflow
KPP	K-profile Parameterisation scheme
MEOP	Marine Mammels Exploring the Ocean Project
N34	Niño 3.4 index
NOAA	National Oceanographic and Atmospheric Administration
NODC	National Oceanographic Data Center
OHC	Ocean Heat Content
OHT	Ocean Heat Transport
OHU	Ocean Heat Uptake
PC2	Second Principle Component time series
QMS	Quantitative Marine Science
RV	Research Vessel
SAM	Southern Annular Mode
SAT	Surface Air Temperature
SLP	Sea Level Pressure
SSH	Sea Surface Height
SST	Sea Surface Temperature
TAO	Tropical Atmosphere Ocean project
PMEL	Pacific Marine Environmental Laboratory
UNSW	University of New South Wales
WMT	Water Mass Transformation
WWV	Warm Water Volume

Data Set Abbreviations

Argo	Subsurface ocean temperature and salinity data set
CORE-NYF	Coordinated Ocean-ice Reference Experiment Normal Year Forcing

ERA-Interim	ECMWF Global Reanalysis data set
HadCRUT5	Hadley Centre/Climatic Research Unit Temperature data set, version 5
HadISST	Hadley Centre Sea Surface Temperature data set
JRA55-do	Japanese Reanalysis Product for ocean-sea ice models
MEOP	Marine Mammels Exploring the Ocean Project data set
NOAA's ERSST v4	NOAA's Extended Reconstructed Sea Surface Temperature data set, version 4
NOAA's OISST v2	NOAA's Optimal Interpolation Sea Surface Temperature data set, version 2
ORA-S5	ECMWF Ocean Reanalysis 5 product
SOSE	Southern Ocean State Estimate reanalysis product
WOA13 v2	World Ocean Atlas 2013 data set, version 2

Modelling Abbreviations

ACCESS-OM2	Australian Community Earth System Simmulator - Ocean Model 2
COSIMA	Consortium of Ocean-Sea Ice Modellers in Australia
CICE5.1.2	Community Ice Code model, version 5.1.2
CMIP5	Coupled Model Intercomparison Project 5
CMIP6	Coupled Model Intercomparison Project 6
FAFMIP	Flux-Anomaly Forced Intercomparison Project
MOM5.1	Modular Ocean Model, version 5.1
NCI	National Computational Infrastructure
OASIS3-MCT	Ocean Atmosphere Sea Ice Soil coupling model, version 3
OMIP-2	Ocean Model Intercomparison Project 2

Variables and Constants

A	Grid cell area
C_D	Unitless drag coefficient $(1.5 \cdot 10^{-3})$

C_p	Specific heat capacity of seawater (3992.1 J kg^{-1} K^{-1})
Δ	Change in a specific quantity
F	Surface forcing
$\boldsymbol{F}$	Vertically integrated ocean heat transport
$\mathcal{G}_{\mathcal{E}}$	WMT volume flux due to eddy mixing
$\mathcal{G}_{\mathcal{F}}$	WMT volume flux due to surface forcing
$\mathcal{G}_{\mathcal{M}}$	WMT volume flux due to vertical mixing
$\mathcal{G}_{\mathcal{I}}$	WMT volume flux due to numerical mixing
H	Grid cell heat content
$\mathbf{H}$	Location of maximum high pressure anomaly
$\mathcal{J}$	WMT volume flux due to surface volume flux
κ	Vertical diffusivity coefficient
$\mathbf{L}$	Location of minimum high pressure anomaly
∇	Gradient
∇_h	Horizontal gradient
Ψ	Volume transport
Q_{net}	Net surface heat flux
ρ_a	Reference density of air at sea level (1.25 kg m^{-3})
ρ_0	Reference density of seawater (1035 kg m^{-3})
σ	Standard deviation
SST_a	Eastern equatorial Pacific sea surface temperature anomaly
$\mathcal{T}_{ITF}$	OHT across the ITF
$\mathcal{T}_{5^\circ N+5^\circ S}$	OHT across 5°N and 5°S
τ_a	Western equatorial Pacific wind stress anomaly
τ_x	Zonal wind stress
$\overline{\tau_x}$	Climatological zonal wind stress
τ_x'	Perturbation zonal wind stresse
τ_y	Meridional wind stress
$\overline{\tau_x}$	Climatological meridional wind stress
τ_x'	Perturbation meridional wind stress
Θ	Conservative temperature
$\boldsymbol{u}$	Three-dimensional velocity field
u_{10}	Zonal wind speed at 10 m above the surface

$\overline{u_{10}}$	Climatological zonal wind speed 10 m above the surface
u'_{10}	Perturbation zonal wind speed 10 m above the surface
U_{10}	Wind speed magnitude at 10 m above the surface
v_{10}	Meridional wind speed at 10 m above the surface
$\overline{v_{10}}$	Climatological meridional wind speed 10 m above the surface
v'_{10}	Perturbation meridional wind speed 10 m above the surface
V	Grid cell volume
z	Depth direction
ZJ	Zetajoule (10^{21} J)

Units

°C	Degree Celsius
°C year^{-1}	Degree Celsius per year
°E	Degree East
°N	Degree North
°S	Degree South
°W	Degree West
hPa	Hectopascal (100 Pa)
J	Jules
J m^{-1} year^{-1}	Jules per metre per year
J m^{-2} year^{-1}	Jules per square metre per year
J year^{-1}	Jules per year
km	Kilometre
kg	Kilogramm
kg kg^{-1}	Kilogramm per kilogramm
kg m^{-2} s^{-1}	Kilogramm per square metre per second
kg m^{-3}	Kilogramm per cubic metre
K	Kelvin
m	Metre
m day^{-1}	Metres per day
m s^{-1}	Metres per second
m^{2} s^{-1}	Square metres per second

m^3	Cubic metre
$m^3\ s^{-1}$	Cubic metres per second
$N\ m^{-2}$	Newton per square metre
Pa	Pascal
Sv	Sverdrup ($10^6\ m^3\ s^{-1}$)
$W\ m^{-2}$	Watts per square metre

Scientific Activities During the Thesis

Oceanographic Voyage

May-June 2021, Research voyage on board the *RV Investigator* from Hobart to Brisbane to recover and re-deploy oceanographic moorings across the continental shelf at 27°S that measured property transports in the East Australian Current (four weeks).

Scientific Training

- February 2022, QMS Physical Oceanography Course, Hobart, Australia (one week)
- June 2019, CLEX Winter School on climate modelling, Melbourne, Australia (one week)
- Reviewer for *Geophysical Research Letters* (ISSN: 1944-8007)

National and International Conferences, Workshop and Seminar Presentations

- AMOS Conferences
    - June 2019, Darwin, Australia (oral and poster presentation)
    - February 2021 and 2022, online (oral presentations)
- AGU Fall Meetings
    - December 2020, online (oral presentation)
    - December 2022, Chicago, United States (poster presentation)
- CLEX Annual Workshops

    - November 2019, Hobart, Australia (poster presentation)
    - November 2020 and 2021, online (poster presentations)
    - November 2022, Lorne, Australia (poster presentation)
- COSIMA Annual Meetings
    - May 2020 and August 2021, online (oral presentations)
    - November 2022, Hobart, Australia (poster presentation)
- EGU General Assemblies
    - April 2021, online (oral presentation)
    - May 2022, Vienna, Austria (oral presentation)
- Ocean Sciences Meetings
    - February 2020, San Diego, United States (poster presentation)
    - February 2022, online (oral presentation)
- November 2020, Invited speaker for the College of Oceanic and Atmospheric Sciences Seminar, Oregon State University, online
- May 2022, Geophysical Fluid Dynamics Meeting, Gerringong, Australia (oral presentation)
- July 2022, Multi-scale Dynamics of the Southern Ocean Conference, Canberra, Australia (poster presentation)
- November 2022, ACEAS Annual Workshop, Hobart, Australia (oral and poster presentation)
- December 2022, Invited speaker for the Climate, Atmospheric Sciences, and Physical Oceanography Seminar, Scripps Institution of Oceanography, La Jolla, United States

Supporting Manuscript and Publications

The following manuscript and publications form the basis of this thesis. The published articles can be found in Appendix A, B and C.

1. **Huguenin, M. F.** [1, 2, 3], Holmes R. M.[1, 3, 4, 5] & England M. H.[1, 2] *Nature Communications.* (2022). **13**, 4921. https://doi.org/10.1038/s41467-022-32540-5
2. **Huguenin, M. F.**[1, 3, 6], Holmes R. M.[1, 3, 4] & England M. H.[1, 3] *Journal of Climate.* (2020b). **33**:9945–9964. https://doi.org/10.1175/JCLI-D-20-0198.1
3. **Huguenin, M. F.**[1, 2, 3], Holmes R. M.[3, 4, 5, 7], Spence P. [8, 9, 10] & England M. H.[2, 11]. Submitted to *Geophysical Research Letters.*

I also worked on the following publication during my PhD candidature. This work was initiated during a research internship prior to the start of my PhD and completed within the first year.

4. **Huguenin, M. F.**[1, 3, 6, 12], Fischer, E. M.[6], Kotlarski, S.[12], Scherrer, S. C.[12], Schwierz, C.[12], & Knutti, R.[6] (2020a). Lack of Change in the Projected Frequency and Persistence of Atmospheric Circulation Types Over Central Europe. *Geophysical Research Letters.* **47**. https://doi.org/10.1029/2019GL086132

1. Climate Change Research Centre, University of New South Wales, Sydney, NSW, Australia 2. ARC Australian Centre for Excellence in Antarctic Science, University of New South Wales, Sydney, NSW, Australia 3. ARC Centre of Excellence in Climate Extremes, University of New South Wales, Sydney, NSW, Australia 4. School of Mathematics and Statistics, University of New South Wales, Sydney, NSW, Australia 5. School of Geosciences, University of Sydney, Sydney, NSW, Australia 6. Institute for Atmospheric and Climate Science, ETH Zürich, Zürich, Switzerland 7. Australian Bureau of Meteorology, Sydney, New South Wales, Australia 8. ARC Australian Centre for Excellence in Antarctic Science, University of Tasmania, Tasmania, Australia 9. Institute for Marine and Antarctic Studies, University of Tasmania, Tasmania, Australia10. Australian Antarctic Partnership Program, University of Tasmania, Tasmania, Australia 11. Centre for Marine Science and Innovation, University of New South Wales, Sydney, New South Wales, Australia12. Federal Office of Meteorology and Climatology, MeteoSwiss, Zürich, Switzerland

Copyright Statements

Parts of this thesis have been reproduced from published work elsewhere. Included here are copyright statements for those works consistent with the requirements stated by the copyright holders. The source for all other material in this thesis is clearly indicated throughout the document using the citations that are listed alphabetically in the Bibliography section at the end.

- Part 1 has been reproduced from an article published in the journal *Nature Communications* under the CC BY licence (Creative Commons Attribution 4.0 International licence): https://creativecommons.org/licenses/by/4.0/.
- Part 2 has been reproduced from an article published in the *Journal of Climate*. ©American Meteorological Society. Used with permission.
- The additional publication in Appendix C is under the CC BY-NC-ND licence.

- The picture of Globi hidden in the thesis has been used with permission. ©Orell Füssli AG, Globi Verlag, Imprint Orell Füssli Verlag.

Preface

Motivation and Objectives

The global ocean covers 71% of our planet's surface and plays a key role in regulating our climate system. Over the last 50 years, the ocean has taken up over 40% of our carbon dioxide emissions and over 90% of the excess heat trapped in the Earth system (von Schuckmann et al., 2020; Cheng et al., 2022). On the one hand, this buffers the worst impacts of climate change in the atmosphere and on land. On the other hand, ocean warming causes sea level rise through thermal expansion of water masses (IPCC, 2019), increases stress for marine ecosystems (McWhorter et al., 2022), and increases the intensity of tropical cyclones because warm sea surface temperatures (SSTs) are needed to sustain them (Knutson et al., 2020). To limit the worst impacts of climate change on the natural world, it is therefore critical to understand what has driven the unprecedented changes in ocean temperatures over the last 50 years, as well as how it is distributed in both space and time.

Our current understanding of ocean heat content (OHC) changes is limited by sparse observational data, especially before the onset of the international Argo program of profiling floats in 2005 (Argo, 2021). These floats measure temperatures and salinity throughout the upper 2000 m between 60°S–60°N, and over 12,000 data profiles are collected each month (Argo, 2023). However, observations are especially rare in the deep ocean and in sea ice covered regions because of access difficulties. Deep Argo, a program that includes floats descending down to 4000 m depth, is currently in its pilot stage (Johnson et al., 2015; Liu et al., 2023; Zilberman et al., 2023).

In observational data sets, it is not possible to separate the individual mechanisms that change ocean temperatures. For example, there is no clear way to attribute a given ocean warming signal to wind- vs. radiation-driven changes. A better understanding through alternative methods is therefore needed to not only separate these different

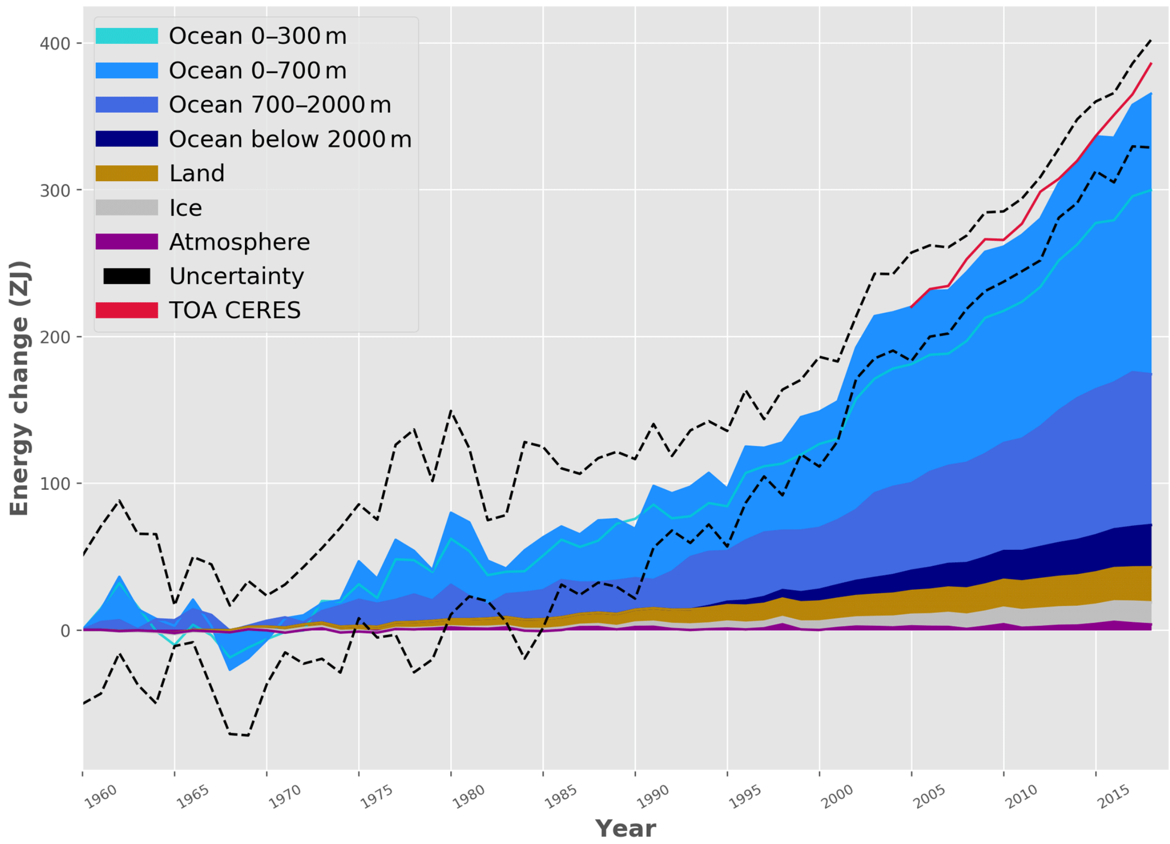

Figure P1: The Earth's heat inventory (ZJ = 10^{21} J) relative to the year 1960 from von Schuckmann et al. (2020). The largest amount of anomalous heat is stored in the upper 700 m of the ocean. The land, ice and atmosphere contributions are much smaller. The uncertainty in the total estimate is given as the black dashed line and decreases with time as more observations became available. The red line represents the net heat flux at the top of the atmosphere (TOA) from the NASA CERES program (e.g., Loeb et al., 2012). This figure has been reproduced from von Schuckmann et al. (2020) under the CC BY licence (see page xxxv).

drivers of ocean warming but also to separate the anthropogenic forcing from internal climate variability, because major modes of internal variability are projected to change in the future (Cai et al., 2014, 2015, 2021; Goyal et al., 2021b; McGregor et al., 2022). This is one of the goals of this PhD thesis.

The dominant mode of global interannual climate variability is El Niño-Southern Oscillation (ENSO). Its impacts include droughts, heatwaves, heavy rainfall and it changes the occurrence of tropical cyclones around the globe (Diaz et al., 2001; Smith et al., 2007). Due to these large impacts on society, it is critical to better understand its underlying dynamics to improve ENSO forecasts, and to understand how climate change might influence this mode in the future. While it is well known that ENSO impacts global ocean temperatures (Roemmich and Gilson, 2011; Roemmich et al., 2015;

Wu et al., 2019a), many uncertainties about its underlying dynamics remain including exactly how its two phases (El Niño and La Niña) recycle heat and how asymmetries in the oscillation manifest as residual ocean heat anomalies. These uncertainties stem in part from the difficulties in measuring and modelling the various processes that contribute to the heat budget in the upper equatorial Pacific where ENSO variability originates from. Part 2 of this thesis will be focusing on these uncertainties.

A key metric to assess the state of ENSO and to predict future events is the equatorial Pacific warm water volume (WWV, defined as the volume of water above 20°C between 5°S and 5°N in the equatorial band). WWV is a key metric because it leads El Niño and La Niña by 6 to 8 months (e.g., Meinen and McPhaden, 2000; Bosc and Delcroix, 2008; McPhaden, 2012; Izumo et al., 2018; Timmermann et al., 2018; Neske and McGregor, 2018). While the horizontal recharge and discharge of WWV into or out of the equatorial band is well understood based on surface wind and surface water mass transport changes (Meinen and McPhaden, 2000, 2001; Lengaigne et al., 2012; McGregor et al., 2013, 2014; Neske and McGregor, 2018), WWV is influenced by more than just horizontal fluxes. Vertical and diabatic processes also influence WWV and are less understood. Research into this area is important as the vertical heat fluxes have the potential to store anomalous heat in layers away from the surface region, causing sea level rise by thermal expansion, or potentially alter ENSO variability when resurfacing later. In Part 2 of this thesis, a WWV heat budget analysis will be used to determine the contributions of all fluxes to heat content changes during ENSO's recharge and discharge phases.

While ENSO's impact on ocean temperatures is largest in the equatorial band, it also has strong links elsewhere in the world, including to West Antarctica due to its atmospheric teleconnections to the Amundsen Sea. These teleconnections are semi-stationary weather patterns that typically co-occur during either El Niño or La Niña events. The dynamics of the atmospheric teleconnection to the Amundsen Sea have been highlighted in various studies (e.g., Turner, 2004; Hoskins and Ambrizzi, 1993; Hosking et al., 2013; Raphael et al., 2016), but their oceanic impact on the West Antarctic circulation still remains largely unknown. Observations in this region are sparse and variability from other sources can mask the ENSO signal. Recent studies by Paolo et al. (2018); Holland et al. (2019); Naughten et al. (2022); Oelerich et al. (2022) suggest that

ENSO, through its teleconnections, can have a considerable impact on West Antarctic shelf temperatures, and thus on melting rates of ice shelves in this region. However, the ocean dynamics driving this shelf warming during El Niño are not well understood. Therefore, in Part 3 of this thesis, the link between atmospheric ENSO anomalies and their imprint on the West Antarctic shelf circulation will be investigated to better understand the interannual variability of ice shelf melting.

Numerical ocean circulation models are important tools to investigate the processes and dynamics of ocean temperature changes highlighted here. These models can be forced by observed atmospheric fields which means that they keep track with the natural variability in the observations. While subject to their own biases and limitations, a major advantage of numerical models is that different drivers of OHC change can be analysed in isolation by conducting perturbation experiments and using heat budget diagnostics. In this way, models can help address some of the limitations arising from using observational products alone. In this thesis, a global ocean-sea ice model will be used to better understand the processes and dynamics of multi-decadal to interannual global and regional ocean temperature changes over the last half century.

As this thesis evolved, three parts with the following goals were defined:

1. To show where and how excess heat is absorbed into the ocean and where it resides today. This is important to understand global and regional thermosteric sea level rise, as well as how it might affect marine ecosystems.
2. To analyse the processes driving variability in Pacific WWV during ENSO events, in particular the diabatic processes associated with surface heat fluxes and turbulent mixing. This can help improve predictions of future ENSO events as WWV leads El Niño and La Niña events by 6 to 8 months (Meinen and McPhaden, 2000; Bosc and Delcroix, 2008; McPhaden, 2012; Izumo et al., 2018; Timmermann et al., 2018; Neske and McGregor, 2018).
3. To examine the impact of ENSO events on subsurface West Antarctic shelf temperatures. This will give valuable information about how El Niño and La Niña can modulate West Antarctic continental shelf temperatures today, and how future events might contribute to accelerated basal melting of grounded ice shelves.

The results from each of these goals are presented chronologically as self-contained studies in Parts 1, 2 and 3 of this thesis. Each part contains an abstract, an introduction, a methods section, a presentation of the results, a discussion that puts the results in the context of other recent studies, and a conclusion. The Concluding Remarks in this thesis briefly summarises the findings of each part and lists potential future projects based on questions that arose while working on this thesis.

Background

This section explains key aspects of the large-scale dynamics in the Southern Ocean, the main processes driving WWV changes during ENSO events as well as ENSO's teleconnections to the Amundsen Sea in more detail than in the ensuing parts of the thesis, where the text had to be kept short to comply with manuscript guidelines.

The Southern Ocean and West Antarctic Circulation

The Southern Ocean plays a key role in global climate, despite covering only about 15% of the total ocean's surface area (when defined south of 45° latitude). This stems from its unique geographical setup with a circumpolar ocean and uninterrupted westerly winds that encircle Antarctica, and drive the eastward flowing Antarctic Circumpolar Current (ACC, Fig. P2, P3). This current has important implications for the global ocean circulation and global climate because it enables exchanges between the Pacific, Indian and Atlantic ocean basins. The Southern Ocean smooths out zonal (East-West) differences in water properties, while also isolating Antarctica from warm waters further north (Rintoul and Naveira Garabato, 2013). The strong westerly winds steepen density surfaces towards the south of the ACC (Rintoul and Naveira Garabato, 2013), bringing cold, nutrient rich water masses towards the surface.

This wind-induced upwelling of cold water masses to the surface allows for efficient heat uptake from the atmosphere, sustained by persistent Ekman transport of these waters northward, where they subduct below warmer (and less dense) subtropical waters into the ocean's interior (Fig. P3 and Lenn and Chereskin (2009); Frölicher et al. (2015);

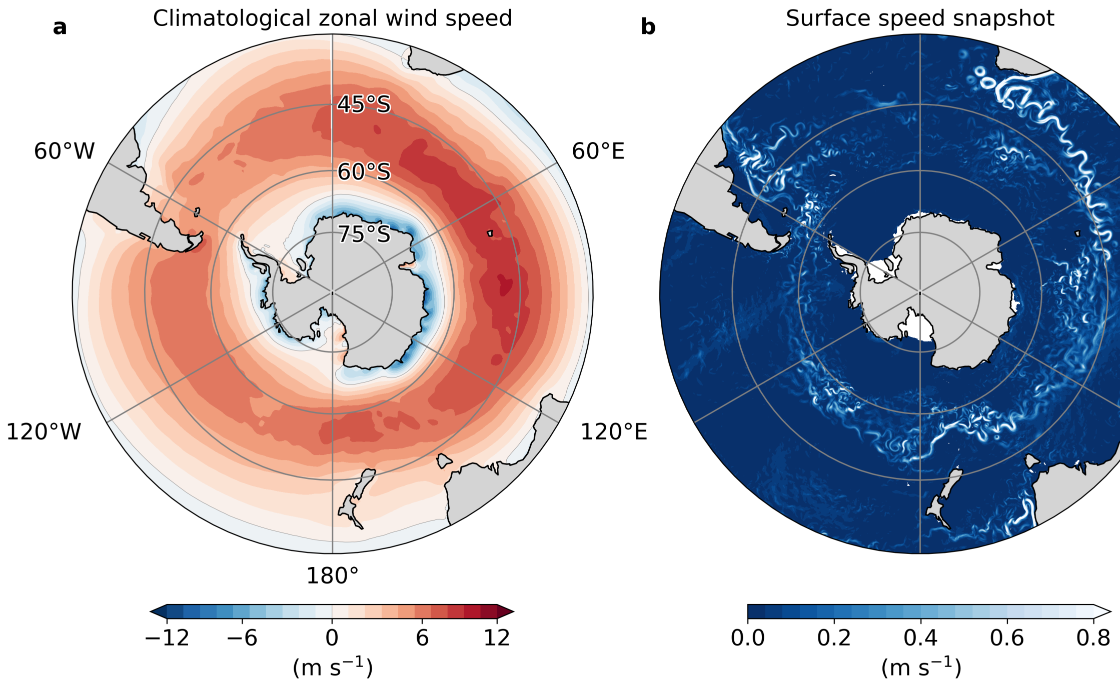

Figure P2: (a) Climatological Southern Ocean zonal winds in the JRA55-do data set (m s^{-1}, Tsujino et al. (2018)). (b) Daily snapshot of mean surface speed (m s^{-1}) from a hindcast simulation of the 1/10° ocean-sea ice model used in this thesis, showing the Antarctic Circumpolar Current and highlighting the key role of mesoscale eddies in property transports around the Antarctic continent.

Armour et al. (2016); Morrison et al. (2015)). The Southern Ocean therefore acts as an important basin in exchanging heat, and also carbon dioxide and oxygen between the atmosphere and the ocean on a global scale (Rintoul and Naveira Garabato, 2013).

Over recent decades and due to anthropogenic climate change, this natural overturning process has experienced changes. Cold upwelled water masses have taken up excess heat from the warmer atmosphere and then transported this excess heat into the ocean's interior (Frölicher et al., 2015; Armour et al., 2016; Shi et al., 2018). However, whether it is only the warming atmosphere and increased radiative fluxes that are driving this anomalous heat uptake, or whether changing surface winds are also contributing, is not clear. Furthermore, it is uncertain where the anomalous heat signal is accumulating today. It is therefore of critical importance to investigate the individual heat uptake drivers and their changes, given that anomalous ocean heat is leading to sea level rise through thermal expansion. The main focus of Part 1 will be on separating the wind- from radiation- and temperature-driven heat uptake, both globally and regionally.

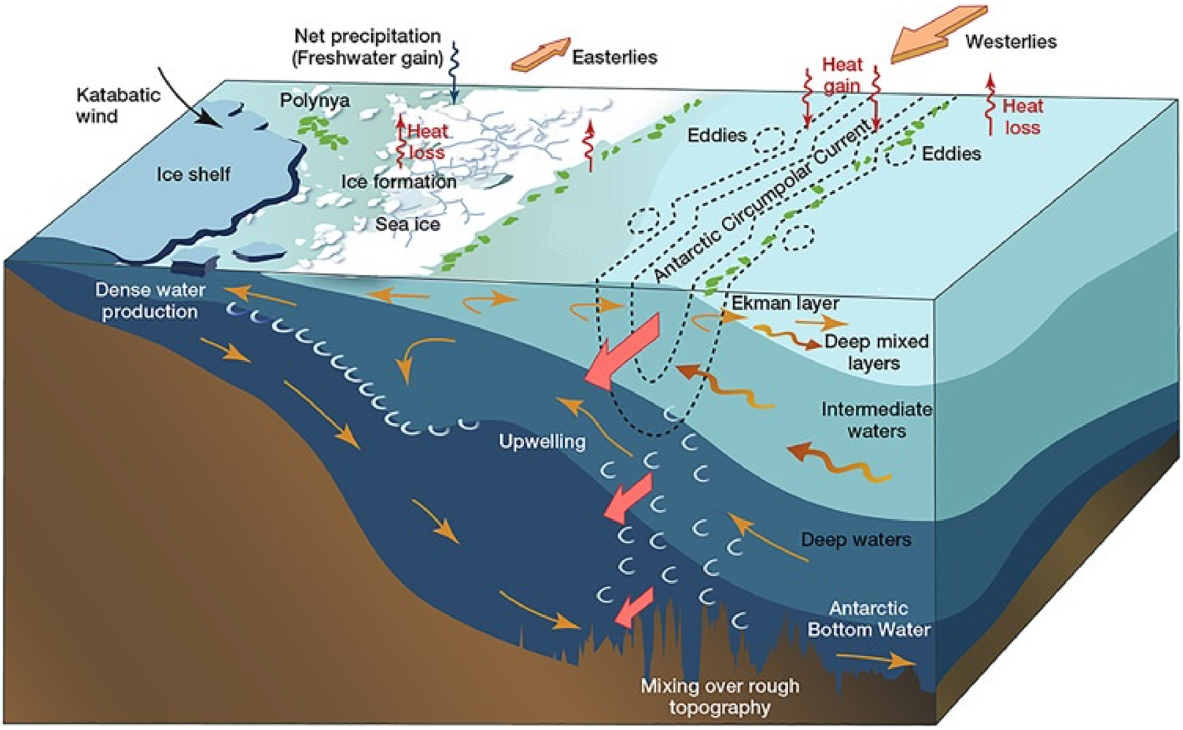

Figure P3: Schematic of key physical processes in the Southern Ocean and Antarctica from Kennicutt et al. (2019). South and West are to the left and foreground of the figure. The westerly winds encircling Antarctica drive the Antarctic Circumpolar Current (the red arrows coming out of the plane) and the exchange of heat and freshwater at the sea surface. These winds also drive a northward Ekman transport of surface waters in the deep mixed layers. The consistent export of waters away from the surface enables upwelling of intermediate waters, and the divergence of the westerly winds creates two branches of these upwelled waters. The northward branch accumulates anomalous heat from the atmosphere above and is eventually subducted below warmer subtropical waters around 45°S. Upwelled waters flowing south towards Antarctica, cool and get saltier when sea ice is formed. They increase in density and are transformed into Dense Shelf Water (DSW) and Antarctic Bottom Water (AABW). These two water masses experience mixing and entrainment with the surrounding southward flowing waters as they cascade into the abyssal ocean. The production of both DSW and AABW around the Antarctic continent is closely linked to the strength of the prevailing coastal easterly and katabatic northerly winds as they modulate the production of sea ice and brine rejection. Brine rejection is the process whereas salty water is expelled during sea ice formation as the salt does not fit into the ice crystal structure. The katabatic winds can open up polynyas, regions of open water surrounded by all sides with sea ice, when the winds advect ice packs away from the coast. The coastal easterlies also drive a wedge of cold water towards the continent via Ekman transport and inhibit the upwelling of warm Circumpolar Deep Water onto the shelf in warm shelf regimes around the continent. This figure has been reproduced from Kennicutt et al. (2019), see page xxxv for the copyright statement.

Further south and towards the continental shelf of Antarctica, the prevailing wind direction is easterly (Fig. P2a and P3). These coastal winds sustain the Antarctic slope current and the Antarctic slope front (Thompson et al., 2018; Huneke et al., 2022; Neme et al., 2022; Dawson et al., 2023, Fig. P4). The Antarctic slope current is a topographically constrained current that modulates the flow of water masses and nutrients along the Antarctic margin, while the Antarctic slope front separates warm Circumpolar Deep Water (CDW) that resides mostly off the continental shelf from colder water masses that reside dominantly on the shelf. The climatological coastal easterly winds sustain a continuous poleward Ekman transport of cold surface waters that keep a large reservoir of warm CDW north of the shelf break.

If the strength of these coastal easterlies decreases (whether through natural climate variability or through anthropogenic forcing), more warm CDW might flow onto the continental shelf, increase basal melting of grounded ice shelves, reduce their buttressing of the Antarctic ice sheet and cause increased sea level rise. Spence et al. (2014, 2017); Holland et al. (2019); Naughten et al. (2022) have shown how wind anomalies associated with changes in the Southern Annular Mode (SAM), decadal Pacific climate variability or anthropogenic forcing can cause changes in the inflow of CDW onto the shelf. However, the isolated role of ENSO on Antarctic shelf temperature variability has not yet been shown in detail. This will be addressed in Part 3 of this thesis.

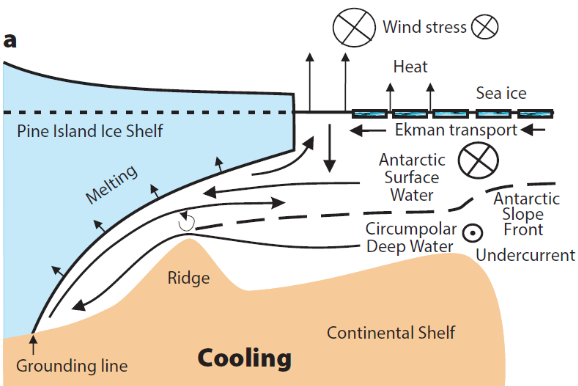

Figure P4: Schematic of the shelf circulation variability in the Amundsen Sea from Jenkins et al. (2016). (a) Cooling of the shelf occurs when the easterly coastal wind/wind stress increases (⊗ indicates a flow into the plane). This increases the chance for polynyas to form, increases DSW formation which in turn decreases the Antarctic slope current and the volume of warm CDW that upwells onto the shelf. (b) Warming is promoted when the easterly winds decrease, and polynyas occur less often. This decreases DSW formation and enhances the inflow of warm CDW onto the shelf and into ice shelf cavities. This figure has been reproduced from Jenkins et al. (2016) under the CC BY 4.0 licence (see page xxxv).

ENSO's Warm Water Volume and its Teleconnections to Antarctica

The fundamental nature of heat recharge and discharge during ENSO events can be understood with the Recharge-Discharge Oscillator theory by Jin (1997b). With this idealised theory, ENSO is defined as a harmonic oscillator with two neutral phases, an El Niño phase and a La Niña phase, and with the depth of the equatorial thermocline (representing the WWV) as a key metric (Figure P5).

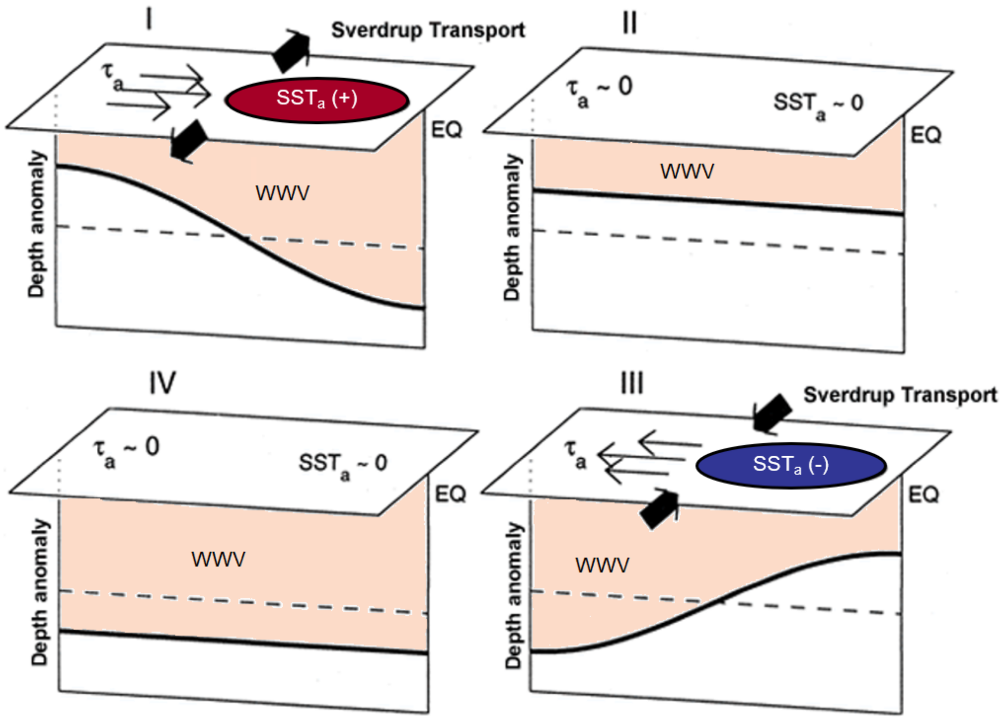

Figure P5: Idealised schematic highlighting the physical concepts of the ENSO Recharge-Discharge Oscillator theory from Jin (1997b). The light arrows show wind stress anomalies (τ_a) in the western equatorial Pacific, the SST_a labels show the anomalous sea surface temperatures in the eastern equatorial Pacific and the bold black arrows wind-induced Sverdrup discharge/recharge of warm water volume out of or into the equatorial band. The solid black line in the depth-longitude panel is the thermocline (i.e., the 20°C isotherm) with the warm water volume (WWV) defined as the volume of water above. The dashed black line is the climatological position of the thermocline. The *EQ* label highlights the equatorial plane. An oscillation follows the panel numbering clockwise from I to IV with Panel I representing El Niño and Panel III La Niña conditions. This schematic and caption have been adapted from Meinen and McPhaden (2000), with permission from the American Meteorological Society (see page xxxv).

ENSO and Warm Water Volume Dynamics

In the climatological neutral state, large-scale ascent of air masses occurs over the western Pacific basin with large-scale descent over the eastern basin (i.e., the atmospheric Walker circulation). The associated atmospheric pressure gradient between these two regions induces easterly trade winds that push warm water towards the western Pacific. Due to Ekman suction, cold water upwells along the eastern boundary and the thermocline slopes towards the surface from West to East. The Bjerknes feedback explains the positive feedback loop that results from changes in the trade winds: a strengthening of the trade winds causes increased upwelling of cold water in the eastern equatorial Pacific, decreases local SSTs, increases the East-West gradient of air pressure across the basin which in turn increases the strength of the trade winds. This positive feedback loop (given stronger trade winds) transitions the coupled atmosphere-ocean system into a La Niña phase (panel III, Fig. P5). In this transition, WWV increases through the wind-induced (Sverdrup) transport of water into the equatorial band (bold black arrows in Panel III that highlight the zonally-integrated WWV transport arising from the changes in the wind stress curl).

The La Niña event decays when easterly trade winds once again return to climatological conditions. However, WWV is still large and this prepares the system to change into an El Niño phase as soon as trade winds become weaker than during the climatology. A weakening of the trade winds in this phase of the oscillation once again induces the positive Bjerknes feedback loop: reducing upwelling of cold water in the eastern equatorial Pacific, warming SSTs there, reducing the East-West air pressure gradient which in turn further decreases the trade wind strength. While the strengthened trade winds during La Niña caused an inflow of warm water into the equatorial band (i.e., WWV recharge), the weaker trade winds during El Niño cause the opposite and most of the WWV previously built up is being discharged (panel I, Fig. P5).

While the recharge and discharge of WWV through adiabatic Sverdrup transport has been highlighted here and is well understood (Meinen and McPhaden, 2000, 2001; Lengaigne et al., 2012; McGregor et al., 2013, 2014; Neske and McGregor, 2018), diabatic surface heat fluxes and vertical mixing also influence this important metric. Their role may be especially large in the eastern equatorial Pacific where SSTs vary strongly throughout the oscillation, yet the role of these diabatic fluxes has not yet been shown conclusively. Highlighting the role of diabatic WWV fluxes will be the focus of Part 2 of this thesis.

ENSO teleconnections to West Antarctica

ENSO impacts the global weather and climate through its atmospheric teleconnections. While the strongest impacts are felt throughout the Indo-Pacific region, these teleconnections extend to the Antarctic continent (Fig. P6).

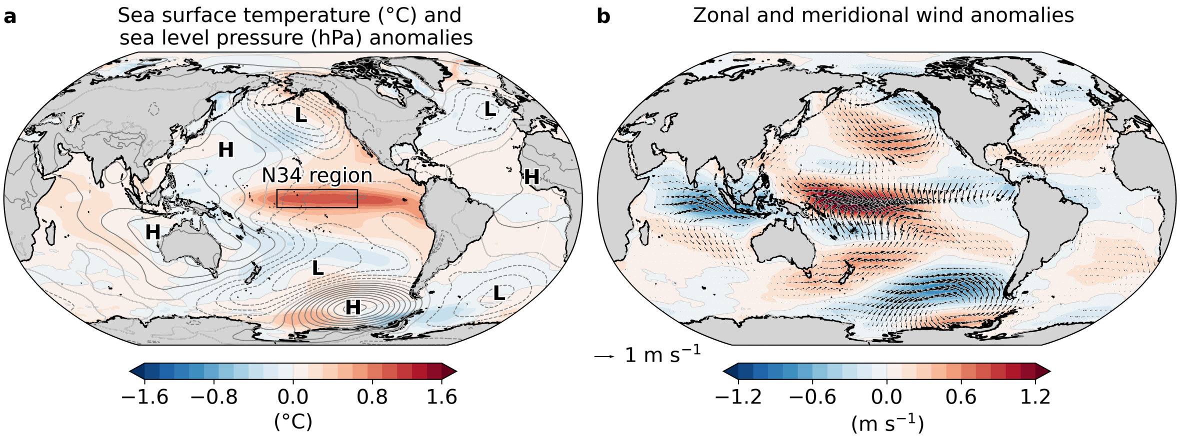

Figure P6: Regression maps of atmospheric teleconnections during ENSO. (a) Map of the Niño 3.4 index regressed onto SST (°C, colour shading) and sea level pressure (hPa, contours) anomalies. (b) ENSO regression map for surface wind anomalies (m s^{-1}) with the zonal component colour shaded. These panels were calculated by regressing the standardised Niño 3.4 index from 1958-2018 onto the atmospheric anomalies throughout the same period and calculating the average over the time dimension.

During El Niño events, the eastward shift in the large-scale Walker circulation that coincides with the SST anomalies excites an atmospheric Rossby wave that travels towards the West Antarctic region and manifests as a weakening of the Amundsen Sea Low (ASL, Hosking et al. (2013); Turner (2004) and the bold **H** symbol over West Antarctica in Fig. P6a that represents the anomalous high pressure anomaly during El Niño). This weakening coincides with an anticyclonic (i.e., anticlockwise) circulation of surface winds (Fig. P6b) together with changes in air temperatures, precipitation and sea ice concentrations in West Antarctica (Hosking et al., 2013). The response during La Niña is largely opposite, with an atmospheric wave excited from the western equatorial Pacific that strengthens the ASL, and causing cyclonic (i.e., clockwise) surface wind anomalies on the West Antarctic continental shelf. While this link between ENSO and the West Antarctic surface climate is well known (Turner, 2004; Hosking et al., 2013; Rahaman et al., 2019; Li et al., 2021), the impact of these atmospheric anomalies, and in particular the wind anomalies, on the ocean circulation has yet to be investigated. This will be explored in Part 3 of this thesis.

Thesis Overview

The remainder of this thesis consists of three parts, each presented as its own self-contained study. Parts 1 and 2 have been published as Huguenin et al. (2022a, 2020) and have been reproduced with copyright permission (see page xxxv). The contents of Part 3 have been submitted for a publication to *Geophysical Research Letters*. The referenced Figures and Tables within each part can be found labelled throughout and in the Extended Data sections for each part. The references to scientific literature are consolidated into a single alphabetic bibliography at the end of the thesis. As each part contains a specific Discussion and Conclusion section, the Concluding Remarks are kept short. The appendices contain copies of the two published journal articles (Parts 1 and 2) alongside a study that was completed during the PhD research.

Part 1 focuses on the drivers and distribution of global ocean heat uptake (OHU) over the last 50 years. This work is motivated by the observational study of Roemmich et al. (2015) who investigated OHC changes over the 2005 to 2015 period and by Frölicher et al. (2015) who used coupled climate models with their own independent climate variability to explore uptake, transport, and regional trends of oceanic anthropogenic carbon and heat over 1861–2005. In this study, a global ocean-sea ice model is first equilibrated to a 1960s climate, a period before the recent accelerated OHU occurred. Then, the model is forced with observed atmospheric fields in different hindcast simulations over the last 50 years. The analysis focuses on which atmospheric changes, and over which part of the global ocean, have contributed to the large heat uptake since the 1970s. Once taken up, it is investigated where the anomalous heat signal is being transported to within the global ocean and where it is accumulating now.

Part 2 examines and quantified the processes that contribute to WWV variability in the equatorial Pacific. Here, the water mass transformation framework in temperature space is employed to isolate the contribution of diabatic surface forcing and vertical mixing to WWV change. Previous studies have found contradictory results, with some suggesting their significance in changing WWV on ENSO time scales (e.g., Meinen and McPhaden, 2000; Clarke et al., 2007; Lengaigne et al., 2012) while others find the opposite (e.g., Bosc and Delcroix, 2008; Brown and Fedorov, 2010). In this part, an in-depth analysis of the WWV budget is performed in both idealised and realistic settings to resolve this disagreement.

Part 3 shows how changing coastal surface winds over West Antarctica during El Niño and La Niña events impact the poleward Ekman transport of surface water masses and enable or inhibit upwelling of warm Circumpolar Deep Water onto the continental shelf. This part builds upon Paolo et al. (2018) that highlights the link between ice shelf mass loss and ENSO events, and Holland et al. (2019) that studied the impact of multi-decadal wind changes on the West Antarctic continental shelf. While these studies find that interannual atmospheric variability has the potential to impact West Antarctic ice shelves, they do not examine the associated ocean dynamics during ENSO events. Here, the analysis focuses on shelf temperature impacts from composites of four strong El Niño and four strong La Niña events observed since 1958.

In summary, this thesis aims to further our understanding of the processes and dynamics underlying the unprecedented ocean temperature changes and their interannual variability over the last 50 years both globally and regionally. This is done using a combination of idealised and realistic numerical ocean model simulations which make it possible to (1) apply precise budget diagnostics to understand contributions to heat content changes and (2) perform sensitivity experiments where individual forcing factors are applied separately.

1

Drivers and Distribution of Global Ocean Heat Uptake Over the Last Half Century

Huguenin, M. F. [1, 2, 3], Holmes R. M.[1, 3, 4, 5] & England M. H.[1, 2] *Nature Communications.* (2022). **13**, 4921. https://doi.org/10.1038/s41467-022-32540-5 *

M. F. H. performed the analyses and wrote the initial draft of the paper in discussion with R. M. H. and M. H. E. All authors formulated the experimental design, contributed to interpreting the results and refinement of the paper.

The published version of this part can be found in Appendix A.

1. Climate Change Research Centre, University of New South Wales, Sydney, NSW, Australia 2. ARC Australian Centre for Excellence in Antarctic Science, University of New South Wales, Sydney, NSW, Australia 3. ARC Centre of Excellence in Climate Extremes, University of New South Wales, Sydney, NSW, Australia 4. School of Mathematics and Statistics, University of New South Wales, Sydney, NSW, Australia 5. School of Geosciences, University of Sydney, Sydney, NSW, Australia ∗. This publication was slightly changed from its original version to ensure consistency throughout this thesis.

Abstract Since the 1970s, the ocean has absorbed almost all of the additional energy in the Earth system due to greenhouse warming. However, sparse observations limit our knowledge of where ocean heat uptake (OHU) has occurred and where this heat is stored today. Here, we equilibrate a reanalysis-forced ocean-sea ice model, using a spin-up that improves on earlier approaches, to investigate recent OHU trends basin-by-basin and associated separately with surface wind trends, thermodynamic properties (temperature, humidity and radiation) or both. Wind and thermodynamic changes each explain ∼50% of global OHU, while Southern Ocean forcing trends can account for almost all of the global OHU. This OHU is enabled by cool sea surface temperatures and sensible heat gain when atmospheric thermodynamic properties are held fixed, while downward longwave radiation dominates when winds are fixed. These results address long-standing limitations in multi-decadal ocean-sea ice model simulations to reconcile estimates of OHU, transport and storage.

1.1 Introduction

The ocean plays a critical role in modulating the Earth's climate system and over the last 50 years it has taken up over 89% of the excess energy due to greenhouse warming (von Schuckmann et al., 2020; Rhein et al., 2013; Levitus et al., 2012; IPCC, 2013; Meyssignac et al., 2019). Since the early 1990s, the rate of ocean warming has likely doubled (IPCC, 2019). However, our current understanding of the spatial distribution of ocean heat uptake (OHU) and storage is limited, not least because of sparse observations with large uncertainties, especially in sea-ice covered regions (Durack et al., 2014) and the deep ocean (Levitus et al., 2012). For example, reliable observations of ocean heat content (OHC) in the upper 2000 m only start in 2005 with the Argo program that covers 60°S to 60°N (Argo, 2021). Before 2005, good observations are only available in the upper 700 m from expendable bathythermographs (Abraham et al., 2013) and from a few select deep ocean cruise ship measurements (Purkey and Johnson, 2010; Desbruyères et al., 2016). Observation-based studies therefore focus mainly on trends over much shorter time periods (e.g., since 2005 (Roemmich et al., 2015) or since the early 1990s (Shi et al., 2021)).

Fully coupled atmosphere-ocean general circulation models and ocean-sea ice models simulate a complete representation of the global ocean and are now increasingly used to assess the OHC evolution. However, fully-coupled models from the Coupled and Flux-Anomaly-Forced Model Intercomparison Projects (CMIP, Eyring et al. (2016) and FAFMIP, Gregory et al. (2016) respectively) generally exhibit larger biases than ocean-sea ice models, and simulate an internal climate variability that is independent of observations. Modelling studies have investigated recent trends mainly in idealised settings (Gregory et al., 2016; Dias et al., 2020) or in coupled simulations with an independent climate variability (Frölicher et al., 2015; Eyring et al., 2016). In contrast, ocean-sea ice models are constrained by atmospheric fields from a reanalysis product, and therefore follow the observed trajectory of internal and forced climate variability.

Global climate models (both fully coupled and ocean-sea ice only) suffer from internal model drift due to errors in the representation of physical processes, and thus they require a spin-up to equilibrate their climate and minimise drift. In ocean-sea ice models, a common spin-up approach, used for the Ocean Model Intercomparison Project phase 2 (OMIP-2, Tsujino et al. (2020), applies six repeat cycles of 1958 to 2018 atmospheric forcing from the Japanese reanalysis data set JRA55-do (Tsujino et al., 2018). However, there are two limitations associated with this approach: (1) after each cycle, the model experiences a large shock and associated recovery period when the forcing suddenly switches from the year 2018 back to 1958 and (2) it is unclear how to account for model drift without a parallel running control simulation (Extended Data Fig. 1.7).

In this study we address these limitations of the OMIP-2 approach by introducing a spin-up protocol for global ocean-sea ice models and illustrate its benefits using the ACCESS-OM2 ocean-sea ice model (Kiss et al., 2020). The spin-up is performed using repeat decadal cycles of the JRA55-do reanalysis forcing from 1962 to 1971, corrected for pre-industrial times, to equilibrate the model to a state prior to the recent rapid acceleration in OHU (Fig. 1.1 and Methods). There are no longer large initial shocks at the beginning of each spin-up cycle and we can account for model drift by subtracting the linear trend from a parallel control repeat decade simulation (Fig. 1.1b, c). Using this approach in an observationally constrained model gives us an estimate of the actual trajectory of OHC, including the multi-decadal internal variability since the 1970s. By decomposing the atmospheric trends into processes and regions (Methods), we can attribute the global heat uptake by drivers and basins over this period.

Limitations in our results arise from the use of a single model with a 1° horizontal resolution, the biases related to errors in the model's representation of physical processes and uncertainties in reconstructing past atmospheric forcing. Uncertainties also arise from inherent uncertainties in the reanalysis product used, including the reliability of the implied radiative heat flux trends due to both greenhouse gases and aerosols, which remain poorly constrained in many observational products. Heat transport and heat loss across the surface can be dependent on the model resolution (Grist et al., 2018) with biases expected to decrease in a finer grid (Tsujino et al., 2020) because mesoscale eddies (that are absent in our 1° configuration) have been shown to strongly impact the ocean circulation and heat uptake on the global scale (Marshall et al., 2017; Martínez-Moreno et al., 2021). The absence of eddies also adds a caveat to our specific partitioning of the wind- and thermal property-driven heat uptake fluxes. However, the model configuration used here matches the typical resolution of most OMIP-2 and CMIP6 ensemble members, and heat content anomalies following the OMIP-2 protocol are similar when using the higher resolution configurations of the model (Extended Data Fig. 1.7b). The low computational cost of the model we employ also allowed us to minimise deep ocean model drift with a long spin-up and permitted a suite of multi-decadal simulations that would otherwise be too expensive to explore using higher-resolution models.

1.2 Results

1.2.1 Global Ocean Heat Uptake

The observations of upper 2000 m global OHC (Levitus et al., 2012) reach 2.40×10^{23} J in 2017 relative to the 1972 to 1981 baseline (dashed red line, Fig. 1.2a). We choose this baseline as it ends before the volcanic eruption of El Chichón in mid-1982 and the OMIP-2 models prior to 1972 undergo a very strong global cooling period (Extended Data Fig. 1.8a). The multi-model mean from the fully coupled CMIP6 model suite

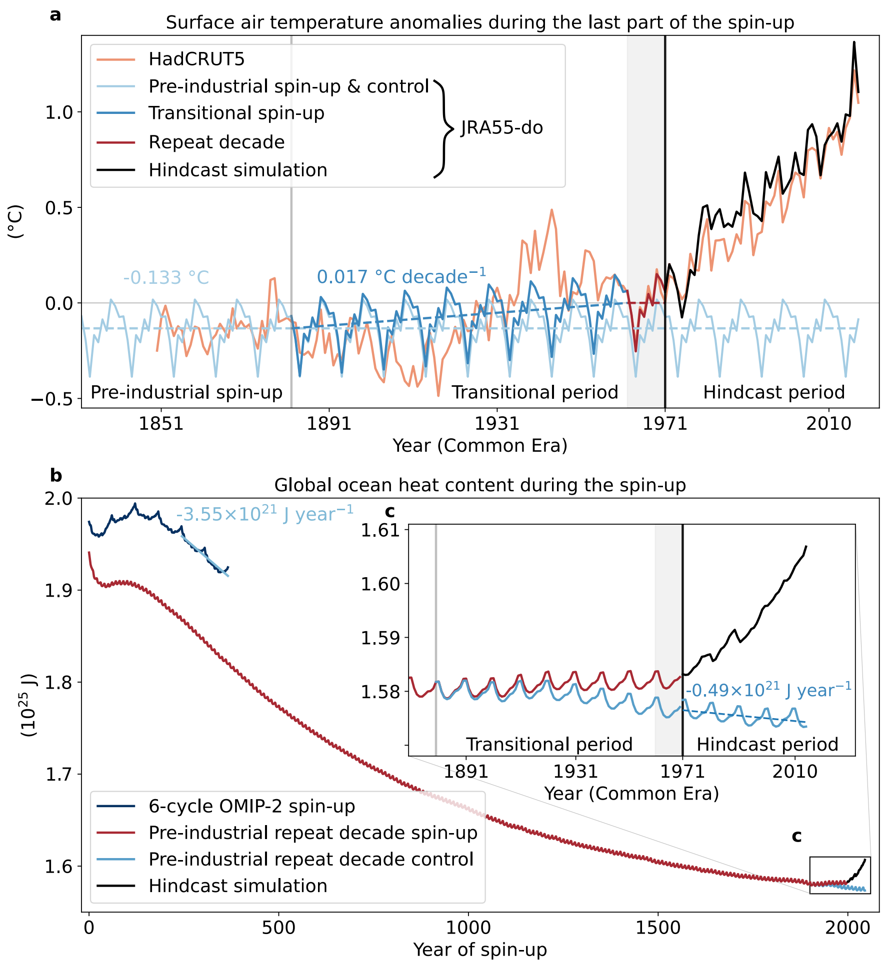

Figure 1.1: Experimental design of the spin-up. **a**, Time series of global mean surface ocean air temperature anomalies from JRA55-do (Tsujino et al., 2018) during the last part of the ocean-sea ice model spin-up. The initial 1900 years of the spin-up are performed by applying repeat cycles of 1962 to 1971 atmospheric reanalysis forcing, from which a pre-industrial offset of 0.133°C has been removed (light blue line and value). In orange the same anomalies from the observational data set HadCRUT5.1 (Morice et al., 2021) which has a mean offset of 0.133°C over 1850-1879 relative to the 1960s. During the transitional spin-up period, the offset increases by 0.017°C decade^{-1} (light blue value and linear trend) back to the 1960s level. This is to simulate the transition from the equilibrated pre-industrial to the warmer 1960s oceanic state. The 1962-1971 decade is shown as the grey shaded period. From 1972 onward, interannual hindcast simulations are then branched off (e.g., the full forcing simulation in black where all the atmospheric forcing fields evolves in time). The parallel control simulation is obtained by continuing the modified pre-industrial spin-up (light blue line) unchanged through the transitional period past 1972. **b**, Time series of global ocean heat content during the five-cycle OMIP-2 spin-up (dark blue line, 10^{25} J and linear trend over the last two cycles, –3.55 $\times$ 10^{21} J year^{-1}) and the pre-industrial spin-up (red line, 10^{25} J). The offset between the two time series at year 1 of the spin-up is due to the use of updated temperature fields and bathymetric changes in the repeat decade spin-up. **c**, Inset of the last part of the spin-up, showing the transitional and hindcast periods with the 1960s period shaded in grey. The control simulation is given in light blue with its linear trend of –0.49 $\times$ 10^{21} J year^{-1} over 1972 to 2017. The black line is the ocean heat content in the full forcing simulation initialised in 1971.

(light blue line in Fig. 1.2a) tracks the observed OHC estimate closely, however with an increasingly large spread among ensemble members. The full forcing ACCESS-OM2 hindcast (where all the atmospheric forcing fields evolve over time) simulates a global OHC increase of 1.73×10^{23} J in the upper 2000 m (capturing 72% of the observational estimate).

This simulation improves considerably on the ACCESS-OM2 simulation that used the OMIP-2 spin-up approach, which lies at the bottom of the OMIP-2 ensemble (cf. black and dark blue lines in Fig. 1.2a). The hindcast also improves on most of the other 11 OMIP-2 models (Tsujino et al., 2020), whose multi-model-mean reaches 0.94 $\times 10^{23}$ J in 2017, and captures a more realistic rise in OHC without the rapid spurious global cooling adjustment prior to 1972 (Extended Data Fig. 1.8a). There is no control simulation available to use for de-drifting in the OMIP-2 protocol, and we have attempted to de-drift the global OHC by fitting and removing a linear trend over the last two OMIP-2 cycles (e.g., black lines, Extended Data Fig. 1.7a). Without this de-drifting, the positive trend in OHC in the OMIP-2 models would be even weaker (see also Fig. 24e in Tsujino et al. (2020)). If a similar additive improvement, that we see in ACCESS-OM2, were applied to the other models in the OMIP-2 ensemble, then the multi-model mean of an ensemble using our alternative spin-up approach would reach an upper 2000 m OHC anomaly of 2.31×10^{23} J in 2017, within four percentage points of the observations (Levitus et al., 2012).

The spatial trend of the upper 2000 m OHC in the full forcing simulation corresponds well with Argo observations (Li et al., 2017) (Fig. 1.2b, c and CMIP5 models over 2005 to 2015 (Rathore et al., 2020)), especially in the tropical Pacific and the Northern Atlantic. However, accumulation of anomalous heat in the model is reduced in the South Atlantic compared to Argo, and is likely caused by reduced ocean heat convergence in this region (see below). Most of the excess heat absorbed during this period is stored in the Southern Hemisphere (66.0% of the globally integrated trend relative to 72.7% in Argo). Over this shorter 2006-2017 period, the hemispheric OHC asymmetry has been linked to decadal climate variability (Rathore et al., 2020), the asymmetry in anthropogenic forcing (Irving et al., 2019), the greater area of the Southern Hemisphere ocean (Wijffels et al., 2016) as well as anomalous ocean heat transport (Roemmich et al., 2015).

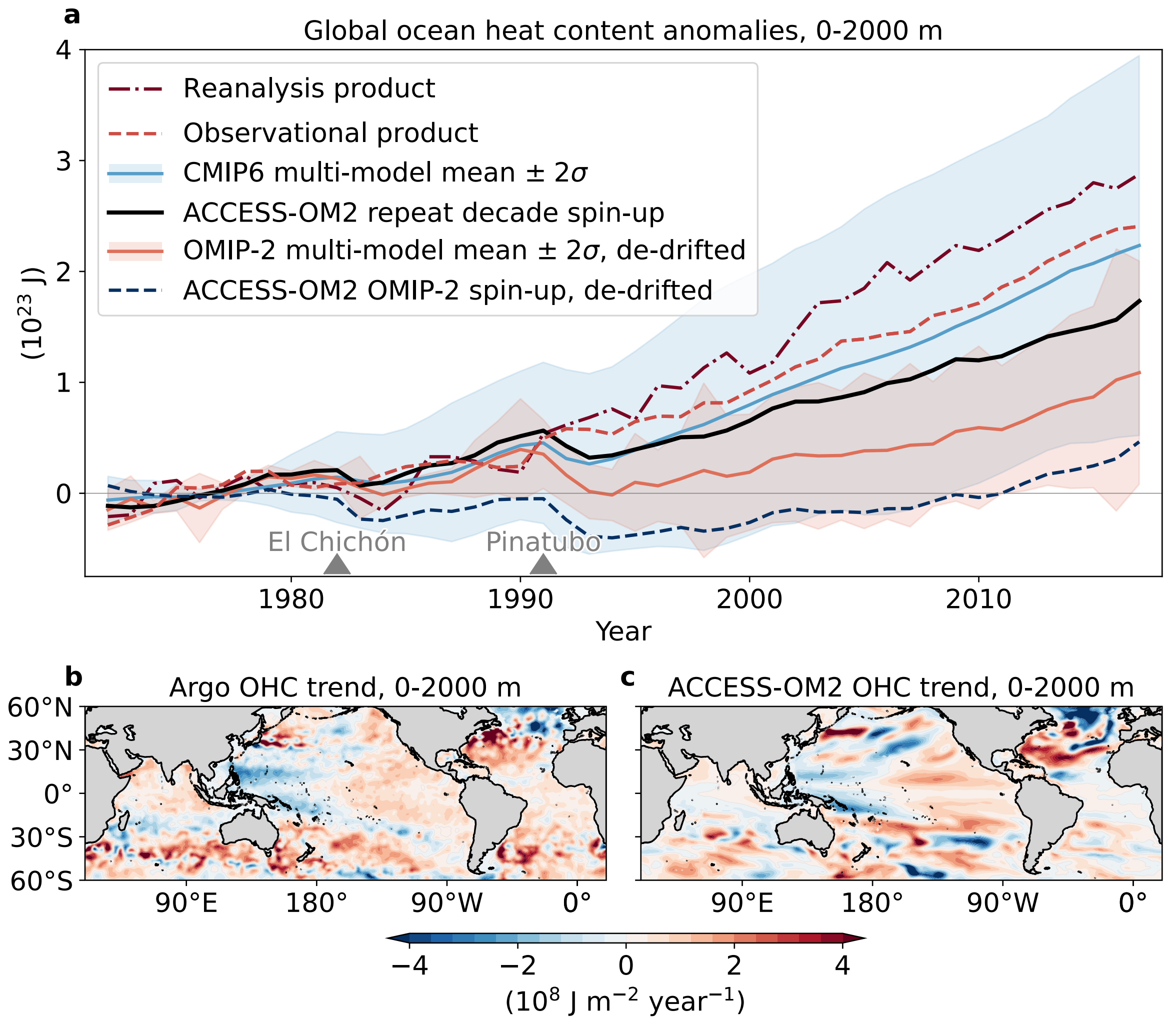

Figure 1.2: Recent global ocean heat content (OHC) anomalies in observations and hindcast model simulations. a, Global ocean heat content anomalies (10^{23} J) in the upper 2000 m from ocean observations, reanalyses, and surface flux data with Earth system model simulations (Cheng et al., 2019), observations (Levitus et al., 2012), 25 fully coupled historical CMIP6 model runs (Eyring et al., 2016) (including their multi-model mean and 2σ variance), the full forcing ocean-sea ice simulation (ACCESS-OM2 repeat decade spin-up, where all atmospheric forcing fields evolve over time), 11 de-drifted OMIP-2 ocean-sea ice model simulations (Tsujino et al., 2020) (including their multi-model mean, and 2σ variance) and the de-drifted ACCESS-OM2 OMIP-2-based simulation. For the individual time series of each CMIP6 and OMIP-2 ensemble member, see Extended Data Fig. 1.8. The two triangle markers highlight the volcanic eruptions of El Chichón in 1982 and Mount Pinatubo in 1991. The baseline period for all time series is 1972 to 1981. **b, c**, Spatial distribution of anomalous upper 2000 m ocean heat content trends over 2006 to 2017 in the Argo observations and in the full forcing ACCESS-OM2 simulation (10^8 J m^{-2} $year^{-1}$).

1.2.2 Heat Uptake, Transport and Storage Rates

In order to quantify the spatial distribution of OHC trends, we consider the vertically integrated heat budget which expresses the OHC tendency (termed here heat storage) as the sum of the anomalous net surface heat flux (heat uptake) and the convergence of the anomalous vertically integrated ocean heat transport (Eq. 1.2, Methods). Globally integrated, the full-depth heat uptake/storage rate over the last half century in the full forcing simulation is 5.4×10^{21} J year^{-1} (Fig. 1.3a). While trends have accelerated over the last 20 years, the spatial pattern of heat uptake has remained robust (cf., Fig. 1.3a and Extended Data Fig. 1.9a). The Southern Ocean dominates heat uptake with a rate of 6.9×10^{21} J year^{-1}. The dominant role of this region is a consequence of the strong heat fluxes into the ocean where sea surface temperatures (SSTs) are colder than the overlying atmosphere. These cold SSTs are maintained by strong westerly winds that drive upwelling of cold water to the surface, insulating the Southern Ocean from forced changes, and driving efficient heat uptake from the atmosphere (Armour et al., 2016; Marshall et al., 2015; Frölicher et al., 2015; Morrison et al., 2016). This warming of cold ocean waters has a relatively small impact on density due to the non-linear equation of state for sea water. It enables the continuous subduction of newly warmed water in the convergent zones on the edges of the Antarctic Circumpolar Current (ACC) that would otherwise be terminated by density feedbacks on the ocean circulation like in the tropics (Fasullo et al., 2020). In this simulation, heat uptake occurs predominantly in the Indian and Pacific sectors of the Southern Ocean. Northward Ekman transport subsequently subducts these water masses along isopycnals into mode and intermediate water layers (Morrison et al., 2016). Heat storage is also significant in the Atlantic sector of the Southern Ocean where it arises primarily from the convergence of oceanic heat transport rather than from local atmospheric heat uptake (Fig. 1.3a, b).

Patterns of heat uptake outside of the Southern Ocean are more variable. Heat loss is dominant in the Atlantic basin (-1.9×10^{21} J year^{-1}), especially north of 45°N. The Atlantic heat loss arises from its connection to the Southern Ocean via the Atlantic Meridional Overturning Circulation (AMOC). The AMOC transports 42% (2.9 ± 0.2 $\times 10^{21}$ J year^{-1}) of the additional heat taken up in the Southern Ocean northward into the Atlantic (red arrow in Fig. 1.3b), where two-thirds thereof is lost to the atmosphere

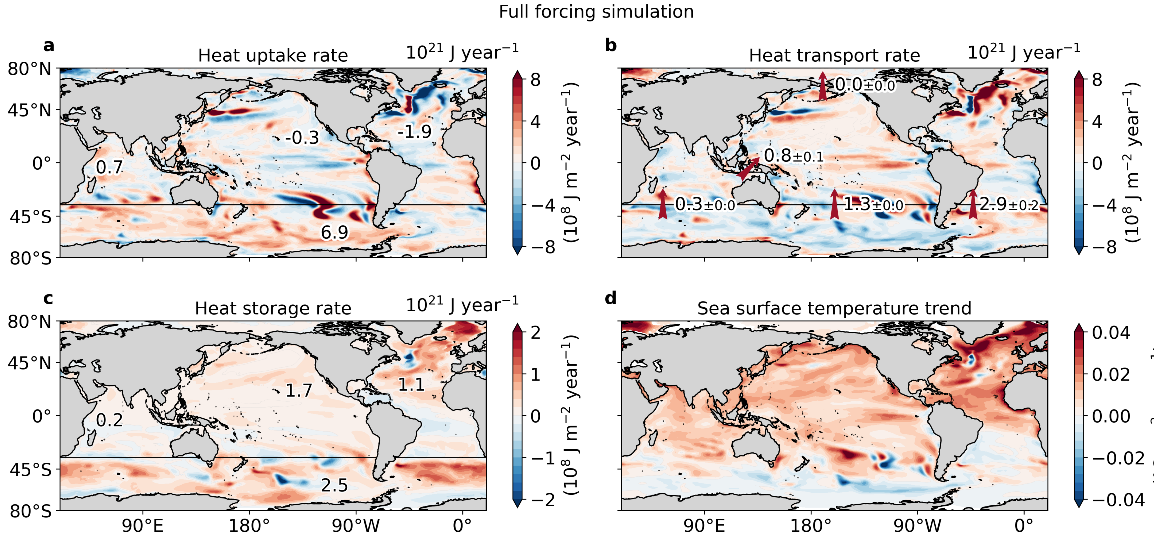

Figure 1.3: Spatial distribution of ocean heat uptake, transport, storage, and sea surface temperature trends over 1972 to 2017 in the full forcing simulation (where all atmospheric forcing fields evolve over time). **a**, Time integrated net surface heat flux anomalies (10^8 J m^{-2} year^{-1}) with positive heat uptake defined as into the ocean. The basin-wide values (10^{21} J year^{-1}) show the total area integrated trends over a particular ocean basin with the boundaries set by the black lines across the Southern Ocean, the Indonesian Throughflow, the Bering Strait and the continental land masses. The Southern Ocean ends at 36°S, the Bering Strait is at 65°N and the Indonesian Throughflow is defined between Java, New Guinea (105°W to 134°W) at 3°S and the Australian continent (20°S to 6°S) at 137°E. The Atlantic Ocean contributions include the Arctic Ocean north of 65°N and the marginal Hudson Bay, Baltic and Mediterranean basins. The Indian Ocean component also includes the Red Sea. The basin-wide values are rounded to one-decimal point accuracy. **b**, Anomalous heat transport convergence calculated as a residual from the **a** heat uptake and **c** heat storage (10^8 J m^{-2} year^{-1}). The anomalous heat transport rates and their uncertainties across transects (10^{21} J m^{-2} year^{-1}) are calculated from anomalous heat and volume transports (Methods). **d**, Simulated sea surface temperature trends (°C year^{-1}). Grid cells in **d** that have a climatological sea ice coverage above 85% have been removed and are shaded white.

via ocean-air heat fluxes. Compared to observations, the model's AMOC maximum at 26.5°N is weak (9.1 Sv relative to the observed estimate of 17 Sv over 2004 to 2012 in McCarthy et al. (2015), 1 Sv = 10^6 m^3 s^{-1}, Extended Data Fig. 1.10a), lower than most other OMIP-2 models (Tsujino et al., 2020), and may thus lead to weaker anomalous Southern Ocean heat export into the Atlantic. However, the changes in the AMOC strength in the full forcing simulation of $\sim$1 Sv are small compared to the decadal variability of $\pm$2 Sv (black line, Extended Data Fig. 1.10a).

Heat uptake in the Indian and Pacific subtropical and tropical basins plays only a minor role on the global scale (Fig. 1.3a). This is likely because the Indian and Pacific basins lack a convection-driven deep circulation (Godfrey et al., 2001; Talley et al., 2011) that would efficiently take up heat over multi-decadal time scales. In addition, heat uptake in the tropics is inhibited by the warming response of the SST (Fig. 1.3d). In contrast, at the high latitudes of the Southern Ocean, the SST increases at a rate that keeps pace with local atmospheric warming (due to wind-driven Ekman effects) creating favourable conditions for continuous ocean heat uptake (Fig. 1.3d).

1.2.3 Wind Versus Thermal Effects

We next consider a set of hindcast simulations that isolate the impact of thermodynamic (including air temperature, humidity and downward radiation) and wind-driven atmospheric changes over the global ocean and specific regions to better understand the drivers of recent OHU (Methods). In the wind-only simulation, zonal and meridional surface winds evolve over time while the other forcing fields are held fixed in the 1960s (and vice versa for the thermal experiment). The approach here differs from coupled and flux-anomaly forced ocean-sea ice model simulations that also aim to isolate contributions from winds and other changes (Gregory et al., 2016; Todd et al., 2020) in that our experiments are forced by atmospheric trends from reanalysis instead of, for example, doubled atmospheric CO_2 concentrations, and thus they capture the observed trajectory of internal climate variability. The strong decadal variability in our simulations arises from the portion of the atmospheric forcing (whether thermal or wind forcing) that cycles through the repeat decade (Fig. 1.4a, b).

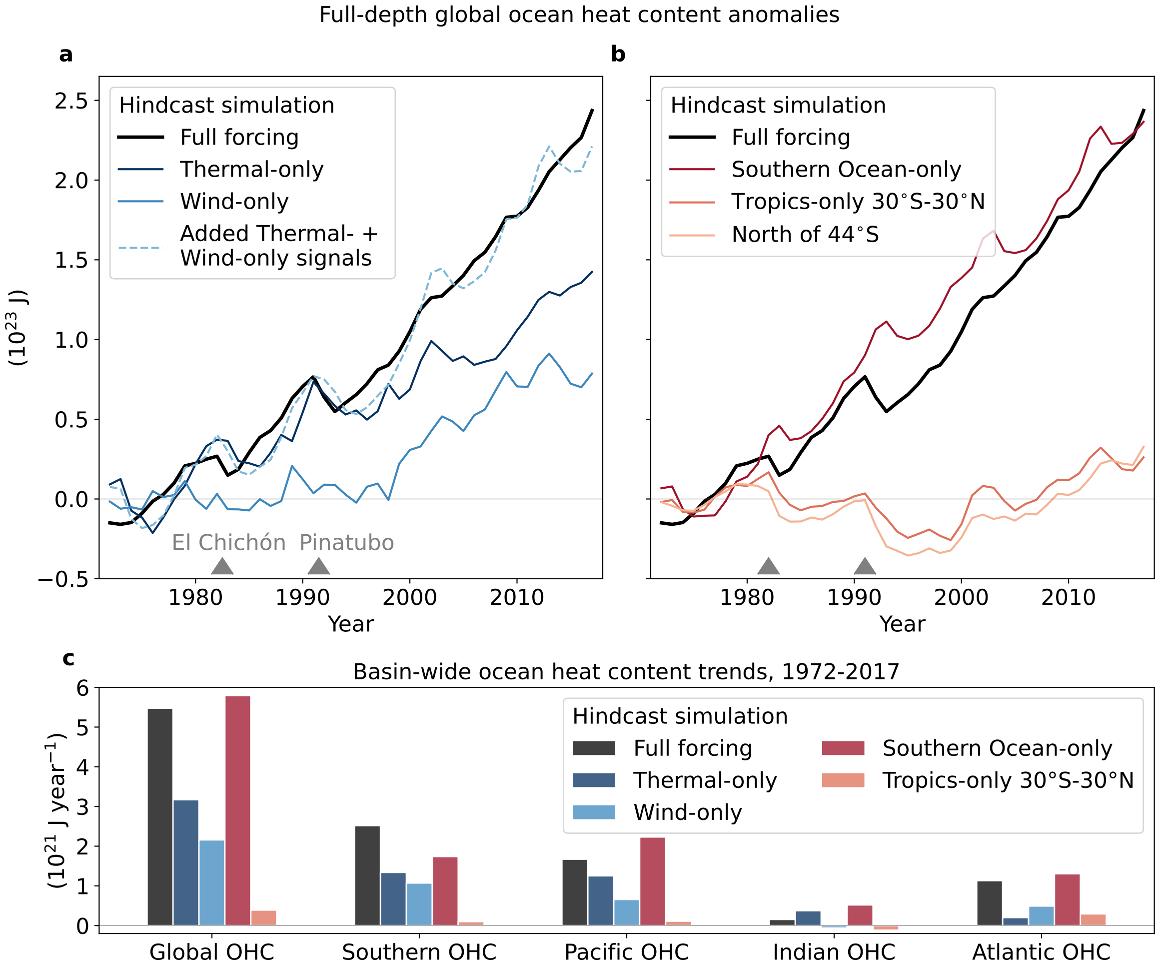

Figure 1.4: Simulated global and regional ocean heat content (OHC) changes due to thermal/wind trends and due to regionally-constrained atmospheric trends. **a**, Time series of full-depth global ocean heat content anomalies (10^{23} J) in the full forcing simulation (black line), when only prescribing surface wind trends (i.e., Wind-only) and when only prescribing thermodynamic trends (i.e., Thermal-only, Methods). The dashed blue line shows the anomalies in both wind- and thermal-only hindcast simulations added together. The two triangle markers highlight the volcanic eruptions of El Chichón in 1982 and Mount Pinatubo in 1991. The baseline period for all time series is 1972 to 1981. **b**, Time series for the hindcast simulations where combined interannual wind and thermal forcing is applied only over the Southern Ocean (south of 44°S), the mid- and high northern latitudes (north of 44°S) and only over the tropics (30°S to 30°N) with the remaining ocean area forced by the control repeat decade forcing. **c**, Basin integrated ocean heat content trends (10^{21} J year^{-1}) in the hindcast simulations of **a** and **b**.

The two simulations that include only either thermal or surface wind trends explain 57% and 40% of the global OHC trend of 5.4×10^{23} J (Fig. 1.4a, c). As in the full forcing simulation, heat uptake in both thermal- and wind-only experiments is dominated by the Southern Ocean (3.1 and 3.9×10^{21} J year^{-1}, Extended Data Fig. 1.11a, e). In the wind-only simulation, Southern Ocean heat uptake is large because the SST cools as a result of enhanced northward Ekman transport of cool fresh Antarctic surface waters (Fig. 1.5a, b). This heat uptake is driven by sensible and upward longwave heat losses associated with the negative SST anomalies (Fig. 1.5c,d). Some compensation by latent and upward shortwave heat flux anomalies, due to increases in sea ice, are associated with cooling in this region (Wendler et al. (1997) and Extended Data Table 1.1). It is important to note that wind changes also have a direct impact on sensible and latent heat fluxes through their dependence on wind speed in the model's bulk formulae. As opposed to the wind-only experiment, heat uptake in the thermal-only experiment is associated mainly with changes in downward longwave radiation (Fig. 1.5c), which appear more important than air temperature changes (as the sensible heat flux anomalies are reduced). Integrated over the Southern Ocean, the sensible heat flux drives almost double the heat uptake than the longwave radiative flux in the wind-only simulation (3.7 vs. 1.9×10^{21} J year^{-1}), while in the thermal-only simulation heat uptake through downward longwave radiation is more dominant (3.0 vs. 2.4×10^{21} J year^{-1}, Extended Data Table 1.1).

Both changes in surface winds and atmospheric thermodynamic properties can affect the export of anomalous heat from the Southern Ocean into the Pacific, Indian and Atlantic basins via the meridional overturning circulation. In particular, in the wind-only simulation, anomalous heat export northward is stronger than in the thermal-only simulation, due to the stronger westerlies which in turn increase the Ekman transport and thus the Southern Ocean's overturning circulation (Extended Data Fig. 1.11b, f). In contrast, the parameterised submesoscale eddy mixing, eddy advection and diffusion schemes play a minor role in contributing to ocean heat transport changes into the Atlantic and Indo-Pacific. In a fully coupled framework, Liu et al. (2018) showed that in response to quadrupled atmospheric CO_2 concentrations, the poleward-strengthened westerlies displace and intensify the Southern Ocean's meridional overturning circulation which results in anomalous heat transport divergence at 60°S and increased surface heat fluxes while the opposite was shown for 45°S. In our wind-only simulation, we see

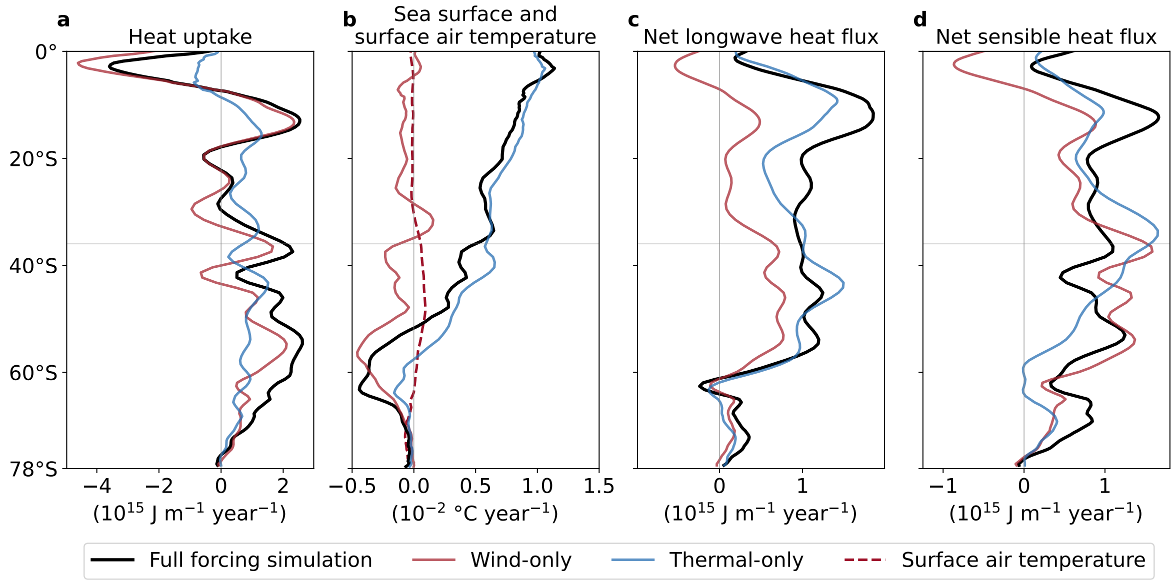

Figure 1.5: Southern Hemisphere ocean heat uptake, sea surface temperature and surface air temperature, net longwave and net sensible heat flux trends over 1972 to 2017. a, Zonally integrated heat uptake in the simulations with full, wind-only and thermal-only forcing (10^{15} J year^{-1}), equal to the zonal integral of the spatial structure shown in Figs. 2a and Extended Data Fig. 1.11a, e. **b**, Zonal mean sea surface temperature and surface air temperature trends (°C year^{-1}). **c, d**, The contribution of net longwave and sensible heat fluxes to the total ocean heat uptake shown in panel **a** (10^{15} J year^{-1}). The horizontal lines at 36°S indicate the northern boundary of the Southern Ocean in our analysis. A 5-grid cell rolling mean has been applied in panels **a**, **c** and **d**.

strong heat transport divergence at almost all latitudes of the Indian and Pacific sectors of the Southern Ocean, while heat converges in the Atlantic sector between 60°S-45°S (Supplementary Figure 5b), likely because the Southern Ocean surface wind trends in JRA55-do are strongest in the Indian and Pacific sectors. We agree with Liu et al. (2018), that wind stress changes are likely the primary drivers of ocean heat content change in the wind-only simulation (through their induced SST changes), rather than the direct wind-speed related turbulent heat flux change.

1.2.4 Regional Contributions

On the global scale, the OHC trend can be reproduced when atmospheric trends in both winds and thermodynamic properties are applied only over the Southern Ocean south of 44°S (with repeat decade forcing applied north of this latitude, Fig. 1.4b). However, an important regional difference between the full forcing and Southern Ocean-only forced simulation is that in the latter, heat storage is larger in the Pacific, Indian and Atlantic Oceans and smaller in the Southern Ocean (cf., black and dark red bars in Fig. 1.4c). This is likely caused by enhanced northward heat transport in the Southern Ocean-only experiment across 36°S, despite similar Southern Ocean heat uptake rates in both simulations (6.98 vs. 6.97 $\times 10^{21}$ J year^{-1}, Fig. 1.3a, b and Extended Data Fig. 1.12a, b). However, heat transport rates in the Southern Ocean-only experiment are influenced by the tapering zones between the repeat decade and interannual forcing in the Southern Ocean-only experiment. In addition, the Pacific and Atlantic basins experience weak heat loss across the surface due to these basins being forced by the cooler 1960s atmosphere (Extended Data Fig. 1.12a).

Performing an experiment with interannual trends applied only north of 44°S or just over the tropics 30°S to 30°N, shows a global OHC trend of 0.3 to 0.4 $\times 10^{21}$ J year^{-1} (Fig. 1.4c). A positive trend, distinct from the repeat decade forcing oscillation, emerges only in the mid–1990s (light pink line, Fig. 1.4a), and is likely linked to the observed shift of the Interdecadal Pacific Oscillation into a negative phase. This favours La Niña-like conditions with increased trade winds and enhanced tropical heat uptake (England et al., 2014; Henley and King, 2017). OHC trends over the 1992 to 2011 period from the tropical 30°S to 30°N experiment appear mainly centred on the Equator in the western Pacific at 150 m depth (Extended Data Fig. 1.13), and are consistent with the observed trends over the same period (England et al., 2014). A rapid increase in Indian Ocean heat content since the year 2000 has also been shown in observations (Lee et al., 2015) and occurs in a simulation with interannual trends restricted to only the Indian Ocean (not shown). This signal has been linked to the enhanced trade winds that strengthened warm water transport across the Indonesian Throughflow since the early 2000s (Lee et al., 2015; Maher et al., 2017). However, over the 50-year time period, Interdecadal Pacific Oscillation-related trade wind and OHC changes for the most part cancel each other out as this climate mode underwent a full oscillation (England et al., 2014; Meehl et al., 2016). Additional model experiments with the interannual atmospheric trend forcing only applied over individual ocean basins north of 44°S/35°S (Pacific-only/Indian- and Atlantic-only experiments, Methods) reveal only minor OHC trends (Extended Data Fig. 1.14, 1.15). This further emphasises the key role of the Southern Ocean in driving global ocean heat content trends over the past half century.

1.3 Discussion

We have documented the evolution of ocean heat uptake, transport and storage over the last 50 years in a global ocean-sea ice model following a spin-up approach that improves on past simulations of OHC trends using the standard OMIP-2 protocol. The full forcing hindcast simulation considerably improves on the simulation with the same model but using the OMIP-2 spin-up, and reproduces the estimated trajectory of OHC in observations better than most OMIP-2 ensemble members. If the OMIP-2 project would follow the spin-up approach presented here, it is likely that both the multi-model mean and ensemble spread in Fig. 1.2a would shift upwards and better capture the observed trends.

Changes in surface winds and thermodynamic properties over the Southern Ocean each drive about half of the global heat uptake signal over the last half century (Fig. 1.6). These heat changes have important consequences for the zonal transport of the Antarctic Circumpolar Current with continued warming likely further accelerating the zonal flow (Shi et al., 2021). As in the simulations with full or basin-wide forcing, heat uptake in the wind- and thermal-only experiments in the Indian and Pacific basins is minor, while the Atlantic Ocean is consistently losing heat across its surface (blue arrows, Fig. 1.6). In the full forcing as well as the wind- and thermal-only simulations, northward heat export from the Southern Ocean into the Atlantic dominates over export into the Indian and Pacific basins. While the Indo-Pacific plays only a minor role in multi-decadal heat uptake and storage, it can substantially impact global OHC trends over shorter periods through enhanced ocean heat uptake and reduced SST warming associated with the Interdecadal Pacific Oscillation (Meehl et al., 2011), e.g., during global warming hiatus periods such as from 2000 to 2009.

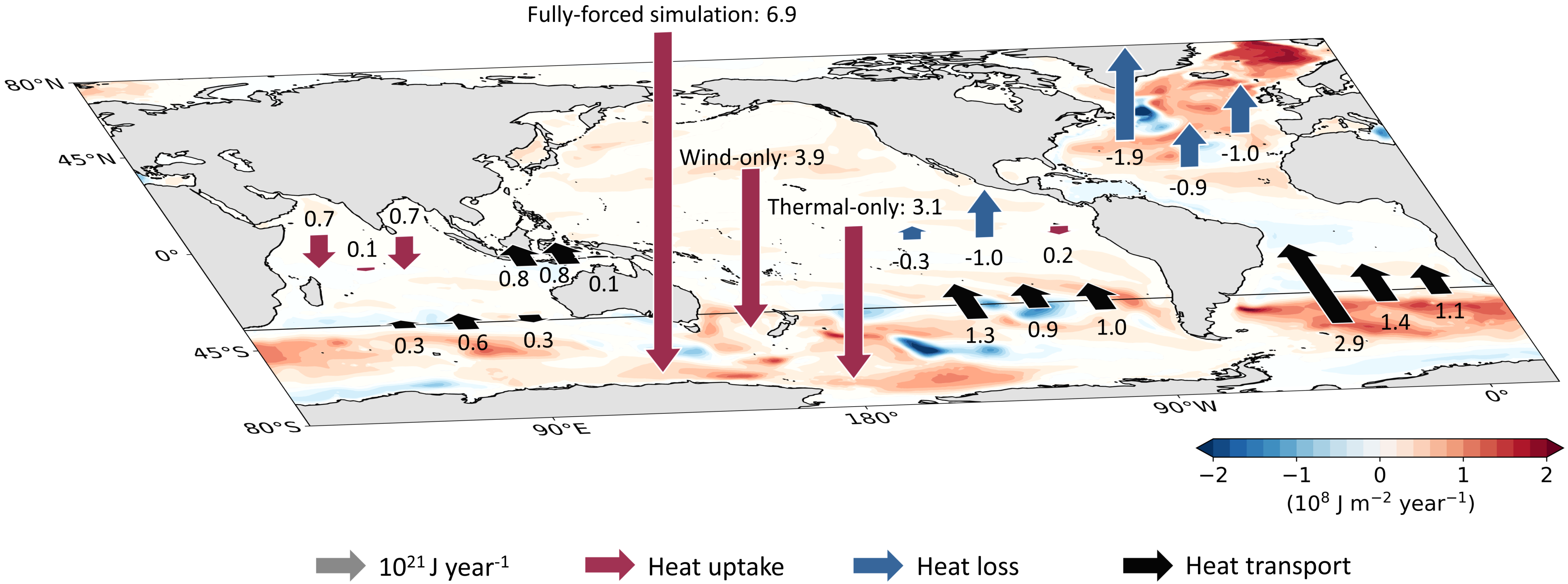

Figure 1.6: Schematic summarising anomalous global ocean heat uptake, heat loss and heat transport over the last half century in different historical simulations. The spatial pattern shows ocean heat storage rates in the full forcing simulation where all atmospheric forcing fields evolve over time (10^8 J m^{-2} year^{-1}). The global ocean is divided into the Southern Ocean and the Indian, Pacific and Atlantic basins as in Fig. 1.3. The red and blue vertical arrows into and out of the plane show the basin integrated heat uptake and heat loss rates in the full forcing (left arrow), wind-only (middle arrow) and thermal-only (right arrow) simulations (10^{21} J year^{-1}). The black arrows show the heat transport rates in the same simulations (from left to right: full, wind-only and thermal-only forcing) across the transects that separate the basins (10^{21} J year^{-1}). The arrows are to scale, and values are rounded to one-decimal point accuracy. The transport rates across the Bering Strait are one magnitude smaller and not shown.

Over the last twenty years of the full forcing simulation, the weakening AMOC in the North Atlantic (Extended Data Fig. 1.10) may be linked to positive redistribution feedbacks that have been previously described in a coupled climate model (Liu et al., 2020). In this feedback, a weakened AMOC decreases meridional heat transport in the North Atlantic, leading to a divergence of heat, cooler SSTs and increased heat uptake in the subpolar gyre, which in turn further weakens the AMOC (Couldrey et al., 2021; Liu et al., 2020). It is unclear if this feedback mechanism is contributing to the North Atlantic changes in the full forcing simulation, as heat uptake north of the Equator decreases (–0.6$\times$ 10^{21} J year^{-1}) and heat transport increases (+0.6$\times$ 10^{21} J year^{-1}) over the last twenty years of the run, compared to the full period.

In summary, our experiments emphasise that recent trends in Southern Ocean surface winds, surface air temperature and radiation have driven almost all of the globally integrated ocean warming of the past half century. Increased observational coverage over the Southern Ocean is also key to reconcile global surface heat fluxes, ocean heat uptake and heat content changes, as well as building increased confidence in climate models and climate change projections for the coming decades.

While not studied here, further analysis of hindcast simulations relative to available ocean reanalysis products (such as ECCO (Fukumori et al., 2021) or ORAS5 (Zuo et al., 2018)) could help improve our understanding of the global energy imbalance, especially when using eddy-resolving higher resolution models. An analysis with the ORAS5 reanalysis product would also give additional insight into the role of the Indonesian Throughflow in interhemispheric heat transport anomalies since 1979 (Trenberth and Zhang, 2019). Further validation with observation-based estimates of surface fluxes from reanalysis budgets (e.g., by using the 2000-2023 CERES data that is used in Loeb et al. (2022); Trenberth and Fasullo (2018)) would also be insightful. A more in-depth comparison, for example with the data in Trenberth et al. (2019) and other large-scale ocean energy budgets in time and space would also be helpful to better understand meridional heat transport rates and the model's AMOC. An extension of the simulations in this project with JRA55-do up to current times would also be beneficial, especially in light of the recent triple La Niña event with potential increased equatorial Pacific heat uptake.

1.4 Methods

1.4.1 Model, Forcing and Spin-up

We use the global ocean-sea ice model ACCESS-OM2 (Kiss et al., 2020) in a 1° horizontal resolution configuration with 50 z* vertical levels. ACCESS-OM2 consists of the Geophysical Fluid Dynamics Laboratory MOM5.1 ocean model (Griffies, 2012) coupled to the Los Alamos CICE5.1.2 sea ice model (Hunke et al., 2015) via OASIS3-MCT (Craig et al., 2017). Atmospheric forcing for the model is derived from a prescribed atmospheric state using the Japanese Reanalysis product JRA55-do-1-3 (Tsujino et al., 2018) which covers the period 1958 to 2018. The forcing fields are 3-hourly zonal and meridional wind speed, air temperature and specific humidity at 10 m as well as downward short- and longwave radiation, rain- and snowfall, and sea level pressure at the ocean's surface at 0.5625° resolution. The river and ice-related runoff forcing field has a daily time step and is provided at 0.25° resolution. These fields are used to calculate zonal and meridional wind stress, surface heat and freshwater fluxes using bulk formulae (Fairall et al., 1996). More details on the model setup and performance can be found in Kiss et al. (2020).

We perform a 2000-year spin up of the model initiated from World Ocean Atlas 2013 v2 conditions (Locarnini et al., 2013) using modified repeat cycles of the JRA55-do 1962 to 1971 decade. We choose this decade as it has no extreme El Niño-Southern Oscillation events or tendencies (Huang et al., 2015) and has close to neutral conditions in the Interdecadal Pacific Oscillation (IPO index: –0.1, Power et al. (1999)). However, it has a positive Southern Annular Mode and three positive Indian Ocean Dipole events occurred in this period (Saji et al., 1999). The choice of this decade is a compromise between an early period with limited observations where our confidence in the atmospheric forcing is low, and later periods where the anthropogenic signal is larger and the hindcast experiments would be shorter.

For the first 1910 years of the spin-up, we subtract from the repeat 1962 to 1971 forcing a pre-industrial offset of 0.133°C from the surface air temperature and 0.7 W m^{-2} from the downward longwave radiation fields. This is to equilibrate the model to an estimate of the pre-industrial climate instead of a 1960s climate that already incorporates an anthropogenic footprint. Additionally, we modify the specific humidity in order to keep the relative humidity constant and avoid overly impacting evaporation and the latent heat flux. The surface air temperature offset is calculated from the difference between the JRA55-do mean during the 1962 to 1971 period and the years 1850 to 1879 in the HadCRUT5 (Morice et al., 2021) data set (light blue and orange lines, Fig. 1.1a). The offset in downward longwave radiation is consistent with values presented in the fifth Assessment Report of the Intergovernmental Panel for Climate Change (IPCC AR5, Fig. SPM.5, IPCC (2013)). The overall ratio of surface air temperature to downward longwave radiation offsets is the same as in the study by Stewart and Hogg (2019) where they used offsets derived from the CMIP5 historical and moderate greenhouse gas emission scenario (RCP4.5) to run idealised climate change hindcast experiments. As in IPCC AR5 Fig. SPM.5 (IPCC, 2013), the uncertainty in the pre-industrial offset of downward longwave radiation (and surface air temperature) is likely as large as the value itself, but it is a reasonable approach given the limited data available from pre-industrial times.

The period 1910 to 2000 of the spin-up (i.e., 1882 to 1971 Current Era) is the transitional period where we linearly reduce the offsets in the forcing fields back to 1962 to 1971 levels (dark blue and dark red lines, Fig. 1.1a). This represents the developing anthropogenic impact on the ocean between the pre-industrial state and the warmer 1960s climate. In year 2000 of the spin-up (i.e., year 1972 Current Era), the interannually-forced hindcast simulations begin. The control simulation is a continuation of the pre-industrial spin-up with modified repeat decade forcing beyond 1972 (light blue line, Fig. 1.1a).

1.4.2 Hindcast Experiments

We run a set of simulations that combine both climatological (1962 to 1971) and interannual (1971 to 2017) forcing to investigate the contribution of changing surface winds, thermodynamic properties and the role of individual oceanic regions to anomalous heat uptake since the 1970s.

The wind and thermal simulations include forcing the model over 1972 to 2017 with interannual zonal and meridional surface wind trends (the wind-only experiment) or combined surface air temperature, humidity, radiation, freshwater and sea level pressure trends (the thermal-only experiment), while repeat decade forcing is used for the other forcing fields. The hindcast experiments here do not allow a complete separation between buoyancy effects (including heating) and wind effects because buoyancy and heat fluxes both change in each of the wind- and thermal-only experiments; for example, the winds can force an SST change that will feed back and alter the sensible heat flux fields. Likewise the thermally-forced experiment can include changes in wind stress wherever ocean circulation changes are simulated, because the wind stress is controlled by the difference between wind speed and ocean current speed, although this effect is generally second order. While surface air temperature and radiation variations dominate the signal in the thermal-only simulation, freshwater fluxes can also contribute to changes in ocean circulation and thus ocean heat uptake and redistribution via changes in, for example, the meridional overturning circulation in the Atlantic and Southern Oceans (Winton et al., 2013; Gregory et al., 2016).

The regional simulations (hereafter Southern Ocean-only, North of 44°S, Tropics-only 30°S to 30°S, Pacific-, Indian- and Atlantic-only forcing simulations) include applying interannual trending atmospheric fields over a specific region of the global ocean while repeat decade forcing is applied over the remaining ocean area (e.g., blue contours in Extended Data Fig. 1.15). For these simulations, a linear smoothing boundary region of 4° latitude/longitude is used to combine the two forcing fields. For the Southern- and Pacific Ocean-only simulations, we choose the boundaries at 44°S as this latitude marks the poleward extent of the shallow subtropical cells. For the Indian and Atlantic Ocean simulations, we set the southern interannual forcing/repeat decade forcing boundary to 35°S at the southern tip of Africa.

1.4.3 Ocean Heat Content Calculations

Heat content,

$$H = \iiint \rho_0 C_p \Theta \, \mathrm{d}V, \tag{1.1}$$

is calculated using a reference density $\rho_0 = 1035$ kg m^{-3}, a specific heat capacity $C_p = 3992.1$ J kg^{-1} K^{-1}, the model's prognostic temperature variable Conservative Temperature Θ (K, McDougall (2003); McDougall and Barker (2011)) and the (time-variable) grid cell volume dV (m^3).

The vertically integrated Eulerian heat budget can be expressed as

$$\frac{\partial}{\partial t}\int_z^0 H dt = Q_{net} - \nabla_h \cdot \boldsymbol{F}, \tag{1.2}$$

where the left-hand side is the depth integrated heat content tendency at a given location (J m^{-2} year^{-1}) between depth z and the surface, Q_{net} is the net surface heat flux and $\nabla_h \cdot \boldsymbol{F}$ is the divergence of the vertically integrated ocean heat transport. Changes in heat content arise from changes in heat exchange with the atmosphere (heat uptake) and/or from changes in the convergence of horizontal ocean heat transport. The anomalous heat uptake rate is calculated by first time integrating the net surface heat flux tendencies, including the turbulent (latent and sensible), radiative (short- and longwave), surface volume flux-associated and sea ice exchange components, before removing the linear trend in the time integrated tendencies of the control simulation, and finally fitting a linear trend to the result. The heat storage rate is calculated similarly. The heat transport convergences are calculated as the residual between heat uptake and storage (Eq. 1.2). These calculations would be more difficult without a parallel-running control simulation (not available as part of OMIP-2) that can be used to remove drift as well as the steady-state pattern of heat input at low-latitudes and heat loss at high-latitudes connected by meridional ocean heat transport.

Ocean heat transport (OHT) rates across individual transects are calculated from the vertical integral of horizontal advective and parameterised diffusive, mesoscale- and submesoscale heat fluxes accumulated online. Uncertainties in these heat transport rates arise from the presence of non-zero net volume fluxes, which result in a dependence of the cross-transect heat transport on the arbitrary reference temperature (Holmes et al., 2019b; Forget and Ferreira, 2019). We estimate the uncertainty in the anomalous heat transport rate based on the change in the volume transport across the transect $\Delta\Psi$ (m^3 s^{-1}) and a maximum possible range for the temperature $(\Delta\Theta)^{max}$ at which that net volume transport could be assumed to return:

$$\Delta \mathrm{OHT} = \pm \rho_0 C_p \frac{(\Delta\Theta)^{\max}}{2} \Delta\Psi. \tag{1.3}$$

We define $(\Delta\Theta)^{\max}$ to be 30°C, an estimate of the maximum temperature range of the model. For example, if the maximum temperature of water transported through the Indonesian Throughflow is 30°C, then the maximum ambiguity in the change in heat transport is estimated by assuming that this water returns back into the Pacific via the Southern Ocean at 0°C. This issue is discussed in more detail in Section S3 in the Supporting Information of Holmes et al. (2019b) and Forget and Ferreira (2019).

1.4.4 CMIP6 Products

To compare the simulations in this study to atmosphere-ocean general circulation models, we analyse 16 ensemble members from CMIP6 as shown in the Extended Data Table 2. The choice of the models and anomaly calculation is based on Irving et al. (2021) and includes first taking a cubic fit of the globally integrated 0 to 2000 m OHC over the length of the pre-industrial control simulation in each model. The length of this control simulation can be between 500 to 6000 years depending on the model. This fit is then subtracted from the historical simulation (ending in 2014) and SSP5-8.5 (2014 to 2017) projection simulation before the removal of the baseline 1972 to 1981 period.

1.5 Data Availability

The model data to recreate the figures in this study have been deposited online in the Zenodo database under https://doi.org/10.5281/zenodo.6873094 (Huguenin et al., 2022b). The full model output is stored on the National Computational Infrastructure and available upon contact to the first author. The Argo data were collected and made freely available by the International Argo Program and the national programs that contribute to it (http://www.argo.ucsd.edu, http://argo.jcommops.org). The Argo Program is part of the Global Ocean Observing System (https://doi.org/10.17882/42182). The product we used here was produced at the China Argo Real-time Data

Center and available at http://www.argo.org.cn/english/. The CMIP6 data is available at the Earth System Grid Federation: https://esgf-node.llnl.gov/projects/cmip6/.

1.6 Code Availability

The analysis scripts to create the forcing for the JRA55-do-1-3 repeat decade spin-up and to reproduce the figures are published online in the Zenodo database under https://doi.org/10.5281/zenodo.6873094 (Huguenin et al., 2022b).

1.7 Extended Data Figures and Tables

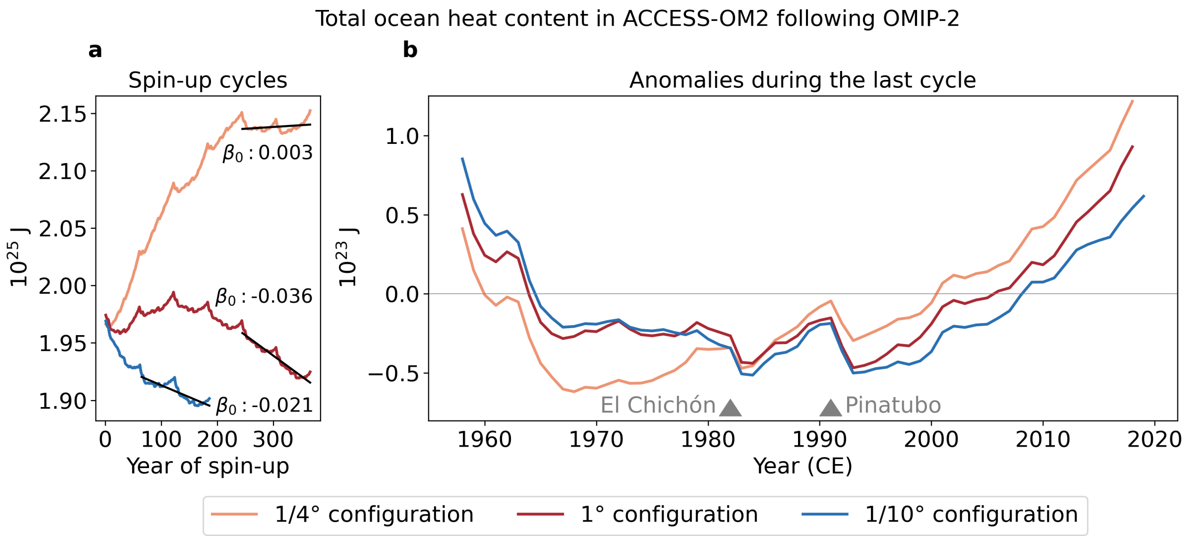

Extended Data Figure 1.7: Total ocean heat content anomalies in ACCESS-OM2. **a**, Total ocean heat content (10^{25} J) in the 1°, 1/4° and 1/10° model configuration following the OMIP-2 protocol. Only three spin-up cycles are available in the 1/10° model due to the cost involved in running this configuration. In black the linear trends over the last two cycles with the trend values β_0 in units of 10^{25} J century^{-1}. **b**, Anomalies for the three configurations of the model during the last cycle, calculated by removing the respective linear trend over the last two cycles in **a**.

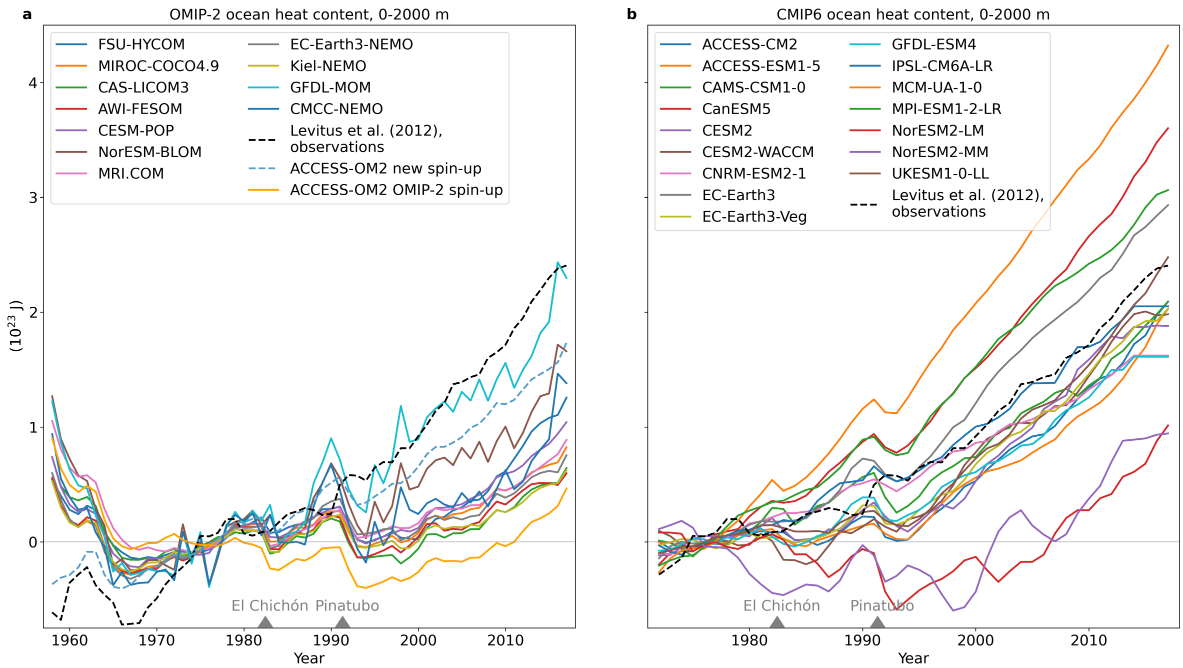

Extended Data Figure 1.8: Simulated global ocean heat content in OMIP-2 and CMIP6. **a**, Time series of 1958-2017 OHC anomalies in the eleven OMIP-2 models presented in Tsujino et al. (2020) and in ACCESS-OM2. The observations from Levitus et al. (2012) are shown as the dashed black line. The new simulation with full interannual forcing is shown as the dashed blue line. The anomalies are calculated by first removing the linear trend over the last two spin-up cycles and then removing the mean of the 1972-1981 baseline period. **b**, As in **a** but for 25 CMIP6 models over 1972-2017.

Extended Data Table 1.1: Heat flux contributions to anomalous Southern Ocean heat uptake. Contributions of the basin-wide integrated heat flux trends over the Southern Ocean south of 36°S in the simulation with full interannual forcing, with wind-only forcing and thermal property-only forcing (10^{21} J year^{-1}). The values are rounded to one-decimal point accuracy. Only the four major heat flux components (net short- and longwave, sensible and latent heat fluxes) are shown here without the surface flux contributions from surface volume exchanges and heat exchanges with sea ice.

	Net shortwave	Net longwave	Sensible	Latent
Full forcing simulation	0.1	3.1	3.3	-0.3
Wind-only forcing	0.6	1.9	3.7	-2.7
Thermal-only forcing	0.1	3.0	2.4	-3.1

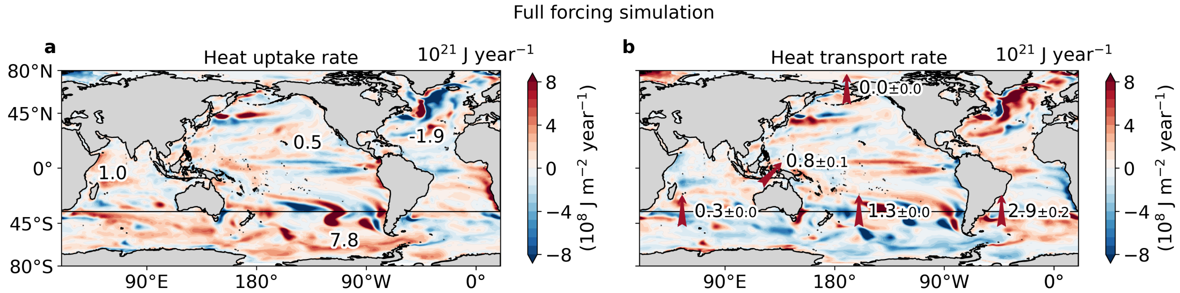

Extended Data Figure 1.9: Spatial distribution of ocean heat uptake and storage trends over 1997-2017 in the simulation with full interannual forcing. a, Time-integrated net surface heat flux anomalies (10^8 J m^{-2} year^{-1}) with positive heat uptake defined as into the ocean. The basin-wide values (10^{21} J year^{-1}) show the total area-integrated trends over a particular ocean basin with the boundaries set by the blue lines. The Southern Ocean ends at 36°S, the Bering Strait is at 65°N and the Indonesian Throughflow is defined between Java, New Guinea (105°W to 134°W) at 3°S and the Australian continent (20°S to 6°S) at 137°W. The Atlantic Ocean contributions include the Arctic Ocean north of 65°N and the marginal Hudson Bay, Baltic and Mediterranean basins. The Indian Ocean component also includes the Red Sea. The basin-wide values are rounded to one-decimal point accuracy. **b**, As in **a** but for the heat storage trends.

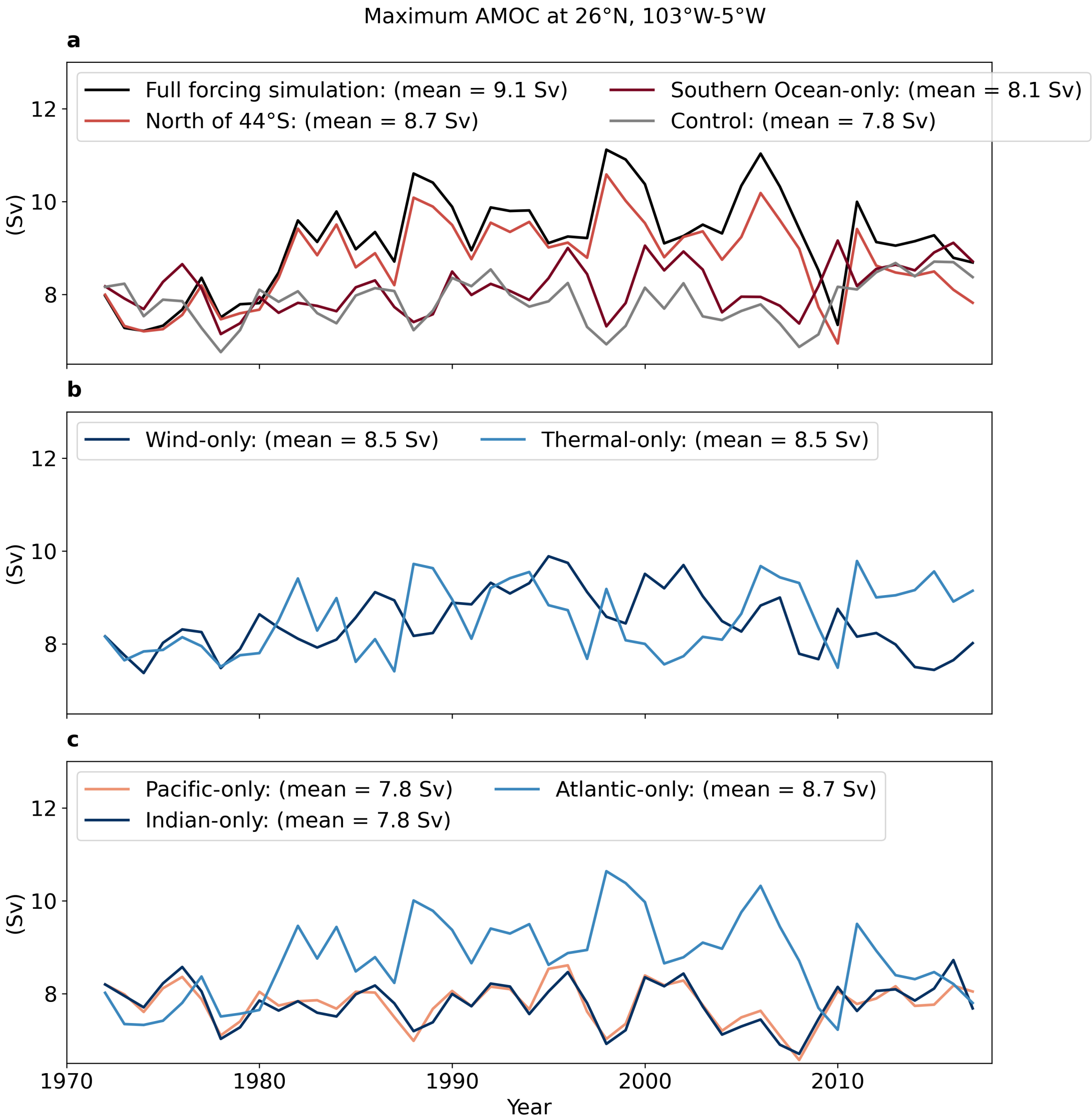

Extended Data Figure 1.10: Maximum strength of the Atlantic Meridional Overturning (AMOC) streamfunction at 26°N between 103°W and 5°W. a, Annual mean upper overturning cell magnitude as a function of time (Sv, 1 Sv = 10^6 m^3 s^{-1}), defined as the maximum value of the global overturning streamfunction computed on density surfaces, measured at 26°N, integrated between 103° and 5°W and for potential density classes that exceed 1035.5 kg m^{-3}. Time series are shown for the full forcing simulation as well as the control simulation, the Southern Ocean-only and the North of 44°S experiments. The mean AMOC strength in these experiments over the full time period is given as the mean for each time series rounded to one decimal point accuracy. **b, c** As in **a** but for the wind- and thermal-only experiments as well as the basin-wide Pacific-, Indian- and Atlantic-only experiments.

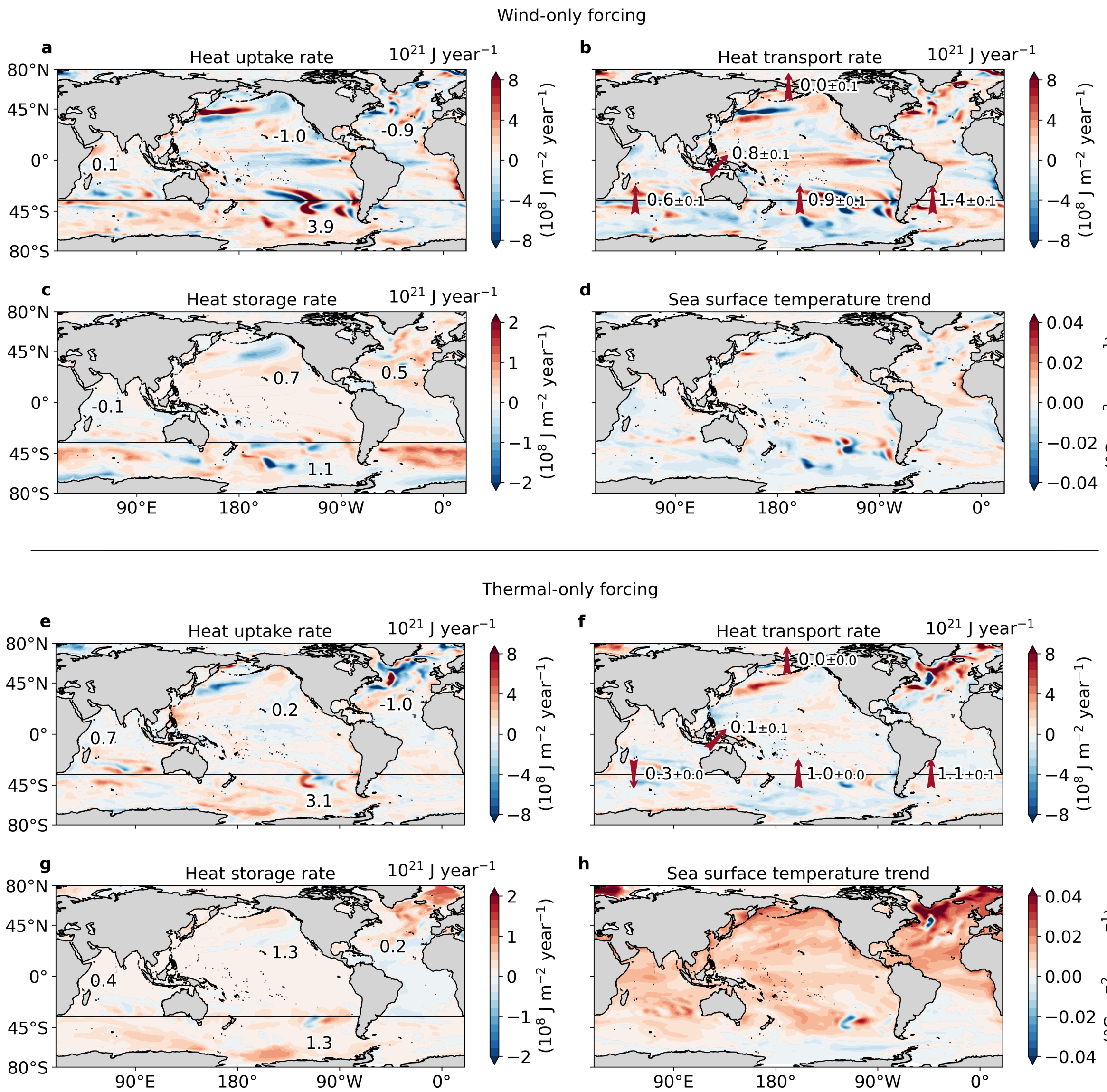

Extended Data Figure 1.11: Spatial distribution of ocean heat uptake, transport, storage and sea surface temperature trends over 1972-2017 in the wind-only and thermal-only forcing experiment. **a**, Time-integrated net surface heat flux anomalies (10^8 J m^{-2} year^{-1}) with positive heat uptake defined as into the ocean. The basin-wide values (10^{21} J year^{-1}) show the total area-integrated trends over a particular ocean basin with the boundaries set by the black lines across the Southern Ocean, the Indonesian Throughflow, the Bering Strait and the continental land masses. The Southern Ocean ends at 36°S, the Bering Strait is at 65°N and the Indonesian Throughflow (ITF) is defined between Java, New Guinea (105°W to 134°W) at 3°S and the Australian continent (20°S to 6°S) at 137°W. The Atlantic Ocean contributions include the Arctic Ocean north of 65°N and the marginal Hudson Bay, Baltic and Mediterranean basins. The Indian Ocean component also includes the Red Sea. The basin-wide values are rounded to one-decimal point accuracy. **b**, Anomalous heat transport convergence calculated as a residual from the a heat uptake and c heat storage (10^8 J m^{-2} year^{-1}). The anomalous heat transport rates and their uncertainties across transects (10^{21} J m^{-2} year^{-1}) are calculated from anomalous heat and volume transports (see Methods). **d**, Simulated SST trends (°C m^{-2} year^{-1}). Grid cells in **d** that have a climatological sea ice coverage above 85% have been removed and are shaded white. **e-f**, As in **a-d** but for the perturbation experiment where only atmospheric trends in thermal properties are applied (surface air temperature, humidity, radiation, precipitation and sea level pressure trends, while repeat decade forcing is used for the other forcing fields.

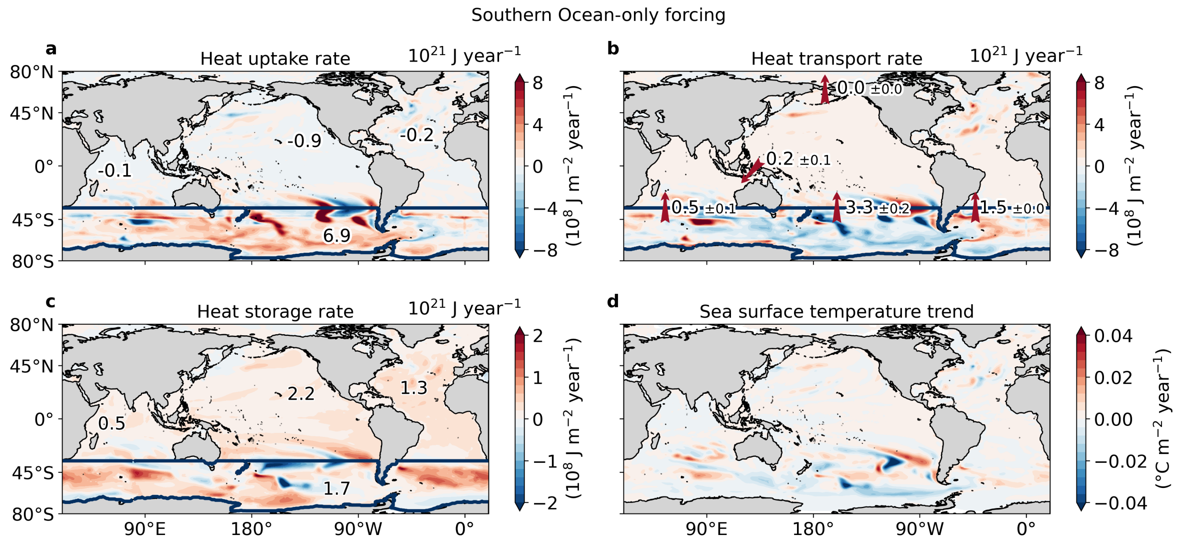

Extended Data Figure 1.12: As in Extended Data Fig. 1.11 but for the Southern Ocean experiment where interannual forcing is applied south of 44°S over the region with blue outlines. Repeat decade forcing is applied north of 40°S and the tapering zone between the two forcing fields is from 44°S to 40°S.

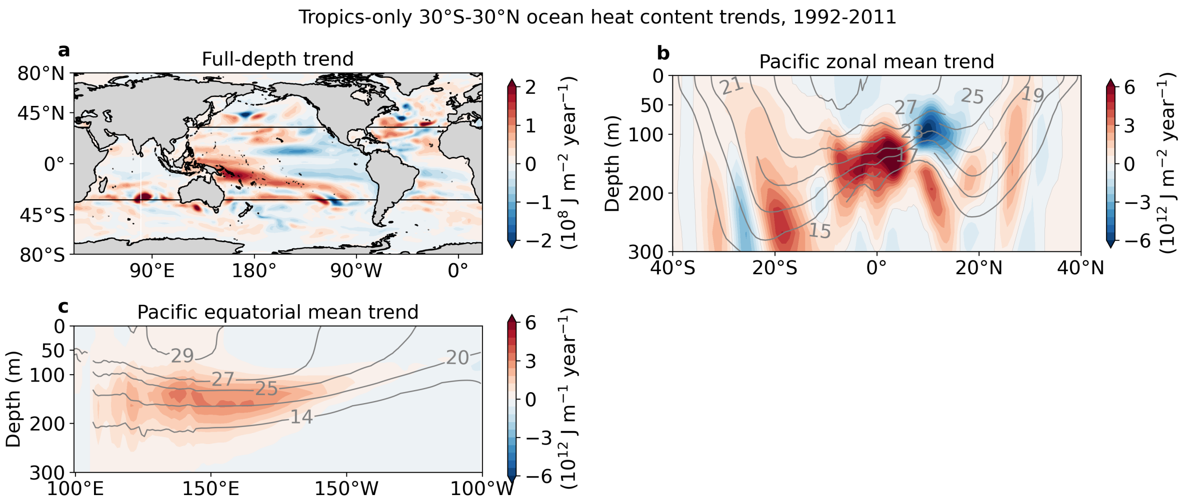

Extended Data Figure 1.13: Ocean heat content trends over 1992-2011 in the Tropics-only 30°S–30°N experiment. **a**, Spatial pattern of anomalous ocean heat content trend over 1992-2011 (108 J m-2 year-1). The horizontal blue lines indicate the region over which interannual forcing is applied (30°S–30°N). **b**, Zonal mean ocean heat content trends in the Pacific Ocean 100°E–100°W (10^{12} J m^{-2} year^{-1}). The contours show the climatological isotherms across the Pacific 40°S–40°N (°C). **c**, Equatorial mean 5°S–5°N ocean heat content trends in the Pacific Ocean (10^{12} J m^{-2} year^{-1}). The contours show the climatological isotherms across the Pacific 100°E-100°W (°C).

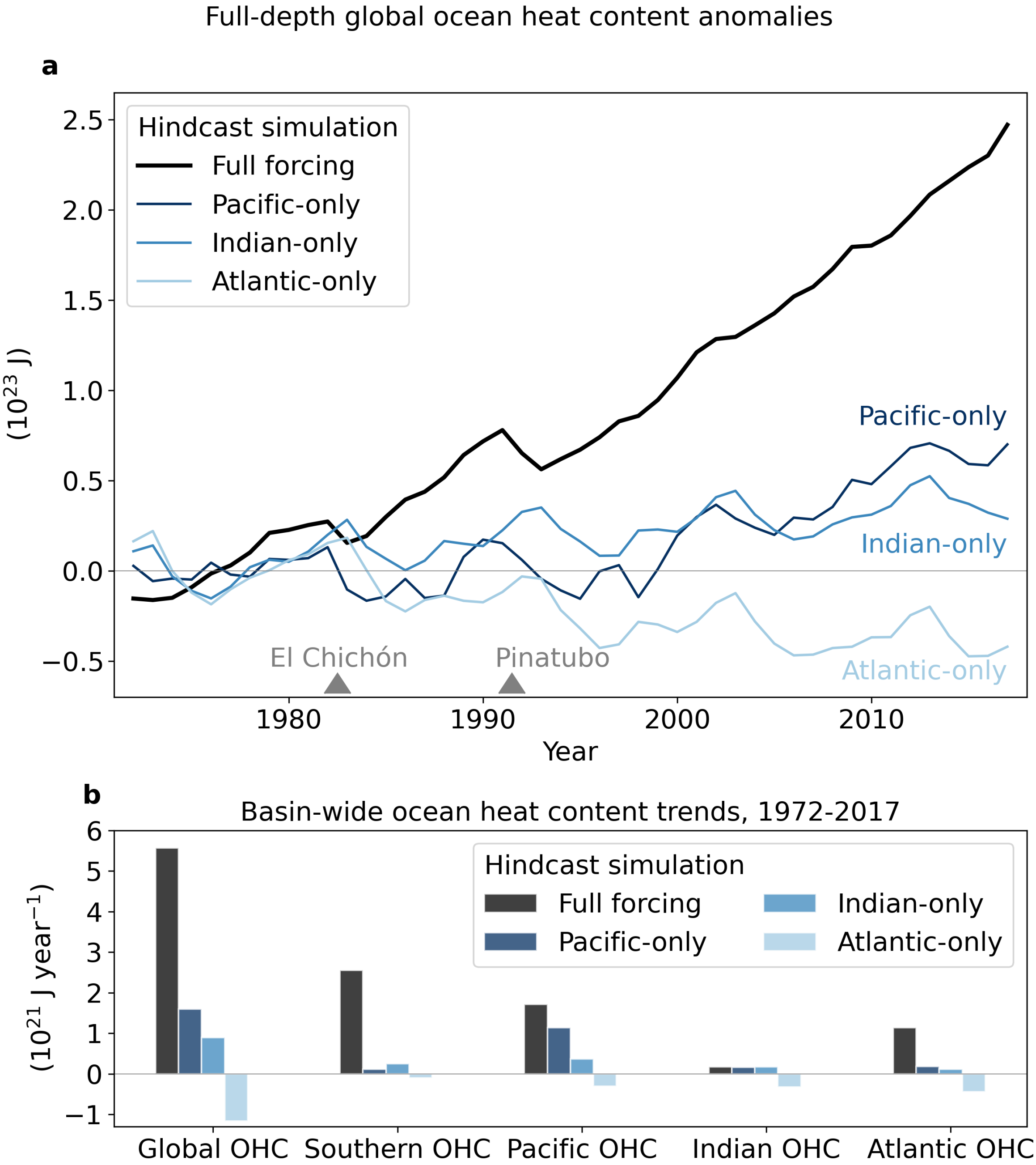

Extended Data Figure 1.14: Ocean heat content changes since 1972 in the basin-wide simulations. **a**, Time series of the full-depth ocean heat content anomalies where interannual forcing is applied only over the Pacific, Indian and Atlantic basins compared with the simulation where interannual forcing is applied over the full ocean area (10^{21} J year^{-1}). For the Pacific Ocean simulation, we choose the southern interannual forcing/repeat decade forcing boundary at 44°S as this latitude marks the poleward extent of the shallow subtropical cells. For the Indian and Atlantic Ocean simulations, we set the boundary to 35°S at the southern tip of Africa. **b**, The basin-integrated ocean heat content trends for the perturbation experiments in a with the boundaries set by the dark blue lines in Fig. 1.3 in the main manuscript.

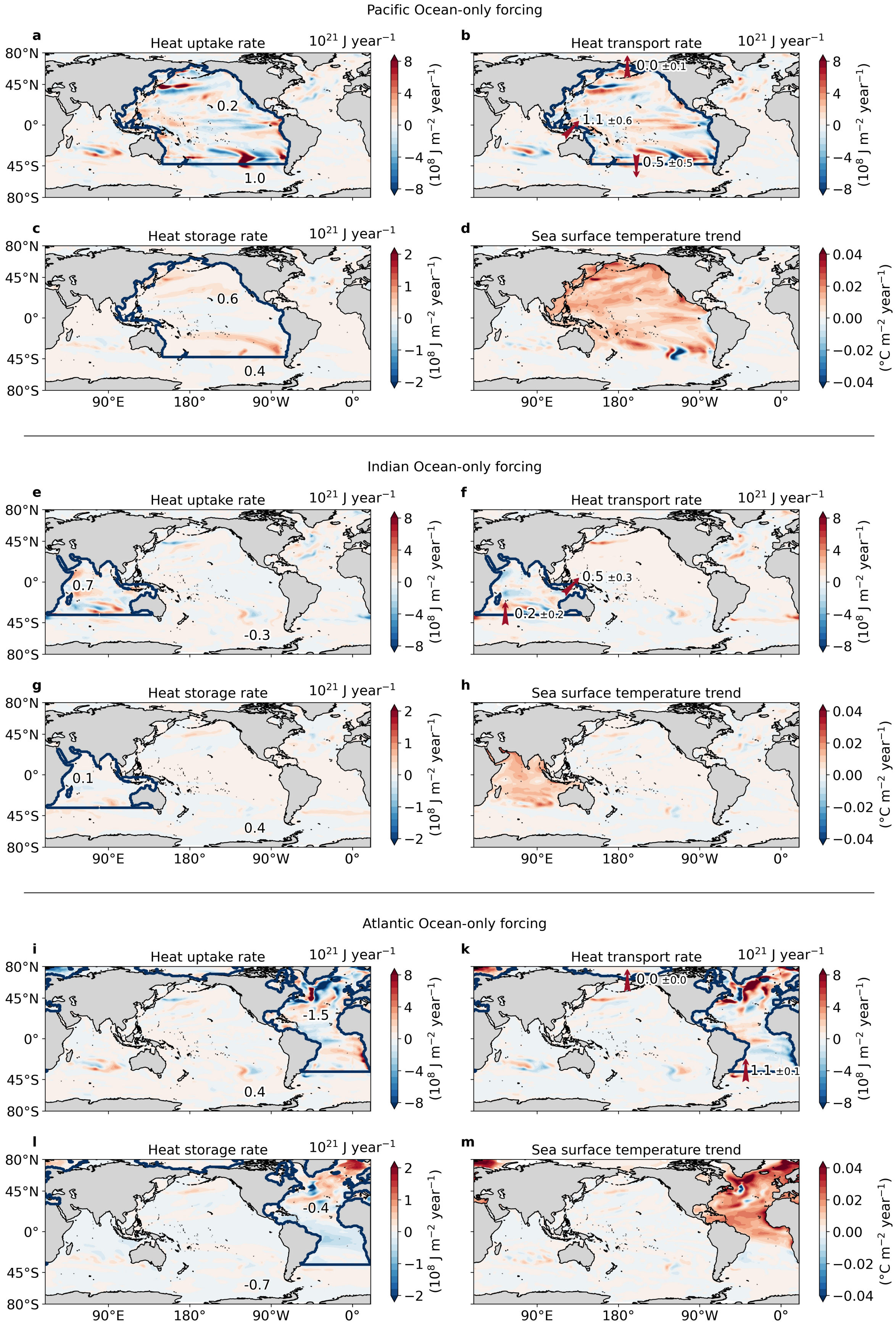

Extended Data Figure 1.15: As in Extended Data Fig. 1.11 but for the **a-d** Pacific Ocean-only, **e-h** Indian Ocean-only and **i-m** Atlantic Ocean-only forcing experiment. The blue outlines indicate the region over which interannual forcing is applied while repeat decade forcing is used over the remaining ocean area.

Extended Data Table 1.2: CMIP6 GCM ensemble model information. For a list of the model acronyms, see http://www.ametsoc.org/PubsAcronymList.

Model acronym	Ensemble member	Reference
ACCESS-CM2	r1i1p1f1	Dix et al. (2019a,b,c)
ACCESS-ESM1-5	r1i1p1f1	Ziehn et al. (2019b,c,a)
CAMS-CSM1-0	r1i1p1f1	Rong (2019a,b,c)
CanESM5	r1i1p1f1	Swart et al. (2019a,b,c)
CESM2	r1i1p1f1	Danabasoglu et al. (2019); Danabasoglu (2019f,g)
CESM2-WACCM-FV2	r1i1p1f1	Danabasoglu (2019a,b,c)
CESM2-WACCM	r1i1p1f1	Danabasoglu (2019d,e,c)
CNRM-ESM2-1	r1i1p1f2	Seferian (2018a,b); Voldoire (2019)
EC-Earth3	r1i1p1f1	EC-Earth Consortium (2019a,b,c)
EC-Earth3-Veg	r1i1p1f1	EC-Earth Consortium (2019d,e,f)
GFDL-ESM4	r1i1p1f1	Krasting et al. (2018a,b); John et al. (2018)
IPSL-CM6A-LR	r1i1p1f1	Boucher et al. (2018a,b, 2019)
MCM-UA-1-0	r1i1p1f1	Stouffer (2019b,c,a)
MPI-ESM1-2-LR	r1i1p1f1	Wieners et al. (2019b,c,a)
NorESM2-LM	r1i1p1f1	Seland et al. (2019a,b,c)
NorESM2-MM	r1i1p1f1	Bentsen et al. (2019a,b,c)
SAM0-UNICON	r1i1p1f1	Park and Shin (2019a,b)
UKESM1-0-LL	r1i1p1f2	Tang et al. (2019a,b); Good et al. (2019)

2

Key Role of Diabatic Processes in Regulating Warm Water Volume Variability Over ENSO Events

Huguenin, M. F. [1, 2, 3], Holmes R. M.[2, 3, 4] & England M. H.[2, 3] *Journal of Climate.* (2020b). **33**:9945–9964. https://doi.org/10.1175/JCLI-D-20-0198.1 *

M. F. H. completed the simulations and wrote the initial manuscript together with input from R. M. H. and M. H. E. All authors formulated the experimental design, contributed to interpreting the results and refinement of the paper.

The published version of this part can be found in Appendix B.

1. Institute for Atmospheric and Climate Science, ETH Zurich, Zurich, Switzerland 2. Climate Change Research Centre, University of New South Wales, Sydney, NSW, Australia 3. ARC Centre of Excellence in Climate Extremes, University of New South Wales, Sydney, NSW, Australia 4. School of Mathematics and Statistics, University of New South Wales, Sydney, NSW, Australia ∗. This publication was slightly changed from its original version to ensure consistency throughout this thesis. Parts of the analysis and discussion around the climatological warm water volume and the idealised El Niño and La Niña events stem from the author's Master's thesis Huguenin-Virchaux et al. (2018).

Abstract The equatorial Pacific Warm Water Volume (WWV), defined as the volume of water warmer than 20°C near the Equator, is a key predictor for the El Niño-Southern Oscillation (ENSO), and yet much about the individual processes that influence it remains unknown. In this study, we conduct idealised ENSO simulations forced with symmetric El Niño- and La Niña-associated atmospheric anomalies as well as a historical 1979 to 2016 hindcast simulation. We use the water mass transformation framework to examine the individual contributions of diabatic and adiabatic processes to changes in WWV. We find that in both sets of simulations, El Niño's discharge and La Niña's recharge periods are initiated by diabatic fluxes of volume across the 20°C isotherm associated with changes in surface forcing and vertical mixing. Changes in adiabatic horizontal volume transport above 20°C between the Equator and subtropical latitudes dominate at a later stage. While surface forcing and vertical mixing deplete WWV during El Niño, surface forcing during La Niña drives a large increase partially compensated for by a decrease driven by vertical mixing. On average, the ratio of diabatic to adiabatic contributions to changes in WWV during El Niño is about 40% : 60%, during La Niña this ratio changes to 75%:25%. The increased importance of the diabatic processes during La Niña, especially the surface heat fluxes, is linked to the shoaling of the 20°C isotherm in the eastern equatorial Pacific and is a major source of asymmetry between the two ENSO phases, even in the idealised simulations where the wind forcing and adiabatic fluxes are symmetric.

2.1 Introduction

The El Niño-Southern Oscillation (ENSO) is a coupled ocean-atmosphere phenomenon in the equatorial Pacific that dominates variability in the Earth's climate system on the interannual time scale. Although ENSO's key dynamics are found in the Pacific, its impacts occur on a global scale. The instrumental record of global surface air temperature (SAT) shows the dominant role of ENSO during recent periods of warming and cooling (Trenberth et al., 2007; Hartmann et al., 2013). High sea surface temperature (SST) values in the equatorial Pacific during the 1997 to 1998 El Niño increased global SAT by 0.2 to 0.64°C (depending on the data product, Reynolds et al., 2007; Morice et al., 2012), while global SAT decreases during La Niña events (Reynolds et al., 2007; Meehl et al., 2011; Roemmich and Gilson, 2011). While variations in global SST and phases of ENSO track each other closely, this is not the case for global ocean heat content Roemmich and Gilson (2011), suggesting a vertical redistribution of heat across ocean layers when Pacific climate variability transitions into and out of El Niño and La Niña events.

As a result of its profound socio-economic and environmental impacts (e.g., Diaz et al., 2001; Collins et al., 2010; Timmermann et al., 2018), an increased understanding of ENSO's underlying dynamics and key metrics is necessary. Warm water volume (WWV, defined as the volume of water above the 20°C isotherm in the equatorial region 120°E to 80°W and 5°N to 5°S) is one such metric, and is commonly used to forecast ENSO events as it leads eastern Pacific SST anomalies by 6 to 8 months (Bosc and Delcroix, 2008; McPhaden, 2012; Neske and McGregor, 2018). Since its suggestion as a key ingredient in ENSO dynamics by Wyrtki (1975, 1985), the Warm Water Volume has played a key role in many conceptual theories of ENSO, such as the discharge/recharge oscillator theory (Suarez and Schopf, 1988; Jin, 1997b,a; Burgers et al., 2005). In recent decades, WWV has been established as an integral component of many analyses, models and statistical forecast schemes for ENSO (e.g., Meinen and McPhaden, 2000; Izumo et al., 2018; Timmermann et al., 2018). However, knowledge of the precise mechanisms influencing WWV remains limited. The goal of this study is to analyse the relative importance of the various processes leading to changes in WWV.

Over a typical ENSO cycle, WWV undergoes discharge and recharge phases resulting from both adiabatic and diabatic volume fluxes. Adiabatic volume fluxes change WWV through horizontal transport (above the 20°C isotherm) into or out of the WWV region, or through surface volume fluxes due to precipitation, evaporation and river runoff (Lengaigne et al., 2012). Diabatic processes induce WWV changes via water mass transformation (WMT) with heating/cooling of water near 20°C leading to a change in the temperature of that water, and thus a movement of volume across the 20°C isotherm (Walin, 1982; Large and Nurser, 2001; Groeskamp et al., 2019; Holmes et al., 2019a).

There are two main diabatic processes that alter WWV; first, the surface heat flux comprising the radiative, sensible and latent heat fluxes, changes the temperature of water masses in the surface layers resulting in across-isotherm volume fluxes. The surface heat flux is strongly dependent on SST, with enhanced heat loss occurring over warm SSTs. During the build-up phase of El Niño the equatorial Pacific accumulates heat, which following the peak of the event is subsequently discharged to extratropical latitudes where it is radiated back into the atmosphere or into space (Trenberth et al., 2002) but also discharged into deeper ocean layers (Roemmich and Gilson, 2011; Johnson and Birnbaum, 2017; Wu et al., 2019b). The other important diabatic process relates to small-scale turbulent mixing, which can also drive significant across-isotherm volume fluxes. Turbulent mixing is an important component of the cold tongue SST budget and contributes to changes in SST over a range of time scales (Moum et al., 2013; Bernie et al., 2005). Strong turbulence in the equatorial Pacific associated with the large vertical shear above the eastward flowing equatorial undercurrent (EUC) mixes the warmer surface waters with cold upwelled waters (Smyth and Moum, 2013) and, depending on depth, leads to diabatic volume exchanges across the 20°C isotherm. This turbulence also plays an important role in the global ocean's heat budget by moving heat into deeper, colder layers that connect with the deep ocean's overturning circulation (Holmes et al., 2019b). The dynamics of upper equatorial turbulence are complex, being influenced by processes such as the diurnal cycle, tropical instability waves, the seasonal cycle, equatorial Kelvin waves and ENSO events themselves (Gregg et al., 1985; Lien et al., 1995; Smyth and Moum, 2013; Holmes and Thomas, 2015; Pham et al., 2017; Warner and Moum, 2019). Additionally, a third diabatic volume flux arises in numerical climate models: numerical mixing, emerging from truncation errors in the model's advection scheme (Holmes et al., 2019a).

While the role of adiabatic fluxes during discharge and recharge periods is relatively well understood based on data from the Tropical Atmosphere and Ocean Array (e.g., Meinen and McPhaden, 2000, 2001) and modelling studies (e.g., McGregor et al., 2013, 2014), much about the diabatic processes remains unknown and will be the focus here. While studies by Meinen and McPhaden (2000); Clarke et al. (2007) and Lengaigne et al. (2012) agree that diabatic processes are important contributors to WWV changes, the observation-based study by Bosc and Delcroix (2008) and the modelling study by Brown and Fedorov (2010) suggest that diabatic volume changes on ENSO-related time scales are negligible, thus highlighting the importance for further analyses with other models and data sets. Lengaigne et al. (2012) suggests that diabatic fluxes may also explain some of the asymmetries and non-linearities in ENSO's underlying dynamics, highlighting the need for a more in-depth analysis of the WWV budget in an idealised setting where asymmetries are controlled. In addition, coarse resolution models do not properly resolve mesoscale eddy characteristics and tropical instability waves which are important in advecting heat into and out of the equatorial Pacific (Jochum and Murtugudde, 2006). In most studies so far, either vertical mixing or both surface forcing and vertical mixing fluxes were inferred by using a residual. Here, we use the WMT framework (Walin, 1982; Large and Nurser, 2001; Holmes et al., 2019a; Groeskamp et al., 2019) in temperature space applied online within a global ocean model to diagnose the diabatic terms directly during idealised, symmetric ENSO events as well as during a hindcast simulation over the 1979 to 2016 period.

The rest of this paper is organised as follows: in Section 2.2, the ocean models, atmospheric forcing and experimental design are described. To simulate idealised ENSO events and examine asymmetries, an approach using Empirical Orthogonal Functions (EOFs) similar to McGregor et al. (2014) is used. In Section 2.3 we discuss ocean-sourced asymmetries in standard ENSO metrics arising in these idealised simulations where the atmospheric forcing is symmetric. Section 2.4 introduces the theoretical aspects of the WWV budget and how it is diagnosed within the models. After investigating the climatological WWV budget in Section 2.5, we take a closer look at the anomalies during the idealised discharge and recharge phases of ENSO (Section 2.6). We then compare the WWV budget terms from the idealised simulations to the event-to-event variability over the 1979 to 2016 period (Section 2.8) before summarising our results and their implications (Section 2.9).

2.2 Model, Data and Methods

2.2.1 The Ocean-Sea Ice Model

In this study, we use a 1/4° global ocean model with 50 z^* vertical levels based on the ocean component of the Geophysical Fluid Dynamics Laboratory (GFDL) CM2.5 coupled climate model (Delworth et al., 2012; Griffies, 2012). Atmospheric forcing for the model is derived from a prescribed atmospheric state using eight fields to calculate zonal and meridional wind stress, and surface heat and freshwater fluxes using bulk formulae (Fairall et al., 1996). The eight atmospheric fields are zonal and meridional wind speed, air temperature and specific humidity at 10 m, and downward long- and short-wave radiation, precipitation and sea level pressure at the ocean's surface. Vertical diffusion is parameterised using the K-profile parameterisation scheme (KPP, Large et al., 1994). Our study focuses on the upper 500 m where the model has 24 of the 50 z* levels, ranging from 1.1 m depth at the surface to a grid cell of 72 m depth at 500 m. The model can be considered eddy-resolving in the tropics (Hallberg, 2013; Jochum et al., 2008). In the baseline model, there is no explicit horizontal diffusion of tracer gradients and thus sharp lateral tracer gradients are smoothed by the numerical advection scheme. The associated diffusion is termed 'numerical mixing' as discussed further in Section 2.4 and in Holmes et al. (2019a). More information and discussion on the model details, diffusive mixing parameterisations and the model performance can be found in Spence et al. (2017), Stewart et al. (2017) and Holmes et al. (2019a).

2.2.2 Forcing for the Idealised, Symmetric Simulations

For the idealised simulations, the model was spun-up over a 500–year period using the climatological Coordinated Ocean-ice Reference Experiment Normal Year Forcing (CORE-NYF, Large and Yeager, 2004). For our idealised simulations, we add ENSO-related perturbations derived from the European Centre for Medium-Range Weather Forecasts' (ECMWF's) ERA-Interim product for 1979 to 2016 (Dee et al., 2011) to the base CORE-NYF fields.

Our perturbation experiments are constructed to isolate the most important aspects of ENSO variability in the atmospheric forcing (as quantified by the leading two EOFs of monthly tropical Pacific wind stress variability) to isolate oceanic-sourced asymmetries. Following the approach by McGregor et al. (2013, 2014), we first regress NOAA's ERSST v4 Niño3.4 (N34) index (Smith and Reynolds (2003), calculated as the SST deviation in the equatorial region 170°W to 120°W and 5°N to 5°S) onto the ERA-Interim wind stress anomalies from 1979 to 2016. This regression yields the spatial pattern of wind stress anomalies that are linearly associated with El Niño ($X_{1,\tau}$, Fig.

2.1a). This pattern captures the weakening of the Walker circulation during an El Niño event and is characterised by westerly wind stress anomalies in the western tropical Pacific, with slightly larger values in the Southern Hemisphere. Calculating the first EOF of equatorial wind stress anomalies instead of regressing N34 gives a time series which is highly correlated with N34 (correlation coefficient $r = 0.76$). As in McGregor et al. (2014) we use the smoother N34 time series here. This first mode captures 58.6% of the wind stress variability in the equatorial region.

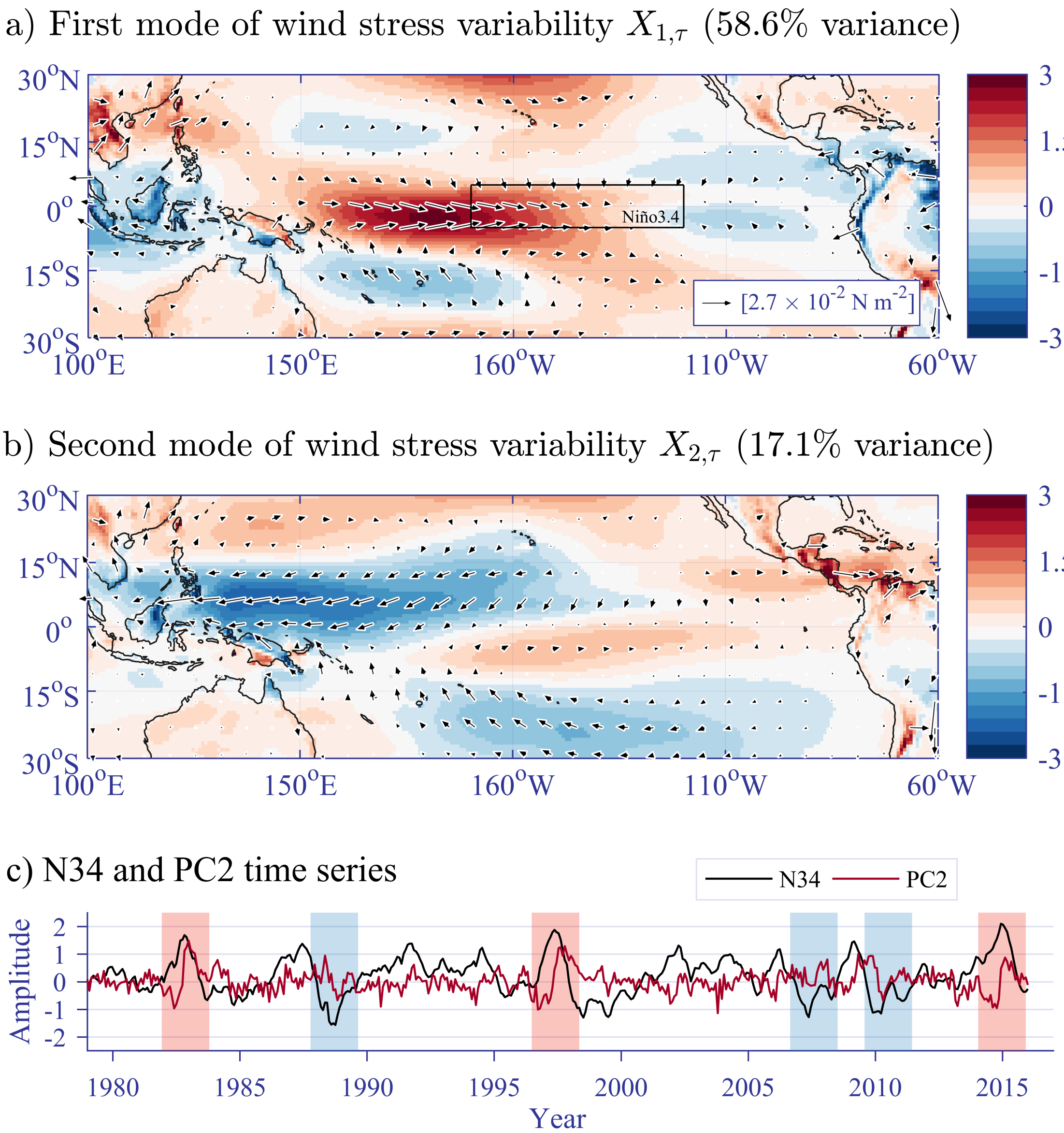

Figure 2.1: The (a) first and (b) second mode of wind stress variability related to ENSO from the ERA-Interim product (10^{-2} N m^{-2}). The zonal wind stress component is shaded. The Niño3.4 area (170°W to 120°W and 5°N to 5°S) is indicated as the framed area in (a). (c) The associated time series with the observed N34 (Reynolds et al., 2007) in black and PC2 in red. The red and blue shaded areas in (c) indicate the three strongest El Niño and La Niña events, each covering a 24-month period centered around the peak N34 anomalies.

To calculate the second pattern, the anomalies associated with $X_{1,\tau}$ and N34 are removed from the wind stress anomaly time series at each spatial location and the first EOF of the residual wind stress over the tropical Pacific region 100°E to 60°W and 10°N to 10°S is calculated (as in McGregor et al., 2014). The resulting wind stress pattern ($X_{2,\tau}$, Fig. 2.1b) and its associated principle component time series, (PC2, Fig. 2.1c) capture a strong meridional gradient of zonal wind anomalies across the Equator and play a crucial role in the winds' non-linearity related to ENSO (Zeller et al., 2019). This mode gains importance when it changes sign during the peak of El Niño and initiates a southward shift of the westerly wind anomalies (Fig. 2.1c, McGregor et al., 2013; Stuecker et al., 2013). The resulting Ekman-induced transport is much higher in the Northern than in the Southern Hemisphere, leading to an equatorial divergence of water masses (McGregor et al., 2014; Stuecker et al., 2015; Timmermann et al., 2018). This second mode drives 17.1% of the variability within the residual wind stress anomalies and combined, the first two EOF patterns explain 75.7% of the total wind stress variability within the ERA-Interim data set.

McGregor et al. (2014) used the two time series N34 and PC2 (Fig. 2.1c) from observations to simulate the variability of the tropical Pacific over the time period 1979 to 2011. Instead of using the full time series, we construct idealised synthetic time series for N34 and PC2 from the three strongest El Niño events as a basis to simulate isolated symmetric El Niño and La Niña events (i.e. we only use the time series during the red shaded periods in Fig. 2.1c). For our first experiments, the evolution of N34 and PC2 during the three strongest El Niño events for 1979 to 2016 are composited and centered at their peak in December (i.e. month 12, Fig. 2.2). Fourth-order polynomials are fitted to the mean of these three events so that anomalies increase from zero amplitude and slowly evolve in a way that approximates the mean of the three strong ENSO events (bold lines in Fig. 2.2). The polynomials are constrained to start close to zero, thereby requiring minimal adjustment at the beginning in order to achieve a smooth event onset. In addition, the N34 time series is adjusted to slowly return to zero during a spin-down period of two years following the event (Months 24 to 48), while the PC2 time series is zero during the full spin-down period (Fig. 2.2). We also simulate a symmetric 'La Niña' event, where the time series are simply set to negative amplitude with respect to the El Niño case. This allows us to investigate any asymmetric responses resulting from ocean-sourced non-linearities in the presence of symmetric atmospheric forcing.

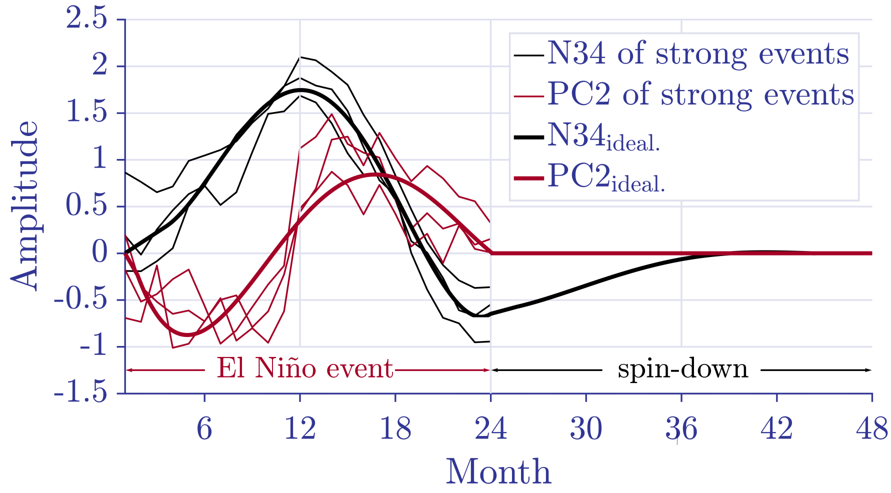

Figure 2.2: The idealised synthetic time series in bold for N34 (black) and PC2 (red) during the two-year-long El Niño event followed by a two-year-long spin-down period. The thin lines show the observed N34 values (black) and the calculated PC2 time series (red) during the three strongest El Niño events in Fig. 2.1c, namely 1982 to 1983, 1997 to 1998 and 2014 to 2016, centered in December.

The atmospheric fields that force the model are then derived using regressions of the N34 index and PC2 time series as described in the Extended Data section. To increase the signal-to-noise ratio, ensemble simulations were also performed. However we found that differences between the ensemble members are more than two orders of magnitude smaller than the variability in the ensemble mean, and so we only present results from one ensemble member. We calculate the anomalies relative to the time-mean fields of eight years in the control simulation, except for ocean heat content where we subtract the time-varying control simulation to better account for the drift in the 200 to 2000 m layers.

2.2.3 Interannual Model Simulation

We follow-up our idealised, symmetric ENSO simulations with an interannual hindcast simulation for the period 1979 to 2016 with an updated configuration of the model (Kiss et al., 2020). The forcing for this configuration is from the JRA55-do v1.3 reanalysis for 1958 to 2018 (Tsujino et al., 2018) and the spin-up was performed by using five repeat cycles of JRA55-do (Kiss et al., 2020). The resolution and model physics in this configuration are identical to the base model, except that it uses an updated 50-level vertical grid and it includes the Gent and McWilliams (1990) parameterisation for mesoscale eddies as well as explicit Redi (1982) along-isopycnal diffusion. However, these parameterisations are scaled with latitude and neither plays an important role in the tropics. For our analysis, we analyse the 1979 to 2016 period of the last cycle where the online WMT diagnostics are output.

2.3 ENSO's Ocean-Sourced Anomalies During Idealised Events

In this section, we first discuss the ocean-sourced anomalies and asymmetries in our idealised symmetrically-forced El Niño and La Niña simulation before presenting an in-depth analysis of the WWV budget in the following sections.

Although ENSO's anomalies are strongest in the Pacific, they have impacts on a global scale (e.g., Roemmich and Gilson, 2011; Wu et al., 2019b; Cheng et al., 2019). Global mean sea surface temperature (GMSST) anomalies during the strong El Niño 1997 to 1998 exceeded 0.2°C in NOAA's OI SST V2 data set (Reynolds et al., 2007; Roemmich and Gilson, 2011). This is mostly caused by the warm eastern equatorial Pacific during El Niño. In our idealised El Niño simulation, maximum GMSST anomalies are reached in December, with a value of 0.092°C (blue line, Fig. 2.3a). These anomalies are lower than the 0.2°C in NOAA's OI SST v2 product, but expected as our idealised simulation is based on a composite events.

The N34 index explains a large part of the increase in GMSST (light blue line in Fig. 2.3c). The maximum value of the N34 index (1.57°C), is slightly lower than given by the idealised time series (dashed line Fig. 2.3c), which is not unexpected since SST is determined dynamically within the model. In the last four months of the El Niño event (months 20 to 24), both the idealised and modelled N34 anomalies are negative, indicating a change to developing La Niña-like conditions. This represents the discharged state of the tropical Pacific at the end of the El Niño event. To first order, the anomalies in the La Niña simulation (Fig. 2.3b, d) are opposite to the El Niño event. In particular, the N34 index and GMSST anomalies are close to the exact opposite during La Niña, with only a slightly increased amplitude (Fig. 2.3).

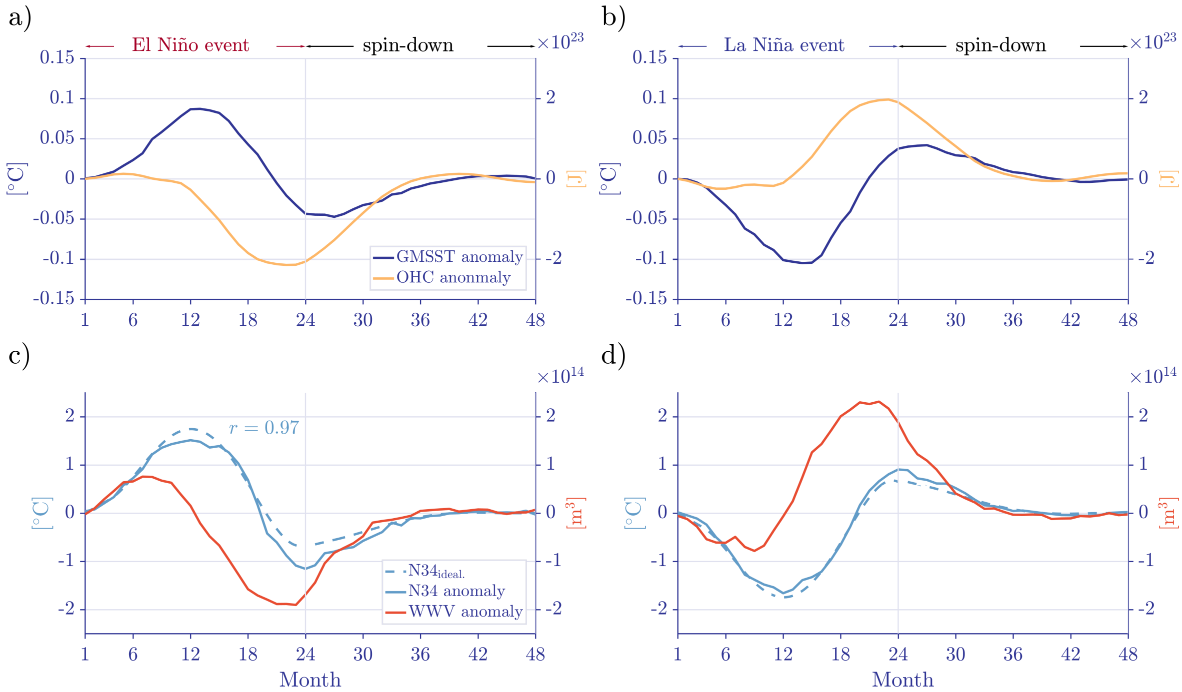

Figure 2.3: Anomalous time series for the (a, b) global mean sea surface temperature (GMSST) (°C) and globally integrated ocean heat content (OHC) (J) as well as (c, d) the idealised N34 index, the simulated N34 index (°C) and the WWV anomalies (m^3) during the idealised and symmetric El Niño and La Niña events. In (c) the correlation coefficient (r) between the observed and simulated N34 index is shown in blue. The vertical lines at months 24 represent the end of the event and the subsequent start of the two-year-long spin-down period with climatological forcing.

The rate of change of the ocean's heat content (OHC) is highest when both GMSST and the N34 index peak at month 12 (orange line, Fig. 2.3a). As expected, this suggests that the warmest equatorial Pacific SST values coincide with the highest anomalous surface heat fluxes into the atmosphere or into space during El Niño (and opposite for month 12 during La Niña in Fig. 4, as in Meinen and McPhaden, 2001; Johnson and Birnbaum, 2017; Cheng et al., 2019). The global ocean's heat release continues until month 20 of the simulation when equatorial SSTs and surface heat fluxes return to neutral conditions. The WWV anomalies as a proxy for the upper equatorial OHC show a similar behaviour as the global OHC anomalies, with discharge during El Niño lasting 15 months and recharge occurring over a period of 14 months during La Niña (red line, Fig. 2.3c, d). Unlike OHC, the anomalous WWV time series shows a considerable positive and negative peak prior to the peak of El Niño and La Niña. This behaviour is caused by the first EOF mode of wind stress anomalies initiating an equatorward surface Ekman transport during El Niño, while causing a poleward transport during La Niña (McGregor et al., 2014). The surface Ekman transport during this stage is more dominant than the subsurface geostrophic transport of the opposing sign, effectively causing a recharge and discharge of WWV (McGregor et al., 2014). The global OHC anomalies do not show this distinct increase or decrease prior to the peak of the events. The WWV anomalies before the discharge phase (Fig. 2.3c) are lower compared to those in Meinen and McPhaden (2000) and likely caused by the weaker build-up prior to the event due to the transition from climatological forcing.

Additionally, our idealised experimental design also contains the following simplifications that could each contribute to deviations from observed events: (1) we use NOAA's ERSST v4 N34 index as in McGregor et al. (2014) to derive the atmospheric forcing. This index, in particular during strong El Niño events, is weaker than the same index in the ERA-Interim reanalysis (Dee et al., 2011) and HadISST (Rayner et al., 2003) products as it has larger parametric uncertainties at smaller spatial and shorter time scales (including for ENSO events, Liu et al., 2015; McGregor et al., 2017). (2) We force the model in these simulation with an interpolated atmospheric field from monthly-averaged anomalies and a grid resolution of 220 km, and thus do not fully capture high-frequency variability such as westerly wind events, which are known to impact WWV anomalies (Menkes et al., 2014). (3) In our simulations, we use only the first two EOF modes of equatorial wind stress anomalies associated with El Niño which account for 75% of the total variance. Despite these approximations, the idealised simulations are able to reproduce the key physical processes throughout ENSO.

2.4 The Warm Water Volume Budget

In this section we give a brief theoretical introduction into the WWV budget and how it is constructed within the model experiments. We define WWV as the volume of water above the 20°C isotherm in the area between Borneo (116°30'E), the South American coastline (78°W) and 5°N to 5°S. This WWV definition has been previously used in studies by Meinen and McPhaden (2000), Lengaigne et al. (2012), McGregor et al. (2014) and others. We define the Indonesian Throughflow (ITF) as the transport between Borneo (116°30'E) and New Guinea (133°45'E) at 2°S.

In order to understand and diagnose the WWV budget, we not only evaluate horizontal adiabatic volume fluxes, but also evaluate how volume is exchanged vertically across the 20°C isotherm. Across-isotherm volume fluxes can be studied by using the WMT framework, first introduced by Walin (1982). It describes the processes that lead to a given water parcel's change in temperature and subsequent movement across isotherms.

Changes in WWV over time are dependent on both adiabatic and diabatic processes:

$$\frac{dWWV}{dt} = \underbrace{\mathcal{T}_{5^\circ N+5^\circ S} + \mathcal{T}_{ITF} + \mathcal{J}}_{Adiabatic\ processes} + \underbrace{\mathcal{G}_{\mathcal{F}} + \mathcal{G}_{\mathcal{M}} + \mathcal{G}_{\mathcal{I}}}_{Diabatic\ processes}, \tag{2.1}$$

where $dWWV/dt$ is the WWV tendency (m^3 s^{-1}), calculated by using snapshots of the temperature field at the beginning and end of each month (the period over which the right-hand side diagnostics in Equation 2.1 are accumulated online). The adiabatic processes include the lateral transport of water masses above 20°C into and out of the WWV region across the three transects 5°N, 5°S ($\mathcal{T}_{5^\circ N+5^\circ S}$), and the ITF ($\mathcal{T}_{ITF}$) (m^3 s^{-1}). In addition, the surface volume flux $\mathcal{J}$ (m^3 s^{-1}) accounts for small adiabatic volume changes due to river runoff, precipitation, and evaporation of water above 20°C when freshwater enters or leaves the ocean at the sea surface. The surface volume fluxes in the model enter and exit the ocean at the sea surface temperature (Holmes et al., 2019a). Thus, there is no additional sensible heat flux into the ocean associated with differences in temperature between the freshwater and the surface sea water. Therefore, in the model, these fluxes are considered adiabatic. These adiabatic variables are diagnosed by summing the associated transports over all temperature classes warmer than 20°C. The calculations (i.e. the binning into temperature classes) take place online at every time step of the model simulation. Here we show the monthly accumulated averages of these online diagnostics.

The three diabatic WMT volume fluxes include surface forcing $\mathcal{G}_{\mathcal{F}}$, vertical mixing $\mathcal{G}_{\mathcal{M}}$ and numerical mixing $\mathcal{G}_{\mathcal{I}}$, each expressed in units of (m^3 s^{-1}). The surface forcing volume flux $\mathcal{G}_{\mathcal{F}}$ across the 20°C isotherm is driven by the surface heat flux and its different components (short-wave, long-wave, sensible and latent heat fluxes). $\mathcal{G}_{\mathcal{F}}$ is the convergence of these heat fluxes within a given temperature class, which indicates fluid warming and therefore crossing isotherms toward warmer or colder fluid. Likewise, $\mathcal{G}_{\mathcal{M}}$ is the WMT volume flux arising from parameterised diffusive vertical mixing processes. Through heating and cooling fluid, diffusive mixing likewise moves water across temperatures classes. These two WMT fluxes are calculated as diagnostics from the heat budget binned into temperature space (Holmes et al., 2019a), and depend on the across-isotherm heat fluxes through,

$$\mathcal{G}_{\mathcal{F}} = \frac{1}{\rho_0 \cdot C_p} \cdot \int\int \left.\frac{\partial \mathcal{F}}{\partial \Theta}\right|_{20^\circ C} dA, \tag{2.2}$$

$$\mathcal{G}_{\mathcal{M}} = \frac{1}{\rho_0 \cdot C_p} \cdot \int\int \left.\frac{\partial \mathcal{M}}{\partial \Theta}\right|_{20^\circ C} dA. \tag{2.3}$$

Here, ρ_0 is the reference density of sea water (1035 kg m^{-3}), C_p is the specific heat capacity of sea water at constant pressure (3992.1 J kg^{-1} K^{-1}) and $\mathcal{F}$ is the total surface heat flux (W m^{-2}) into all fluid warmer than a given potential temperature Θ at each horizontal location (taking into account the penetration of short-wave radiation into the interior). Similarly, $\mathcal{M}$ is the total heat flux into all fluid warmer than Θ at each horizontal location due to vertical diffusion and the non-local heat flux component of the KPP boundary layer mixing scheme (W m^{-2}) of Large and Yeager (2004), although this non-local term plays a minor role. Both $\mathcal{F}$ and $\mathcal{M}$ are diagnosed online by binning the corresponding Eulerian heat budget diagnostics into temperature classes at every time step. The temperature bin size is 0.5°C. We evaluate the WWV budget at 20°C and the area integral is performed over the WWV region (116°30'E to 78°W and 5°N to 5°S). More details on the numerical implementation of these WMT diagnostics are presented in Holmes et al. (2019a).

Lastly, the WMT flux $\mathcal{G}_{\mathcal{I}}$ arises from numerical diffusion associated with truncation errors in the model's tracer advection scheme (i.e. numerical mixing). The advection scheme is three-dimensional and acts to smooth both vertical and horizontal tracer gradients at the grid scale (Colella and Woodward, 1984). Due to choices made to minimise sources of explicit diffusion (namely, zero explicit lateral diffusion or background vertical diffusivity), numerical diffusion makes a non-negligible contribution to the global climatological heat budget (Holmes et al. (2019a); their Fig. 3) and the WWV budget. We calculate $\mathcal{G}_{\mathcal{I}}$ as the residual of Equation 2.1.

The WWV budget additionally includes terms associated with the parameterisation of submesoscale eddies (Fox-Kemper et al., 2008) and, in the 1979 to 2016 hindcast simulation, mesoscale eddies (Redi, 1982; Gent and McWilliams, 1990). These fluxes make negligible contributions to the WWV budget but are included in our calculation as $\mathcal{G}_{\mathcal{E}}$ (eddy mixing) in order to accurately calculate numerical mixing as the residual.

2.5 The Climatological Warm Water Volume Budget

Before our analysis of the anomalous WWV budget terms during ENSO, we first investigate its climatology as the anomalous fluxes are tightly linked to the seasonal cycle.

The climatological WWV in the control simulation exhibits a small long-term spin-up trend of 9.1×10^{12} m^3 yr^{-1} (equivalent to 0.28 Sv). It is closely linked to the equatorial overturning circulation and comprises a balance between the adiabatic and diabatic fluxes. Vertical mixing in the annual mean cools surface water masses and simultaneously warms deeper layers, represented by the negative (blue) and positive (red) across-isotherm (or diathermal) velocity regions in Fig. 2.4a. Surface forcing is consistently warming the surface region (Fig. 2.4b). The annual mean 20°C isotherm is positioned on average in the warming region of both diabatic fluxes, indicating a net upward volume flux across the isotherm into the WWV above. Thus, vertical mixing (+6.7 Sv, Sv = 10^6 m^3 s^{-1}) and surface forcing (+2.7 Sv) both show positive contributions to the annual mean budget. Numerical mixing plays only a minor role. The convergent diathermal transport is balanced by negative contributions from the predominantly eastward trade winds driving a divergent Ekman transport across 5°N and 5°S (−6.1 Sv) and transport through the ITF (−6.2 Sv, Schott et al., 2004). The impact of the surface volume flux is negligible compared to the other terms (as in Meinen and McPhaden, 2001; Lengaigne et al., 2012; Brown and Fedorov, 2010) and will not be discussed further.

These processes (both adiabatic and diabatic) have a seasonal cycle linked to the strength of the equatorial trade winds (Horel, 1982). The WWV peaks near the end of the year, increasing in the second half of the year, and decreasing in the first half (black line Fig. 2.5a). While meridional transport explains part of the WWV recharge in the second half of the year, most of this increase stems from the enhanced diabatic fluxes (Fig. 2.5b). The stronger trade winds in the second half of the year increase upwelling of cold water masses, shoaling of the 20°C isotherm and heat absorption from the atmosphere (Fig. 2.4d). At the same time, shear- and wind-driven turbulence in the

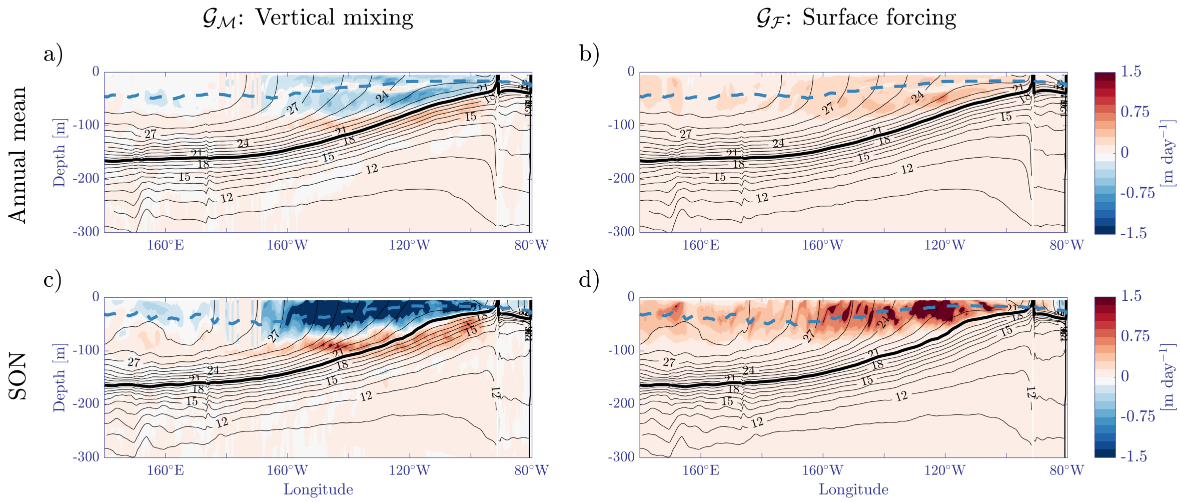

Figure 2.4: Depth-longitude transects across the equatorial Pacific of the water mass transformation velocities (Equations 2.3 and 2.2) for (a, c) vertical mixing $\mathcal{G}_{\mathcal{M}}$ and (b, d) surface forcing $\mathcal{G}_{\mathcal{F}}$ (m day^{-1}) in the CORE-NYF control simulation. The WMT velocities are accumulated in temperature space and remapped to depth using the mean isotherm depths. The upper two panels show the annual mean and the lower panels the mean over the September-November (SON) period when the diabatic fluxes are seasonally intense (Fig. 2.5b). The contours show the distribution of the equatorial isotherms with the 20°C isotherm in bold. The dashed blue line in the upper-most layers indicates the mixed layer depth defined as a 0.032 kg m^{-3} density difference from the surface. The discontinuity at 90°W is caused by the model's bathymetry near the Galápagos Islands.

upper EUC intensifies, driving stronger diabatic upwelling via vertical mixing across the shallower 20°C isotherm (Fig. 2.4c, Moum et al., 2013; Liu et al., 2016). Combined, the two diabatic fluxes result in positive diathermal velocities across the 20°C isotherm in the eastern equatorial Pacific and an increase in WWV (i.e. the sum of Fig. 2.4c and d results in an overall positive, red spatial pattern). Further, the stronger trade winds also cause an increased sea surface height (SSH) difference between the Indian and Pacific Ocean leading to an increased strength of the ITF, which partially offsets the two diabatic fluxes in the second half of the year (green line, Fig. 2.5a, Shinoda et al., 2012).

2.6 The Warm Water Volume Budget During Idealised ENSO Events

We now examine the anomalous WWV budget terms and asymmetries during the idealised, symmetric events before comparing them to events in the hindcast simulation. Over the ENSO cycle, WWV undergoes changes associated with the recharge and dis-

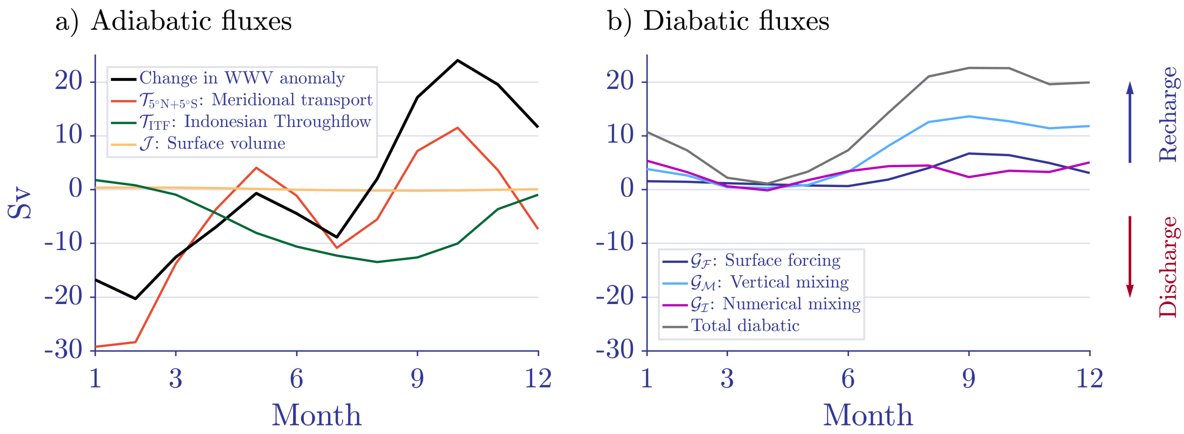

Figure 2.5: Annual cycle of the climatological (a) adiabatic and (b) diabatic WWV budget terms (Sv $\equiv 10^6$ m^3 s^{-1}) in the CORE-NYF control simulation. The change in WWV as the sum of the other fluxes is shown as the black line in (a). Positive values indicate a volume flux into the WWV region (i.e. a recharge) and negative values indicate a volume flux out of the region (i.e. a discharge). A 3–month running mean has been applied.

charge of heat. We define the discharge phase during the idealised El Niño as the period when the WWV anomaly is decreasing, i.e. the rate of change in WWV is negative (red shaded period from month 7 to 21, Fig. 2.6a, c). To ensure a symmetric analysis, we define the recharge phase during La Niña as the same time period (blue shading, Fig. 2.6b, d). The anomalies are calculated by subtracting off the climatological budget discussed in the previous section.

2.6.1 The Idealised Symmetric El Niño Discharge

The discharge phase during El Niño is initiated in July when the rate of change in the WWV anomaly becomes negative (Fig. 2.6a). WWV depletion in this simulation thus starts five months ahead of the peak of El Niño and leads over the 15-month period to a total volume decrease of 2.5×10^{14} m^3 (corresponding to 6.3 Sv or a shoaling of the 20°C isotherm by 12.8 m when averaged over the WWV region). Depletion of WWV occurs in two phases, with an initial decrease driven mainly by diabatic fluxes across the 20°C isotherm (approximately months 7 to 14) followed by a period with dominant horizontal adiabatic transport out of the equatorial region (approximately months 12 to 21, red area, Fig. 2.6a, c).

Changes in surface forcing and vertical mixing drive the initial phase of WWV decrease (blue lines, Fig. 2.6c). This is consistent with the observation-based study by

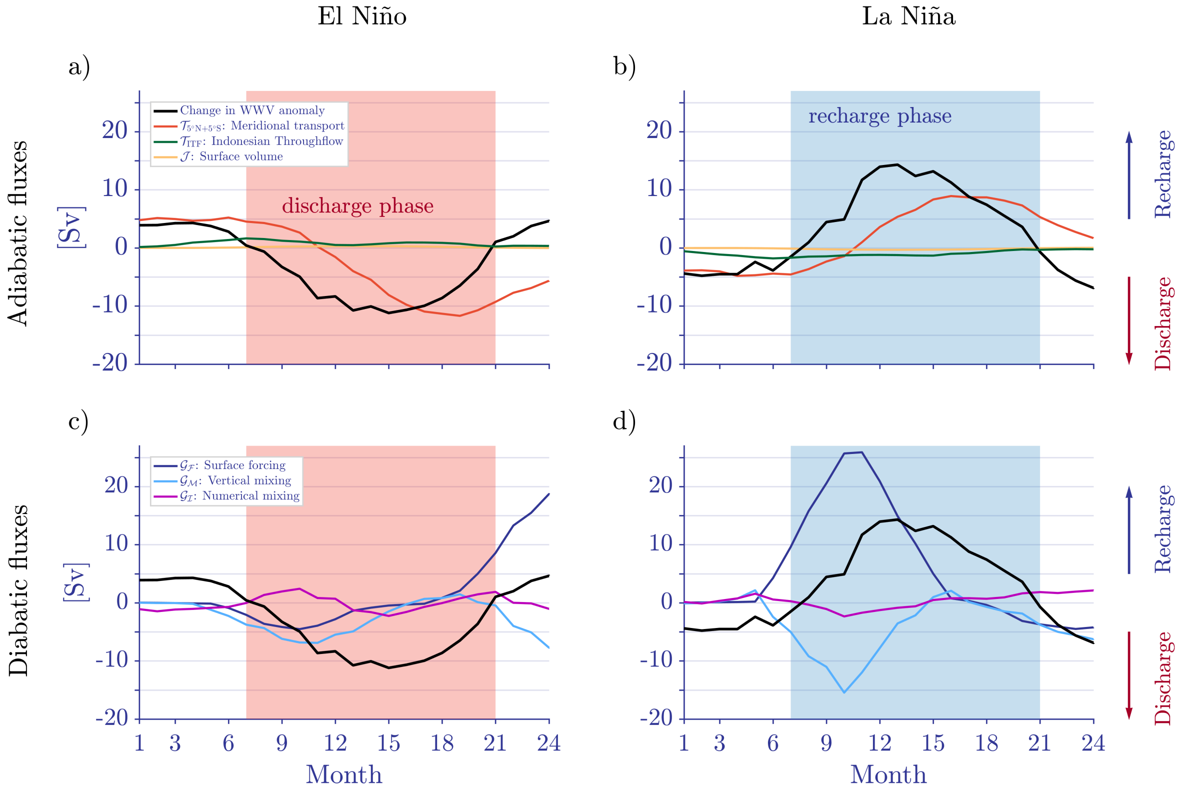

Figure 2.6: The (a, b) adiabatic and (c, d) diabatic WWV budget terms (Sv) as anomalies throughout the idealised, symmetric El Niño and La Niña simulations. A five-month running mean as in Meinen and McPhaden (2000) has been applied. The discharge phase (red shaded period in panel a) is defined as the period when the change in WWV is negative from months 7 to 21. To ensure a symmetric analysis during La Niña, the recharge phase (blue shaded period) covers the same period. Positive values indicate volume transport into the WWV region (i.e. a recharge), negative values represent transport out of the WWV region (i.e. a discharge).

Meinen and McPhaden (2001) where there are suggestions that the WWV discharge due to diabatic processes (inferred as the residual of the WWV change minus the lateral transport) is dominant in the early part of the 1997 El Niño (e.g., Fig. 13 of Meinen and McPhaden, 2001). However, uncertainties in their calculations are large (estimated as ±6 Sv). This highlights the need for future observation-based studies to better reconcile the role of the observed diabatic, vertical fluxes. The weaker trade winds during El Niño reduce upwelling of cold water masses to the surface, decrease shear- and wind driven mixing and deepen the 20°C isotherm. These effects combined result in an overall reduced/anomalous surface forcing and vertical mixing flux across the 20°C isotherm compared to climatological conditions (compare Figs. 2.7a and 2.4c).

The reduced surface forcing and vertical mixing fluxes until the peak of El Niño agree well with the observational study by Warner and Moum (2019). Numerical mixing anomalies play a minor role throughout the discharge phase contributing only 4%

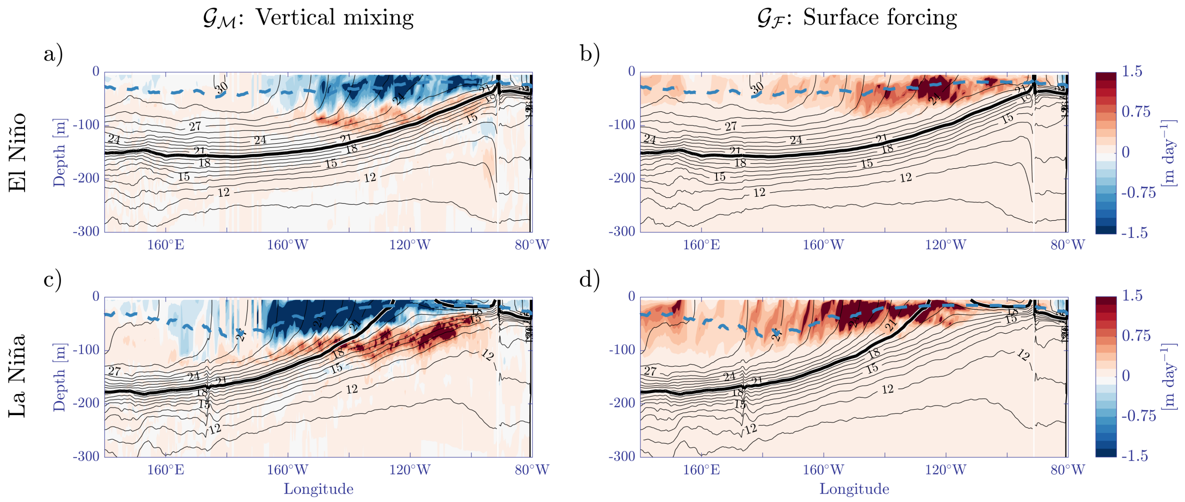

Figure 2.7: Mean depth-longitude transects for September-November across the equatorial Pacific of the water mass transformation velocities for (a, c) vertical mixing $\mathcal{G}_{\mathcal{M}}$ and (b, d) surface forcing $\mathcal{G}_{\mathcal{F}}$ (m day^{-1}) during the idealised, symmetric El Niño and La Niña events. The contours show the distribution of the equatorial isotherms with the 20°C isotherm in bold. The dashed blue line in the upper-most layers indicates the mixed layer depth as defined in Fig. 2.4.

to the overall changes in WWV (Fig. 2.8a). Together, the total diabatic volume flux throughout the discharge phase amounts to a volume change of -1.1×10^{14} m^3, contributing ∼45% to the total change (Fig. 2.8a), and is comparable to the average estimate over the 1976 to 2004 time period in Lengaigne et al. (2012).

The second phase of WWV discharge occurs about six months later, with meridional transport as the dominant driver (red line in Fig. 2.6a). During the initial discharge phase (months 7 to 11), anomalous adiabatic transport through 5°N and 5°S opposes WWV depletion by off-equatorial westerly wind bursts, moving more warm water into the equatorial band (McGregor et al., 2016). The high amplitude of the first EOF mode (Fig. 2.1a) combined with the positive amplitude of the second EOF mode (Fig. 2.1b) of wind stress anomalies during the second year of the simulation drive a strong Ekman divergence and geostrophic transport of warm water masses across 20°C to higher latitudes (McGregor et al., 2012, 2014; Zeller et al., 2019).

While the large-scale horizontal transport through 5°N and 5°S during the second phase of discharge is high, the strength of the ITF is decreased throughout the full discharge phase (green line in Fig. 2.6a, which is slightly positive throughout the time period). This is the result of the reduced SSH gradient between the Indian and the Pacific Ocean during El Niño (Sprintall and Révelard, 2014; Feng et al., 2018). Including

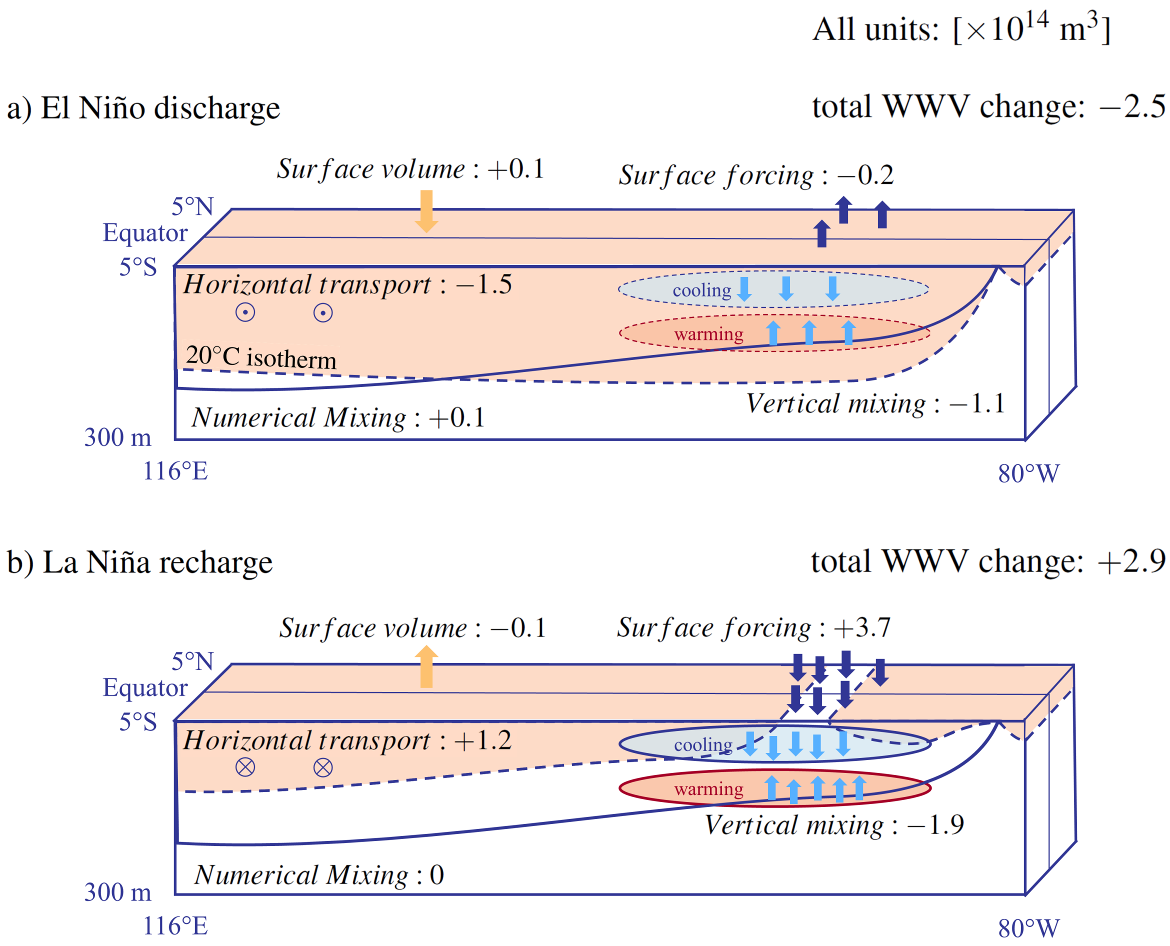

Figure 2.8: Snapshots of the warm water volume during the peak of the idealised, symmetric (a) El Niño discharge and (b) La Niña recharge phases alongside the time-integrated contribution of the WWV budget terms over the full discharge/recharge period. The solid line between 116°E to 80°W displays the climatological 20°C isotherm depth and the dashed line its anomalous position during the event. Before the El Niño event, WWV is anomalously large (hence a deep isotherm) and the integrated WWV budget terms over the event result in the net discharge of WWV. The blue and red shaded areas in the eastern equatorial Pacific indicate where vertical mixing is cooling and warming water masses that lead to buoyancy-driven vertical heat and volume fluxes across isotherms indicated by the light blue arrows. The dark blue arrows show how anomalous surface forcing leads to (a) depletion and (b) build-up of WWV across the 20°C isotherm. The two symbols ⊗ and ⊙ illustrate meridional WWV transport out of and into the equatorial region respectively. Meridional transport here combines the horizontal transport across 5°N, 5°S and the ITF.

the ITF, the total adiabatic transport during the discharge period contributes 1.4×10^{14} m^3, or about 55%, to the total WWV changes (Fig. 2.8a). During this second phase (months 11 to 21), the diabatic volume fluxes play only a minor role.

The change to La Niña-like conditions at the end of the discharge phase concurrent with the negative amplitude of the idealised N34 index (black line, Fig. 2.2) is also evident here in the increase in WWV (months 20 to 24, Fig. 2.3a). This is caused by the shallower 20°C isotherm and colder SST values in the eastern Pacific, leading to increased ocean heat absorption around the 20°C isotherm as indicated by an increase in the surface forcing term (dark blue line, Fig. 2.3a).

2.6.2 The Idealised Symmetric La Niña Recharge

As during El Niño, the change in WWV during La Niña occurs over two stages. The initial phase is dominated by diabatic volume fluxes and the latter half of the recharge phase is mainly controlled by meridional transport (Fig. 2.6b, d). During La Niña's recharge, the total change in WWV (i.e. blue region in Fig. 2.6b, d) is 2.9×10^{14} m^3, slightly higher than the change in volume during El Niño's discharge phase (Fig. 2.8b) despite the symmetric atmospheric forcing (this is equivalent to a discharge of 7.4 Sv or a deepening of the 20°C isotherm by about 15 m when averaged over the WWV region). It is likely caused by the ocean being able to absorb more heat when conditions are cool in contrast to El Niño's heat loss.

Compared to El Niño's discharge phase, not all volume fluxes are opposite and of the same magnitude. The most striking differences lie in the vertical mixing and surface forcing fluxes (compare blue curves in Figs. 2.6c and 2.6d). The strengthened trade winds during La Niña drive increased vertical mixing in the upper ocean (Fig. 2.7c, Warner and Moum, 2019), yet counter-intuitively, the vertical mixing volume flux does not increase but decreases WWV (i.e. in the same sense as during El Niño events). This remarkable asymmetry is a result of the strong non-linearity associated with shifts in the 20°C isotherm position. Specifically, the shoaling of the 20°C isotherm in the eastern equatorial Pacific moves the isotherm from the subsurface, where mixing warms water, toward the surface where mixing cools water masses (Fig. 2.7c, 2.8b). This leads to a downward volume flux across the 20°C isotherm due to mixing throughout much of the eastern Pacific toward cooler and deeper layers, and thus a decrease of WWV.

In contrast, the surface forcing volume flux clearly dominates WWV build-up, with a much stronger response compared to El Niño's discharge period. The increased trade wind strength, the shallower 20°C isotherm (where it is more strongly influenced by surface forcing) and the cold SST values lead to a high anomalous heat absorption in the eastern equatorial Pacific. This warm water is then subsequently advected westward and accumulates in the western Pacific warm pool, deepening the 20°C isotherm there (Fig. 2.7d). The total contribution of the surface forcing volume flux to the WWV increase is 3.7×10^{14} m^3 (128% of the total change in WWV). However, as the vertical mixing contribution opposes this surface forcing volume flux, the overall diabatic volume transport accounts for ∼62% (Fig. 2.8b). This interplay between strong vertical mixing and strong surface forcing fluxes during the transition to the peak of La Niña is also supported in the observational study by Warner and Moum (2019). Numerical mixing during La Niña's recharge phase, as during El Niño's discharge of heat, again plays only a minor role (purple line in Fig. 2.6c, d). It contributes only ∼1% to the changes in WWV (Fig. 2.8b).

Contrary to the vertical fluxes, meridional transport into the WWV region during the recharge phase is largely symmetric with respect to El Niño's discharge. This is caused by the prescribed symmetric wind stress perturbations, which drive most of the adiabatic transport (e.g., McGregor et al., 2012, 2014; Zeller et al., 2019). The small asymmetry in the adiabatic transport relative to the idealised El Niño may be related to differences in the 20°C isotherm depth capturing a different fraction of the geostrophic return flow despite symmetric wind stress forcing. Consistent with the recharge oscillator theory, Meinen et al. (2001) and McGregor et al. (2014), horizontal transport lags the peak SST/wind stress anomalies (roughly when the WWV changes are largest) by about four months. The ITF is consistently stronger than normal throughout the full recharge period (green line in Fig. 2.6b), as strong trade winds increase the SSH in the western equatorial Pacific, driving higher transport into the Indian Ocean. In total, the adiabatic horizontal transport (and surface volume flux) is responsible for ∼38% of the total recharge as compared to the ∼55% contribution during El Niño's discharge (Fig. 2.8b).

In summary, we see that the meridional, adiabatic transport of WWV between the two symmetrically-forced ENSO phases is largely symmetric. The diabatic processes however are a considerable source of asymmetry arising from the dependence of the heat fluxes on SST and the vertical movement of the 20°C isotherm coupled with mixing changes.

La Niña events typically last longer and have a reduced amplitude relative to their corresponding El Niño events as they often re-intensify during the following winter (Okumura and Deser, 2010). Our idealised forcing based on the exact opposite of a composite of El Niño events therefore overestimates the magnitude of La Niña. Additionally, La Niña events do not include a clear shift from negative to positive values in the PC2 time series (red line during red periods, Fig. 2.1c). It is therefore important to compare our idealised symmetric simulations to ENSO events and their event-to-event variability in a simulation with atmospheric forcing more closely following observations. The next section first validates the 1979 to 2016 hindcast simulation against observations before an in-depth analysis of the variability in the WWV budget between events.

2.7 ENSO's Ocean-Sourced Anomalies During 1979 to 2016

The simulated N34 index over the 1979 to 2016 period captures the observed variations in NOAA's ERSST v4 N34 index (Smith and Reynolds, 2003) reasonably well (blue lines, Fig. 2.9). The three strong El Niño events in 1982/83, 1997/98 and 2015-16, on which our analysis focuses on, are slightly overestimated in the simulation compared to the observational time series. As expected, the anomalous WWV time series leads the N34 index by three to six months (red lines, Fig. 2.9). While the correlation between the simulated and observed WWV time series is high ($r = 0.92$), the magnitude is somewhat underestimated during the El Niño in 1997/98 and the La Niña event 2010/11.

As the position of the 20°C isotherm is a key factor influencing WWV, it is important to validate it against observations during El Niño and La Niña events. As mentioned above, a shallow position increases diabatic WWV transport through enhanced vertical mixing and the penetrating solar heat fluxes while a deep 20°C isotherm leads to a reduced effect. The climatological position of the 20°C isotherm compares reasonably well to observations (black lines, Fig. 2.10, Kiss et al., 2020), although it is slightly shallower west of 140°W (by ∼20 m) and deeper (by ∼15 m) east of 140°W. During the 1997 to 1998 El Niño, as warm water reaches the eastern equatorial Pacific, the 20°C

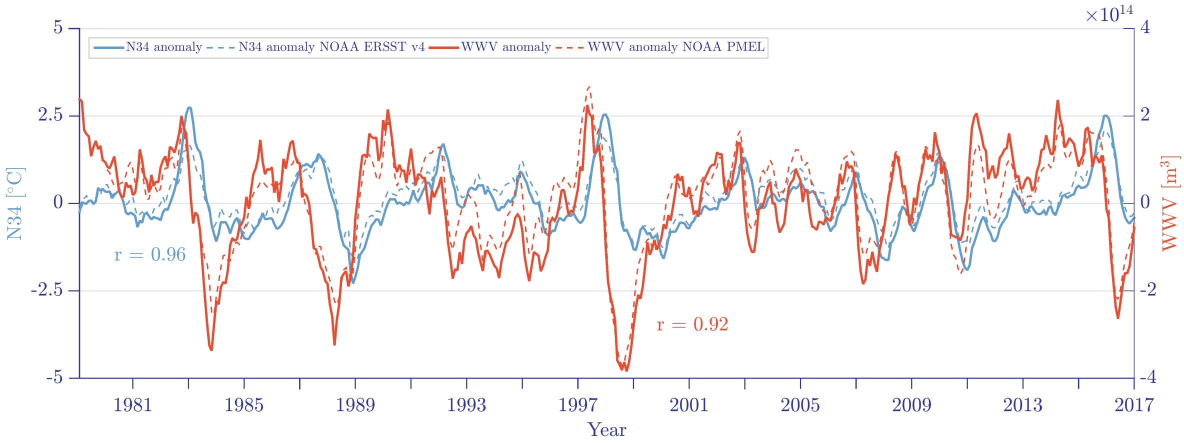

Figure 2.9: Time series of the simulated N34 index (°C) and anomalous WWV (m^3) during the 1979 to 2016 hindcast simulation compared to observations in Reynolds et al. (2007) and Meinen and McPhaden (2000). The observed indices are given as dashed blue and red lines and the correlation coefficients (r) between the simulated and observed time series are indicated with blue and red values.

isotherm in the east deepens by about 120 m in ECMWF's (ORA-S5, Zuo et al. (2018), Fig. 2.10). The hindcast simulation captures this downward shift of the isotherm, although with a negative bias of $\sim$ 30 m around 140°W and a positive bias of $\sim$ 30 m at 80°W near the South American coastline. The isotherm position shown in Fig. 2.10 is the mean over the September-November period. During the following La Niña in 1998/99, the simulation exhibits a somewhat too shallow 20°C isotherm in the central Pacific and a negative bias of about 20 to 25 m in the surface region at 110°W compared to ORA-S5 (blue lines, Fig. 2.10). These tilt differences in the isotherm position also occur during other events and likely explain most of the offset between the simulated and observed anomalous WWV time series in Fig. 2.9.

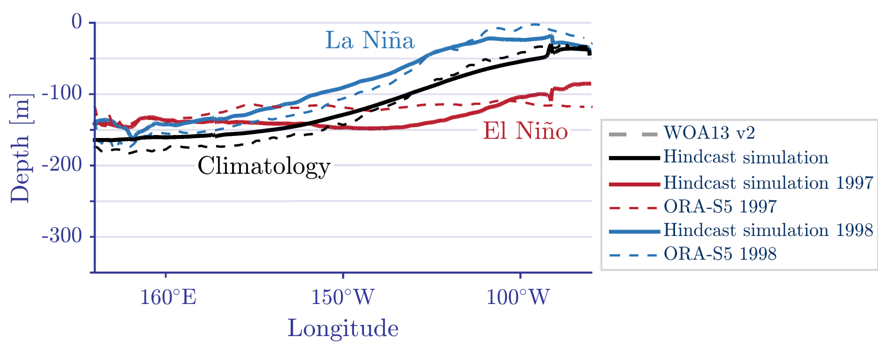

Figure 2.10: Depth-longitude transect of the 20°C isotherm for September-November across the equatorial Pacific during the El Niño event in 1997 (blue lines) and La Niña event in 1998 (red lines) in the 1979 to 2016 hindcast simulation. The dashed blue and red lines show the isotherm distribution during the same time period in the ORA-S5 ocean reanalysis product (Zuo et al., 2018). In black the climatological position of the 20°C isotherm compared to the observations in the World Ocean Atlas (WOA13v2, Locarnini et al., 2013).

2.8 The Warm Water Volume Budget During 1979 to 2016

Over the 38-year period between 1979 to 2016, the equatorial Pacific undergoes multiple discharge and recharge phases of WWV (red shaded and blue shaded periods, Fig. 2.11). While there are more than three El Niño and La Niña events during this period, our analysis here will focus on three strong events each. We define these discharge and recharge events as when the rate of change in WWV anomalies (black line in Fig. 2.11a) is negative and positive respectively.

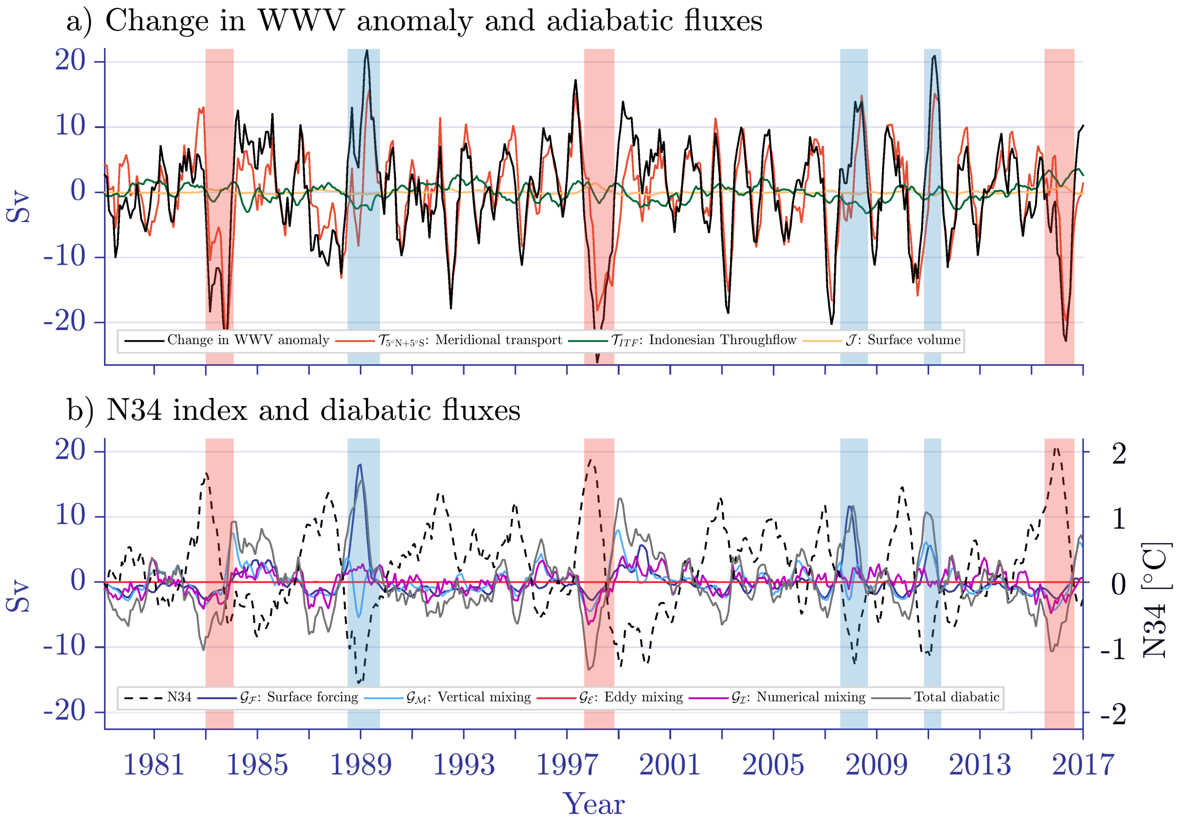

Figure 2.11: (a) The change in the WWV anomaly as well as the adiabatic and (b) diabatic volume fluxes (Sv) during the 1979 to 2016 hindcast simulation. A five-month running mean as in Meinen and McPhaden (2000) has been applied. The red discharge and blue recharge periods for the three strongest El Niño and La Niña events are defined as when the rate of change in the WWV anomaly (black line in (a)) is negative and positive respectively. In (b) we also show the N34 index (°C]) as a dashed black line and the total diabatic volume fluxes in grey. Positive and negative values indicate a contribution to the recharge and discharge of WWV respectively.

During El Niño, discharge peaks between 22 and 27 Sv and is much stronger than the 11 Sv in the idealised simulation (Fig. 2.9a). As a consequence, the overall total change in WWV associated with these events is much larger (3.5 to 5.5 × 10^{14} m^3

compared to the 2.5×10^{14} m^3 in Fig. 2.8a). The length of the discharge phases (red shaded period in Fig. 2.11) is largely constant between events and consistent with the length in the idealised El Niño simulation. La Niña events on the other hand show a larger event-to-event variability in the total change in WWV (2.5 to 4.2×10^{14} m^3) as well as the length of the recharge period (8 to 15 months, blue shaded period in Fig. 2.11).

2.8.1 First Phase: Diabatic Fluxes

As in the idealised simulation, the initial discharge phase during El Niño is dominated by the diabatic volume fluxes. Over all three strong El Niño events, both surface forcing and vertical mixing deplete WWV (light and dark blue lines during the red periods, Fig. 2.11b). The contribution of the diabatic fluxes to the total change in WWV over the discharge periods in 1982/83 and 1997/98 is 23% and 38%. For the 1997/98 El Niño event, this value is lower compared to the 50% in both Lengaigne et al. (2012) and Meinen and McPhaden (2001). However, we expect differences compared to Lengaigne et al. (2012) arising from the temporal filtering (Lengaigne et al. 2012 use a 16 month to 8 year band pass filter while we employ a five-month running mean) as well as model and forcing differences (parameterisations, numerical mixing and surface forcing products). Compared to the observations in Meinen and McPhaden (2001), the lower diabatic contribution may be caused by the fact that the 20°C isotherm is biased deep. A too deep isotherm in the eastern equatorial Pacific likely results in a lower contribution of the diabatic fluxes to changes in warm water volume, as these fluxes are strongest near the surface. However, the observational estimates also include large uncertainties due to missing data (e.g., Meinen and McPhaden (2001) mention that their error bars are generally as large as their signal).

In the three strong El Niño events the timing and behaviour of the diabatic fluxes correspond well to the idealised simulation (compare Fig. 2.11b and Fig. 2.6c). One notable exception is that numerical mixing plays a somewhat larger role.

The diabatic fluxes during the 1988/89 and 2007/08 La Niña events also share a strong similarity with the idealised event (despite the symmetric nature of the idealised

La Niña): strong surface forcing at the peak of the event increases WWV while at the same time its increase is compensated by a negative vertical mixing flux (blue shaded periods, Fig. 2.11b). During the 1988/89 event, mixing undergoes changes associated with positive and negative contributions that mostly cancel out over the full recharge period (light blue line, Fig. 2.11b). In July 1988, the 20°C isotherm is largely within the warming region of vertical mixing, effectively causing a net positive volume flux into the WWV (Fig. 2.12a). Six months later, as the isotherm outcrops in the far eastern equatorial Pacific, the cooling via mixing near the surface exceeds the warming further west where the isotherm is deeper (Fig. 2.12b). Finally, as the isotherm returns to its deeper position in May 1989, it moves back into the region where mixing warms water masses (Fig. 2.12c). The results in Lengaigne et al. (2012) do not show these compensating fluxes throughout different phases of WWV recharge, possibly due to their low-pass temporal filter. During the strong La Niña event in 2010/11, surface forcing exhibits a reduced amplitude compared to the previous La Niña events, and vertical mixing is increasing WWV. This behaviour of the diabatic fluxes is caused by the 20°C isotherm being positioned much deeper than during the previous events in the region where vertical mixing warms waters.

The consistent behaviour of the diabatic fluxes during the three strong El Niño events is revealed when all three events are composited (Fig. 2.13a). The depletion of WWV by the diabatic fluxes leads the peak of the event (i.e. the peak of the N34 index) by three to six months, similar to the idealised simulation (Fig. 2.6c). Vertical mixing in all three El Niño events increases from September the following year (i.e. month 20, Fig. 2.13a), indicating the shift to La Niña-like conditions after El Niño. During La Niña, the composite time series reveal the strong effect of surface forcing, mainly caused by the high amplitude during the 1988/89 event, and highlight the compensating stages of vertical mixing (Fig. 2.13c). While the behaviour of the diabatic fluxes is similar in strong and moderate El Niño events (although with a lower magnitude, not shown), moderate La Niña events do not show a strong surface forcing flux, but rather an increase in vertical mixing (Fig. 2.13e). These effects arise from the reduced upward shift of the 20°C isotherm, its prolonged position in the vertical mixing-warming (i.e. recharging) region, and the enhanced turbulence in the eastern equatorial Pacific.

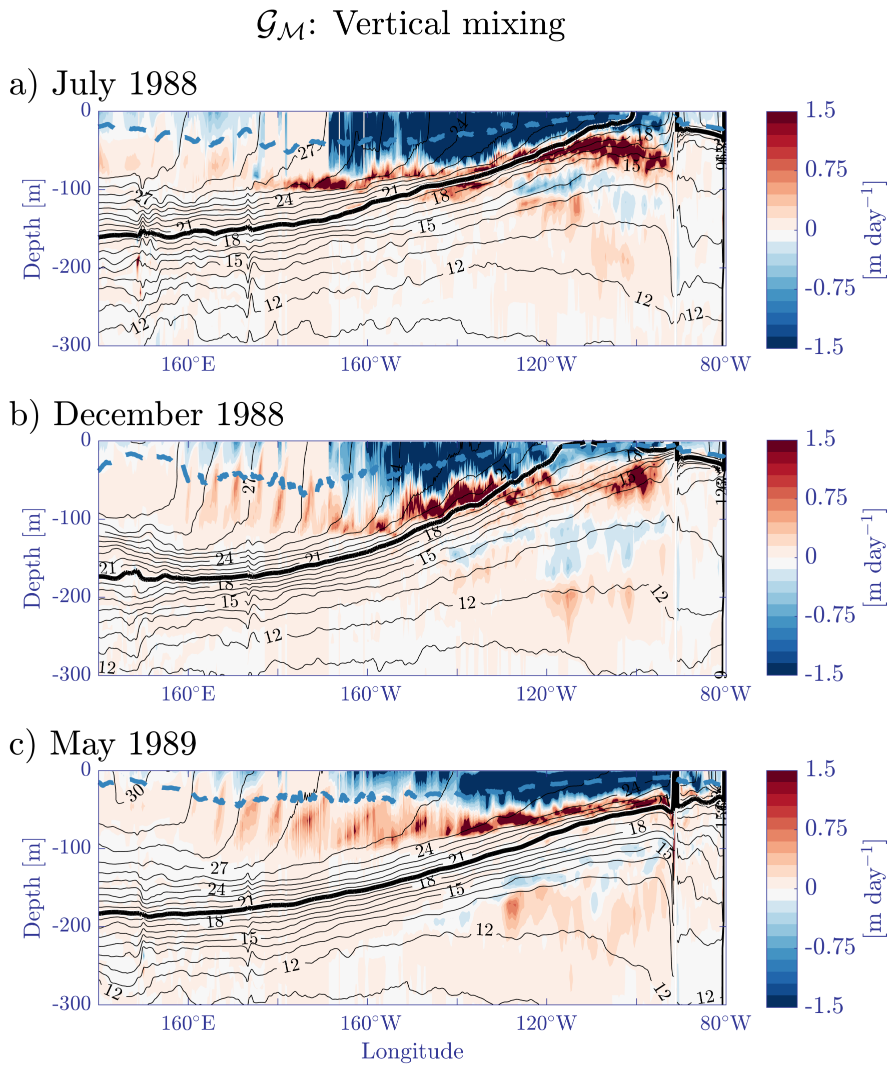

Figure 2.12: Depth-longitude transects across the equatorial Pacific of the vertical mixing water mass transformation velocities $\mathcal{G}_{\mathcal{M}}$ during the 1988/89 La Niña event in the hindcast simulation. The contours show the distribution of the equatorial isotherms with the 20°C isotherm in bold. The dashed blue line in the upper-most layers indicates the mixed layer depth as defined in Fig. 2.4. As La Niña develops, the 20°C isotherm shifts upward into the surface region where enhanced vertical mixing cools water masses (blue region) and leads to strong downward volume flux across the isotherm into deeper layers. After the peak of the event, vertical mixing decreases and the isotherms return to their original position below the region where vertical mixing warms water masses (red region).

2.8.2 Second Phase: Adiabatic Fluxes

The second phase of WWV changes during all discharge and recharge periods is linked to increased adiabatic transport across 5°N and 5°S, and is strongly in-phase with the overall changes in WWV (Fig. 2.13b, d). The positive transport anomalies before the peak of the event are consistent across the three strong El Niño events, as in the idealised simulation (red line, Fig. 2.13b). Peak adiabatic transport during El Niño events ranges between −22.2 to −18.2 Sv, and is about 25% larger than the transport

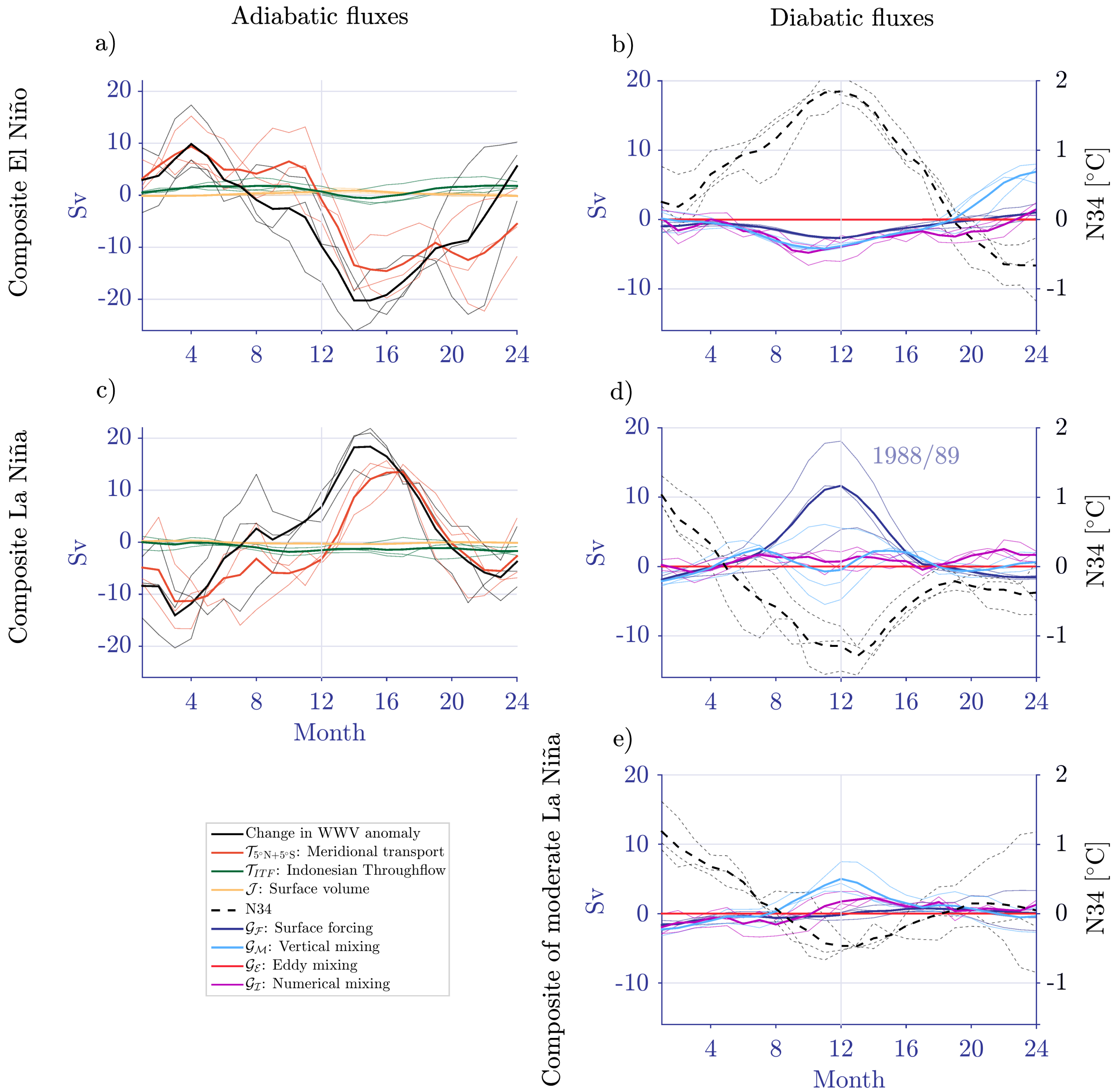

Figure 2.13: Composite time series centered in December (month 12) of the (a, c) diabatic WWV budget terms as well as (b, d) the rate of change in WWV and the adiabatic terms (Sv) during the three strong El Niño and La Niña events shaded in red and blue in Fig. 2.11. The label 1988/89 in (c) shows the time series of the surface forcing term during the 1988/89 La Niña event. In (e) the composite diabatic time series for three moderate La Niña events in 1984/85, 1995/96, 2006/07. In the left panels we also show the time series for the N34 index (°C) (dashed black line). The faint lines are the time series corresponding to the three events while the solid lines are the composites.

during La Niña events (14.9 to 15.1 Sv). This highlights, as in the idealised simulations, the increased importance of the adiabatic fluxes during El Niño. The volume flux across 5°N during all three El Niño events in Fig. 2.11 is more dominant than the one across 5°S (not shown), agreeing with the studies of McGregor et al. (2013, 2014) and Zeller et al. (2019). This results from the interplay between the two EOF modes of wind stress anomalies and Ekman-induced surface transport (McGregor et al., 2014). The Indonesian Throughflow (green line, Fig. 2.11a) is opposing changes in the adiabatic transport across 5°N and 5°S during all ENSO events, caused by a reduced volume transport during El Niño and increased transport during La Niña as discussed above. The contributions of meridional transport and the ITF to changes in WWV over the 1982/83 and 1997/98 El Niño events (79% and 67%) are higher compared to the values for the same events (63% and 45%) in Lengaigne et al. (2012). The differences during these events, as well as during the 1988/89 La Niña, may arise from their 16 month to 8 years low pass temporal filter reducing the contribution of meridional transport.

2.9 Conclusions

In this study, we analysed the diabatic and adiabatic volume fluxes and associated non-linear ocean processes that contribute to WWV variability during ENSO events. To this end, we constructed idealised, symmetric ENSO-related atmospheric fields to force a global high-resolution ocean-sea ice model and compared these simulations with the event-to-event variability from a 1979 to 2016 hindcast simulation. The use of the WMT framework made it possible to individually calculate all fluxes that contribute to changes in WWV.

Changes to the WWV during El Niño's discharge were initiated by the diabatic volume fluxes associated with surface forcing and vertical mixing, both strongly linked to the 20°C isotherm position and the strength of the trade winds. Weaker trade winds during El Niño reduce upwelling of cold water moving the 20°C isotherm away from the surface while also increasing eastern equatorial SSTs and driving an anomalous surface heat flux into the atmosphere. This results in an anomalous decrease of WWV due to surface forcing (dark blue sections, Fig. 2.14a). At the same time, the deepening 20°C isotherm moves away from the region of strong wind- and shear-driven mixing, whose intensity also reduces (light blue sections, Fig. 2.14a). The second phase of WWV discharge, occurring about six months later, was controlled by meridional adiabatic transport across 5°N and 5°S with the ITF always acting to oppose changes in WWV (red and green sections, Fig. 2.14a).

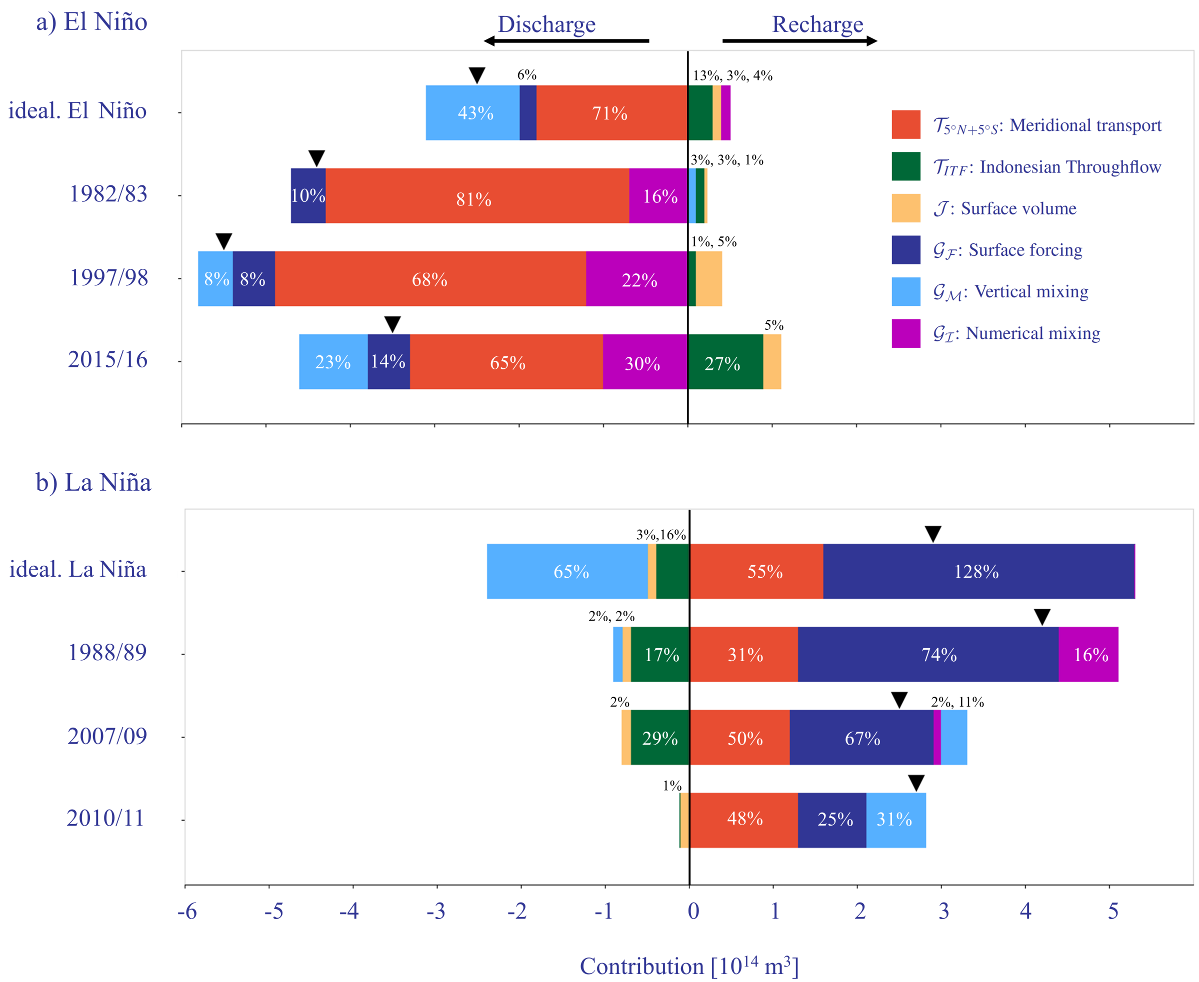

Figure 2.14: The total time-integrated contribution of each anomalous WWV budget term (10^{14} m^3) during (a) El Niño and (b) La Niña periods as defined by the red and blue shaded periods in Fig. 2.6 (idealised) and Fig. 2.11 (hindcast). A negative value of a given flux indicates its role in discharging WWV and a positive value indicates a recharge respectively. The percentage values in each section show the time-integrated contribution to the total change in WWV and are calculated from values rounded to 1-digit accuracy. The triangular markers show the total change in WWV over a particular event.

During La Niña, the stronger trade winds increase upwelling of cold water masses and the 20°C isotherm shoals, sometimes outcropping in the eastern Pacific. Exposure of the 20°C isotherm to increased heat uptake by surface forcing in this region creates a strong across-isotherm volume flux responsible for most of the WWV recharge (dark blue sections, Fig. 2.14b). While turbulence is enhanced during La Niña, the shoaling of the isotherm into the surface layers, where mixing drives cooling of water rather than warming, means that vertical mixing can drive an anomalous decrease in WWV (light blue sections, Fig. 2.14b). This key asymmetry, that mixing drives anomalous discharge in both El Niño and La Niña events, arises from the strong dependence of the diabatic fluxes on the position of the 20°C isotherm. However, in the hindcast simulation (as opposed to the idealised simulations) the contribution of vertical mixing to the overall discharge during La Niña is concealed by opposing volume fluxes occurring at different times as the 20°C isotherm transitions through regions of vertical mixing-driven warming and cooling. In contrast, the idealised simulations, which are forced with symmetric atmospheric forcing, highlight the key role of the diabatic fluxes in driving ocean-sourced asymmetries in the WWV budget. On average, the ratio of the diabatic to adiabatic contributions to WWV changes during El Niño is about 40%:60% while for La Niña, this ratio changes to 75%:25%.

While the diabatic fluxes in the observed WWV budget in Meinen and McPhaden (2001) could only be derived as the residual from the horizontal transport, the model study by Brown and Fedorov (2010) showed that errors in the calculation of horizontal fluxes can be of the same magnitude as the vertical fluxes. They further present evidence that the vertical fluxes on ENSO-related time scales in the eastern Pacific are small, contradicting the observational studies by Meinen and McPhaden (2000, 2001) and the modelling study by Lengaigne et al. (2012). By revisiting the WWV budget with a precise online calculation of the individual fluxes, we were able to further minimise errors associated with the closure of this budget and thereby highlight the dominant role of the diabatic fluxes during La Niña. Despite differences to Meinen and McPhaden (2000) and Lengaigne et al. (2012) in the methods used to calculate the WWV budget terms (limited observations vs. the use of different models, parameterisation schemes and atmospheric forcing) our study supports the main finding that diabatic volume fluxes are as important as adiabatic volume fluxes in driving WWV changes on ENSO time scales. Our results are at odds with the conclusions of Brown and Fedorov (2010).

The differences may arise because their short 6-year simulation over 1992 to 98 does not capture a strong La Niña where diabatic fluxes play a larger role. They also define the WWV as the volume of water above the 25 kg m^{-3} isopycnal that is up to 25 m shallower than the 20°C isotherm in the EUC (see their Fig. 1b) and use a 30-day running mean for their diapycnal transport.

The results in this study highlight the key role of diabatic processes in the eastern equatorial Pacific on ENSO time scales. A good representation of diffusive mixing and turbulence in models is therefore needed in order to correctly simulate these processes. The large event-to-event variability of ENSO in the hindcast simulation motivates future research into the evolution, spatial extent and amplitude of different events. Furthermore, it will be of value to investigate the decadal to multidecadal variability of WWV and ocean heat content to gain insight into the role of the equatorial Pacific in long-term heat uptake and redistribution, especially in light of current climate change.

2.10 Code Availability

The analysis scripts and the data to recreate the figures in this study have been deposited online in the github repository https://github.com/mauricehuguenin/enso_diabatic_fluxes.

2.11 Extended Data and Figures

Derivation of Atmospheric Forcing for the Idealised Model Simulations

The regression analysis and the idealised time series in Section 2.2b provide the spatial evolution for wind stress perturbations related to ENSO. The patterns of the atmospheric variables used in the idealised model simulations are obtained by regressing the full 38-year-long N34 and PC2 time series onto each ERA-Interim anomaly field, resulting in two spatial patterns for each variable (Examples are shown in Fig. 2.15).

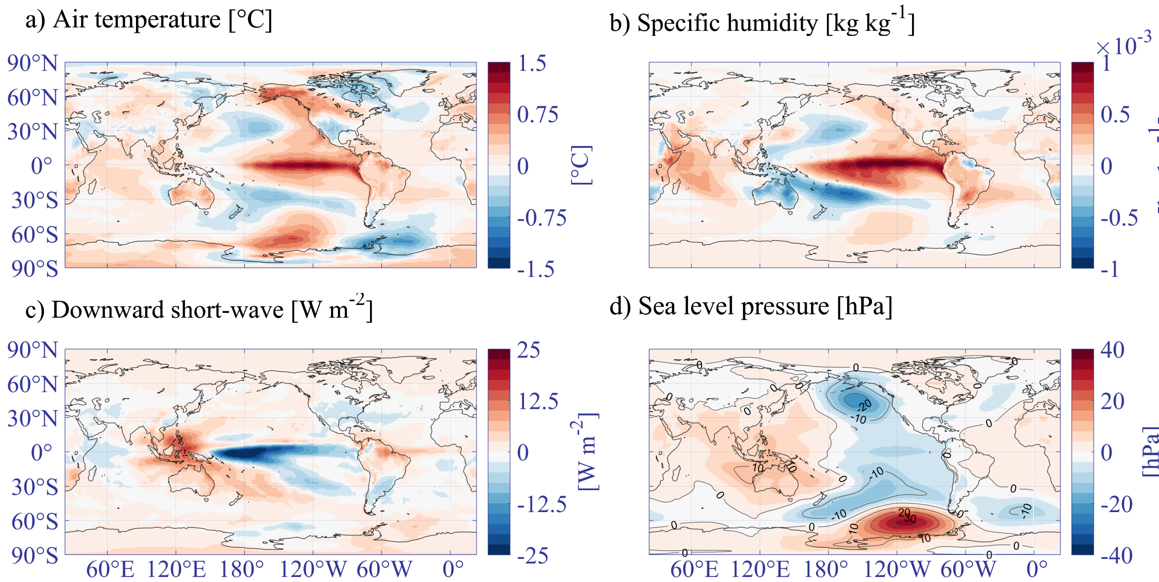

Extended Data Figure 2.15: Examples of four out of the eight atmospheric regression patterns X_1 associated with ENSO used in the atmospheric forcing for the idealised symmetric events. These spatial patterns are calculated by regressing the observed N34 index (Reynolds et al., 2007) onto anomalous spatial maps from the ERA-Interim reanalysis product for 1979–2016 (Dee et al., 2011) and taking the time mean. (a) Air temperature (°C), (b) specific humidity (kg kg^{-1}), (c) downward short-wave radiation (W m^{-2}) and (d) sea level pressure (Pa).

The time evolution for the total atmospheric forcing is then calculated by multiplying the X_1 and X_2 spatial patterns with their associated idealised time series and adding them to the CORE-NYF climatological forcing:

$$\underbrace{F_{ideal.}(x,y,t)}_{forcing} = \underbrace{\overline{F(x,y,t)}}_{climatology} + \underbrace{X_{1,F}(x,y) \cdot N34_{ideal.}(t)}_{perturbation} + \underbrace{X_{2,F}(x,y) \cdot PC2_{ideal.}(t)}_{perturbation}, \tag{2.4}$$

where $F_{ideal.}(x,y,t)$ is one of the six idealised forcing anomaly fields dependent on time, $\overline{F(x,y,t)}$ is the base forcing field without any interannual variability from the CORE-NYF data set, $X_{1,F}(x,y)$, $X_{2,F}(x,y)$ are the two regression patterns of a given field F derived from the ERA-Interim product (Fig. 2.1), and $N34_{ideal.}(t)$ and $PC2_{ideal.}(t)$ are the associated idealised time series (Fig. 2.2). Put most simply, the ENSO perturbation forcing fields are derived from regressions of the $N34_{ideal.}(t)$ and $PC2_{ideal.}(t)$ time-series onto the respective atmospheric fields required to construct the bulk formulae for heat and freshwater forcing.

For the remaining two input variables (zonal and meridional wind speed) we use a different method to derive the symmetric fields. In the model, wind speed is converted to wind stress by the wind stress law (Fairall et al., 1996):

$$\vec{\tau} = (\tau_x, \tau_y) = \rho_a \cdot C_D \cdot \underbrace{\sqrt{u_{10}^2 + v_{10}^2}}_{U_{10}} \cdot (u_{10}, v_{10}), \tag{2.5}$$

where $\vec{\tau}$ is the wind stress vector with its zonal (τ_x) and meridional (τ_y) components (N m^{-2}), ρ_a is the density of air at sea level (1.25 kg m^{-3}), C_D is the unitless drag coefficient , u_{10} and v_{10} are the zonal and meridional wind speeds (m s^{-1}) and U_{10} is the wind speed magnitude (m s^{-1}). For the derivation of the atmospheric forcing, we use a constant drag coefficient of 1.5×10^{-3} (Kara et al., 2007) for simplicity. Differences relative to the wind speed-dependent drag coefficient are negligible.

Due to the quadratic dependence of this equation on wind speed, the resulting wind stress anomalies if given symmetric ENSO-related wind speed anomalies are asymmetric. As we aimed for symmetric wind stress anomalies during our El Niño and La Niña simulations, we therefore solved this equation in an inverse manner for the two unknowns u_{10} and v_{10}. To solve Equation 2.5 for wind speed, we first obtained the wind stress anomaly fields τ_x' and τ_y' from the EOF analysis described in Section 2.2, i.e. from

$\tau'_x = X_{1,\tau'_x} \cdot N34_{ideal.} + X_{2,\tau'_x} \cdot PC2_{ideal.}$ for the zonal component during El Niño (Fig. 2.1a, b and Fig. 2.2). The following section sets out how we then used the wind stress law to solve for the two unknowns u_{10} and v_{10}.

First, the zonal component of the wind stress law is rewritten as a Reynolds decomposition:

$$\begin{aligned} \underbrace{\overline{\tau_x} + \tau'_x}_{l} &= \underbrace{\rho_a \cdot C_D}_{k} \cdot \underbrace{\sqrt{(\overline{u_{10}} + u'_{10})^2 + (\overline{v_{10}} + v'_{10})^2}}_{U_{10}} \cdot (\overline{u_{10}} + u'_{10}) \\ \Rightarrow \quad l &= k \cdot U_{10} \cdot (\overline{u_{10}} + u'_{10}), \end{aligned} \tag{2.6}$$

where $\overline{u_{10}}$ and $\overline{v_{10}}$ are the climatological values from the CORE-NYF data set, $\overline{\tau_x}$ is calculated from $\overline{u_{10}}$ and $\overline{v_{10}}$ by Equation 2.5, τ'_x, u'_{10} and v'_{10} are the perturbation values, l is the total zonal wind stress forcing including climatological and perturbation values and k contains the two constants for the density of air and the drag coefficient. Solving the second line of Equation 2.6 for u'_{10} results in

$$u'_{10} = \frac{l}{k \cdot U_{10}} - \overline{u_{10}}. \tag{2.7}$$

The same procedure as in Equation 2.6 is applied to the meridional component and yields

$$v'_{10} = \frac{m}{k \cdot U_{10}} - \overline{v_{10}}, \tag{2.8}$$

where $m = k \cdot U_{10} \cdot (\overline{v_{10}} + v'_{10})$ is the total meridional wind stress forcing including climatological and perturbation values.

As a next step we combine l and m resulting in the following expression:

$$\begin{aligned} l^2 + m^2 &= k^2 \cdot U_{10}^2 \cdot [(\overline{u_{10}} + u'_{10})^2 + (\overline{v_{10}} + v'_{10})^2] \\ &= k^2 \cdot U_{10}^4, \end{aligned} \tag{2.9}$$

and solve for the positive wind speed magnitude U_{10}:

$$U_{10} = |\frac{\sqrt[4]{l^2 + m^2}}{\sqrt{k}}|. \tag{2.10}$$

Inserting Equation (2.10) into Equations 2.7 and 2.8 allows us to solve for the two unknowns u'_{10} and v'_{10}:

$$u'_{10} = \pm \frac{l \cdot \sqrt{k}}{k \cdot \sqrt[4]{l^2 + m^2}} - \overline{u_{10}}, \tag{2.11}$$

$$v'_{10} = \pm \frac{m \cdot \sqrt{k}}{k \cdot \sqrt[4]{l^2 + m^2}} - \overline{v_{10}}, \tag{2.12}$$

where the correct sign is determined using the wind stress anomaly spatial patterns.

By using this approach, it is ensured that desired symmetric wind stress anomalies are applied to the model. However, wind speed values from Equation 2.11 and Equation 2.12 are also used to calculate the wind speed magnitude in the bulk formulae of sensible and latent heat fluxes (Equations 2a, b and Equation 3 in Fairall et al., 1996). Using the asymmetric wind speed values thus leads to asymmetric sensible and latent heat fluxes and furthermore also results in an 18% higher mean wind speed magnitude during La Niña than El Niño. While this asymmetry in sensible and latent heat fluxes as well as in wind speed magnitude is not ideal, it is of less importance than applying the correct symmetric wind stress values.

3

Subsurface warming of the West Antarctic continental shelf linked to El Niño-Southern Oscillation

Huguenin, M. F. [1, 2, 3], Holmes R. M.[3, 4, 5, 6], Spence P.[7, 8, 9] & England M. H.[2, 10]
Submitted to *Geophysical Research Letters*.

M. F. H. completed the simulations and wrote the initial manuscript together with input from R. M. H., P. S. and M. H. E. All authors formulated the experimental design, contributed to interpreting the results and refinement of the paper.

1. Climate Change Research Centre, University of New South Wales, Sydney, NSW, Australia 2. ARC Australian Centre for Excellence in Antarctic Science, University of New South Wales, Sydney, NSW, Australia 3. ARC Centre of Excellence in Climate Extremes, University of New South Wales, Sydney, NSW, Australia 4. School of Mathematics and Statistics, University of New South Wales, Sydney, NSW, Australia 5. School of Geosciences, University of Sydney, Sydney, NSW, Australia 6. Australian Bureau of Meteorology, Sydney, New South Wales, Australia 7. ARC Australian Centre for Excellence in Antarctic Science, University of Tasmania, Tasmania, Australia 8. Institute for Marine and Antarctic Studies, University of Tasmania, Tasmania, Australia 9. Australian Antarctic Partnership Program, University of Tasmania, Tasmania, Australia 10. Centre for Marine Science and Innovation, University of New South Wales, Sydney, New South Wales, Australia

Key Points

- Ocean-sea ice model simulations of isolated strong El Niño and La Niña events illustrate how they modulate West Antarctic shelf temperatures
- El Niño weakens coastal easterlies, reduces poleward Ekman flow of cold waters, causing cross-shelf upwelling of warm Circumpolar Deep Water
- The La Niña shelf circulation response is largely opposite and inhibits cross-shelf upwelling of Circumpolar Deep Water

Abstract Recent satellite observations suggest that El Niño–Southern Oscillation (ENSO) impacts basal melting of West Antarctic ice shelves, yet sparse ocean observations limit our understanding of the associated processes. Here we investigate how strong ENSO events modulate subsurface West Antarctic shelf temperatures using high-resolution global ocean-sea ice model simulations. During El Niño, the subsurface shelf warming is coherent in depth and can be up to 0.5°C in front of ice shelves. This warming arises from a weaker Amundsen Sea Low (ASL) and weaker coastal easterlies, which in turn reduce poleward Ekman transport of cold surface waters, enabling enhanced transport of warm Circumpolar Deep Water (CDW) onto the shelf. During La Niña we see an opposite sign response, with a stronger ASL and Ekman transport resulting in weaker CDW upwelling and cooling in the subsurface ocean. These findings have implications for interpreting basal melt on interannual time-scales in the West Antarctic sector.

Plain Language Summary El Niño-Southern Oscillation (ENSO) is the Earth's dominant mode of year-to-year climate variation. The impacts of its two phases, El Niño and La Niña, extend from the tropics to Antarctica through large-scale atmospheric waves. Past studies have suggested that West Antarctic ice shelves melt at their base during El Niño. However, the processes responsible for this melting remain unclear. It is also uncertain if opposite changes occur during La Niña. Here, we use an ocean circulation model to show that during El Niño, the poleward flow of cold surface waters in West Antarctic, driven by the coastal easterly winds, is reduced because the winds weaken. To balance out this mass deficit at the surface, more warm Circumpolar Deep Water (CDW) flows onto the continental shelf. During La Niña, we see a largely

opposite response; the easterlies become stronger, they increase the poleward flow of cold surface waters and CDW remains off the shelf. Our results highlight the link between ENSO and mass loss of the West Antarctic ice shelves and ice sheet.

3.1 Introduction

Over recent decades, mass loss from the West Antarctic ice sheet has accelerated (e.g., Schmidtko et al., 2014; Paolo et al., 2015; Scambos et al., 2017; Shepherd et al., 2018; Rignot et al., 2019). This mass loss occurs primarily via basal melting induced by warm Circumpolar Deep Water (CDW) intruding into ice shelf cavities (Pritchard et al., 2012; Jenkins et al., 2016; Kimura et al., 2017; Tamsitt et al., 2021), impacting the buttressing and stability of the ice shelves (Gudmundsson, 2013; Fürst et al., 2016; Gudmundsson et al., 2019), causing large-scale calving (Greene et al., 2022) and thus contributing to rapid sea level rise. Superimposed on this long-term observed melting signal is melting induced by interannual climate variability. A better understanding of the impact of interannual climate variability on the West Antarctic region is needed not only to separate the forced anthropogenic signal from natural variability but also because major modes of climate variability may change in the future (Cai et al., 2014, 2015, 2021; Goyal et al., 2021b; McGregor et al., 2022).

The most dominant mode of global interannual climate variability is El Niño-Southern Oscillation (ENSO), and it is known to impact the atmospheric circulation in West Antarctica through its teleconnection to the Amundsen Sea (e.g., Karoly, 1989; Hoskins and Ambrizzi, 1993; Turner, 2004; Lachlan-Cope and Connolley, 2006). Recent satellite records of the West Antarctic ice shelves have shown that during El Niño events, the height of the ice shelves in the Amundsen and Bellingshausen Seas increases but their overall mass decreases (Paolo et al., 2018). This is due to increased accumulation of low density snow at the top, while at the same time it has been suggested that more CDW reaches the ice shelves and increases basal melting of high density ice from below (Paolo et al., 2018). This mechanism is supported by both models and observations when considering decadal-scale connections between the tropical Pacific and the Amundsen Sea region (Holland et al., 2019; Naughten et al., 2022), and also by a modelling study highlighting how changes in the ASL affect surface heat fluxes and warming on the Bellingshausen Sea continental shelf (Oelerich et al., 2022). While these previous studies find that interannual atmospheric variability associated with ENSO impacts West Antarctic ice shelves, they have not examined the driving ocean dynamics in detail. That is the purpose of this article.

The ENSO signal on the West Antarctic shelf (Fig. 3.1a and Extended Data Fig. 3.5) is difficult to identify as it can be masked by other components of climate variability, such as the Southern Annular Mode (SAM, Marshall (2003); Martinson et al. (2008); Walker and Gardner (2017)), zonal-wave 3 variations (Goyal et al., 2021a, 2022) and also the Interdecadal Pacific Oscillation (IPO, Holland et al. (2019). Separating out the impacts of all these modes of variability on the West Antarctic sector is further complicated by higher frequency variability, such as storm systems and other weather patterns.

Observations on the Antarctic shelf are sparse, and only since 2004 do we have reasonable observational coverage in this region, thanks to the Marine Mammals Exploring the Oceans Pole to Pole project (Treasure et al., 2017, MEOP). Even then, observations are too heterogeneous in space and time to tease out the footprint of particular climate modes (Morrison et al., 2023). In addition, there have only been a few ENSO events since the MEOP project began ∼20 years ago, which adds to the difficulty in identifying the impacts of this climate mode. Cruise ship and mooring measurements are also very sparse outside of the Peninsula region because of sea ice coverage and icebergs (Heywood et al., 2016; Boehme and Rosso, 2021). It is also difficult to rely on coupled climate models to examine the impact of ENSO teleconnections on Antarctic shelf ocean behaviour due to their inherent biases in their representation of the Antarctic shelf temperature structure and Dense Shelf Water formation (Heuzé et al., 2013; Heuzé, 2021; Purich and England, 2021; Li et al., 2023).

Here we highlight how atmospheric ENSO teleconnections impact the ocean circulation and heat content over the West Antarctic continental shelf using perturbation experiments in a high-resolution global ocean-sea ice model. Our aim is to isolate the ENSO-associated teleconnections and examine their role in driving ocean circulation and shelf temperature changes over the West Antarctic sector.

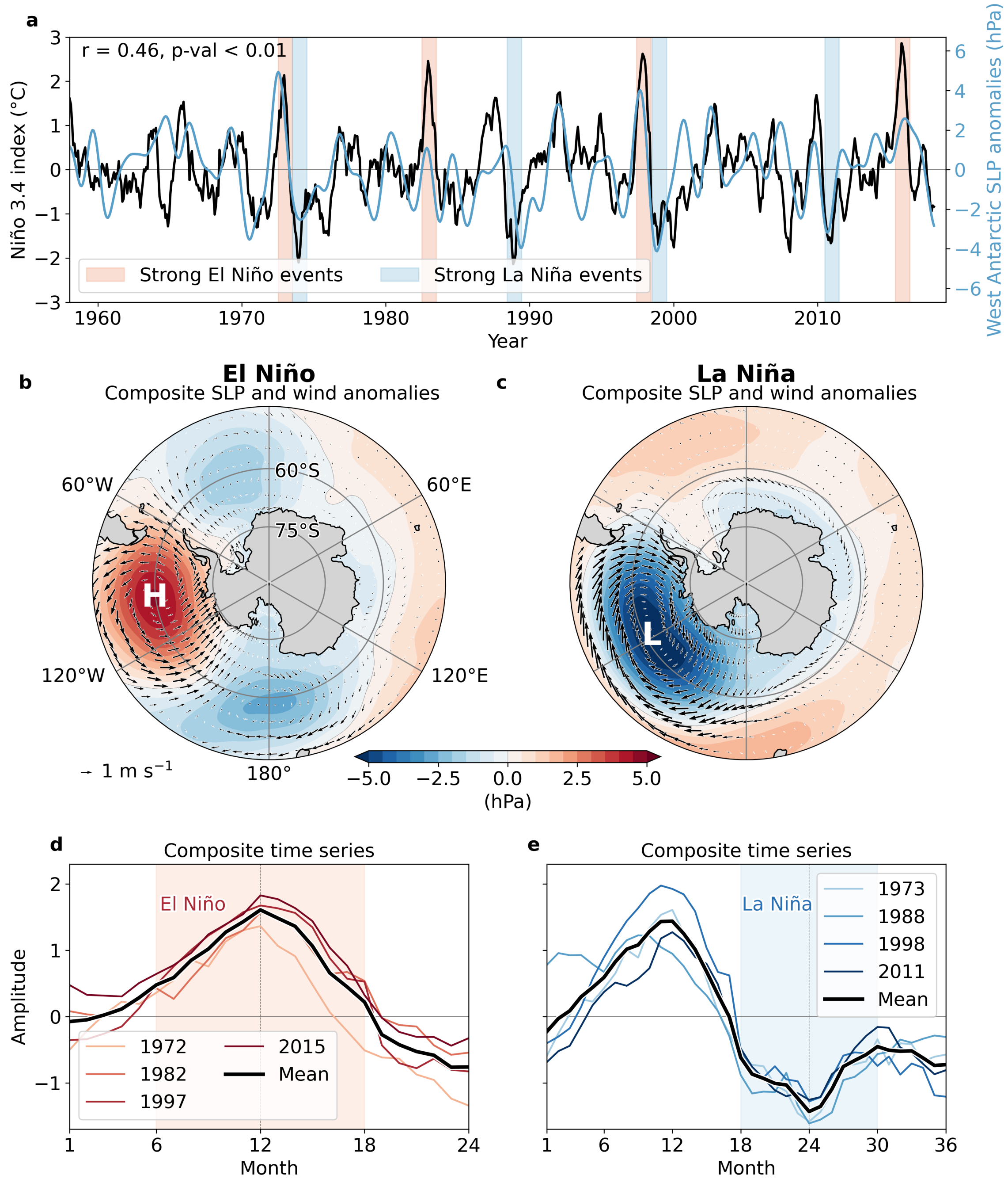

Figure 3.1: Time series and spatial patterns highlighting the teleconnection between ENSO and West Antarctica. (a) Time series of the Niño 3.4 index (i.e., the mean sea surface temperature anomalies (°C) in the region 5°S–5°N and 170°W–120°W) and mean West Antarctic sea level pressure (SLP) anomalies in the region 80°S–45°S and 60°W–150°W (hPa). The peak periods of four strong ENSO events have been shaded in orange and light blue respectively. A low-pass filter has been applied to the SLP time series. In the top left is the correlation coefficient (r) and significance value (p-val.) between the time series. (b, c) Composite mean SLP (hPa, colour shaded) and surface wind anomalies (m s^{-1}, arrows) during the events shaded in (a). The **H** and **L** symbols indicate the location of the largest SLP anomalies during El Niño and during La Niña events, respectively. (d, e) Composite time series based on the Niño 3.4 index during the events shaded in (a), centered around the peak event in month 12 and 24 respectively.

3.2 Methods

3.2.1 Model and forcing

We use the global ocean-sea ice model ACCESS-OM2 with an eddy-rich horizontal resolution of 1/10° (3.2 km at 73°S) and 75 z* vertical levels (Kiss et al., 2020). This model combines the MOM5.1 ocean model (Griffies, 2012) and the CICE5.1.2 sea ice model (Hunke et al., 2015) and it is forced by atmospheric fields from the JRA55-do version 1.3 data set (Tsujino et al., 2018). This data set is provided as 3-hourly fields at 0.5625° resolution, except for the river and ice-related runoff field that has a daily time step at 0.25° resolution.

ACCESS-OM2 does not have ice shelf cavities, time-constant melt water anomalies are applied at the surface. The model does not feature an undercurrent in the Amundsen Sea that has been shown to be important in advecting warm CDW through canyons onto the shelf (Silvano et al., 2022). To investigate ENSO-associated impacts, we use a repeat year forcing spin-up with added atmospheric ENSO anomalies. The repeat year spin-up is initialised from World Ocean Atlas 2013 v2 conditions (Locarnini et al., 2013) and integrated over repeat cycles of the 1990–1991 atmospheric forcing for 245 years (Stewart et al., 2020). This period was chosen for the spin-up and control experiment as it has relatively neutral conditions in SAM and ENSO (Stewart et al., 2020). A more detailed discussion of the base model configuration can be found in Kiss et al. (2020).

Evaluation of the model at the polar margin is limited because of sparse observations around Antarctica and the relatively short record from the early 2000s onward that is not long enough for a climatological analysis. Nonetheless, the 1/10° ACCESS-OM2 model in a hindcast simulation from Kiss et al. (2020) represents the West Antarctic shelf temperature structure reasonably well compared to the Southern Ocean State estimate (Verdy and Mazloff, 2017, SOSE, Extended Data Fig. 3.6) and elephant seal observations (Treasure et al., 2017; Roquet et al., 2013, 2014, Extended Data Fig. 3.7). The model correctly simulates the cold Antarctic shelf waters near the surface and the warmer CDW below, although the subsurface is warmer than in SOSE (Extended Data Fig. 3.6a, c). Compared to the MEOP data, the 1/10° configuration simulates a warmer Amundsen Sea and cooler shelf conditions in the Peninsula region but has an overall better representation of shelf temperatures than the 1° version of the same model. Further validation of ACCESS-OM2 against observations around the Antarctic shelf can be found in Kiss et al. (2020); Huneke et al. (2022); Dawson et al. (2023); Li et al. (2023).

3.2.2 Experimental design

Our perturbation experiments are formulated by considering the composite mean atmospheric fields from four strong El Niño and four strong La Niña events which capture the strongest teleconnections to the West Antarctic region. The anomalous ENSO forcing added to the repeat year baseline is applied as time-constant spatial patterns multiplied by time series that correspond to the evolution of eastern equatorial Pacific sea surface temperatures (SSTs). This approach was taken as the analysis of the full spatial-temporal evolution of the Amundsen sea level pressure (SLP) events in Fig. 3.1a would not have isolated the ENSO signal from other types of internal climate variability.

The spatial patterns for all forcing fields are constructed as the mean anomalies during the peak of the four strong ENSO events, respectively, six months either side of the peak amplitude, (Fig. 3.1b, c and Extended Data Fig. 3.8, 3.9). While only SLP and surface wind anomalies are shown here in Fig. 3.1b, c, we use this method for all input fields, including specific humidity, surface air temperature, zonal and meridional wind speed at 10 m as well as SLP, rain- and snowfall, surface runoff, sea ice freshwater fluxes, and downward long- and shortwave radiation (Extended Data Fig. 3.10, 3.11). Overall the spatial pattern of SLP anomalies during El Niño and La Niña is an opposite sign teleconnection, although La Niña anomalies show a peak signature further west and broader in extent than during El Niño. This is because during La Niña, convective heating anomalies excite a Rossby wave train from the western rather than the central equatorial Pacific (Chiodi and Harrison, 2015), and SLP anomalies are more elongated because the ASL centre during the 1988/89 La Niña was located much further west than during the other three events (Extended Data Fig. 3.9b). While using spatial anomalies from composites during strong ENSO events can also incorporate anomalies associated with SAM variability, the SAM influence and thus its signature on the Amundsen Sea appears to be overall small during these events (Extended Data Fig. 3.12). A limitation of this approach is that West Antarctic sea level pressure anomalies peak ~5 months before the Niño 3.4 index (Fig. 3.1a) because the subtropical westerly jet peaks in austral winter, which may reduce the simulated temperature response in our model compared to reality.

To calculate the forcing anomalies, the spatial regression patterns are scaled by the corresponding composite time series throughout the events (Fig. 3.1d, e). The time series are constructed by taking the mean Niño 3.4 index during the above mentioned four strong El Niño and four strong La Niña events, centered around the peak amplitude (bold black line, Fig. 3.1d, e). For the La Niña simulation, we extend the time series back in time as most strong La Niña events follow immediately after El Niño events, and our goal is to keep this memory in case it is relevant to the La Niña response. Each time series has been normalised by matching the amplitude to the mean SST anomalies in the Niño 3.4 region during the peak of the four strong events (i.e., the time series were divided by 1.56°C for El Niño and 1.33°C for La Niña, Extended Data Fig. 3.13).

3.2.3 The West Antarctic subsurface heat budget

To investigate the drivers of West Antarctic shelf temperature changes during ENSO phases, we consider the subsurface heat budget between 100 m and the shelf bottom over a region bounded by 150°W–60°W, the Antarctic coast to the south and the 1000 m isobath to the north (hereafter the West Antarctic shelf region). The change in heat content with time is defined as the sum of the advective heat transport convergence, vertical mixing across the 100-m depth level and any shortwave radiation penetrating below 100m (which is negligible), are all calculated online in the model. Changes in the heat budget arise primarily from the first two terms.

The heat transport convergence term can be decomposed into its vertical, along-shelf and cross-shelf components, and we do these calculations offline using monthly averages. Over a short test period, the offline calculations match closely the online calculations where sub-monthly correlations between velocities and temperatures are taken into account. The vertical heat flux is calculated across 100 m depth and the along-shelf heat flux is calculated as the sum of the heat fluxes across the shelf transects at 150°W and 60°W. We calculate the remaining component, i.e., the cross-shelf component, which corresponds to the heat flux across the 1000 m isobath, by residual from these two former terms.

Due to the potential for non-zero anomalous mass fluxes, separating the heat transport convergence into components introduces an uncertainty for each component associated with the choice of an arbitrary reference temperature (Holmes et al., 2019b; Forget and Ferreira, 2019). Here, we estimate uncertainty ranges of the individual anomalous heat flux components by multiplying the change in the volume flux of each component by the ±1 standard deviation range (assuming the values follow a normal distribution) of the climatological temperature across the volume considered in the heat budget. Effectively, this approximates the possible range of temperatures at which the anomalous volume flux could be returned (see the supplementary material of Holmes et al. (2019b) for more discussion).

3.3 Shelf temperature response

We first analyse the spatial distribution of ENSO-associated temperature anomalies during the peak of the event in austral summer. Around the Pine Island Bay (at 101°W) and along the Peninsula region close to the coastline, depth-averaged shelf warming reaches up to 0.5°C (Fig. 3.2a), and it is this localised warming signal that is important for ice shelf melting at their margins. This is the region where mass loss of the West Antarctic ice shelves has experienced the highest acceleration over recent years (Paolo et al., 2015; Rignot et al., 2019). Despite overall shelf water warming during El Niño, some localised areas also experience subsurface cooling, predominantly along the outer shelf region, likely caused by small-scale processes.

During the peak of the La Niña, subsurface cooling occurs with a similar magnitude and in similar regions as the warming during El Niño. Again, there is significant small-scale variability with some regions in the outer shelf region experiencing warming compared to the large-scale cooling signal. As the atmospheric anomalies are strongest

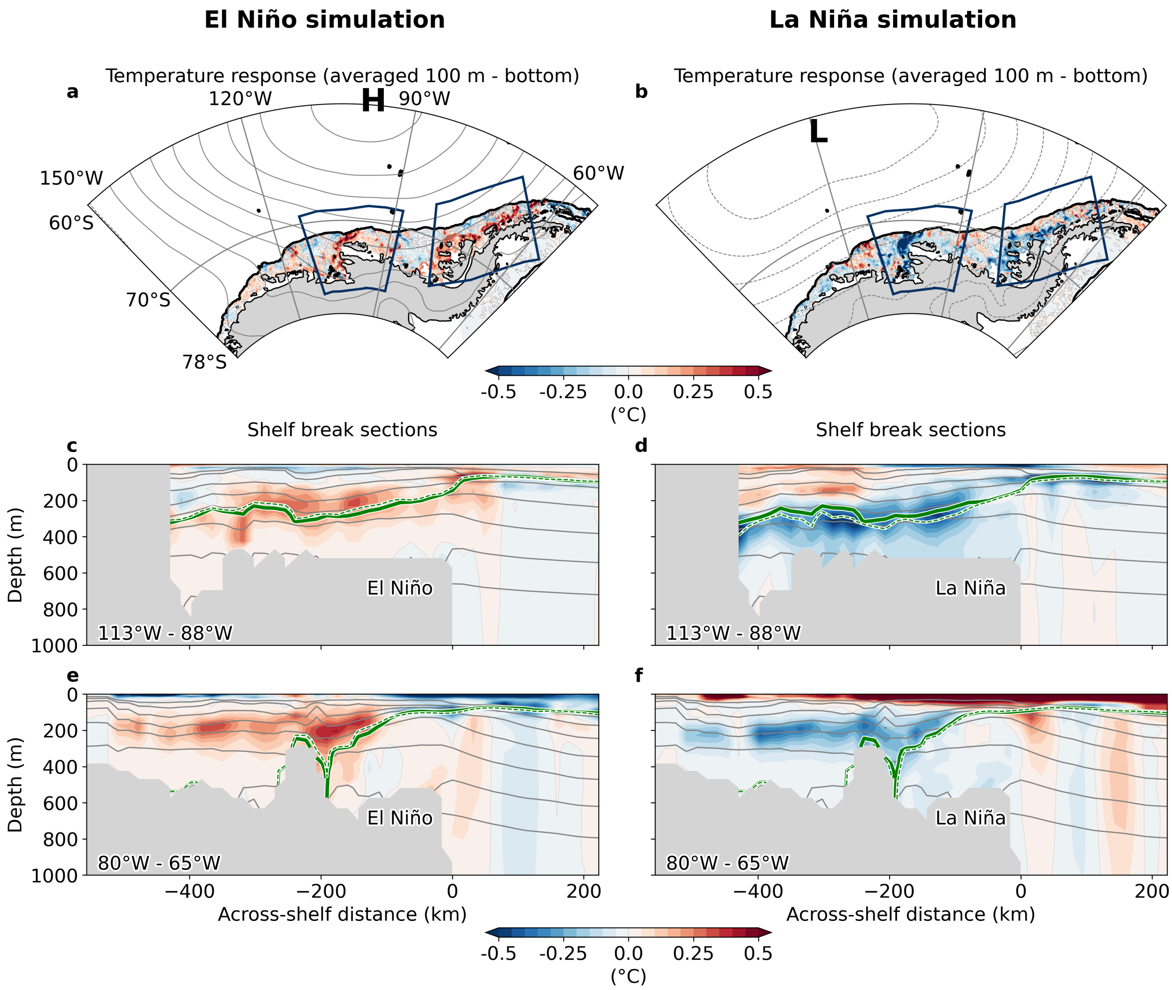

Figure 3.2: Response of the West Antarctic continental shelf during the peak of the El Niño and La Niña simulations. (a, b) Mean subsurface shelf temperature response (°C). The 1000 m isobath is given as the black contour. The cross-shelf rectangles outline the regions for the depth-latitude panels in c-f. The grey contours show SLP anomalies (solid positive, dashed negative), and the **H** and **L** symbols indicate the location of the largest SLP anomalies. (c-f) Mean cross-shelf temperature anomalies (°C) in the regions outlined above, with the alongshore mean taken relative to the 1000 m isobath. These panels were created by subsetting the data into rectangles perpendicular to the shelf break, rotating them and taking the mean for each region. The bold and dashed green lines are the climatological and event 0°C isotherms. The 0°C isotherms near the surface region have been masked out. The grey contours represent the climatological isopycnals in 0.1 kg m^{-3} intervals between 1027.3 and 1028 kg m^{-3}.

over the West Antarctic, shelf temperatures outside of this region are minimally impacted and thus not shown here.

El Niño-induced warming peaks at around 200 m depth and 180 km south of the shelf break in both the Amundsen-Bellingshausen Sea and in the Peninsula region, extending to the shelf bottom (Fig. 3.2c, e). Warming anomalies averaged along-shelf in these regions reach 0.5°C, although mean vertical shifts in isopycnals and isotherms are relatively small (only climatological isopycnals are shown). Many ice shelves in this region have grounding lines at depths of ∼500 m or more (Davis et al., 2023). Thus the warming signal we simulate in response to El Niño has the potential to cause basal melting of the ice shelves.

3.4 Driving Mechanisms

3.4.1 El Niño warming

The subsurface West Antarctic continental shelf warming persists for almost one year after the peak of the El Niño event, and even throughout the six-month extension of the simulation where forcing returns to the climatology (Fig. 3.3a). This is consistent with Tamsitt et al. (2021) who highlighted the >1 year residence time of warm waters on the West Antarctic continental shelf. To explore the mechanisms driving this warming, we now analyse the ocean heat budget over the West Antarctic region.

The build-up of heat during El Niño occurs before the event peaks (black line, Fig. 3.3e). The dominant advective heat flux component, that almost always dominates the overall heat budget, is the cross-shelf heat flux onto the continental shelf (red line and red shaded interval, Fig. 3.3e). This heat flux is associated with the cross-shelf upwelling of warm CDW, the result of ENSO-related atmospheric anomalies over the shelf region. During the build-up phase of El Niño, the Amundsen Sea Low and coastal easterly surface winds weaken around West Antarctica (Fig. 3.1b). The reduced winds decrease the poleward Ekman transport of cold surface waters (Fig. 3.3c), effectively creating a mass deficit on the shelf that is balanced by upwelling of warm CDW that typically resides at mid-depth layers off the shelf break (Spence et al., 2014; Stewart and Thompson, 2015; Nakayama et al., 2018). In comparison, the vertical advective heat flux and vertical mixing across 100 m depth into the subsurface region are small.

A reversal of the warming tendency on the shelf is initiated about six months after the peak of the El Niño event (Fig. 3.3a). The return to climatological shelf temperatures is a much slower process than the heat build-up, even though the atmospheric anomalies are largely symmetric in the increasing and decreasing stages of the simulation (Fig. 3.1d). As easterly winds return back to climatological conditions, anomalous

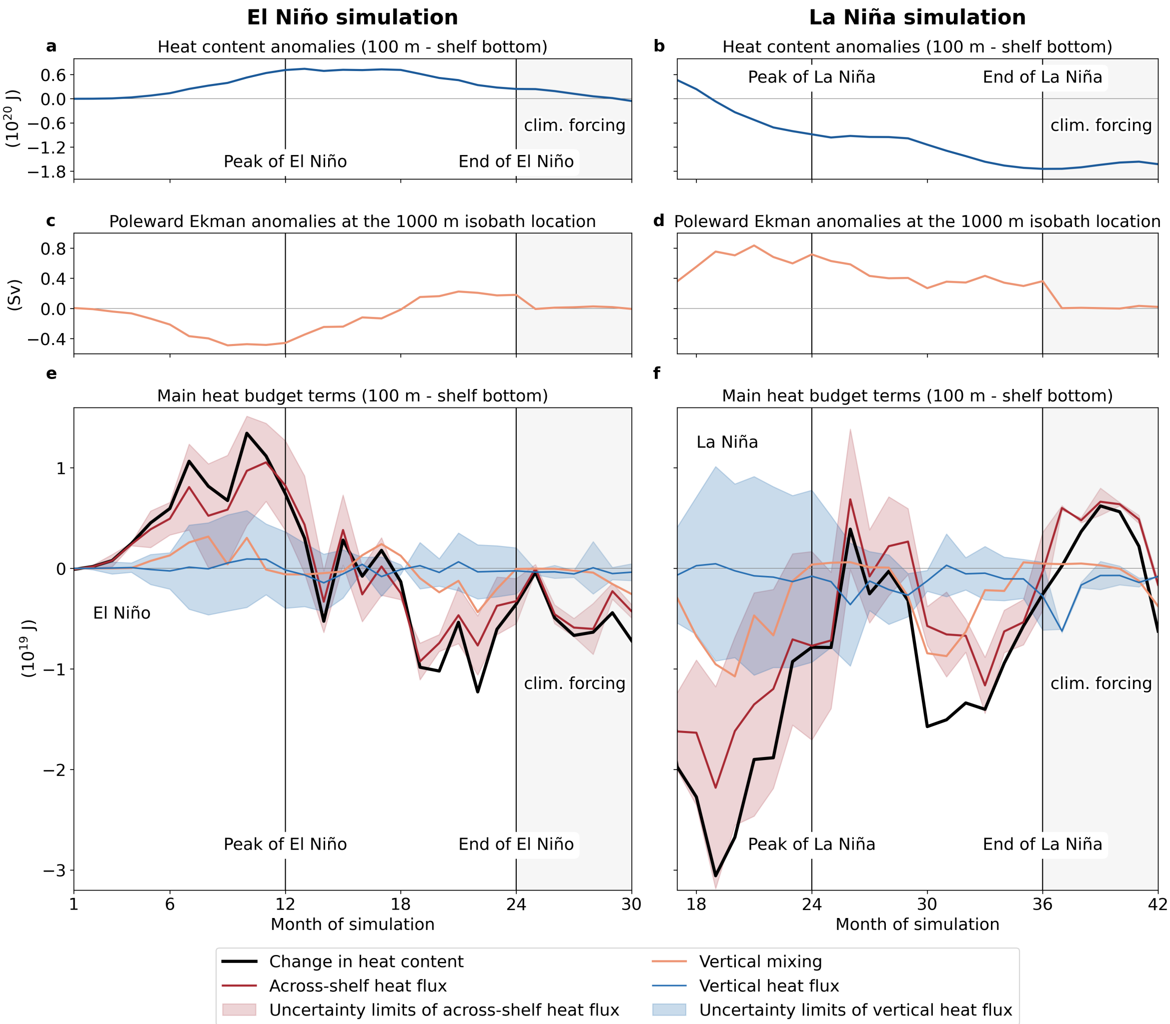

Figure 3.3: Time series of West Antarctic subsurface heat anomalies, Ekman transport anomalies and the main heat budget terms during the El Niño and La Niña simulations. (a, b) The mean subsurface heat anomalies on the West Antarctic shelf (10^{20} J). The vertical labelled lines indicate the peak and end of the simulated event. The grey shaded period indicates the six month extension of the simulation with climatological forcing. (c, d) Mean poleward Ekman transport anomalies (Sv, 1 Sv = 10^6 m^3 s^{-1}) at the location of the 1000 m isobath. (e, f) The main Eulerian heat budget terms on the West Antarctic shelf (10^{19} J). The colour-shaded intervals indicate the uncertainties in the cross-shelf and vertical heat fluxes (Section 3.2.3). The second-order terms are shown in Extended Data Fig. 3.14.

heat is slowly discharged across the shelf northwards and to a small extent across the shelf transects at 150°W and 60°W out of the West Antarctic sector (Fig. 3.3e and Extended Data Fig. 3.14). Warmer than average shelf temperatures persist beyond month 18 (Fig. 3.3a). This occurs despite El Niño slowly transitioning into a negative La Niña-like state with stronger easterly winds on the shelf (Fig. 3.1b,d).

3.4.2 La Niña cooling

During La Niña, the ASL strengthens and West Antarctic coastal easterlies increase (Fig. 3.1c). This increases poleward Ekman transport of surface waters (Fig. 3.3d), driving cold water onto the continental shelf and inhibiting upwelling of CDW. At the same time, mixing of cooler water across the 100 m depth level is enhanced. The shelf temperature cooling during La Niña persists throughout the full simulation (Fig. 3.3b). Overall, cooling rates are much larger than warming rates during the El Niño simulation (months 20 to 24, Fig. 3.3f), despite the La Niña following the tail end of an El Niño. La Niña events also often re-intensify the following year (Okumura and Deser, 2010), a feature that can be seen in our model forcing (Fig. 3.1e), and thus subsurface West Antarctic cooling on the shelf intensifies again in month 28 of the simulation (Fig. 3.3f). The uncertainties associated with the vertical advective heat flux are larger than during El Niño because Ekman-induced vertical downwelling of cool surface waters is enhanced. Subsurface cooling continues through to the end of the La Niña and even during the 6-month extension of the simulation when no atmospheric ENSO anomalies are applied (months 36 to 40, Fig. 3.3f).

3.5 Discussion and Conclusions

ENSO events show considerable event-to-event variability with differing teleconnections to the Amundsen Sea (e.g., Figs. S3, S4). While the mechanisms presented here will likely be overall consistent across events, we expect the strongest impacts on shelf temperatures to be during events such as the 2015/16 El Niño and the 2011/12 La Niña, when West Antarctic wind anomalies were well-aligned to the shelf break geometry (Extended Data Fig. 3.8d, 3.94d), thus exerting the strongest change in the cross-shelf Ekman transport setup. Shelf temperature changes during these events might be even stronger when ENSO coincides with an opposite phase of the SAM, as this is when the ENSO teleconnection to the Amundsen Sea Low is strongest (Fogt et al., 2011; Paolo et al., 2015).

When considering the full climate variability, Oelerich et al. (2022) find that when the ASL is strengthened, Bellingshausen Sea subsurface temperatures below 300 m decrease, while an anomalous northward heat transport takes place. This is consistent with the mechanisms presented here during La Niña, when a strengthening of the ASL (Fig. 3.1c) cools the Bellingshausen Sea shelf region (Fig. 3.2b), and this cooling is linked to weaker cross-shelf advective heat fluxes in the warm CDW layer (Fig. 3.3f).

Future climate change simulations predict an increase in the variability and amplitude of ENSO events by 2100 Wang et al. (2022); Cai et al. (2021), and also suggest a net West Antarctic shelf warming impact because El Niño-induced warming appears to be overall greater than the associated La Niña-induced cooling (Dommenget et al., 2013; Cai et al., 2023). However, this past work by Cai et al. (2023) relies on coarse-resolution models, which may overestimate future ENSO-related teleconnections due to warming biases in these models in the West Antarctic sector (Heuzé (2021); Li et al. (2023) and Fig. 2 in Purich and England (2021)). Despite these known CMIP6 shelf water biases and the uncertainties in the base state change of ENSO, our model suggests possibly similar rectification effects on Antarctic shelf temperatures as in Cai et al. (2023) because in our simulation, the shelf warms for longer than it cools over one strong ENSO cycle (Extended Data Fig. 3.15). However, key to this net effect is also the amplitude of the warming, with basal melting rates responding more rapidly to increases than to decreases in advective heat fluxes Kimura et al. (2017).

We have investigated how atmospheric ENSO teleconnections modulate temperatures on the West Antarctic continental shelf. During El Niño, the ASL and coastal surface easterlies weaken. Accordingly, poleward Ekman transport of cold surface water is reduced and this enhances upwelling of warm CDW onto the shelf (Fig. 3.4a). During La Niña, we find a largely opposite response, with a stronger ASL, stronger surface easterlies and increased poleward flow of cold surface waters that inhibits upwelling of warm CDW onto the shelf (Fig. 3.4b). These results highlight the need to reconcile the role of interannual climate variability alongside future climate change in this vital sector of the Antarctic margin.

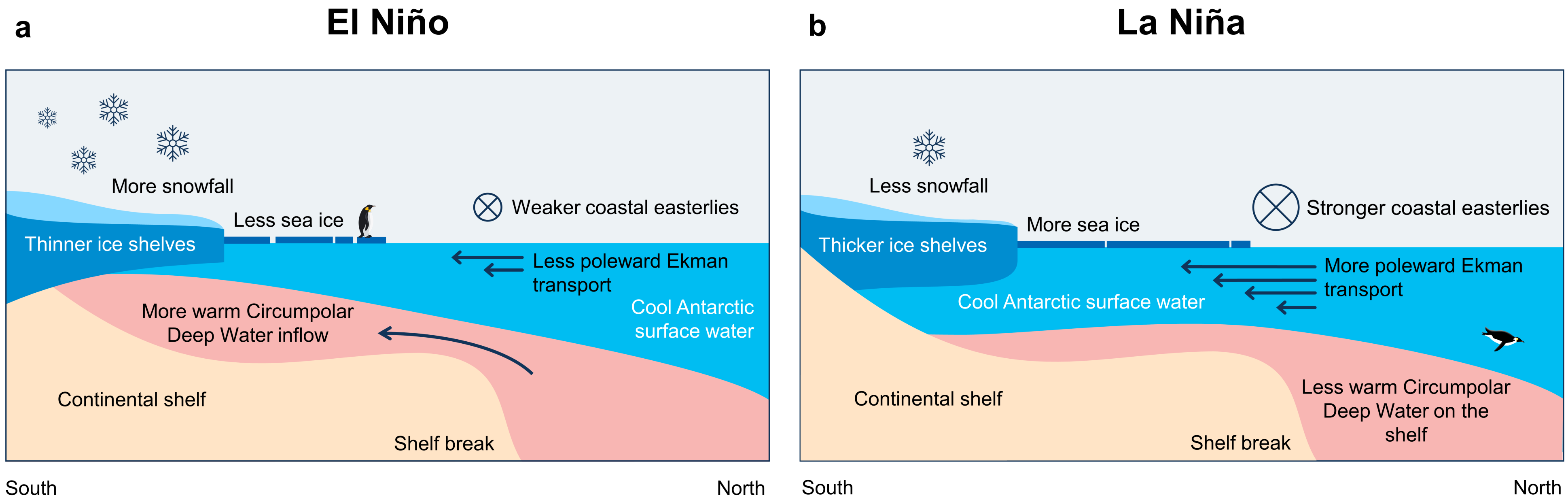

Figure 3.4: Schematic of physical mechanisms on the West Antarctic continental shelf during the (a) El Niño and (b) La Niña simulations. During El Niño, the Amundsen Sea Low (ASL) and coastal easterlies weaken, and they decrease poleward Ekman transport of cold surface water. The symbols $\otimes$ and $\odot$ show the reduction in the cyclonic (clockwise) ASL circulation. As a result, warm Circumpolar Deep Water (CDW) is advected onto the continental shelf. El Niño also increases snowfall over the West Antarctic ice shelves (Extended Data Fig. 3.10g), decreases their mass (Paolo et al., 2018) and reduces sea ice volume (Extended Data Fig. 3.16c). During La Niña, a largely opposite response occurs; the ASL strengthens, coastal easterlies and poleward Ekman transport increase which inhibits cross-shelf CDW upwelling. La Niña also reduces snowfall (Extended Data Fig. 3.11g), increases ice shelf mass (Paolo et al., 2018) and sea ice volume (Extended Data Fig. 3.16d) compared to El Niño. The emperor penguins have been added as artistic expression. Ecological impacts on sea birds have not been investigated here.

3.6 Open Research

The python scripts to create the perturbation experiment forcing and the scripts for the analysis in this study have been deposited online in the github repository https://github.com/mauricehuguenin/ENSO-Antarctica. The marine mammal data were collected and made freely available by the International MEOP Consortium and the national programs that contribute to it. The marine mammal data set can be accessed on https://www.meop.net/database/download-the-data.html by filling out a simple form, asking for one's name, e-mail, who they are and what they plan to do with the data. The ACCESS-OM2 model source code is available at https://github.com/COSIMA/access-om2.

3.7 Extended Data Figures

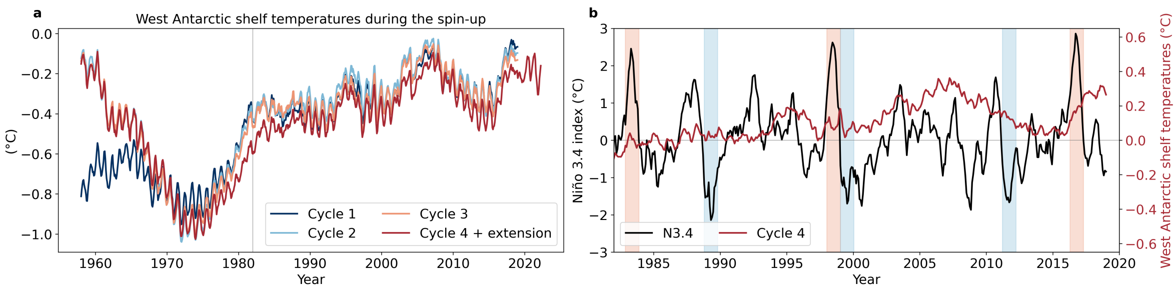

Extended Data Figure 3.5: (a) Time series of West Antarctic shelf temperatures (°C) during the four cycle spin-up in the 1/10° ACCESS-OM2 model. The fourth cycle has been extended to 2022. The vertical line in 1982 separates the earlier period that undergoes rapid adjustments due to the spin-up design from the later decades (for more information on this spin-up, see Extended Data Figure 1.7 on page 36). (b) The Niño 3.4 index (N3.4 in black, °C) and West Antarctic subsurface shelf temperatures (blue, °C) during the fourth spin-up cycle. The West Antarctic shelf region is defined as between 100 m and the shelf bottom, as well as between 60°W, 150°W and the 1000 m isobath.

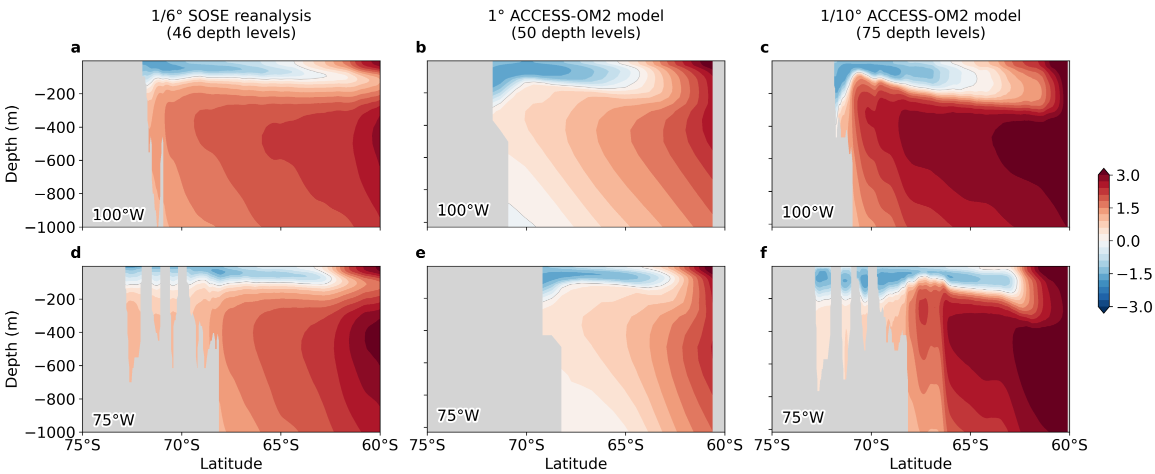

Extended Data Figure 3.6: Comparison of the ocean temperature structure in reanalysis and in the ACCESS-OM2 ocean-sea ice model over December 2012 to April 2017. (a, d) Temperature transects (°C) across 100° and 75°W in the Southern Ocean State Estimate data set Verdy and Mazloff (2017). This data has been regridded to the 1/10° ACCESS-OM2 model grid. (b, f) The same data in the 1° and the 1/10° configuration of the ACCESS-OM2 model.

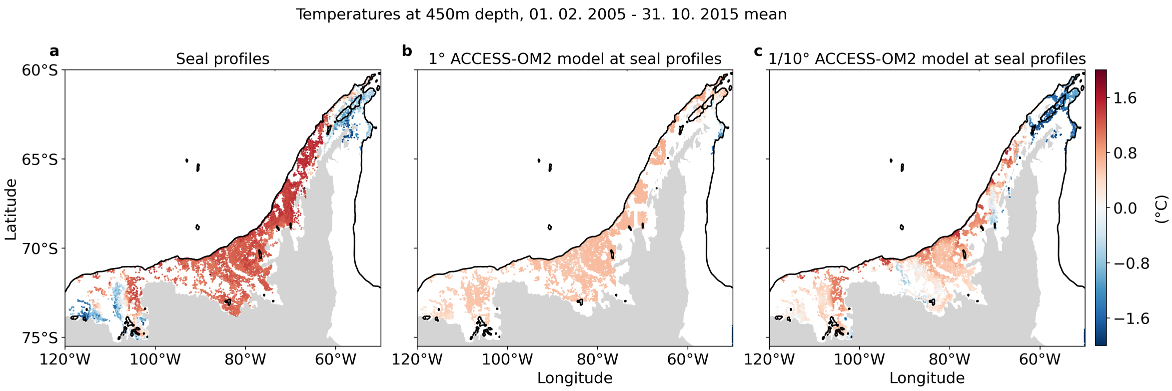

Extended Data Figure 3.7: Comparison of mean seal observation temperatures with ocean-sea ice model data over February 2005 to October 2015. (a) Mean temperature observations (°C) above 1000 m depth on the West Antarctic continental shelf from the Marine Mammals Exploring the Oceans Pole to Pole (MEOP) project Treasure et al. (2017). In black the 1000 m isobath around the Antarctic continent. (b, c) The temperatures in the 1° ACCESS-OM2 and 1/10° ACCESS-OM2 models evaluated at the location of the seal data set.

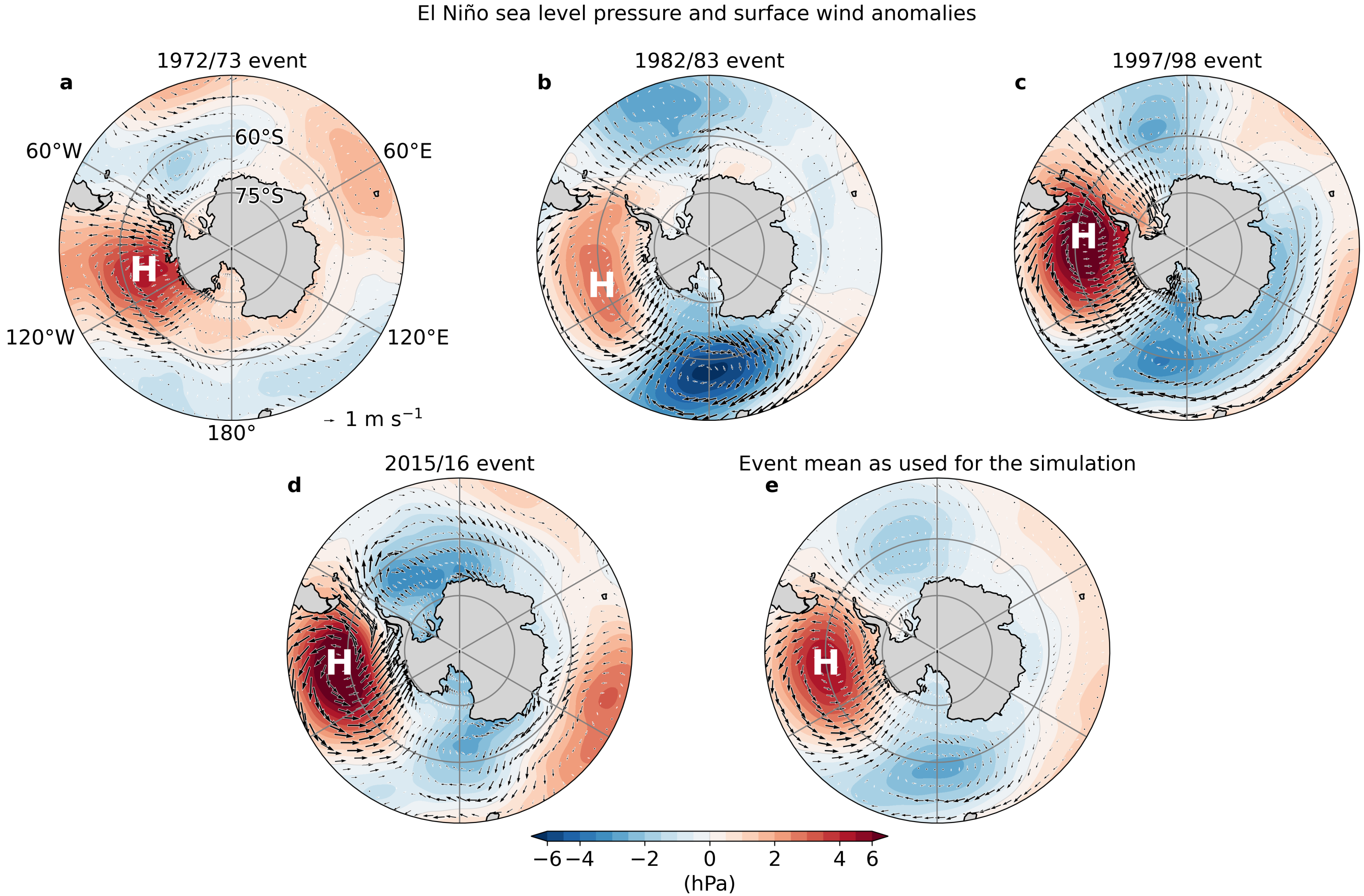

Extended Data Figure 3.8: Spatial maps of sea level pressure (hPa) and surface wind (m s^{-1}) anomalies during the peak of four strong El Niño events since 1958. (a-d) The mean spatial anomalies for the strong events in 1972–1973, 1982–1983, 1997–1998 and 2015–2016 and for the time period spanning six months prior to and six months after the peak of the N34 index (i.e., the orange shaded periods in Fig. 1a of the main manuscript. (e) The mean of panels (a-d). The **H** symbol indicates the location of the most positive anomaly.

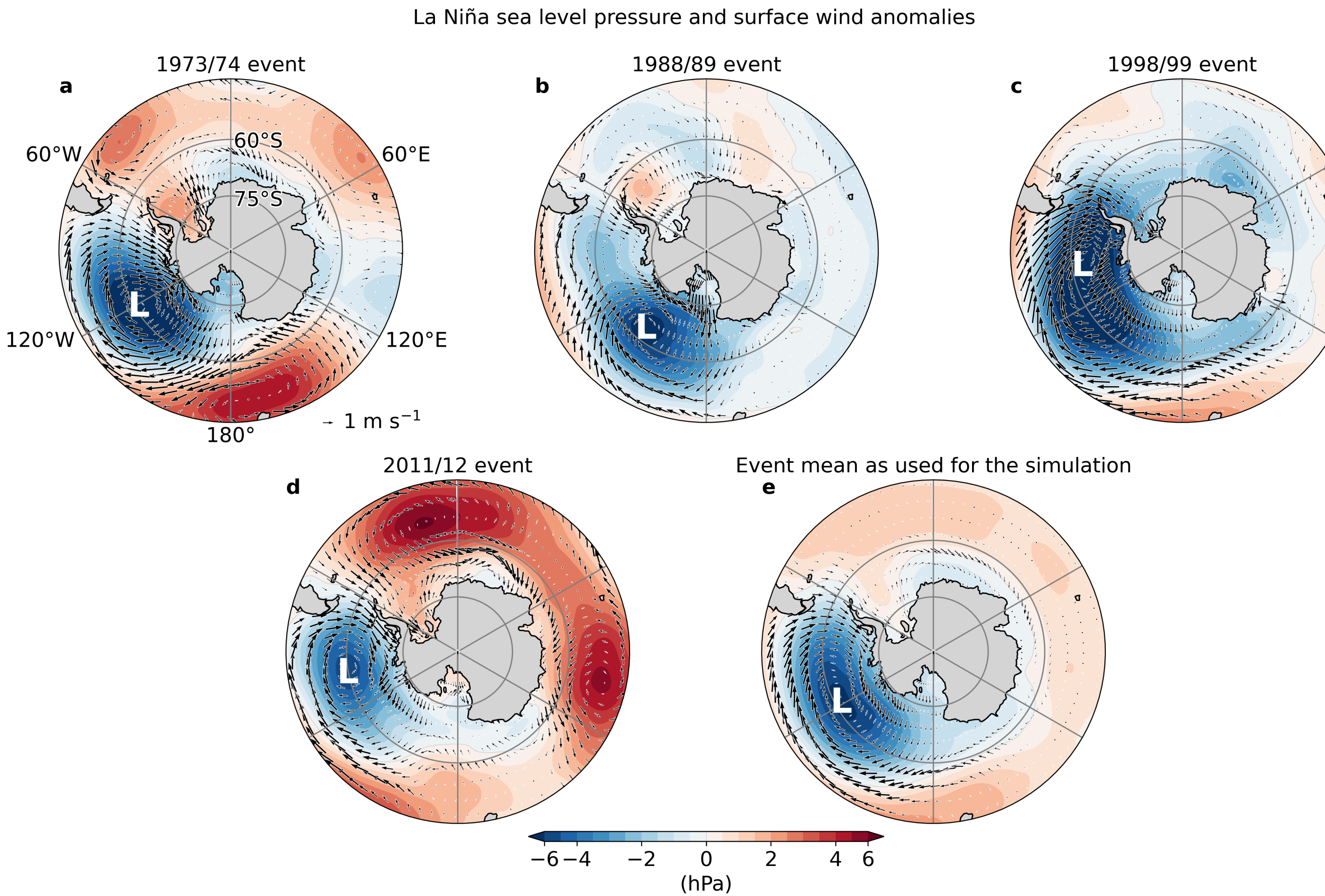

Extended Data Figure 3.9: As in Fig. 3.8 but for four strong La Niña events since 1958 and the **L** symbol indicating the location of the most negative sea level pressure anomaly.

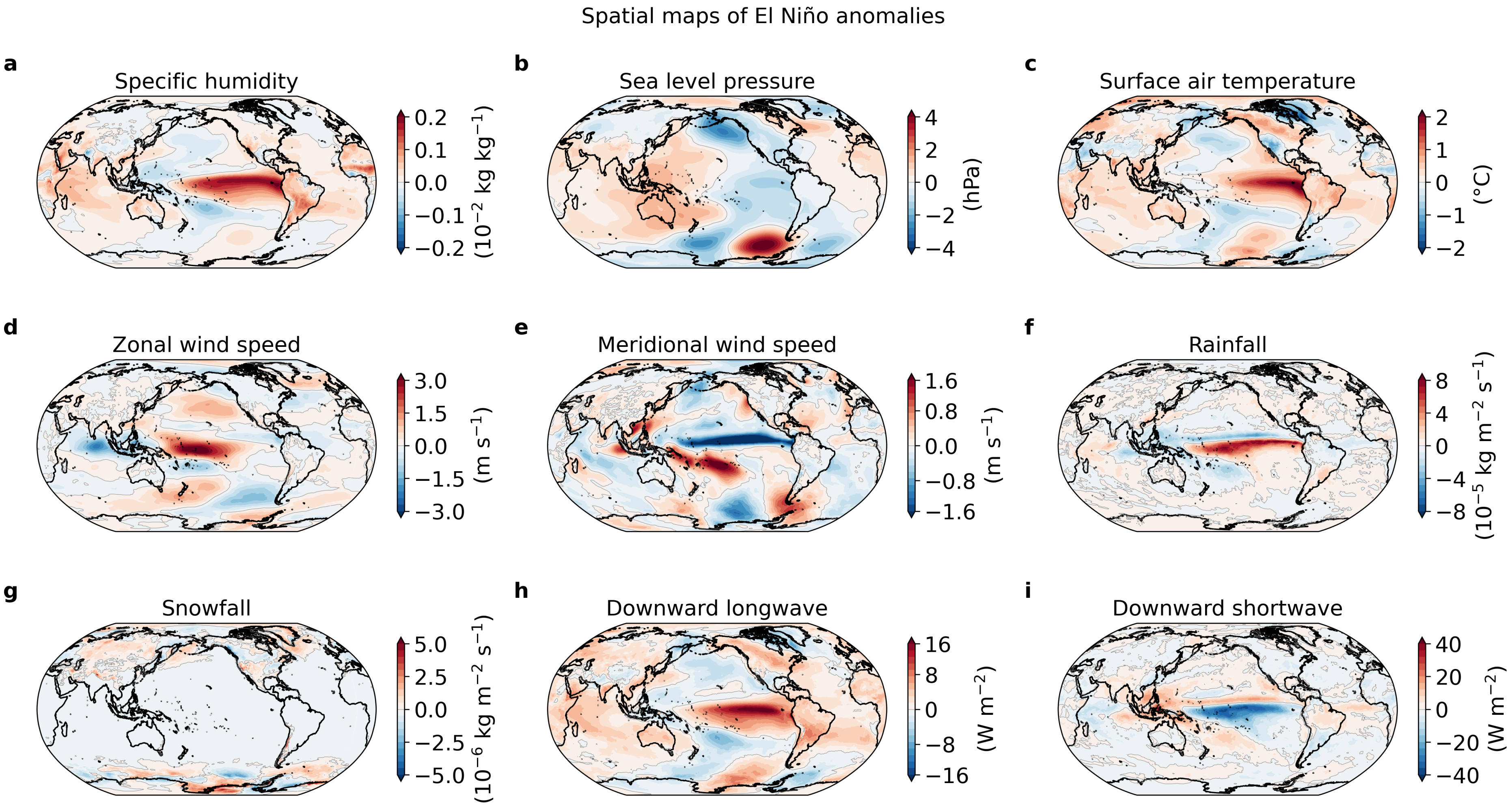

Extended Data Figure 3.10: Spatial maps of the atmospheric forcing fields used for the El Niño simulation. (a) Specific humidity (10^{-2} kg kg^{-1}), (b) sea level pressure (hPa), (c) surface air temperature (°C, (d, e) zonal and meridional wind speed (m s^{-1}), (f, g) rain- and snowfall (10^{-6} kg m^{-2} s^{-1}) and (h, i) downward long- and shortwave radiation (W m^{-2}). The river runoff map is not shown here as its impact is negligible (but still included in the forcing). The light grey contour at the zero level in all panels indicates the boundary between negative and positive anomalies.

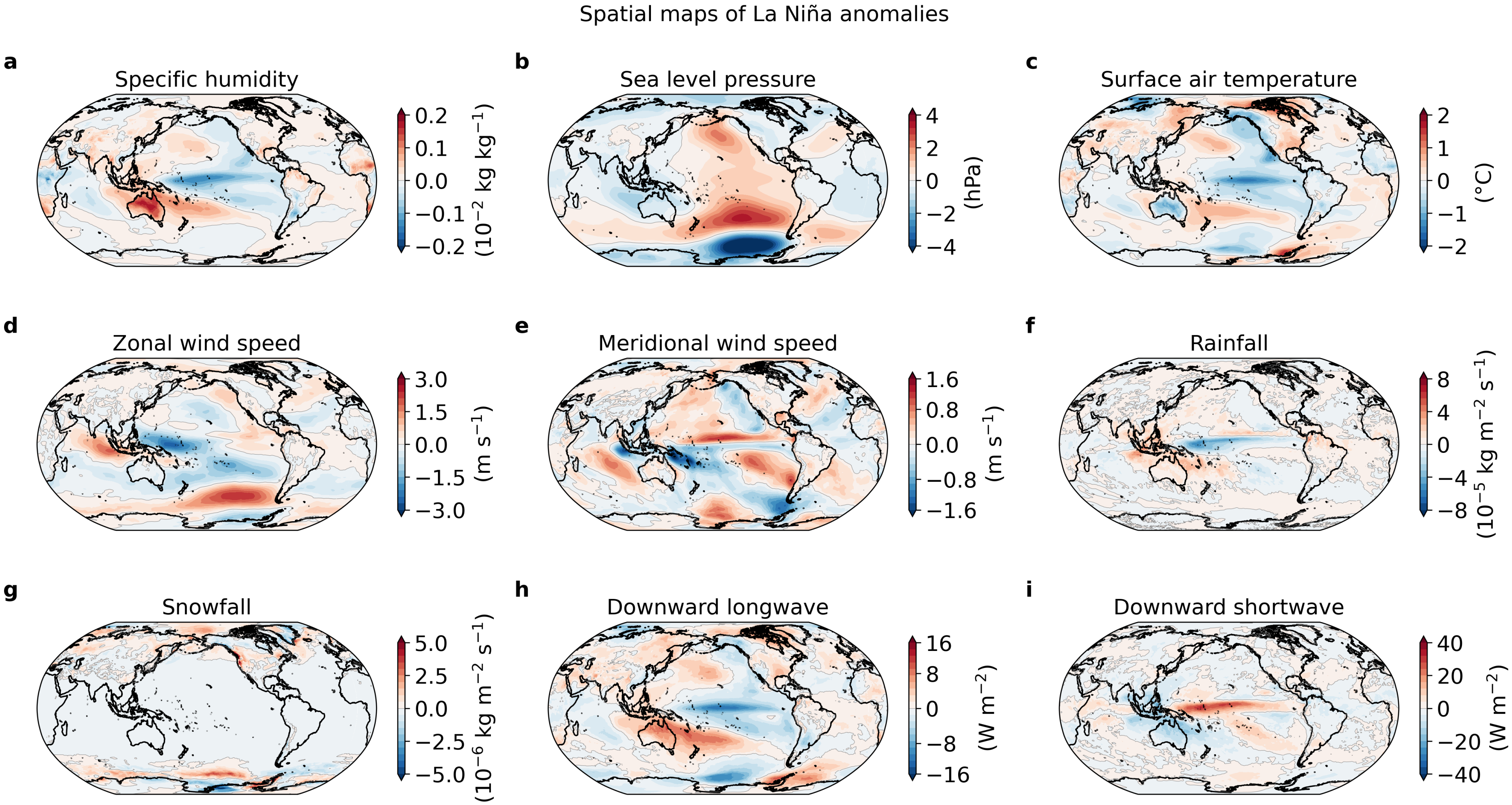

Extended Data Figure 3.11: As in Fig. 3.10 but for the La Niña simulation.

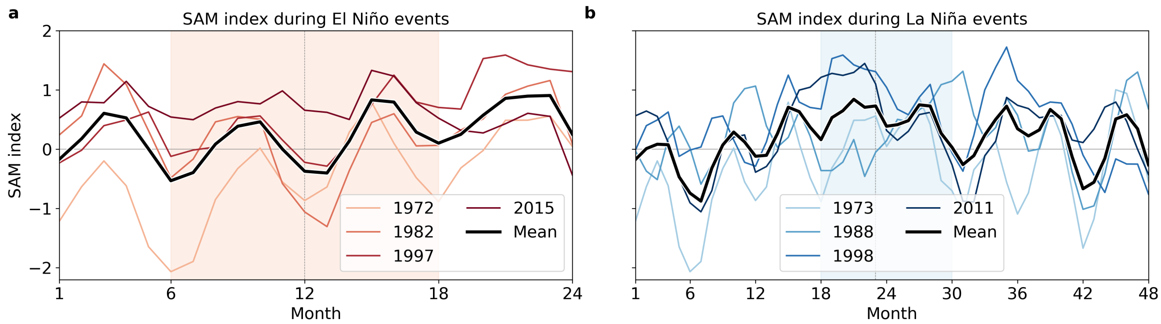

Extended Data Figure 3.12: Individual and composite time series of the Southern Annular Mode (SAM) index during strong (a) El Niño and (b) La Niña events. The index has been calculated using JRA55-do data following Keppler and Landschützer (2019).

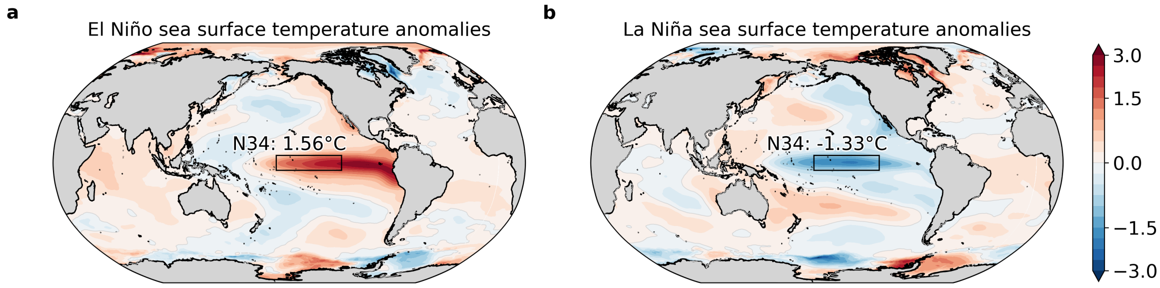

Extended Data Figure 3.13: Spatial maps of mean sea surface temperature anomalies during the peak of four strong El Niño and four strong La Niña events since 1958. (a) Map for El Niño and (b) for La Niña events (°C) with the Niño 3.4 region outlined in black and the mean sea surface temperature anomaly within the region given as a value.

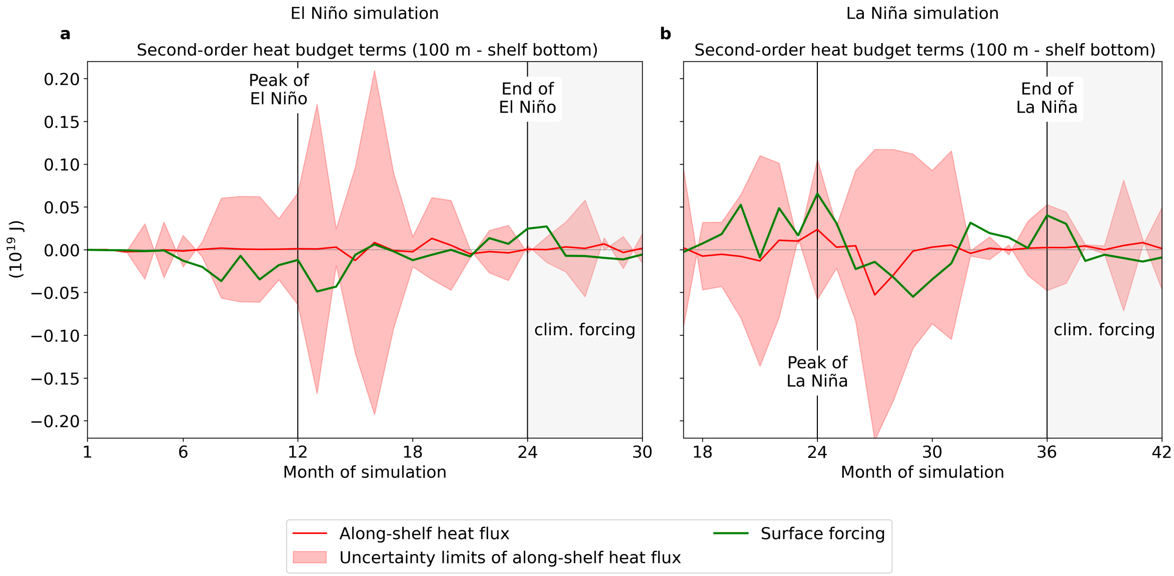

Extended Data Figure 3.14: The second-order subsurface Eulerian heat budget anomalies on the West Antarctic continental shelf (100 m - 1000 m, 150°W - 60°W and the shelf bottom) during the (a) El Niño and (b) La Niña simulations (10^{19} J). The surface volume flux is not shown here as it can only be non-zero in the top four grid cells near the surface. The vertical lines with labels indicate the peak and end of the simulated event. The steps to calculate the uncertainty range for the along-shelf heat flux are detailed in the Methods section of the main manuscript. The grey shaded period indicates where simulations are extended for six months with climatological forcing.

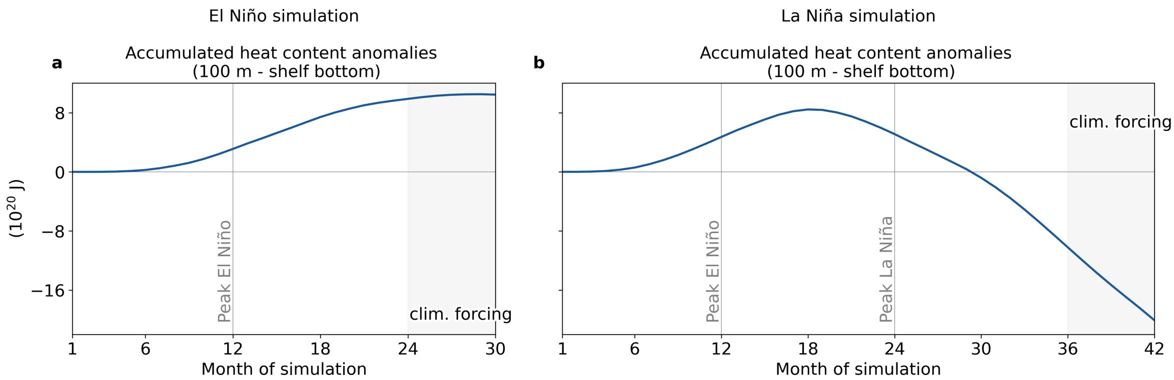

Extended Data Figure 3.15: Time series of the accumulated anomalous heat content on the West Antarctic continental shelf during the (a) El Niño and (b) La Niña simulation (10^{20} J). The vertical lines at month 12 and 24 indicate the peak of the event. The grey shaded period indicates where simulations are extended for six months with climatological forcing.

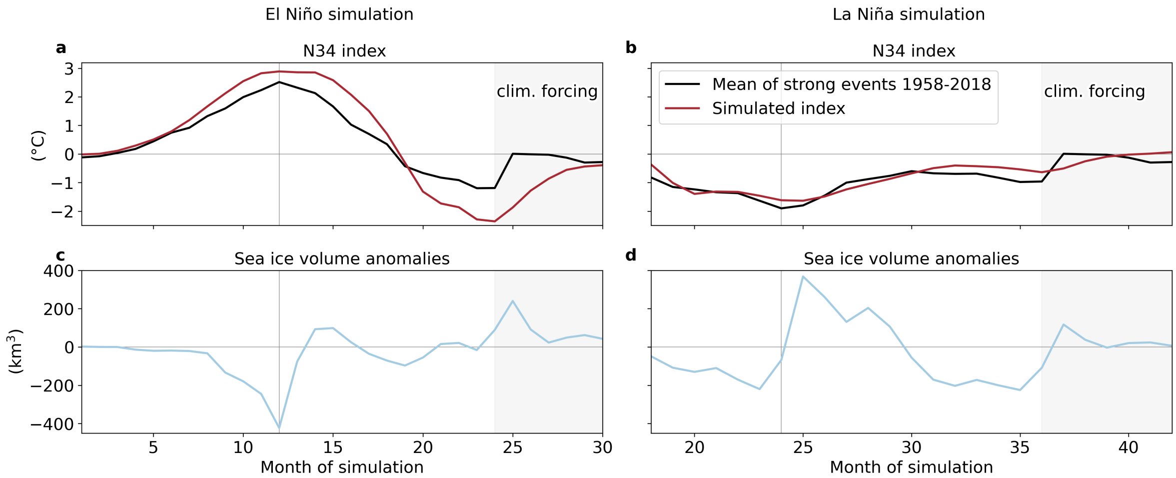

Extended Data Figure 3.16: Time series of the simulated Niño 3.4 index and sea ice volume anomalies during the El Niño and La Niña simulations. (a, b) The composite mean Niño 3.4 time series from JRA55-do and the simulated time series (in black and dark red, respectively, °C). The Niño 3.4 index is defined as the mean sea surface temperature anomalies in the equatorial region 5°S to °N and 170°W to 120°W. The vertical lines at month 12 and 24 indicate the peak of the event. The grey shaded period indicates where simulations are extended for six months with climatological forcing. (c, d) Time series of sea ice volume anomalies on the continental shelf during the events (km^3).

Concluding Remarks

Summary of Findings

A major challenge in assessing recent ocean temperature changes is the difficulty in isolating its drivers, in separating the anthropogenic signal from natural climate variability and the limited data available from observations. Research in this topic is not only important to understand Earth's climate system from a fundamental point of view, but also to understand how this system might change in the future. For example, ocean warming leads to global sea level rise through thermal expansion of sea water and through melting of Antarctic ice shelves - and therefore a better understanding of the mechanisms driving ocean warming is critical. This thesis sought to improve our understanding of the physical mechanisms driving recent ocean temperature changes on multi-decadal and interannual time scales. First, the focus was on the role of surface wind, radiation and surface air temperature changes on global ocean heat uptake and redistribution, before following with an in-depth budget analysis of ENSO-associated ocean warming and cooling both in the equatorial Pacific and on the West Antarctic continental shelf.

Part 1

The goal of this first part was to determine where and how ocean heat uptake associated with anthropogenic climate change since the 1970s has occurred and where it is stored today. First, a repeat decade forcing spin-up was performed in the global ocean-sea ice model to equilibrate the model's oceanic state to a 1960s climate, a period before the most recent heat uptake took place. This novel spin-up approach considerably improved upon previous approaches following the OMIP-2 spin-up framework (Tsujino et al., 2020), leading to a better match to the observed ocean heat content trend. If they were to use the new spin-up approach, the OMIP-2 models would very likely see a similar improvement of their ocean heat content trends.

The role of changing surface winds and atmospheric warming in driving anomalous heat uptake since the 1970s was highlighted using a suite of perturbation experiments. In these experiments, trends in atmospheric properties were either set to evolve over the last 50 years, or were set to zero. The simulations highlighted that the Southern Ocean has dominated anthropogenic heat uptake over the last 50 years, and thereby controlled the rate of climate change. This is because of the geographical setup with uninterrupted westerly winds around Antarctica that drive upwelling of cold water masses to the surface, enabling efficient heat uptake from the atmosphere prior to their subduction below warmer subtropical waters. Changes in surface winds and combined changes in surface air temperature and radiation each explain ∼50% of the Southern Ocean heat uptake. The simulations also revealed that the Indian, Pacific and Atlantic basins only showed minor ocean heat uptake over the full 50 year time span. However, on shorter decadal and interannual time scales, internal climate variability such as the Interdecadal Pacific Oscillation or ENSO can strongly impact global ocean heat content anomalies (England et al., 2014; Roemmich and Gilson, 2011).

While the large Southern Ocean heat uptake has been noted in previous studies (Frölicher et al., 2015; Armour et al., 2016), this past work used coupled climate models with their own independent internal climate variability. The previous were thus not able to capture the impacts of, for example, observed ENSO events or the changes in the phase of the Interdecadal Pacific Oscillation. The results obtained in this thesis showed how Southern Ocean heat uptake plays an integral part in buffering current climate change impacts, but whether this heat uptake mechanism will continue with the same efficiency in the future remains an open question.

Part 2

In this part, the overarching goal was to decompose the equatorial Pacific warm water volume budget during ENSO events into its different components to reconcile contradictory findings in previous studies. That is, the role of diabatic surface forcing and vertical mixing processes had both been highlighted as being important (Meinen and McPhaden, 2000; Clarke et al., 2007; Lengaigne et al., 2012) or negligible (Brown and Fedorov, 2010). The water mass transformation framework in temperature space was used to separate the diabatic volume fluxes into surface forcing, vertical mixing and numerical mixing components. Prior to this project, either surface forcing, vertical mixing or both have been inferred by using a residual, while here each diabatic flux was calculated accurately online.

The individual warm water volume budget terms highlighted that both surface forcing and vertical mixing initiate changes prior to the peak of ENSO events, while adiabatic transport dominates later. This is caused by changes in the equatorial trade winds that shift the position of the 20°C isotherm and reduce/enhance diabatic heat fluxes across this isotherm during El Niño/La Niña. While both surface forcing and vertical mixing deplete warm water volume during El Niño, the volume increase during La Niña, that is caused by large surface heat fluxes, is partially compensated by a decrease driven by vertical mixing. This occurs due to the shoaling of the 20°C isotherm in the eastern equatorial Pacific and its shift into a region of strong surface flux-driven heating and, at the same time, into a region of strong subsurface cooling induced by vertical mixing. These compensating effects in the eastern equatorial Pacific were seen both in idealised symmetric and realistic hindcast ENSO events. These results highlight the importance of accurately representing diabatic processes in numerical models to improve the representation of ENSO.

Part 3

The aim of this part was to examine the impacts of ENSO events on subsurface West Antarctic shelf temperatures. Continental shelf warming has the potential to drive basal melting of grounded ice shelves and thus accelerate global sea level rise via reduced buttressing of the ice sheets behind the ice shelves. Previous studies (Paolo et al., 2018; Holland et al., 2019; Naughten et al., 2022; Oelerich et al., 2022) have highlighted the link between shelf temperature variations and ENSO in West Antarctica, however they have not investigated the underlying ocean dynamics.

Here, perturbation experiments in the global ocean-sea ice model with ENSO-associated atmospheric anomalies were conducted in a 1/10° configuration of an ocean-sea ice model. During El Niño, the Amundsen Sea Low weakens, in turn weakening the coastal easterlies in the West Antarctic region and reducing the poleward Ekman transport of surface water masses. Consequently, warm Circumpolar Deep Water is transported onto the continental shelf to balance this mass deficit. During La Niña, a largely opposite response occurs: the Amundsen Sea Low strengthens, increasing the strength of coastal easterlies and in turn the poleward Ekman transport of cold surface waters toward the West Antarctic coastline. This inhibits upwelling of warm Circumpolar Deep Water onto the continental shelf. These results have implications for interpreting ice shelf melting on interannual time scales in the West Antarctic region.

Future Perspectives

This thesis focused on the drivers of ocean temperature changes over the last 50 years from multi-decadal to interannual time-scales and from global to regional space scales. The three parts in this work have opened a number of research questions that warrant further investigation.

Will Southern Ocean heat uptake continue for the rest of the century?

Future projections of CMIP5 climate models predict that the ocean will take up 5 to 7 times more heat (relative to the 1970s) under the Representative Concentration Pathway 8.5 (RCP8.5) scenario over the rest of the century (IPCC, 2019). This scenario represents an increase of +8.5 W m^{-2} radiative forcing at the top of the atmosphere by 2100. The coupled CMIP5 models share a relatively coarse 1° ocean model resolution and many important small-scale processes such as mesoscale eddies (Saenko et al., 2018; Huot et al., 2022), which play a key role in ocean heat uptake, are not resolved. Therefore, it is important to investigate changes in the Southern Ocean heat uptake efficiency in a higher resolution model. This is however largely unfeasible in a coupled modelling context due to high computational costs. On the other hand, Li et al. (2023) show how this might be achieved using a high resolution ocean-only model, namely by adding multi-model-mean atmospheric anomalies from the future Shared Socioeconomic Pathway 5-8.5 (SSP5-8.5) climate scenario run of CMIP6 models to the model's climatology forcing. The results from this study would provide important insight into the role of eddies (and their changes) on future global ocean heat uptake.

How do different ENSO event types and model resolution impact the warm water volume?

In Part 2, the mechanisms driving WWV variability during strong ENSO events have been investigated, with Fig. 2.14 highlighting the different time-integrated contributions of each WWV budget term. The various statements on the WWV budget do not distinguish between ENSO types (Central Pacific vs. Eastern Pacific). It would be beneficial to further investigate the processes governing WWV changes in simulations representing different ENSO event flavours as there may be large variability in the fluxes associated with the zonal structure of different El Niño events. The diabatic fluxes may also become less important during central Pacific ENSO events as their strength is strongly linked to the shoaling of the thermocline in the East. Perturbation simulations with radiative fluxes from newer reanalysis products (e.g., by using ERA5 data from Hersbach et al. (2020)) for the bulk formulae could show how large the ERA-Interim biases might be and how they relate to the results in Part 2. Performing the simulations in the 1/10° ACCESS-OM2 model with better resolved mesoscale processes such as tropical instability waves may provide information how model resolution impacts changes in both adiabatic and diabatic terms.

Further insights could also be gained by implementing the water mass transformation framework in the coupled ACCESS-ESM or ACCESS-CM2 models that both share a 1° horizontal resolution ocean model. Evaluating ENSO dynamics in these coupled models with the water mass transformation framework could help increase our understanding of these model's strengths and limitations in reproducing ENSO characteristics, WWV variability as well as ENSO's power spectra, diversity and asymmetry.

What is the rectified impact of ENSO on West Antarctic shelf temperatures?

Part 3 highlighted the dynamics driving West Antarctic shelf temperature variability during isolated ENSO events, showing a significant asymmetry between the impact of

El Niño and La Niña events. This suggests that ENSO may have a rectified (i.e., an integrated long-term) impact on West Antarctic shelf temperatures. CMIP6 models suggest that by the end of the 21st century, ENSO rectification effects could result in residual warming on the West Antarctic continental shelf because ENSO variability is projected to increase (Cai et al., 2021, 2023). However, the CMIP6 models have a very low resolution on the Antarctic shelf and it is not clear whether these changes might manifest. By running high-resolution multi-decadal ocean-sea ice simulations (that properly capture the important dynamics) with atmospheric ENSO anomalies, the non-linear rectification effects and their impacts could be studied. ENSO events in these simulations could be based on either fully symmetric or composite events (as highlighted in the Methods sections of Parts 2 and 3), in order to separate rectification effects coming from ENSO asymmetries themselves, compared to asymmetric responses of the Antarctic shelf dynamics. Coupling to an idealised ice shelf model may also permit an examination of asymmetric melting responses to ENSO's ocean temperature changes.

Future work could also focus on providing a commentary on how the 1° ACCESS-OM2 model represents these processes. This coarse resolution configuration will likely miss the responses of the eddy-mediated fluxes (and their sensitivity) of heat and momentum onto the West Antarctic continental shelf.

Do ENSO events together with phases of the SAM lead to larger temperature responses on the West Antarctic shelf?

In Part 3 of this thesis, the isolated impact of ENSO on Antarctic shelf temperatures has been explored. However, ENSO events often occur in coincidence with SAM events, which also have an impact on Antarctic shelf temperatures. Fogt et al. (2011); Paolo et al. (2018) suggest how an El Niño event and a negative phase of the SAM strengthen the atmospheric circulation anomalies at the mid-to-high latitudes (and vice versa for a La Niña event and a positive phase of the SAM), and therefore coincident El Niño and positive SAM events could result in stronger shelf warming signals. However, Herraiz-Borreguero and Naveira Garabato (2022) present a contradictory statement, namely that a positive phase of the SAM is linked to warmer Antarctic shelf temperatures via increased Circumpolar Deep Water intrusions. In addition, the SAM is projected to trend toward its positive phase over the coming century (Goyal et al., 2021b). It would thus be worthwhile to re-visit the perturbation experiments presented in Part 3, exploring the impacts of El Niño co-occurring with different phases of the SAM to reconcile the studies by Fogt et al. (2011); Paolo et al. (2018) and Herraiz-Borreguero and Naveira Garabato (2022). Similar combined La Niña and SAM anomalies could also be explored. This would enable a deeper analysis into the interactions between these two modes of climate variability and their impact on the Antarctic margin.

Final Remark

Research into recent ocean temperature changes on different temporal and spatial scales is crucial to understand current climate change. While many open questions still remain, this thesis has added to our knowledge of this topic by focusing on the role of atmospheric changes over the Southern Ocean and during El Niño-Southern Oscillation events. It is hoped that the findings presented here will lead to (1) a better understanding of global sea level rise through ocean warming and its associated thermosteric contribution, (2) improved ENSO predictions through an increased knowledge of its key precursor, the warm water volume, and (3) a better understanding of how ENSO events impact Antarctica and the rate of Antarctic ice shelf mass loss through basal melting.

Bibliography

Abraham, J. P., Baringer, M., Bindoff, N. L., Boyer, T., Cheng, L. J., Church, J. A., Conroy, J. L., Domingues, C. M., Fasullo, J. T., Gilson, J., Goni, G., Good, S. A., Gorman, J. M., Gouretski, V., Ishii, M., Johnson, G. C., Kizu, S., Lyman, J. M., Macdonald, A. M., Minkowycz, W. J., Moffitt, S. E., Palmer, M. D., Piola, A. R., Reseghetti, F., Schuckmann, K., Trenberth, K. E., Velicogna, I., and Willis, J. K. A review of global ocean temperature observations: Implications for ocean heat content estimates and climate change. *Reviews of Geophysics*, 51(3):450–483, 2013. https://doi.org/10.1002/rog.20022.

Argo. Argo float data and metadata from Global Data Assembly Centre (Argo GDAC), 2021. https://doi.org/10.17882/42182.

Argo. What is Argo?, 2023. URL https://argo.ucsd.edu/about/.

Armour, K. C., Marshall, J., Scott, J. R., Donohoe, A., and Newsom, E. R. Southern Ocean warming delayed by circumpolar upwelling and equatorward transport. *Nature Geoscience*, 9(7):549–554, 2016. https://doi.org/10.1038/ngeo2731.

Bentsen, M., Olivié, D. J. L., Seland, y., Toniazzo, T., Gjermundsen, A., Graff, L. S., Debernard, J. B., Gupta, A. K., He, Y., Kirkevåg, A., Schwinger, J., Tjiputra, J., Aas, K. S., Bethke, I., Fan, Y., Griesfeller, J., Grini, A., Guo, C., Ilicak, M., Karset, I. H. H., Landgren, O. A., Liakka, J., Moseid, K. O., Nummelin, A., Spensberger, C., Tang, H., Zhang, Z., Heinze, C., Iversen, T., and Schulz, M. NCC NorESM2-MM model output prepared for CMIP6 CMIP historical, 2019a. https://doi.org/10.22033/ESGF/CMIP6.8040.

Bentsen, M., Olivié, D. J. L., Seland, y., Toniazzo, T., Gjermundsen, A., Graff, L. S., Debernard, J. B., Gupta, A. K., He, Y., Kirkevåg, A., Schwinger, J., Tjiputra, J., Aas, K. S., Bethke, I., Fan, Y., Griesfeller, J., Grini, A., Guo, C., Ilicak, M., Karset, I. H. H., Landgren, O. A., Liakka, J., Moseid, K. O., Nummelin, A., Spensberger, C., Tang, H., Zhang, Z., Heinze, C., Iversen, T., and Schulz, M.

NCC NorESM2-MM model output prepared for CMIP6 CMIP piControl, 2019b. https://doi.org/10.22033/ESGF/CMIP6.8221.

Bentsen, M., Olivià, D. J. L., Seland, y., Toniazzo, T., Gjermundsen, A., Graff, L. S., Debernard, J. B., Gupta, A. K., He, Y., Kirkevåg, A., Schwinger, J., Tjiputra, J., Aas, K. S., Bethke, I., Fan, Y., Griesfeller, J., Grini, A., Guo, C., Ilicak, M., Karset, I. H. H., Landgren, O. A., Liakka, J., Moseid, K. O., Nummelin, A., Spensberger, C., Tang, H., Zhang, Z., Heinze, C., Iversen, T., and Schulz, M. NCC NorESM2-MM model output prepared for CMIP6 ScenarioMIP, 2019c. https://doi.org/10.22033/ESGF/CMIP6.608.

Bernie, D. J., Woolnough, S. J., Slingo, J. M., and Guilyardi, E. Modeling diurnal and intraseasonal variability of the ocean mixed layer. *Journal of Climate*, 18(8): 1190–1202, 2005. https://doi.org/10.1175/JCLI3319.1.

Boehme, L. and Rosso, I. Classifying oceanographic structures in the Amundsen Sea, Antarctica. *Geophysical Research Letters*, 48(5):e2020GL089412, 2021. https://doi.org/10.1029/2020GL089412.

Bosc, C. and Delcroix, T. Observed equatorial Rossby waves and ENSO-related warm water volume changes in the equatorial Pacific Ocean. *Journal of Geophysical Research: Oceans*, 113(C6), 2008. https://doi.org/10.1029/2007JC004613.

Boucher, O., Denvil, S., Levavasseur, G., Cozic, A., Caubel, A., Foujols, M.-A., Meurdesoif, Y., Cadule, P., Devilliers, M., Ghattas, J., Lebas, N., Lurton, T., Mellul, L., Musat, I., Mignot, J., and Cheruy, F. IPSL IPSL-CM6A-LR model output prepared for CMIP6 CMIP historical, 2018a. https://doi.org/10.22033/ESGF/CMIP6.5195.

Boucher, O., Denvil, S., Levavasseur, G., Cozic, A., Caubel, A., Foujols, M.-A., Meurdesoif, Y., Cadule, P., Devilliers, M., Ghattas, J., Lebas, N., Lurton, T., Mellul, L., Musat, I., Mignot, J., and Cheruy, F. IPSL IPSL-CM6A-LR model output prepared for CMIP6 CMIP piControl, 2018b. https://doi.org/10.22033/ESGF/CMIP6.5251.

Boucher, O., Denvil, S., Levavasseur, G., Cozic, A., Caubel, A., Foujols, M.-A., Meurdesoif, Y., Cadule, P., Devilliers, M., Dupont, E., and Lurton, T. IPSL IPSL-CM6A-LR model output prepared for CMIP6 ScenarioMIP ssp585, 2019. https://doi.org/10.22033/ESGF/CMIP6.5271.

Brown, J. N. and Fedorov, A. V. Estimating the diapycnal transport contribution to warm water volume variations in the tropical Pacific Ocean. *Journal of Climate*, 23 (2):221–237, 2010. https://doi.org/10.1175/2009JCLI2347.1.

Burgers, G., Jin, F.-F., and van Oldenborgh, G. J. The simplest ENSO recharge oscillator. *Geophysical Research Letters*, 32(13), 2005. https://doi.org/10.1029/2005GL022951.

Cai, W., Borlace, S., Lengaigne, M., Van Rensch, P., Collins, M., Vecchi, G., Timmermann, A., Santoso, A., McPhaden, M. J., Wu, L., et al. Increasing frequency of extreme El Niño events due to greenhouse warming. *Nature Climate Change*, 4(2): 111–116, 2014. https://doi.org/10.1038/nclimate2100.

Cai, W., Wang, G., Santoso, A., McPhaden, M. J., Wu, L., Jin, F.-F., Timmermann, A., Collins, M., Vecchi, G., Lengaigne, M., et al. Increased frequency of extreme La Niña events under greenhouse warming. *Nature Climate Change*, 5(2):132–137, 2015. https://doi.org/10.1038/nclimate2492.

Cai, W., Santoso, A., Collins, M., Dewitte, B., Karamperidou, C., Kug, J.-S., Lengaigne, M., McPhaden, M. J., Stuecker, M. F., Taschetto, A. S., Timmermann, A., Wu, L., Yeh, S.-W., Wang, G., Ng, B., Jia, F., Yang, Y., Ying, J., Zheng, X.-T., Bayr, T., Brown, J. R., Capotondi, A., Cobb, K. M., Gan, B., Geng, T., Ham, Y.-G., Jin, F.-F., Jo, H.-S., Li, X., Lin, X., McGregor, S., Park, J.-H., Stein, K., Yang, K., Zhang, L., and Zhong, W. Changing El Niño–Southern Oscillation in a warming climate. *Nature Reviews Earth & Environment*, 2(9):628–644, 2021. https://doi.org/10.1038/s43017-021-00199-z.

Cai, W., Jia, F., Li, S., Purich, A., Wang, G., Wu, L., Gan, B., Santoso, A., Geng, T., Ng, B., Yang, Y., Ferreira, D., Meehl, G. A., and McPhaden, M. J. Antarctic shelf ocean warming and sea ice melt affected by projected El Niño changes. *Nature Climate Change*, 2023. https://doi.org/10.1038/s41558-023-01610-x.

Cheng, L., Trenberth, K. E., Fasullo, J. T., Mayer, M., Balmaseda, M., and Zhu, J. Evolution of ocean heat content related to ENSO. *Journal of Climate*, 32(12): 3529–3556, 2019. https://doi.org/10.1175/JCLI-D-18-0607.1.

Cheng, L., von Schuckmann, K., Abraham, J. P., Trenberth, K. E., Mann, M. E., Zanna, L., England, M. H., Zika, J. D., Fasullo, J. T., Yu, Y., Pan, Y., Zhu, J., Newsom, E. R., Bronselaer, B., and Lin, X. Past and future ocean warming. *Nature Reviews Earth & Environment*, 3(11):776–794, 2022. https://doi.org/10.1038/s43017-022-00345-1.

Chiodi, A. M. and Harrison, D. E. Global seasonal precipitation anomalies robustly associated with El Niño and La Niña events—an OLR perspective. *Journal of Climate*, 28(15):6133 – 6159, 2015. https://doi.org/10.1175/JCLI-D-14-00387.1.

Clarke, A. J., Van Gorder, S., and Colantuono, G. Wind stress curl and ENSO discharge/recharge in the equatorial Pacific. *Journal of Physical Oceanography*, 37(4):1077–1091, 2007. https://doi.org/10.1175/JPO3035.1.

Colella, P. and Woodward, P. R. The Piecewise Parabolic Method (PPM) for gas-dynamical simulations. *Journal of Computational Physics*, 54(1):174–201, 1984. https://doi.org/10.1016/0021-9991(84)90143-8.

Collins, M., An, S.-I., Cai, W., Ganachaud, A., Guilyardi, E., Jin, F.-F., Jochum, M., Lengaigne, M., Power, S., Timmermann, A., et al. The impact of global warming on the tropical Pacific Ocean and El Niño. *Nature Geoscience*, 3(6):391, 2010. https://doi.org/10.1038/ngeo868.

Couldrey, M. P., Gregory, J. M., Boeira Dias, F., Dobrohotoff, P., Domingues, C. M., Garuba, O., Griffies, S. M., Haak, H., Hu, A., Ishii, M., Jungclaus, J., Köhl, A., Marsland, S. J., Ojha, S., Saenko, O. A., Savita, A., Shao, A., Stammer, D., Suzuki, T., Todd, A., and Zanna, L. What causes the spread of model projections of ocean dynamic sea-level change in response to greenhouse gas forcing? *Climate Dynamics*, 56(1-2):155–187, 2021. https://doi.org/10.1007/s00382-020-05471-4.

Craig, A., Valcke, S., and Coquart, L. Development and performance of a new version of the OASIS coupler, OASIS3-MCT_3.0. *Geoscientific Model Development*, 10(9):3297–3308, 2017. https://doi.org/10.5194/gmd-10-3297-2017.

Danabasoglu, G. NCAR CESM2-WACCM-FV2 model output prepared for CMIP6 CMIP historical, 2019a. https://doi.org/10.22033/ESGF/CMIP6.11298.

Danabasoglu, G. NCAR CESM2-WACCM-FV2 model output prepared for CMIP6 CMIP piControl, 2019b. https://doi.org/10.22033/ESGF/CMIP6.11302.

Danabasoglu, G. NCAR CESM2-WACCM model output prepared for CMIP6 ScenarioMIP ssp585, 2019c. https://doi.org/10.22033/ESGF/CMIP6.10115.

Danabasoglu, G. NCAR CESM2-WACCM model output prepared for CMIP6 CMIP historical, 2019d. https://doi.org/10.22033/ESGF/CMIP6.10071.

Danabasoglu, G. NCAR CESM2-WACCM model output prepared for CMIP6 CMIP piControl, 2019e. https://doi.org/10.22033/ESGF/CMIP6.10094.

Danabasoglu, G. NCAR CESM2 model output prepared for CMIP6 CMIP historical, 2019f. https://doi.org/10.22033/ESGF/CMIP6.7627.

Danabasoglu, G. NCAR CESM2 model output prepared for CMIP6 ScenarioMIP ssp585, 2019g. https://doi.org/10.22033/ESGF/CMIP6.7768.

Danabasoglu, G., Lawrence, D., Lindsay, K., Lipscomb, W., and Strand, G. NCAR CESM2 model output prepared for CMIP6 CMIP piControl, 2019. https://doi.org/10.22033/ESGF/CMIP6.7733.

Davis, P. E. D., Nicholls, K. W., Holland, D. M., Schmidt, B. E., Washam, P., Riverman, K. L., Arthern, R. J., Vaňková, I., Eayrs, C., Smith, J. A., Anker, P. G. D., Mullen, A. D., Dichek, D., Lawrence, J. D., Meister, M. M., Clyne, E., Basinski-Ferris, A., Rignot, E., Queste, B. Y., Boehme, L., Heywood, K. J., Anandakrishnan, S., and Makinson, K. Suppressed basal melting in the eastern Thwaites Glacier grounding zone. *Nature*, 614(7948):479–485, 2023. https://doi.org/10.1038/s41586-022-05586-0.

Dawson, H. R. S., Morrison, A. K., England, M. H., and Tamsitt, V. Pathways and timescales of connectivity around the Antarctic continental shelf. *Journal of Geophysical Research: Oceans*, 128(2):e2022JC018962, 2023. https://doi.org/10.1029/2022JC018962.

Dee, D., Uppala, S., Simmons, A., Berrisford, P., Poli, P., Kobayashi, S., Andrae, U., Balmaseda, M., Balsamo, G., Bauer, P., et al. The ERA-Interim reanalysis: configuration and performance of the data assimilation system. *Quarterly Journal of the Royal Meteorological Society*, 137(656):553–597, 2011. https://doi.org/10.1002/qj.828.

Delworth, T. L., Rosati, A., Anderson, W., Adcroft, A. J., Balaji, V., Benson, R., Dixon, K., Griffies, S. M., Lee, H.-C., Pacanowski, R. C., et al. Simulated climate and climate Change in the GFDL CM2.5 high-resolution coupled climate model. *Journal of Climate*, 25(8):2755–2781, 2012. https://doi.org/10.1175/JCLI-D-11-00316.1.

Desbruyères, D. G., Purkey, S. G., McDonagh, E. L., Johnson, G. C., and King, B. A. Deep and abyssal ocean warming from 35 years of repeat hydrography. *Geophysical Research Letters*, 43(19):10,356–10,365, 2016. https://doi.org/10.1002/2016GL070413.

Dias, F. B., Fiedler, R., Marsland, S. J., Domingues, C. M., Clément, L., Rintoul, S. R., Mcdonagh, E. L., Mata, M. M., and Savita, A. Ocean heat storage in response to changing ocean circulation Processes. *Journal of Climate*, 33(21):9065 – 9082, 2020. https://doi.org/10.1175/JCLI-D-19-1016.1.

Diaz, H. F., Hoerling, M. P., and Eischeid, J. K. ENSO variability, teleconnections and climate change. *International Journal of Climatology*, 21(15):1845–1862, 2001. https://doi.org/10.1002/joc.631.

Dix, M., Bi, D., Dobrohotoff, P., Fiedler, R., Harman, I., Law, R., Mackallah, C., Marsland, S., O'Farrell, S., Rashid, H., Srbinovsky, J., Sullivan, A., Trenham, C., Vohralik, P., Watterson, I., Williams, G., Woodhouse, M., Bodman, R., Dias, F. B., Domingues, C. M., Hannah, N., Heerdegen, A., Savita, A., Wales, S., Allen, C., Druken, K., Evans, B., Richards, C., Ridzwan, S. M., Roberts, D., Smillie, J., Snow, K., Ward, M., and Yang, R. CSIRO-ARCCSS ACCESS-CM2 model output prepared for CMIP6 CMIP historical, 2019a. https://doi.org/10.22033/ESGF/CMIP6.4271.

Dix, M., Bi, D., Dobrohotoff, P., Fiedler, R., Harman, I., Law, R., Mackallah, C., Marsland, S., O'Farrell, S., Rashid, H., Srbinovsky, J., Sullivan, A., Trenham, C., Vohralik, P., Watterson, I., Williams, G., Woodhouse, M., Bodman, R., Dias, F. B., Domingues, C. M., Hannah, N., Heerdegen, A., Savita, A., Wales, S., Allen, C., Druken, K., Evans, B., Richards, C., Ridzwan, S. M., Roberts, D., Smillie, J., Snow, K., Ward, M., and Yang, R. CSIRO-ARCCSS ACCESS-CM2 model output prepared for CMIP6 CMIP piControl, 2019b. https://doi.org/10.22033/ESGF/CMIP6.4311.

Dix, M., Bi, D., Dobrohotoff, P., Fiedler, R., Harman, I., Law, R., Mackallah, C., Marsland, S., O'Farrell, S., Rashid, H., Srbinovsky, J., Sullivan, A., Trenham, C., Vohralik, P., Watterson, I., Williams, G., Woodhouse, M., Bodman, R., Dias, F. B., Domingues, C. M., Hannah, N., Heerdegen, A., Savita, A., Wales, S., Allen, C., Druken, K., Evans, B., Richards, C., Ridzwan, S. M., Roberts, D., Smillie, J., Snow, K., Ward, M., and Yang, R. CSIRO-ARCCSS ACCESS-CM2 model output prepared for CMIP6 ScenarioMIP ssp126, 2019c. https://doi.org/10.22033/ESGF/CMIP6.4319.

Dommenget, D., Bayr, T., and Frauen, C. Analysis of the non-linearity in the pattern and time evolution of El Niño Southern Oscillation. *Climate Dynamics*, 40(11):2825–2847, 2013. https://doi.org/10.1007/s00382-012-1475-0.

Durack, P. J., Gleckler, P. J., Landerer, F. W., and Taylor, K. E. Quantifying underestimates of long-term upper-ocean warming. *Nature Climate Change*, 4(11):999–1005, 2014. https://doi.org/10.1038/nclimate2389.

EC-Earth Consortium. EC-Earth-Consortium EC-Earth3 model output prepared for CMIP6 CMIP historical, 2019a. https://doi.org/10.22033/ESGF/CMIP6.4700.

EC-Earth Consortium. EC-Earth-Consortium EC-Earth3 model output prepared for CMIP6 CMIP piControl, 2019b. https://doi.org/10.22033/ESGF/CMIP6.4842.

EC-Earth Consortium. EC-Earth-Consortium EC-Earth3 model output prepared for CMIP6 ScenarioMIP ssp585, 2019c. https://doi.org/10.22033/ESGF/CMIP6.4912.

EC-Earth Consortium. EC-Earth-Consortium EC-Earth3-Veg model output prepared for CMIP6 CMIP historical, 2019d. https://doi.org/10.22033/ESGF/CMIP6.4706.

EC-Earth Consortium. EC-Earth-Consortium EC-Earth3-Veg model output prepared for CMIP6 CMIP piControl, 2019e. https://doi.org/10.22033/ESGF/CMIP6.4848.

EC-Earth Consortium. EC-Earth-Consortium EC-Earth3-Veg model output prepared for CMIP6 ScenarioMIP ssp585, 2019f. https://doi.org/10.22033/ESGF/CMIP6.4912.

England, M. H., McGregor, S., Spence, P., Meehl, G. A., Timmermann, A., Cai, W., Gupta, A. S., McPhaden, M. J., Purich, A., and Santoso, A. Recent intensification of wind-driven circulation in the Pacific and the ongoing warming hiatus. *Nature Climate Change*, 4(3):222–227, 2014. https://doi.org/10.1038/NCLIMATE2106.

Eyring, V., Bony, S., Meehl, G. A., Senior, C. A., Stevens, B., Stouffer, R. J., and Taylor, K. E. Overview of the Coupled Model Intercomparison Project Phase 6 (CMIP6) experimental design and organization. *Geoscientific Model Development*, 9 (5):1937–1958, 2016. https://doi.org/10.5194/gmd-9-1937-2016.

Fairall, C. W., Bradley, E. F., Rogers, D. P., Edson, J. B., and Young, G. S. Bulk parameterization of air-sea fluxes for tropical ocean-global atmosphere coupled-ocean atmosphere response experiment. *Journal of Geophysical Research: Oceans*, 101(C2): 3747–3764, 1996. https://doi.org/10.1029/95JC03205.

Fasullo, J. T., Gent, P. R., and Nerem, R. S. Forced patterns of sea level rise in the Community Earth System Model Large Ensemble from 1920 to 2100. *Journal of Geophysical Research: Oceans*, 125(6):e2019JC016030, 2020. https://doi.org/10.1029/2019JC016030.

Feng, M., Zhang, N., Liu, Q., and Wijffels, S. The Indonesian Throughflow, its variability and centennial change. *Geoscience Letters*, 5:3, 2018. https://doi.org/10.1186/s40562-018-0102-2.

Fogt, R. L., Bromwich, D. H., and Hines, K. M. Understanding the SAM influence on the South Pacific ENSO teleconnection. *Climate Dynamics*, 36(7):1555–1576, 2011. https://doi.org/10.1007/s00382-010-0905-0.

Forget, G. and Ferreira, D. Global ocean heat transport dominated by heat export from the tropical Pacific. *Nature Geoscience*, 12(5):351–354, 2019. https://doi.org/10.1038/s41561-019-0333-7.

Fox-Kemper, B., Ferrari, R., and Hallberg, R. Parameterization of mixed layer eddies. Part I: Theory and diagnosis. *Journal of Physical Oceanography*, 38:1145–1165, 2008. https://doi.org/10.1175/2007JPO3792.1.

Frölicher, T. L., Sarmiento, J. L., Paynter, D. J., Dunne, J. P., Krasting, J. P., and Winton, M. Dominance of the Southern Ocean in anthropogenic carbon and heat uptake in CMIP5 models. *Journal of Climate*, 28(2):862–886, 2015. https://doi.org/10.1175/JCLI-D-14-00117.1.

Fukumori, I., Wang, O., Fenty, I., Forget, G., Patrick, H., and Ponte, R. M. Synopsis of the ECCO central production global ocean and sea-ice state estimate, version 4 Release 4, February 2021. https://10.5281/zenodo.4533349.

Fürst, J. J., Durand, G., Gillet-Chaulet, F., Tavard, L., Rankl, M., Braun, M., and Gagliardini, O. The safety band of Antarctic ice shelves. *Nature Climate Change*, 6 (5):479–482, 2016. https://doi.org/10.1038/nclimate2912.

Gent, P. R. and McWilliams, J. C. Isopycnal mixing in ocean circulation models. *Journal of Physical Oceanography*, 20(1):150–155, 1990. https://doi.org/10.1175/1520-0485(1990)020<0150:IMIOCM>2.0.CO;2.

Godfrey, J., C.Johnson, G., McPhaden, M., Reverdin, G., and Wijffels, S. E. Chapter 4.3 The tropical ocean circulation. In Siedler, G., Church, J., and Gould, J., editors, *Ocean Circulation and Climate*, volume 77 of *International Geophysics*, pages 215–246. Academic Press, 2001. https://doi.org/10.1016/S0074-6142(01)80121-2.

Good, P., Sellar, A., Tang, Y., Rumbold, S., Ellis, R., Kelley, D., and Kuhlbrodt, T. MOHC UKESM1.0-LL model output prepared for CMIP6 ScenarioMIP ssp585, 2019. https://doi.org/10.22033/ESGF/CMIP6.6405.

Goyal, R., Jucker, M., Sen Gupta, A., Hendon, H. H., and England, M. H. Zonal wave 3 pattern in the Southern Hemisphere generated by tropical convection. *Nature Geoscience*, 14(10):732–738, 2021a. https://doi.org/10.1038/s41561-021-00811-3.

Goyal, R., Sen Gupta, A., Jucker, M., and England, M. H. Historical and projected changes in the Southern Hemisphere surface westerlies. *Geophysical Research Letters*, 48(4):e2020GL090849, 2021b. https://doi.org/10.1029/2020GL090849.

Goyal, R., Jucker, M., Gupta, A. S., and England, M. H. A new zonal wave-3 index for the Southern Hemisphere. *Journal of Climate*, 35(15):5137 – 5149, 2022. https://doi.org/10.1175/JCLI-D-21-0927.1.

Greene, C. A., Gardner, A. S., Schlegel, N.-J., and Fraser, A. D. Antarctic calving loss rivals ice-shelf thinning. *Nature*, 2022. https://doi.org/10.1038/s41586-022-05037-w.

Gregg, M. C., Peters, H., Wesson, J. C., Oakey, N. S., and Shay, T. J. Intensive measurements of turbulence and shear in the equatorial undercurrent. *Nature*, 318: 140, nov 1985. https://doi.org/10.1038/318140a0.

Gregory, J. M., Bouttes, N., Griffies, S. M., Haak, H., Hurlin, W. J., Jungclaus, J., Kelley, M., Lee, W. G., Marshall, J., Romanou, A., Saenko, O. A., Stammer, D., and Winton, M. The Flux-Anomaly-Forced Model Intercomparison Project (FAFMIP) contribution to CMIP6: investigation of sea-level and ocean climate change in response to CO_2 forcing. *Geoscientific Model Development*, 9(11):3993–4017, 2016. https://doi.org/10.5194/gmd-9-3993-2016.

Griffies, S. M. Elements of the modular ocean model (MOM). *GFDL Ocean Group Tech. Rep*, 7:620, 2012.

Grist, J. P., Josey, S. A., New, A. L., Roberts, M., Koenigk, T., and Iovino, D. Increasing Atlantic Ocean heat transport in the latest generation coupled ocean-atmosphere models: the role of air-sea interaction. *Journal of Geophysical Research: Oceans*, 123 (11):8624–8637, 2018. https://doi.org/10.1029/2018JC014387.

Groeskamp, S., Griffies, S. M., Iudicone, D., Marsh, R., Nurser, A. G., and Zika, J. D. The water mass transformation framework for ocean physics and biogeochemistry. *Annual Review of Marine Science*, 11(1):271–305, 2019. https://doi.org/10.1146/annurev-marine-010318-095421.

Gudmundsson, G. H. Ice-shelf buttressing and the stability of marine ice sheets. *The Cryosphere*, 7(2):647–655, 2013. https://doi.org/10.5194/tc-7-647-2013.

Gudmundsson, G. H., Paolo, F. S., Adusumilli, S., and Fricker, H. A. Instantaneous Antarctic ice sheet mass loss driven by thinning ice shelves. *Geophysical Research Letters*, 46(23):13903–13909, 2019. https://doi.org/10.1029/2019GL085027.

Hallberg, R. Using a resolution function to regulate parameterizations of oceanic mesoscale eddy effects. *Ocean Modelling*, 72:92 – 103, 2013. https://doi.org/10.1016/j.ocemod.2013.08.007.

Hartmann, D. L., Tank, A. M. K., Rusticucci, M., Alexander, L. V., Brönnimann, S., Charabi, Y. A. R., Dentener, F. J., Dlugokencky, E. J., Easterling, D. R., Kaplan, A., et al. Observations: atmosphere and surface. In *Climate Change 2013 the Physical Science Basis: Working Group I Contribution to the Fifth Assessment Report of the Intergovernmental Panel on Climate Change*. Cambridge University Press, 2013.

Henley, B. J. and King, A. D. Trajectories toward the 1.5°C Paris target: modulation by the Interdecadal Pacific Oscillation. *Geophysical Research Letters*, 44(9):4256–4262, 2017. https://doi.org/10.1002/2017GL073480.

Herraiz-Borreguero, L. and Naveira Garabato, A. C. Poleward shift of Circumpolar Deep Water threatens the East Antarctic Ice Sheet. *Nature Climate Change*, 12(8): 728–734, 2022. https://doi.org/10.1038/s41558-022-01424-3.

Hersbach, H., Bell, B., Berrisford, P., Hirahara, S., Horányi, A., Muñoz-Sabater, J., Nicolas, J., Peubey, C., Radu, R., Schepers, D., Simmons, A., Soci, C., Abdalla, S., Abellan, X., Balsamo, G., Bechtold, P., Biavati, G., Bidlot, J., Bonavita, M., De Chiara, G., Dahlgren, P., Dee, D., Diamantakis, M., Dragani, R., Flemming, J., Forbes, R., Fuentes, M., Geer, A., Haimberger, L., Healy, S., Hogan, R. J., Hólm, E., Janisková, M., Keeley, S., Laloyaux, P., Lopez, P., Lupu, C., Radnoti, G., de Rosnay, P., Rozum, I., Vamborg, F., Villaume, S., and Thépaut, J.-N. The ERA5 global reanalysis. *Quarterly Journal of the Royal Meteorological Society*, 146(730):1999–2049, 2020. https://doi.org/10.1002/qj.3803.

Heuzé, C., Heywood, K. J., Stevens, D. P., and Ridley, J. K. Southern Ocean bottom water characteristics in CMIP5 models. *Geophysical Research Letters*, 40(7):1409–1414, 2013. https://doi.org/10.1002/grl.50287.

Heuzé, C. Antarctic Bottom Water and North Atlantic Deep Water in CMIP6 models. *Ocean Science*, 17(1):59–90, 2021. https://doi.org/10.5194/os-17-59-2021.

Heywood, K. J., Biddle, L. C., Boehme, L., Dutrieux, P., Fedak, M., Jenkins, A., Jones, R. W., Kaiser, J., Mallett, H., Garabato, A. C. N., Renfrew, I. A., Stevens, D. P., and Webber, B. G. Between the Devil and the deep blue sea: the role of the Amundsen Sea continental shelf in exchanges between ocean and ice shelves. *Oceanography*, December 2016. https://doi.org/10.5670/oceanog.2016.104.

Holland, P. R., Bracegirdle, T. J., Dutrieux, P., Jenkins, A., and Steig, E. J. West Antarctic ice loss influenced by internal climate variability and anthropogenic forcing. *Nature Geoscience*, 12(9):718–724, 2019. https://doi.org/10.1038/s41561-019-0420-9.

Holmes, R. M. and Thomas, L. N. The modulation of equatorial turbulence by tropical instability waves in a regional ocean model. *Journal of Physical Oceanography*, 45 (4):1155–1173, 2015. https://doi.org/10.1175/JPO-D-14-0209.1.

Holmes, R. M., Zika, J. D., and England, M. H. Diathermal heat transport in a global ocean model. *Journal of Physical Oceanography*, 49(1):141–161, 2019a. https://doi.org/10.1175/JPO-D-18-0098.1.

Holmes, R. M., Zika, J. D., Ferrari, R., Thompson, A. F., Newsom, E. R., and England, M. H. Atlantic ocean heat transport enabled by Indo-Pacific heat uptake and mixing. *Geophysical Research Letters*, 46(23):13939–13949, 2019b. https://doi.org/10.1029/2019GL085160.

Horel, J. D. On the annual cycle of the tropical Pacific atmosphere and ocean. *Monthly Weather Review*, 110(12):1863–1878, 1982. https://doi.org/10.1175/1520-0493(1982)110<1863:OTACOT>2.0.CO;2.

Hosking, J. S., Orr, A., Marshall, G. J., Turner, J., and Phillips, T. The influence of the Amundsen–Bellingshausen Seas Low on the climate of West Antarctica and its representation in coupled climate model simulations. *Journal of Climate*, 26(17):6633 – 6648, 2013. https://doi.org/10.1175/JCLI-D-12-00813.1.

Hoskins, B. J. and Ambrizzi, T. Rossby wave propagation on a realistic longitudinally varying flow. *Journal of Atmospheric Sciences*, 50(12):1661 – 1671, 1993. https://doi.org/10.1175/1520-0469(1993)050<1661:RWPOAR>2.0.CO;2.

Huang, B., Banzon, V. F., Freeman, E., Lawrimore, J., Liu, W., Peterson, T. C., Smith, T. M., Thorne, P. W., Woodruff, S. D., and Zhang, H.-M. Extended reconstructed sea surface temperature version 4 (ERSST. v4). Part I: upgrades and intercomparisons. *Journal of climate*, 28(3):911–930, 2015. https://doi.org/10.1175/JCLI-D-14-00006.1.

Huguenin, M. F., Holmes, R. M., and England, M. H. Key role of diabatic processes in regulating warm water volume variability over ENSO events. *Journal of Climate*, 33 (22):9945 – 9964, 2020. https://doi.org/10.1175/JCLI-D-20-0198.1.

Huguenin, M. F., Holmes, R. M., and England, M. H. Drivers and distribution of global ocean heat uptake over the last half century. *Nature Communications*, 13(1):4921, 2022a. https://doi.org/10.1038/s41467-022-32540-5.

Huguenin, M. F., Holmes, R. M., and England, M. H. Data and analysis scripts for: drivers and distribution of global ocean heat content over the last half century, July 2022b. https://doi.org/10.5281/zenodo.6825334.

Huguenin-Virchaux, M. F., Holmes, R. M., England, M. H., Medhaug, I., and Knutti, R. Mechanisms driving ocean heat uptake and warm water volume variability over idealized ENSO events, 2018.

Huneke, W. G. C., Morrison, A. K., and Hogg, A. M. Spatial and subannual variability of the Antarctic Slope Current in an eddying ocean–sea ice model. *Journal of Physical Oceanography*, 52(3):347 – 361, 2022. https://doi.org/10.1175/JPO-D-21-0143.1.

Hunke, E., Lipscomb, W., and Turner, A. CICE: the Los Alamos sea ice model, documentation and software, version 5.1 (Tech. Rep. LA-CC-06-012). *Los Alamos National Laboratory*, 2015.

Huot, P.-V., Kittel, C., Fichefet, T., Jourdain, N. C., and Fettweis, X. Effects of ocean mesoscale eddies on atmosphere–sea ice–ocean interactions off Adélie Land, East Antarctica. *Climate Dynamics*, 59(1):41–60, 2022. https://doi.org/0.1007/s00382-021-06115-x.

IPCC. Summary for Policymakers. In *Climate Change 2013: The Physical Science Basis Contribution of Working Group I to the Fifth Assessment Report of the Intergovernmental Panel on Climate Change [Stocker, T.F., D. Qin, G.-K. Plattner, M. Tignor, S.K. Allen, J. Boschung, A. Nauels, Y. Xia, V. Bex and P.M. Midgley (eds.)]*. Cambridge University Press, Cambridge, United Kingdom and New York, NY, USA, 2013.

IPCC. Summary for Policymakers. In *IPCC Special Report on the Ocean and Cryosphere in a Changing Climate [H.-O. Pörtner, D.C.Roberts, V. Masson-Delmotte, P. Zhai, M. Tignor, E. Poloczanska, K. Mintenbeck, M. Nicolai, A. Okem, J. Petzold, B. Rama, N. Weyer (eds.)]*. In press., 2019.

Irving, D. B., Wijffels, S., and Church, J. A. Anthropogenic aerosols, greenhouse gases, and the uptake, transport, and storage of excess heat in the climate system. *Geophysical Research Letters*, 46(9):4894–4903, 2019. https://doi.org/10.1029/2019GL082015.

Irving, D., Hobbs, W., Church, J., and Zika, J. A mass and energy conservation analysis of drift in the CMIP6 ensemble. *Journal of Climate*, 34(8):3157 – 3170, 2021. https://doi.org/10.1175/JCLI-D-20-0281.1.

Izumo, T., Lengaigne, M., Vialard, J., Suresh, I., and Planton, Y. On the physical interpretation of the lead relation between warm water volume and the El Niño Southern Oscillation. *Climate Dynamics*, pages 1–20, 2018. https://doi.org/10.1007/s00382-018-4313-1.

Jenkins, A., Dutrieux, P., Jacobs, S., Steig, E. J., Gudmundsson, G. H., Smith, J., and Heywood, K. J. Decadal ocean forcing and Antarctic ice sheet response: lessons from the Amundsen Sea. *Oceanography*, December 2016.

Jin, F.-F. An equatorial ocean recharge paradigm for ENSO. Part II: a stripped-down coupled model. *Journal of the Atmospheric Sciences*, 54:830–847, 04 1997a. https://doi.org/10.1175/1520-0469(1997)054<0830:AEORPF>2.0.CO;2.

Jin, F.-F. An equatorial ocean recharge paradigm for ENSO. Part I: conceptual model. *Journal of the Atmospheric Sciences*, 54(7):811–829, 1997b. https://doi.org/10.1175/1520-0469(1997)054<0830:AEORPF>2.0.CO;2.

Jochum, M., Danabasoglu, G., Holland, M., Kwon, Y.-O., and Large, W. G. Ocean viscosity and climate. *Journal of Geophysical Research: Oceans*, 113(C6), 2008. https://doi.org/10.1029/2007JC004515.

Jochum, M. and Murtugudde, R. Temperature advection by Tropical Instability Waves. *Journal of Physical Oceanography*, 36(4):592 – 605, 2006. https://doi.org/10.1175/JPO2870.1.

John, J. G., Blanton, C., McHugh, C., Radhakrishnan, A., Rand, K., Vahlenkamp, H., Wilson, C., Zadeh, N. T., Dunne, J. P., Dussin, R., Horowitz, L. W., Krasting, J. P., Lin, P., Malyshev, S., Naik, V., Ploshay, J., Shevliakova, E., Silvers, L., Stock, C., Winton, M., and Zeng, Y. NOAA-GFDL GFDL-ESM4 model output prepared for CMIP6 ScenarioMIP ssp585, 2018. https://doi.org/10.22033/ESGF/CMIP6.8706.

Johnson, G. C. and Birnbaum, A. N. As El Niño builds, Pacific Warm Pool expands, ocean gains more heat. *Geophysical Research Letters*, 44(1):438–445, 2017. https://doi.org/10.1002/2016GL071767.

Johnson, G. C., Lyman, J. M., and Purkey, S. G. Informing Deep Argo array design using Argo and full-depth hydrographic section data. *Journal of Atmospheric and Oceanic Technology*, 32(11):2187 – 2198, 2015. https://doi.org/10.1175/JTECH-D-15-0139.1.

Kara, A. B., Wallcraft, A. J., Metzger, E. J., Hurlburt, H. E., and Fairall, C. W. Wind stress drag coefficient over the global ocean. *Journal of Climate*, 20(23):5856–5864, 2007. https://doi.org/10.1175/2007JCLI1825.1.

Karoly, D. J. Southern Hemisphere circulation features associated with El Niño-Southern Oscillation events. *Journal of Climate*, 2(11):1239 – 1252, 1989. https://doi.org/10.1175/1520-0442(1989)002<1239:SHCFAW>2.0.CO;2.

Kennicutt, M. C., Bromwich, D., Liggett, D., Njåstad, B., Peck, L., Rintoul, S. R., Ritz, C., Siegert, M. J., Aitken, A., Brooks, C. M., Cassano, J., Chaturvedi, S., Chen, D., Dodds, K., Golledge, N. R., Le Bohec, C., Leppe, M., Murray, A., Nath, P. C., Raphael, M. N., Rogan-Finnemore, M., Schroeder, D. M., Talley, L., Travouillon, T., Vaughan, D. G., Wang, L., Weatherwax, A. T., Yang, H., and Chown, S. L. Sustained Antarctic research: A 21st century imperative. *One Earth*, 1(1):95–113, 2019. ISSN 2590-3322. https://doi.org/10.1016/j.oneear.2019.08.014.

Keppler, L. and Landschützer, P. Regional wind variability modulates the Southern Ocean carbon sink. *Scientific Reports*, 9(1):7384, 2019. https://doi.org/10.1038/s41598-019-43826-y.

Kimura, S., Jenkins, A., Regan, H., Holland, P. R., Assmann, K. M., Whitt, D. B., Van Wessem, M., van de Berg, W. J., Reijmer, C. H., and Dutrieux, P. Oceanographic controls on the variability of ice-shelf basal melting and circulation of glacial meltwater in the Amundsen Sea Embayment, Antarctica. *Journal of Geophysical Research: Oceans*, 122(12):10131–10155, 2017. https://doi.org/10.1002/2017JC012926.

Kiss, A. E., Hogg, A. M., Hannah, N., Boeira Dias, F., Brassington, G. B., Chamberlain, M. A., Chapman, C., Dobrohotoff, P., Domingues, C. M., Duran, E. R., England, M. H., Fiedler, R., Griffies, S. M., Heerdegen, A., Heil, P., Holmes, R. M., Klocker, A., Marsland, S. J., Morrison, A. K., Munroe, J., Oke, P. R., Nikurashin, M., Pilo, G. S., Richet, O., Savita, A., Spence, P., Stewart, K. D., Ward, M. L., Wu, F., and Zhang, X. ACCESS-OM2: A global ocean-sea ice model at three resolutions. *Geoscientific Model Development Discussions*, pages 1–58, 2020. https://doi.org/10.5194/gmd-13-401-2020.

Knutson, T., Camargo, S. J., Chan, J. C. L., Emanuel, K., Ho, C.-H., Kossin, J., Mohapatra, M., Satoh, M., Sugi, M., Walsh, K., and Wu, L. Tropical cyclones and climate change assessment: part II: projected response to anthropogenic warming. *Bulletin of the American Meteorological Society*, 101(3):E303 – E322, 2020. https://doi.org/10.1175/BAMS-D-18-0194.1.

Krasting, J. P., John, J. G., Blanton, C., McHugh, C., Nikonov, S., Radhakrishnan, A., Rand, K., Zadeh, N. T., Balaji, V., Durachta, J., Dupuis, C., Menzel, R., Robinson, T., Underwood, S., Vahlenkamp, H., Dunne, K. A., Gauthier, P. P., Ginoux, P., Griffies, S. M., Hallberg, R., Harrison, M., Hurlin, W., Malyshev, S., Naik, V., Paulot, F., Paynter, D. J., Ploshay, J., Reichl, B. G., Schwarzkopf, D. M., Seman, C. J., Silvers, L., Wyman, B., Zeng, Y., Adcroft, A., Dunne, J. P., Dussin, R., Guo, H., He, J., Held, I. M., Horowitz, L. W., Lin, P., Milly, P., Shevliakova, E., Stock, C., Winton, M., Wittenberg, A. T., Xie, Y., and Zhao, M. NOAA-GFDL GFDL-ESM4 model output prepared for CMIP6 CMIP historical, 2018a. https://doi.org/10.22033/ESGF/CMIP6.8597.

Krasting, J. P., John, J. G., Blanton, C., McHugh, C., Nikonov, S., Radhakrishnan, A., Rand, K., Zadeh, N. T., Balaji, V., Durachta, J., Dupuis, C., Menzel, R., Robinson, T., Underwood, S., Vahlenkamp, H., Dunne, K. A., Gauthier, P. P., Ginoux, P., Griffies, S. M., Hallberg, R., Harrison, M., Hurlin, W., Malyshev, S., Naik, V., Paulot, F., Paynter, D. J., Ploshay, J., Reichl, B. G., Schwarzkopf, D. M., Seman, C. J., Silvers, L., Wyman, B., Zeng, Y., Adcroft, A., Dunne, J. P., Dussin, R., Guo, H., He, J., Held, I. M., Horowitz, L. W., Lin, P., Milly, P., Shevliakova, E., Stock, C., Winton, M., Wittenberg, A. T., Xie, Y., and Zhao, M. NOAA-GFDL GFDL-ESM4 model output prepared for CMIP6 CMIP piControl, 2018b. https://doi.org/10.22033/ESGF/CMIP6.8669.

Lachlan-Cope, T. and Connolley, W. Teleconnections between the tropical Pacific and the Amundsen-Bellinghausen Sea: role of the El Niño/Southern Oscillation. *Journal of Geophysical Research: Atmospheres*, 111(D23), 2006. https://doi.org/10.1029/2005JD006386.

Large, W. G. and Nurser, A. G. Chapter 5.1 Ocean surface water mass transformation. In *Ocean Circulation and Climate*, volume 77 of *International Geophysics*, pages 317–336. Academic Press, 2001. https://doi.org/10.1016/S0074-6142(01)80126-1.

Large, W. G., McWilliams, J. C., and Doney, S. C. Oceanic vertical mixing: a review and a model with a non-local boundary layer parameterization. *Reviews of Geophysics*, 32(4):363–403, 1994. https://doi.org/10.1029/94rg01872.

Large, W. G. and Yeager, S. G. Diurnal to decadal gobal forcing for ocean and sea-ice models: the data sets and flux climatologies. *NCAR Technical Note*, 2004. https://doi.org/10.5065/D6KK98Q6.

Lee, S. K., Park, W., Baringer, M. O., Gordon, A. L., Huber, B., and Liu, Y. Pacific origin of the abrupt increase in Indian Ocean heat content during the warming hiatus. *Nature Geoscience*, 8(6):445–449, 2015. https://doi.org/10.1038/NGEO2438.

Lengaigne, M., Hausmann, U., Madec, G., Menkes, C., Vialard, J., and Molines, J.-M. Mechanisms controlling warm water volume interannual variations in the equatorial Pacific: Diabatic versus adiabatic processes. *Climate Dynamics*, 38(5-6):1031–1046, 2012. https://doi.org/10.1007/s00382-011-1051-z.

Lenn, Y.-D. and Chereskin, T. K. Observations of Ekman currents in the Southern Ocean. *Journal of Physical Oceanography*, 39(3):768 – 779, 2009. https://doi.org/10.1175/2008JPO3943.1.

Levitus, S., Antonov, J. I., Boyer, T. P., Baranova, O. K., Garcia, H. E., Locarnini, R. A., Mishonov, A. V., Reagan, J. R., Seidov, D., Yarosh, E. S., and Zweng, M. M. World ocean heat content and thermosteric sea level change (0–2000 m), 1955–2010. *Geophysical Research Letters*, 39(10), 2012. https://doi.org/10.1029/2012GL051106.

Li, H., Xu, F., Zhou, W., Wang, D., Wright, J. S., Liu, Z., and Lin, Y. Development of a global gridded Argo data set with Barnes successive corrections. *Journal of Geophysical Research: Oceans*, 122(2):866–889, 2017. https://doi.org/10.1002/2016JC012285.

Li, Q., England, M. H., Hogg, A. M., Rintoul, S. R., and Morrison, A. K. Abyssal ocean overturning slowdown and warming driven by Antarctic meltwater. *Nature*, 615(7954):841–847, 2023. https://doi.org/10.1038/s41586-023-05762-w.

Li, X., Cai, W., Meehl, G. A., Chen, D., Yuan, X., Raphael, M., Holland, D. M., Ding, Q., Fogt, R. L., Markle, B. R., Wang, G., Bromwich, D. H., Turner, J., Xie, S.-P., Steig, E. J., Gille, S. T., Xiao, C., Wu, B., Lazzara, M. A., Chen, X., Stammerjohn, S., Holland, P. R., Holland, M. M., Cheng, X., Price, S. F., Wang, Z., Bitz, C. M., Shi, J., Gerber, E. P., Liang, X., Goosse, H., Yoo, C., Ding, M., Geng, L., Xin, M., Li, C., Dou, T., Liu, C., Sun, W., Wang, X., and Song, C. Tropical teleconnection impacts on Antarctic climate changes. *Nature Reviews Earth & Environment*, 2(10): 680–698, 2021. https://doi.org/10.1038/s43017-021-00204-5.

Lien, R.-C., Caldwell, D. R., Gregg, M. C., and Moum, J. N. Turbulence variability at the equator in the central Pacific at the beginning of the 1991—1993 El Niño. *Journal of Geophysical Research: Oceans*, 100(C4):6881–6898, 1995. https://doi.org/10.1029/94JC03312.

Liu, C., Köhl, A., Liu, Z., Wang, F., and Stammer, D. Deep-reaching thermocline mixing in the equatorial Pacific cold tongue. *Nature Communications*, 7:11576, 2016. https://doi.org/10.1038/ncomms11576.

Liu, W., Huang, B., Thorne, P. W., Banzon, V. F., Zhang, H.-M., Freeman, E., Lawrimore, J., Peterson, T. C., Smith, T. M., and Woodruff, S. D. Extended reconstructed sea surface temperature Version 4 (ERSST.v4): Part II: parametric and structural uncertainty estimations. *Journal of Climate*, 28(3):931–951, 2015. https://doi.org/10.1175/JCLI-D-14-00007.1.

Liu, W., Lu, J., Xie, S.-P., and Fedorov, A. Southern Ocean heat uptake, redistribution, and storage in a warming climate: the role of meridional overturning circulation. *Journal of Climate*, 31(12):4727–4743, 2018. https://doi.org/10.1175/JCLI-D-17-0761.1.

Liu, W., Fedorov, A. V., Xie, S. P., and Hu, S. Climate impacts of a weakened Atlantic Meridional Overturning Circulation in a warming climate. *Science Advances*, 6(26): 1–8, 2020. https://doi.org/10.1126/sciadv.aaz4876.

Liu, Z., Xing, X., Chen, Z., Lu, S., Wu, X., Li, H., Zhang, C., Cheng, L., Li, Z., Sun, C., Xu, J., Chen, D., and Chai, F. Twenty years of ocean observations with China Argo. *Acta Oceanologica Sinica*, 42(2):1–16, 2023. https://doi.org/10.1007/s13131-022-2076-3.

Locarnini, R. A., Mishonov, A. V., Antonov, J. I., Boyer, T. P., Garcia, H. E., Baranova, O. K., Zweng, M. M., Paver, C. R., Reagan, J. R., Johnson, D. R., et al. World Ocean Atlas 2013, volume 1: temperature. In S, L., editor, *NOAA Atlas NESDIS 73:40*, page 40 pp. US Government Printing Office, Washington D.C., 2013.

Loeb, N. G., Lyman, J. M., Johnson, G. C., Allan, R. P., Doelling, D. R., Wong, T., Soden, B. J., and Stephens, G. L. Observed changes in top-of-the-atmosphere radiation and upper-ocean heating consistent within uncertainty. *Nature Geoscience*, 5(2):110–113, 2012. https://doi.org/10.1038/ngeo1375.

Loeb, N. G., Mayer, M., Kato, S., Fasullo, J. T., Zuo, H., Senan, R., Lyman, J. M., Johnson, G. C., and Balmaseda, M. Evaluating twenty-year trends in Earth's energy flows from observations and reanalyses. *Journal of Geophysical Research: Atmospheres*, 127(12):e2022JD036686, 2022. https://doi.org/10.1029/2022JD036686.

Maher, N., England, M. H., Gupta, A. S., and Spence, P. Role of Pacific trade winds in driving ocean temperatures during the recent slowdown and projections under a wind trend reversal. *Climate Dynamics*, pages 1–16, 2017. https://doi.org/10.1007/s00382-017-3923-3.

Marshall, G. J. Trends in the Southern Annular Mode from Observations and Reanalyses. *Journal of Climate*, 16(24):4134 – 4143, 2003. https://doi.org/10.1175/1520-0442(2003)016<4134:TITSAM>2.0.CO;2.

Marshall, J., Scott, J. R., Armour, K. C., Campin, J. M., Kelley, M., and Romanou, A. The ocean's role in the transient response of climate to abrupt greenhouse gas forcing. *Climate Dynamics*, 44(7-8):2287–2299, 2015. https://doi.org/10.1007/s00382-014-2308-0.

Marshall, J., Scott, J. R., Romanou, A., Kelley, M., and Leboissetier, A. The dependence of the ocean's MOC on mesoscale eddy diffusivities: a model study. *Ocean Modelling*, 111:1–8, 2017. ISSN 1463-5003. https://doi.org/10.1016/j.ocemod.2017.01.001.

Martínez-Moreno, J., Hogg, A. M., England, M. H., Constantinou, N. C., Kiss, A. E., and Morrison, A. K. Global changes in oceanic mesoscale currents over the satellite altimetry record. *Nature Climate Change*, 11(5):397–403, 2021. ISSN 1758-6798. https://10.1038/s41558-021-01006-9.

Martinson, D. G., Stammerjohn, S. E., Iannuzzi, R. A., Smith, R. C., and Vernet, M. Western Antarctic Peninsula physical oceanography and spatio–temporal variability. *Deep Sea Research Part II: Topical Studies in Oceanography*, 55(18):1964–1987, 2008. https://doi.org/10.1016/j.dsr2.2008.04.038. Palmer, Antarctica Long Term Ecological Research.

McCarthy, G., Smeed, D., Johns, W., Frajka-Williams, E., Moat, B., Rayner, D., Baringer, M., Meinen, C., Collins, J., and Bryden, H. Measuring the Atlantic Meridional Overturning Circulation at 26°N. *Progress in Oceanography*, 130:91–111, 2015. https://doi.org/10.1016/j.pocean.2014.10.006.

McDougall, T. J. Potential enthalpy: A conservative oceanic variable for evaluating heat content and heat fluxes. *J. Phys. Oceanogr.*, 33(5):945–963, 2003. https://doi.org/10.1175/1520-0485(2003)033<0945:PEACOV>2.0.CO;2.

McDougall, T. J. and Barker, P. M. Getting started with TEOS-10 and the Gibbs Seawater (GSW) oceanographic toolbox. *SCOR/IAPSO WG*, 127:1–28, 2011.

McGregor, S., Timmermann, A., Schneider, N., Stuecker, M. F., and England, M. H. The effect of the South Pacific convergence zone on the termination of El Niño events and the meridional asymmetry of ENSO. *Journal of Climate*, 25(16):5566–5586, 2012. https://doi.org/10.1175/JCLI-D-11-00332.1.

McGregor, S., Ramesh, N., Spence, P., England, M. H., McPhaden, M. J., and Santoso, A. Meridional movement of wind anomalies during ENSO events and their role in event termination. *Geophysical Research Letters*, 40(4):749–754, 2013. https://doi.org/10.1002/grl.50136.

McGregor, S., Spence, P., Schwarzkopf, F. U., England, M. H., Santoso, A., Kessler, W. S., Timmermann, A., and Böning, C. W. ENSO-driven interhemispheric Pacific mass transports. *Journal of Geophysical Research: Oceans*, 119(9):6221–6237, 2014. https://doi.org/10.1002/2014JC010286.

McGregor, S., Timmermann, A., Jin, F.-F., and Kessler, W. S. Charging El Niño with off-equatorial westerly wind events. *Climate Dynamics*, 47(3):1111–1125, 2016. https://doi.org/10.1007/s00382-015-2891-8.

McGregor, S., Sen Gupta, A., Dommenget, D., Lee, T., McPhaden, M. J., and Kessler, W. S. Factors influencing the skill of synthesized satellite wind products in the tropical Pacific. *Journal of Geophysical Research: Oceans*, 122(2):1072–1089, 2017. https://doi.org/10.1002/2016JC012340.

McGregor, S., Cassou, C., Kosaka, Y., and Phillips, A. S. Projected ENSO teleconnection changes in CMIP6. *Geophysical Research Letters*, 49(11):e2021GL097511, 2022. https://doi.org/10.1029/2021GL097511.

McPhaden, M. J. A 21st century shift in the relationship between ENSO SST and warm water volume anomalies. *Geophysical Research Letters*, 39(9), 2012. https://doi.org/10.1029/2012GL051826.

McWhorter, J. K., Halloran, P. R., Roff, G., Skirving, W. J., Perry, C. T., and Mumby, P. J. The importance of 1.5°C warming for the Great Barrier Reef. *Global Change Biology*, 28(4):1332–1341, 2022. https://doi.org/10.1111/gcb.15994.

Meehl, G. A., Arblaster, J. M., Fasullo, J. T., Hu, A., and Trenberth, K. E. Model-based evidence of deep-ocean heat uptake during surface-temperature hiatus periods. *Nature Climate Change*, 1:360, sep 2011. https://doi.org/10.1038/nclimate1229.

Meehl, G. A., Hu, A., and Teng, H. Initialized decadal prediction for transition to positive phase of the Interdecadal Pacific Oscillation. *Nature Communications*, 7(1): 11718, 2016. https://doi.org/10.1038/ncomms11718.

Meinen, C. S. and McPhaden, M. J. Observations of warm water volume changes in the equatorial Pacific and their relationship to El Niño and La Niña. *Journal of Climate*, 13(20):3551–3559, 2000. https://doi.org/10.1175/1520-0442(2000)013<3551:OOWWVC>2.0.CO;2.

Meinen, C. S. and McPhaden, M. J. Interannual variability in warm water volume transports in the equatorial Pacific during 1993–99. *Journal of Physical Oceanography*, 31(5):1324–1345, 2001. https://doi.org/10.1175/1520-0485(2001)031<1324:IVIWWV>2.0.CO;2.

Meinen, C. S., McPhaden, M. J., and Johnson, G. C. Vertical velocities and transports in the equatorial Pacific during 1993–99. *Journal of physical oceanography*, 31(11):3230–3248, 2001. https://doi.org/10.1175/1520-0485(2001)031<3230:VVATIT>2.0.CO;2.

Menkes, C. E., Lengaigne, M., Vialard, J., Puy, M., Marchesiello, P., Cravatte, S., and Cambon, G. About the role of westerly wind events in the possible development of an El Niño in 2014. *Geophysical Research Letters*, 41(18):6476–6483, 2014. https://doi.org/10.1002/2014GL061186.

Meyssignac, B., Boyer, T., Zhao, Z., Hakuba, M. Z., Landerer, F. W., Stammer, D., Köhl, A., Kato, S., L'Ecuyer, T., Ablain, M., Abraham, J. P., Blazquez, A., Cazenave, A., Church, J. A., Cowley, R., Cheng, L., Domingues, C. M., Giglio, D., Gouretski, V., Ishii, M., Johnson, G. C., Killick, R. E., Legler, D., Llovel, W., Lyman, J., Palmer, M. D., Piotrowicz, S., Purkey, S. G., Roemmich, D., Roca, R., Savita, A., Schuckmann, K. v., Speich, S., Stephens, G., Wang, G., Wijffels, S. E., and Zilberman, N. Measuring global ocean heat content to estimate the Earth energy imbalance. *Frontiers in Marine Science*, 6:432, 2019. https://doi.org/10.3389/fmars.2019.00432.

Morice, C. P., Kennedy, J. J., Rayner, N. A., Winn, J. P., Hogan, E., Killick, R. E., Dunn, R. J. H., Osborn, T. J., Jones, P. D., and Simpson, I. R. An updated assessment of near-surface temperature change from 1850: the HadCRUT5 data set. *Journal of Geophysical Research: Atmospheres*, 126(3):e2019JD032361, 2021. https://doi.org/10.1029/2019JD032361.

Morice, C. P., Kennedy, J. J., Rayner, N. A., and Jones, P. D. Quantifying uncertainties in global and regional temperature change using an ensemble of observational estimates: The HadCRUT4 data set. *Journal of Geophysical Research: Atmospheres*, 117(D8), 2012. https://doi.org/10.1029/2011JD017187.

Morrison, A. K., Frölicher, T. L., and Sarmiento, J. L. Upwelling in the Southern Ocean. *Phys. Today*, 68:27–32, 2015. https://doi.org/10.1063/PT.3.2654".

Morrison, A. K., Griffies, S. M., Winton, M., Anderson, W. G., and Sarmiento, J. L. Mechanisms of Southern Ocean heat uptake and transport in a global eddying climate model. *Journal of Climate*, 29(6):2059 – 2075, 2016. https://doi.org/10.1175/JCLI-D-15-0579.1.

Morrison, A. K., England, M. H., Hogg, A. M., and Kiss, A. E. Weddell Sea Control of Ocean Temperature Variability on the Western Antarctic Peninsula. *Geophysical Research Letters*, 50(15):e2023GL103018, 2023. https://doi.org/10.1029/2023GL103018.

Moum, J. N., Perlin, A., Nash, J. D., and McPhaden, M. J. Seasonal sea surface cooling in the equatorial Pacific cold tongue controlled by ocean mixing. *Nature*, 500(7460): 64, 2013. https://doi.org/10.1038/nature12363.

Nakayama, Y., Menemenlis, D., Zhang, H., Schodlok, M., and Rignot, E. Origin of Circumpolar Deep Water intruding onto the Amundsen and Bellingshausen Sea continental shelves. *Nature Communications*, 9(1):3403, 2018. https://doi.org/10.1038/s41467-018-05813-1.

Naughten, K. A., Holland, P. R., Dutrieux, P., Kimura, S., Bett, D. T., and Jenkins, A. Simulated twentieth-century ocean warming in the Amundsen Sea, West Antarctica. *Geophysical Research Letters*, 49(5):e2021GL094566, 2022. https://doi.org/10.1029/2021GL094566.

Neme, J., England, M. H., and McC. Hogg, A. Projected changes of surface winds over the Antarctic continental margin. *Geophysical Research Letters*, 49(16): e2022GL098820, 2022. https://doi.org/10.1029/2022GL098820.

Neske, S. and McGregor, S. Understanding the warm water volume precursor of ENSO events and its interdecadal variation. *Geophysical Research Letters*, 45(3):1577–1585, 2018. https://doi.org/10.1002/2017GL076439.

Oelerich, R., Heywood, K. J., Damerell, G. M., and Thompson, A. F. Wind-induced variability of warm water on the southern Bellingshausen Sea continental shelf. *Journal of Geophysical Research: Oceans*, 127(11):e2022JC018636, 2022. https://doi.org/10.1029/2022JC018636.

Okumura, Y. M. and Deser, C. Asymmetry in the duration of El Niño and La Niña. *Journal of Climate*, 23(21):5826–5843, 2010. https://doi.org/10.1175/2010JCLI3592.1.

Paolo, F. S., Padman, L., Fricker, H. A., Adusumilli, S., Howard, S., and Siegfried, M. R. Response of Pacific-sector Antarctic ice shelves to the El Niño/Southern Oscillation. *Nature Geoscience*, 11:121–126, 2018. https://doi.org/10.1038/s41561-017-0033-0.

Paolo, F. S., Fricker, H. A., and Padman, L. Volume loss from Antarctic ice shelves is accelerating. *Science*, 348(6232):327–331, 2015. https://doi.org/10.1126/science.aaa0940.

Park, S. and Shin, J. SNU SAM0-UNICON model output prepared for CMIP6 CMIP historical, 2019a. https://doi.org/10.22033/ESGF/CMIP6.7789.

Park, S. and Shin, J. SNU SAM0-UNICON model output prepared for CMIP6 CMIP piControl, 2019b. https://doi.org/10.22033/ESGF/CMIP6.7791.

Pham, H. T., Smyth, W. D., Sarkar, S., and Moum, J. N. Seasonality of deep cycle turbulence in the eastern equatorial Pacific. *Journal of Physical Oceanography*, 47 (9):2189–2209, 2017. https://doi.org/10.1175/JPO-D-17-0008.1.

Power, S., Casey, T., Folland, C., Colman, A., and Mehta, V. Inter-decadal modulation of the impact of ENSO on Australia. *Climate Dynamics*, 15(5):319–324, 1999. https://doi.org/10.1007/s003820050284.

Pritchard, H. D., Ligtenberg, S. R. M., Fricker, H. A., Vaughan, D. G., van den Broeke, M. R., and Padman, L. Antarctic ice-sheet loss driven by basal melting of ice shelves. *Nature*, 484(7395):502–505, 2012. https://doi.org/10.1038/nature10968.

Purich, A. and England, M. H. Historical and future projected warming of Antarctic Shelf Bottom Water in CMIP6 models. *Geophysical Research Letters*, 48(10): e2021GL092752, 2021. https://doi.org/10.1029/2021GL092752.

Purkey, S. G. and Johnson, G. C. Warming of global abyssal and deep Southern Ocean waters between the 1990s and 2000s: contributions to global heat and sea level rise budgets. *Journal of Climate*, 23(23):6336 – 6351, 2010. https://doi.org/10.1175/2010JCLI3682.1.

Rahaman, W., Chatterjee, S., Ejaz, T., and Thamban, M. Increased influence of ENSO on Antarctic temperature since the Industrial Era. *Scientific Reports*, 9(1):6006, 2019. https://doi.org/10.1038/s41598-019-42499-x.

Raphael, M. N., Marshall, G. J., Turner, J., Fogt, R. L., Schneider, D., Dixon, D. A., Hosking, J. S., Jones, J. M., and Hobbs, W. R. The Amundsen Sea Low: variability, change, and impact on Antarctic climate. *Bulletin of the American Meteorological Society*, 97(1):111 – 121, 2016. https://doi.org/10.1175/BAMS-D-14-00018.1.

Rathore, S., Bindoff, N. L., Phillips, H. E., and Feng, M. Recent hemispheric asymmetry in global ocean warming induced by climate change and internal variability. *Nature Communications*, 11(1):2008, 2020. https://doi.org/10.1038/s41467-020-15754-3.

Rayner, N., Parker, D. E., Horton, E., Folland, C., Alexander, L., Rowell, D., Kent, E., and Kaplan, A. Global analyses of sea surface temperature, sea ice, and night marine air temperature since the late nineteenth century. *Journal of Geophysical Research: Atmospheres*, 108(D14), 2003. https://doi.org/10.1029/2002JD002670.

Redi, M. H. Oceanic isopycnal mixing by coordinate rotation. *Journal of Physical Oceanography*, 12(10):1154–1158, 1982. https://doi.org/10.1175/1520-0485(1982)012<1154:OIMBCR>2.0.CO;2.

Reynolds, R. W., Smith, T. M., Liu, C., Chelton, D. B., Casey, K. S., and Schlax, M. G. Daily high-resolution-blended analyses for sea surface temperature. *Journal of Climate*, 20(22):5473–5496, 2007. https://doi.org/10.1175/2007JCLI1824.1.

Rhein, M., Rintoul, S., Aoki, S., Campos, E., Chambers, D., Feely, R., and Wang, F. Observations: Ocean. In: Climate Change 2013: The Physical Science Basis. Contribution of Working Group I to the Fifth Assessment Report of the Intergovernmental Panel on Climate Change. *Fifth Assessment Report of the Intergovernmental Panel on Climate Change*, pages 255–315, 01 2013.

Rignot, E., Mouginot, J., Scheuchl, B., van den Broeke, M., van Wessem, M. J., and Morlighem, M. Four decades of Antarctic Ice Sheet mass balance from 1979–2017. *Proceedings of the National Academy of Sciences*, 116(4):1095–1103, 2019. https://doi.org/10.1073/pnas.1812883116.

Rintoul, S. R. and Naveira Garabato, A. C. Chapter 18 - dynamics of the southern ocean circulation. In Siedler, G., Griffies, S. M., Gould, J., and Church, J. A., editors, *Ocean Circulation and Climate*, volume 103 of *International Geophysics*, pages 471–492. Academic Press, 2013. https://doi.org/10.1016/B978-0-12-391851-2.00018-0.

Roemmich, D. and Gilson, J. The global ocean imprint of ENSO. *Geophysical Research Letters*, 38(13), 2011. https://doi.org/10.1029/2011GL047992.

Roemmich, D., Church, J., Gilson, J., Monselesan, D., Sutton, P., and Wijffels, S. Unabated planetary warming and its ocean structure since 2006. *Nature Climate Change*, 5(3):240–245, 2015. https://doi.org/10.1038/nclimate2513.

Rong, X. CAMS CAMS_CSM1.0 model output prepared for CMIP6 CMIP historical, 2019a. https://doi.org/10.22033/ESGF/CMIP6.9754.

Rong, X. CAMS CAMS_CSM1.0 model output prepared for CMIP6 CMIP piControl, 2019b. https://doi.org/10.22033/ESGF/CMIP6.9797.

Rong, X. CAMS CAMS-CSM1.0 model output prepared for CMIP6 ScenarioMIP, 2019c. https://doi.org/10.22033/ESGF/CMIP6.11004.

Roquet, F., Wunsch, C., Forget, G., Heimbach, P., Guinet, C., Reverdin, G., Charrassin, J.-B., Bailleul, F., Costa, D. P., Huckstadt, L. A., Goetz, K. T., Kovacs, K. M., Lydersen, C., Biuw, M., Nøst, O. A., Bornemann, H., Ploetz, J., Bester, M. N., McIntyre, T., Muelbert, M. C., Hindell, M. A., McMahon, C. R., Williams, G., Harcourt, R., Field, I. C., Chafik, L., Nicholls, K. W., Boehme, L., and Fedak, M. A. Estimates of the Southern Ocean general circulation improved by animal-borne instruments. *Geophysical Research Letters*, 40(23):6176–6180, 2013. https://doi.org/10.1002/2013GL058304.

Roquet, F., Williams, G., Hindell, M. A., Harcourt, R., McMahon, C., Guinet, C., Charrassin, J.-B., Reverdin, G., Boehme, L., Lovell, P., and Fedak, M. A Southern Indian Ocean database of hydrographic profiles obtained with instrumented elephant seals. *Scientific Data*, 1(1):140028, 2014. https://doi.org/10.1038/sdata.2014.28.

Saenko, O. A., Yang, D., and Gregory, J. M. Impact of mesoscale eddy transfer on heat uptake in an eddy-parameterizing ocean model. *Journal of Climate*, 31(20):8589 – 8606, 2018. https://doi.org/10.1175/JCLI-D-18-0186.1.

Saji, N. H., Goswami, B. N., Vinayachandran, P. N., and Yamagata, T. A dipole mode in the tropical Indian Ocean. *Nature*, 401(6751):360–363, 1999. https://doi.org/10.1038/43854.

Scambos, T., Bell, R., Alley, R., Anandakrishnan, S., Bromwich, D., Brunt, K., Christianson, K., Creyts, T., Das, S., DeConto, R., Dutrieux, P., Fricker, H., Holland, D., MacGregor, J., Medley, B., Nicolas, J., Pollard, D., Siegfried, M., Smith, A., Steig, E., Trusel, L., Vaughan, D., and Yager, P. How much, how fast?: A science review and outlook for research on the instability of Antarctica's Thwaites Glacier in the 21st century. *Global and Planetary Change*, 153:16–34, 2017. https://doi.org/10.1016/j.gloplacha.2017.04.008.

Schmidtko, S., Heywood, K. J., Thompson, A. F., and Aoki, S. Multidecadal warming of Antarctic waters. *Science*, 346(6214):1227–1231, 2014. https://doi.org/10.1126/science.1256117.

Schott, F. A., McCreary Jr, J. P., and Johnson, G. C. Shallow overturning circulations of the tropical-subtropical oceans. *Earth's Climate*, 147:261–304, 2004. https://doi.org/10.1029/147GM15.

Seferian, R. CNRM-CERFACS CNRM-ESM2-1 model output prepared for CMIP6 CMIP historical, 2018a. https://doi.org/10.22033/ESGF/CMIP6.4068.

Seferian, R. CNRM-CERFACS CNRM-ESM2-1 model output prepared for CMIP6 CMIP piControl, 2018b. https://doi.org/10.22033/ESGF/CMIP6.4165.

Seland, Ø., Bentsen, M., Oliviè, D. J. L., Toniazzo, T., Gjermundsen, A., Graff, L. S., Debernard, J. B., Gupta, A. K., He, Y., Kirkevåg, A., Schwinger, J., Tjiputra, J., Aas, K. S., Bethke, I., Fan, Y., Griesfeller, J., Grini, A., Guo, C., Ilicak, M., Karset, I. H. H., Landgren, O. A., Liakka, J., Moseid, K. O., Nummelin, A., Spensberger, C., Tang, H., Zhang, Z., Heinze, C., Iversen, T., and Schulz, M. NCC NorESM2-LM model output prepared for CMIP6 CMIP historical, 2019a. https://doi.org/10.22033/ESGF/CMIP6.8036.

Seland, Ø., Bentsen, M., Oliviè, D. J. L., Toniazzo, T., Gjermundsen, A., Graff, L. S., Debernard, J. B., Gupta, A. K., He, Y., Kirkevåg, A., Schwinger, J., Tjiputra, J., Aas, K. S., Bethke, I., Fan, Y., Griesfeller, J., Grini, A., Guo, C., Ilicak, M., Karset, I. H. H., Landgren, O. A., Liakka, J., Moseid, K. O., Nummelin, A., Spensberger, C., Tang, H., Zhang, Z., Heinze, C., Iversen, T., and Schulz, M. NCC NorESM2-LM model output prepared for CMIP6 CMIP piControl, 2019b. https://doi.org/10.22033/ESGF/CMIP6.8217.

Seland, Ø., Bentsen, M., Oliviè, D. J. L., Toniazzo, T., Gjermundsen, A., Graff, L. S., Debernard, J. B., Gupta, A. K., He, Y., Kirkevåg, A., Schwinger, J., Tjiputra, J., Aas, K. S., Bethke, I., Fan, Y., Griesfeller, J., Grini, A., Guo, C., Ilicak, M., Karset, I. H. H., Landgren, O. A., Liakka, J., Moseid, K. O., Nummelin, A., Spensberger, C., Tang, H., Zhang, Z., Heinze, C., Iversen, T., and Schulz, M. NCC NorESM2-LM model output prepared for CMIP6 CMIP, 2019c. https://doi.org/10.22033/ESGF/CMIP6.502.

Shepherd, A., Ivins, E., Rignot, E., Smith, B., van den Broeke, M., Velicogna, I., Whitehouse, P., Briggs, K., Joughin, I., Krinner, G., Nowicki, S., Payne, T., Scambos, T., Schlegel, N., A, G., Agosta, C., Ahlstrøm, A., Babonis, G., Barletta, V., Blazquez, A., Bonin, J., Csatho, B., Cullather, R., Felikson, D., Fettweis, X., Forsberg, R., Gallee, H., Gardner, A., Gilbert, L., Groh, A., Gunter, B., Hanna, E., Harig, C., Helm, V., Horvath, A., Horwath, M., Khan, S., Kjeldsen, K. K., Konrad, H., Langen, P., Lecavalier, B., Loomis, B., Luthcke, S., McMillan, M., Melini, D., Mernild, S., Mohajerani, Y., Moore, P., Mouginot, J., Moyano, G., Muir, A., Nagler, T., Nield, G., Nilsson, J., Noel, B., Otosaka, I., Pattle, M. E., Peltier, W. R., Pie, N., Rietbroek, R., Rott, H., Sandberg-Sørensen, L., Sasgen, I., Save, H., Scheuchl, B., Schrama, E., Schröder, L., Seo, K.-W., Simonsen, S., Slater, T., Spada, G., Sutterley, T., Talpe, M., Tarasov, L., van de Berg, W. J., van der Wal, W., van Wessem, M., Vishwakarma, B. D., Wiese, D., Wouters, B., and Team, T. I. Mass balance of the Antarctic Ice Sheet from 1992 to 2017. *Nature*, 558(7709):219–222, 2018. https://doi.org/10.1038/s41586-018-0179-y.

Shi, J.-R., Xie, S.-P., and Talley, L. D. Evolving Relative Importance of the Southern Ocean and North Atlantic in Anthropogenic Ocean Heat Uptake. *Journal of Climate*, 31(18):7459 – 7479, 2018. https://doi.org/10.1175/JCLI-D-18-0170.1.

Shi, J.-R., Talley, L. D., Xie, S.-P., Peng, Q., and Liu, W. Ocean warming and accelerating Southern Ocean zonal flow. *Nature Climate Change*, 11(12):1090–1097, 2021. https://doi.org/10.1038/s41558-021-01212-5.

Shinoda, T., Han, W., Metzger, E. J., and Hurlburt, H. E. Seasonal variation of the Indonesian Throughflow in Makassar Strait. *Journal of Physical Oceanography*, 42 (7):1099–1123, 2012. https://doi.org/10.1175/JPO-D-11-0120.1.

Silvano, A., Holland, P. R., Naughten, K. A., Dragomir, O., Dutrieux, P., Jenkins, A., Si, Y., Stewart, A. L., Peña Molino, B., Janzing, G. W., Dotto, T. S., and Naveira Garabato, A. C. Baroclinic Ocean Response to Climate Forcing Regulates Decadal Variability of Ice-Shelf Melting in the Amundsen Sea. *Geophysical Research Letters*, 49(24):e2022GL100646, 2022. https://doi.org/10.1029/2022GL100646.

Smith, S. R., Brolley, J., O'Brien, J. J., and Tartaglione, C. A. ENSO's impact on regional US hurricane activity. *Journal of Climate*, 20(7):1404–1414, 2007. https://doi.org/10.1175/JCLI4063.1.

Smith, T. M. and Reynolds, R. W. Extended reconstruction of global sea surface temperatures based on COADS data (1854–1997). *Journal of Climate*, 16(10):1495–1510, 2003. https://doi.org/10.1175/1520-0442-16.10.1495.

Smyth, W. D. and Moum, J. N. Marginal instability and deep cycle turbulence in the eastern equatorial Pacific Ocean. *Geophysical Research Letters*, 40(23):6181–6185, 2013. https://doi.org/10.1002/2013GL058403.

Spence, P., Griffies, S. M., England, M. H., Hogg, A. M., Saenko, O. A., and Jourdain, N. C. Rapid subsurface warming and circulation changes of Antarctic coastal waters by poleward shifting winds. *Geophysical Research Letters*, 41(13):4601–4610, 2014. https://doi.org/10.1002/2014GL060613.

Spence, P., Holmes, R. M., Hogg, A. M., Griffies, S. M., Stewart, K. D., and England, M. H. Localized rapid warming of West Antarctic subsurface waters by remote winds. *Nature Climate Change*, 7(8):595, 2017. https://doi.org/10.1038/nclimate3335.

Sprintall, J. and Révelard, A. The Indonesian Throughflow response to Indo-Pacific climate variability. *Journal of Geophysical Research: Oceans*, 119(2):1161–1175, 2014. https://doi.org/10.1002/2013JC009533.

Stewart, A. L. and Thompson, A. F. Eddy-mediated transport of warm Circumpolar Deep Water across the Antarctic Shelf Break. *Geophysical Research Letters*, 42(2): 432–440, 2015. https://doi.org/10.1002/2014GL062281.

Stewart, K. and Hogg, A. Southern Ocean heat and momentum uptake are sensitive to the vertical resolution at the ocean surface. *Ocean Modelling*, 143:101456, 2019. https://doi.org/10.1016/j.ocemod.2019.101456.

Stewart, K., Hogg, A. M., Griffies, S., Heerdegen, A., Ward, M., Spence, P., and England, M. Vertical resolution of baroclinic modes in global ocean models. *Ocean Modelling*, 113:50–65, 2017. https://doi.org/10.1016/j.ocemod.2017.03.012.

Stewart, K., Kim, W., Urakawa, S., Hogg, A., Yeager, S., Tsujino, H., Nakano, H., Kiss, A., and Danabasoglu, G. JRA55-do-based repeat year forcing datasets for driving ocean–sea-ice models. *Ocean Modelling*, 147:101557, 2020. https://doi.org/10.1016/j.ocemod.2019.101557.

Stouffer, R. U of Arizona MCM-UA-1-0 model output prepared for CMIP6 CMIP, 2019a. https://doi.org/10.22033/ESGF/CMIP6.2421.

Stouffer, R. UA MCM-UA-1-0 model output prepared for CMIP6 CMIP historical, 2019b. https://doi.org/10.22033/ESGF/CMIP6.8888.

Stouffer, R. UA MCM-UA-1-0 model output prepared for CMIP6 CMIP piControl, 2019c. https://doi.org/10.22033/ESGF/CMIP6.8890.

Stuecker, M. F., Timmermann, A., Jin, F.-F., McGregor, S., and Ren, H.-L. A combination mode of the annual cycle and the El Niño/Southern Oscillation. *Nature Geoscience*, 6(7):540, 2013. https://doi.org/10.1175/JCLI-D-14-00225.1.

Stuecker, M. F., Jin, F.-F., Timmermann, A., and McGregor, S. Combination mode dynamics of the anomalous Northwest Pacific Anticyclone. *Journal of Climate*, 28 (3):1093–1111, 2015. https://doi.org/10.1038/ngeo1826.

Suarez, M. J. and Schopf, P. S. A delayed action oscillator for ENSO. *Journal of the Atmospheric Sciences*, 45(21):3283–3287, 11 1988. https://doi.org/10.1175/1520-0469(1988)045<3283:ADAOFE>2.0.CO;2.

Swart, N. C., Cole, J. N., Kharin, V. V., Lazare, M., Scinocca, J. F., Gillett, N. P., Anstey, J., Arora, V., Christian, J. R., Jiao, Y., Lee, W. G., Majaess, F., Saenko, O. A., Seiler, C., Seinen, C., Shao, A., Solheim, L., von Salzen, K., Yang, D., Winter, B., and Sigmond, M. CCCma CanESM5-CanOE model output prepared for CMIP6 CMIP historical, 2019a. https://doi.org/10.22033/ESGF/CMIP6.10260.

Swart, N. C., Cole, J. N., Kharin, V. V., Lazare, M., Scinocca, J. F., Gillett, N. P., Anstey, J., Arora, V., Christian, J. R., Jiao, Y., Lee, W. G., Majaess, F., Saenko, O. A., Seiler, C., Seinen, C., Shao, A., Solheim, L., von Salzen, K., Yang, D., Winter, B., and Sigmond, M. CCCma CanESM5-CanOE model output prepared for CMIP6 CMIP piControl, 2019b. https://doi.org/10.22033/ESGF/CMIP6.10266.

Swart, N. C., Cole, J. N., Kharin, V. V., Lazare, M., Scinocca, J. F., Gillett, N. P., Anstey, J., Arora, V., Christian, J. R., Jiao, Y., Lee, W. G., Majaess, F., Saenko, O. A., Seiler, C., Seinen, C., Shao, A., Solheim, L., von Salzen, K., Yang, D., Winter, B., and Sigmond, M. CCCma CanESM5-CanOE model output prepared for CMIP6 ScenarioMIP ssp585, 2019c. https://doi.org/10.22033/ESGF/CMIP6.10276.

Talley, L. D., Pickard, G. L., Emery, W. J., and Swift, J. H. *Descriptive Physical Oceanography - An Introduction*, chapter 10, pages 303–362. ELSEVIER, 32 Jamestown Road, London NW1 7BY, UK, 6 edition, 7 2011.

Tamsitt, V., England, M. H., Rintoul, S. R., and Morrison, A. K. Residence time and transformation of warm Circumpolar Deep Water on the Antarctic continental shelf. *Geophysical Research Letters*, 48(20), 2021. https://doi.org/10.1029/2021GL096092.

Tang, Y., Rumbold, S., Ellis, R., Kelley, D., Mulcahy, J., Sellar, A., Walton, J., and Jones, C. MOHC UKESM1.0-LL model output prepared for CMIP6 CMIP historical, 2019a. https://doi.org/10.22033/ESGF/CMIP6.6113.

Tang, Y., Rumbold, S., Ellis, R., Kelley, D., Mulcahy, J., Sellar, A., Walton, J., and Jones, C. MOHC UKESM1.0-LL model output prepared for CMIP6 CMIP piControl, 2019b. https://doi.org/10.22033/ESGF/CMIP6.6298.

Thompson, A. F., Stewart, A. L., Spence, P., and Heywood, K. J. The Antarctic Slope Current in a Changing Climate. *Reviews of Geophysics*, 56(4):741–770, 2018. https://doi.org/10.1029/2018RG000624.

Timmermann, A., An, S.-I., Kug, J.-S., Jin, F.-F., Cai, W., Capotondi, A., Cobb, K., Lengaigne, M., McPhaden, M. J., Stuecker, M. F., Stein, K., Wittenberg, A. T., Yun, K.-S., Bayr, T., Chen, H.-C., Chikamoto, Y., Dewitte, B., Dommenget, D., Grothe, P., Guilyardi, E., Ham, Y.-G., Hayashi, M., Ineson, S., Kang, D., Kim, S., Kim, W., Lee, J.-Y., Li, T., Luo, J.-J., McGregor, S., Planton, Y., Power, S., Rashid, H., Ren, H.-L., Santoso, A., Takahashi, K., Todd, A., Wang, G., Wang, G., Xie, R., Yang, W.-H., Yeh, S.-W., Yoon, J., Zeller, E., and Zhang, X. El Niño–Southern Oscillation complexity. *Nature*, 559(7715):535–545, 2018. https://doi.org/10.1038/s41586-018-0252-6.

Todd, A., Zanna, L., Couldrey, M., Gregory, J., Wu, Q., Church, J. A., Farneti, R., Navarro-Labastida, R., Lyu, K., Saenko, O., Yang, D., and Zhang, X. Ocean-Only FAFMIP: understanding regional patterns of ocean heat content and dynamic sea level change. *Journal of Advances in Modeling Earth Systems*, 12(8):e2019MS002027, 2020. https://doi.org/10.1029/2019MS002027.

Treasure, A., Roquet, F., Ansorge, I., Bester, M., Boehme, L., Bornemann, H., Charrassin, J.-B., Chevallier, D., Costa, D., Fedak, M., Guinet, C., Hammill, M., Harcourt, R., Hindell, M., Kovacs, K., Lea, M.-A., Lovell, P., Lowther, A., Lydersen, C., McIntyre, T., McMahon, C., Muelbert, M., Nicholls, K., Picard, B., Reverdin, G., Trites, A., Williams, G., and de Bruyn, P. Marine mammals exploring the oceans pole to pole: a review of the MEOP consortium. *Oceanography*, 2017.

Trenberth, K., Jones, P., Ambenje, P., Bojariu, R., Easterling, D., Klein Tank, A., Parker, D., Rahimzadeh, F., Renwick, J., Rusticucci, M., et al. Observations: surface and atmospheric climate change. Chapter 3. *Climate change*, pages 235–336, 2007.

Trenberth, K. E. and Fasullo, J. T. Applications of an updated atmospheric energetics formulation. *Journal of Climate*, 31(16):6263 – 6279, 2018. https://doi.org/10.1175/JCLI-D-17-0838.1.

Trenberth, K. E. and Zhang, Y. Observed interhemispheric meridional heat transports and the role of the Indonesian Throughflow in the Pacific Ocean. *Journal of Climate*, 32(24):8523 – 8536, 2019. https://doi.org/10.1175/JCLI-D-19-0465.1.

Trenberth, K. E., Caron, J. M., Stepaniak, D. P., and Worley, S. Evolution of El Niño—Southern Oscillation and global atmospheric surface temperatures. *Journal of Geophysical Research: Atmospheres*, 107(D8):AAC 5–1–AAC 5–17, 2002. https://doi.org/10.1029/2000JD000298.

Trenberth, K. E., Zhang, Y., Fasullo, J. T., and Cheng, L. Observation-based estimates of global and basin ocean meridional heat transport time series. *Journal of Climate*, 32(14):4567 – 4583, 2019. https://doi.org/10.1175/JCLI-D-18-0872.1.

Tsujino, H., Urakawa, L. S., Griffies, S. M., Danabasoglu, G., Adcroft, A. J., Amaral, A. E., Arsouze, T., Bentsen, M., Bernardello, R., Böning, C. W., Bozec, A., Chassignet, E. P., Danilov, S., Dussin, R., Exarchou, E., Fogli, P. G., Fox-Kemper, B., Guo, C., Ilicak, M., Iovino, D., Kim, W. M., Koldunov, N., Lapin, V., Li, Y., Lin, P., Lindsay, K., Liu, H., Long, M. C., Komuro, Y., Marsland, S. J., Masina, S., Nummelin, A., Rieck, J. K., Ruprich-Robert, Y., Scheinert, M., Sicardi, V., Sidorenko, D., Suzuki, T., Tatebe, H., Wang, Q., Yeager, S. G., and Yu, Z. Evaluation of global ocean–sea-ice model simulations based on the experimental protocols of the Ocean Model Intercomparison Project phase 2 (OMIP-2). *Geoscientific Model Development*, 13(8):3643–3708, 2020. https://doi.org/10.5194/gmd-13-3643-2020.

Tsujino, H., Urakawa, S., Nakano, H., Small, R. J., Kim, W. M., Yeager, S. G., Danabasoglu, G., Suzuki, T., Bamber, J. L., Bentsen, M., et al. JRA-55 based surface dataset for driving ocean–sea-ice models (JRA55-do). *Ocean Modelling*, 130:79–139, 2018. https://doi.org/10.1016/j.ocemod.2018.07.002.

Turner, J. The El Niño–Southern Oscillation and Antarctica. *International Journal of Climatology*, 24(1):1–31, 2004. https://doi.org/10.1002/joc.965.

Verdy, A. and Mazloff, M. R. A data assimilating model for estimating Southern Ocean biogeochemistry. *Journal of Geophysical Research: Oceans*, 122(9):6968–6988, 2017. https://doi.org/10.1002/2016JC012650.

Voldoire, A. CNRM-CERFACS CNRM-ESM2-1 model output prepared for CMIP6 ScenarioMIP ssp585, 2019. https://doi.org/10.22033/ESGF/CMIP6.4226.

von Schuckmann, K., Cheng, L., Palmer, M. D., Hansen, J., Tassone, C., Aich, V., Adusumilli, S., Beltrami, H., Boyer, T., Cuesta-Valero, F. J., Desbruyères, D., Domingues, C., García-García, A., Gentine, P., Gilson, J., Gorfer, M., Haimberger, L., Ishii, M., Johnson, G. C., Killick, R., King, B. A., Kirchengast, G., Kolodziejczyk, N., Lyman, J., Marzeion, B., Mayer, M., Monier, M., Monselesan, D. P., Purkey, S., Roemmich, D., Schweiger, A., Seneviratne, S. I., Shepherd, A., Slater, D. A., Steiner, A. K., Straneo, F., Timmermans, M.-L., and Wijffels, S. E. Heat stored in the Earth system: where does the energy go? *Earth System Science Data*, 12(3):2013–2041, 2020. https://doi.org/10.5194/essd-12-2013-2020.

Walin, G. On the relation between sea-surface heat flow and thermal circulation in the ocean. *Tellus*, 34(2):187–195, 1982. https://doi.org/10.3402/tellusa.v34i2.10801.

Walker, C. and Gardner, A. Rapid drawdown of Antarctica's Wordie Ice Shelf glaciers in response to ENSO/Southern Annular Mode-driven warming in the Southern Ocean. *Earth and Planetary Science Letters*, 476:100–110, 2017. https://doi.org/10.1016/j.epsl.2017.08.005.

Wang, G., Cai, W., Santoso, A., Wu, L., Fyfe, J. C., Yeh, S.-W., Ng, B., Yang, K., and McPhaden, M. J. Future Southern Ocean warming linked to projected ENSO variability. *Nature Climate Change*, 12(7):649–654, 2022. https://doi.org/10.1038/s41558-022-01398-2.

Warner, S. J. and Moum, J. N. Feedback of mixing to ENSO phase change. *Geophysical Research Letters*, 46(23):13920–13927, 2019. https://doi.org/10.1029/2019GL085415.

Wendler, G., Adolphs, U., Hauser, A., and Moore, B. On the surface energy budget of sea ice. *Journal of Glaciology*, 43(143):122–130, 1997. https://doi.org/10.3189/S0022143000002884.

Wieners, K.-H., Giorgetta, M., Jungclaus, J., Reick, C., Esch, M., Bittner, M., Gayler, V., Haak, H., de Vrese, P., Raddatz, T., Mauritsen, T., von Storch, J.-S., Behrens, J., Brovkin, V., Claussen, M., Crueger, T., Fast, I., Fiedler, S., Hagemann, S., Hohenegger, C., Jahns, T., Kloster, S., Kinne, S., Lasslop, G., Kornblueh, L., Marotzke, J., Matei, D., Meraner, K., Mikolajewicz, U., Modali, K., Müller, W., Nabel, J., Notz, D., Peters-von Gehlen, K., Pincus, R., Pohlmann, H., Pongratz, J., Rast, S., Schmidt, H., Schnur, R., Schulzweida, U., Six, K., Stevens, B., Voigt, A., and Roeckner, E. MPI-M MPI-ESM1.2-LR model output prepared for CMIP6 ScenarioMIP ssp585, 2019a. https://doi.org/10.22033/ESGF/CMIP6.6705.

Wieners, K.-H., Giorgetta, M., Jungclaus, J., Reick, C., Esch, M., Bittner, M., Legutke, S., Schupfner, M., Wachsmann, F., Gayler, V., Haak, H., de Vrese, P., Raddatz, T., Mauritsen, T., von Storch, J.-S., Behrens, J., Brovkin, V., Claussen, M., Crueger, T., Fast, I., Fiedler, S., Hagemann, S., Hohenegger, C., Jahns, T., Kloster, S., Kinne, S., Lasslop, G., Kornblueh, L., Marotzke, J., Matei, D., Meraner, K., Mikolajewicz, U., Modali, K., Müller, W., Nabel, J., Notz, D., Peters-von Gehlen, K., Pincus, R., Pohlmann, H., Pongratz, J., Rast, S., Schmidt, H., Schnur, R., Schulzweida, U., Six, K., Stevens, B., Voigt, A., and Roeckner, E. MPI-M MPI-ESM1.2-LR model output prepared for CMIP6 CMIP historical, 2019b. https://doi.org/10.22033/ESGF/CMIP6.6595.

Wieners, K.-H., Giorgetta, M., Jungclaus, J., Reick, C., Esch, M., Bittner, M., Legutke, S., Schupfner, M., Wachsmann, F., Gayler, V., Haak, H., de Vrese, P., Raddatz, T., Mauritsen, T., von Storch, J.-S., Behrens, J., Brovkin, V., Claussen, M., Crueger, T., Fast, I., Fiedler, S., Hagemann, S., Hohenegger, C., Jahns, T., Kloster, S., Kinne, S., Lasslop, G., Kornblueh, L., Marotzke, J., Matei, D., Meraner, K., Mikolajewicz, U., Modali, K., Müller, W., Nabel, J., Notz, D., Peters-von Gehlen, K., Pincus, R., Pohlmann, H., Pongratz, J., Rast, S., Schmidt, H., Schnur, R., Schulzweida, U., Six, K., Stevens, B., Voigt, A., and Roeckner, E. MPI-M MPI-ESM1.2-LR model output prepared for CMIP6 CMIP piControl, 2019c. https://doi.org/10.22033/ESGF/CMIP6.6675.

Wijffels, S., Roemmich, D., Monselesan, D., Church, J., and Gilson, J. Ocean temperatures chronicle the ongoing warming of Earth. *Nature Climate Change*, 6(2):116–118, 2016. https://doi.org/10.1038/nclimate2924.

Winton, M., Griffies, S. M., Samuels, B. L., Sarmiento, J. L., and Frölicher, T. L. Connecting changing ocean circulation with changing climate. *Journal of Climate*, 26(7):2268 – 2278, 2013. https://doi.org/10.1175/JCLI-D-12-00296.1.

Wu, Q., Zhang, X., Church, J. A., and Hu, J. ENSO-Related global ocean heat content variations. *Journal of Climate*, 32(1):45 – 68, 2019a. https://doi.org/10.1175/JCLI-D-17-0861.1.

Wu, Q., Zhang, X., Church, J. A., and Hu, J. ENSO-Related Global Ocean Heat Content Variations. *Journal of Climate*, 32(1):45–68, 2019b. https://doi.org/10.1175/JCLI-D-17-0861.1.

Wyrtki, K. El Niño—the dynamic response of the equatorial Pacific Ocean to atmospheric forcing. *Journal of Physical Oceanography*, 5(4):572–584, 10 1975. https://doi.org/10.1175/1520-0485(1975)005<0572:ENTDRO>2.0.CO;2.

Wyrtki, K. Water displacements in the Pacific and the genesis of El Nino cycles. *Journal of Geophysical Research: Oceans*, 90(C4):7129–7132, 1985. https://doi.org/10.1029/JC090iC04p07129.

Zeller, M., McGregor, S., and Spence, P. Hemispheric asymmetry of the Pacific shallow meridional overturning circulation. *Journal of Geophysical Research: Oceans*, 124(8): 5765–5786, 2019. https://doi.org/10.1029/2018JC014840.

Ziehn, T., Chamberlain, M., Lenton, A., Law, R., Bodman, R., Dix, M., Mackallah, C., Druken, K., and Ridzwan, S. M. CSIRO ACCESS-ESM1.5 model output prepared for CMIP6 C4MIP esm-ssp585, 2019a. https://doi.org/10.22033/ESGF/CMIP6.4252.

Ziehn, T., Chamberlain, M., Lenton, A., Law, R., Bodman, R., Dix, M., Wang, Y., Dobrohotoff, P., Srbinovsky, J., Stevens, L., Vohralik, P., Mackallah, C., Sullivan, A., O'Farrell, S., and Druken, K. CSIRO ACCESS-ESM1.5 model output prepared for CMIP6 CMIP historical, 2019b. https://doi.org/10.22033/ESGF/CMIP6.4272.

Ziehn, T., Chamberlain, M., Lenton, A., Law, R., Bodman, R., Dix, M., Wang, Y., Dobrohotoff, P., Srbinovsky, J., Stevens, L., Vohralik, P., Mackallah, C., Sullivan, A., O'Farrell, S., and Druken, K. CSIRO ACCESS-ESM1.5 model output prepared for CMIP6 CMIP piControl, 2019c. https://doi.org/10.22033/ESGF/CMIP6.4312.

Zilberman, N. V., Scanderbeg, M., Gray, A. R., and Oke, P. R. Scripps Argo trajectory-based velocity product: global estimates of absolute velocity derived from core, biogeochemical, and Deep Argo float trajectories at parking depth. *Journal of Atmospheric and Oceanic Technology*, 2023. https://doi.org/10.1175/JTECH-D-22-0065.1.

Zuo, H., Balmaseda, M., Mogensen, K., and Tietsche, S. *OCEAN5: the ECMWF ocean reanalysis system and its real-time analysis component.* European Centre for Medium-Range Weather Forecasts, 2018.

A

Appendix to Part 1

A copy of the published article that constitutes the material in Part 1 is included hereafter:

Huguenin, M. F.[1, 2, 3], Holmes R. M.[1,3, 4, 5] & England M. H.[1,2] *Nature Communications.* (2022). **13**, 4921. https://doi.org/10.1038/s41467-022-32540-5

1. Climate Change Research Centre, University of New South Wales, Sydney, NSW, Australia 2. ARC Australian Centre for Excellence in Antarctic Science, University of New South Wales, Sydney, NSW, Australia 3. ARC Centre of Excellence in Climate Extremes, University of New South Wales, Sydney, NSW, Australia 4. School of Mathematics and Statistics, University of New South Wales, Sydney, NSW, Australia 5. School of Geosciences, University of Sydney, Sydney, NSW, Australia

nature communications

Article https://doi.org/10.1038/s41467-022-32540-5

Drivers and distribution of global ocean heat uptake over the last half century

Received: 28 January 2022

Accepted: 4 August 2022

Published online: 07 September 2022

Check for updates

Maurice F. Huguenin[1,2,3], Ryan M. Holmes[1,3,4,5] & Matthew H. England[1,2]

Since the 1970s, the ocean has absorbed almost all of the additional energy in the Earth system due to greenhouse warming. However, sparse observations limit our knowledge of where ocean heat uptake (OHU) has occurred and where this heat is stored today. Here, we equilibrate a reanalysis-forced ocean-sea ice model, using a spin-up that improves on earlier approaches, to investigate recent OHU trends basin-by-basin and associated separately with surface wind trends, thermodynamic properties (temperature, humidity and radiation) or both. Wind and thermodynamic changes each explain ~ 50% of global OHU, while Southern Ocean forcing trends can account for almost all of the global OHU. This OHU is enabled by cool sea surface temperatures and sensible heat gain when atmospheric thermodynamic properties are held fixed, while downward longwave radiation dominates when winds are fixed. These results address long-standing limitations in multidecadal ocean-sea ice model simulations to reconcile estimates of OHU, transport and storage.

The ocean plays a critical role in modulating the Earth's climate system and over the last 50 years it has taken up over 89% of the excess energy due to greenhouse warming[1–5]. Since the early 1990s, the rate of ocean warming has likely doubled[6]. However, our current understanding of the spatial distribution of ocean heat uptake (OHU) and storage is limited, not least because of sparse observations with large uncertainties, especially in sea-ice covered regions[7] and the deep ocean[3]. For example, reliable observations of ocean heat content (OHC) in the upper 2000 m only start in 2005 with the Argo program that covers 60°S–60°N[8]. Before 2005, good observations are only available in the upper 700 m from expendable bathythermographs[9] and from a few select deep ocean cruise ship measurements[10,11]. Observation-based studies therefore focus mainly on trends over much shorter time periods (e.g., since 2005[12] or since the early 1990s[13]).

Fully coupled atmosphere-ocean general circulation models and ocean-sea ice models simulate a complete representation of the global ocean and are now increasingly used to assess the OHC evolution. However, fully-coupled models from the Coupled and Flux-Anomaly-Forced Model Intercomparison Projects (CMIP[14] and FAFMIP[15] respectively) generally exhibit larger biases than ocean-sea ice models, and simulate an internal climate variability that is independent of observations. Modelling studies have investigated recent trends mainly in idealised settings[15,16] or in coupled simulations with an independent climate variability[14,17]. In contrast, ocean-sea ice models are constrained by atmospheric fields from a reanalysis product, and therefore follow the observed trajectory of internal and forced climate variability.

Global climate models (both fully coupled and ocean-sea ice only) suffer from internal model drift due to errors in the representation of physical processes, and thus they require a spin-up to equilibrate their climate and minimise drift. In ocean-sea ice models, a common spin-up approach, used for the Ocean Model Intercomparison Project phase 2 (OMIP-2)[18], applies six repeat cycles of 1958–2018 atmospheric forcing from the Japanese reanalysis data set JRA55-do[19]. However, there are two limitations associated with this approach: (1) after each cycle, the model experiences a large shock and associated recovery period when the forcing suddenly switches from the year 2018 back to 1958 and (2) it is unclear how to account for model drift without a parallel running control simulation (Supplementary Fig. 1a).

In this study we address these limitations of the OMIP-2 approach by introducing a spin-up protocol for global ocean-sea ice models and

[1]Climate Change Research Centre, University of New South Wales, Sydney, NSW, Australia. [2]ARC Australian Centre for Excellence in Antarctic Science, University of New South Wales, Sydney, NSW, Australia. [3]ARC Centre of Excellence in Climate Extremes, University of New South Wales, Sydney, NSW, Australia. [4]School of Mathematics and Statistics, University of New South Wales, Sydney, NSW, Australia. [5]School of Geosciences, University of Sydney, Sydney, NSW, Australia. e-mail: m.huguenin-virchaux@unsw.edu.au

 https://doi.org/10.1038/s41467-022-32540-5

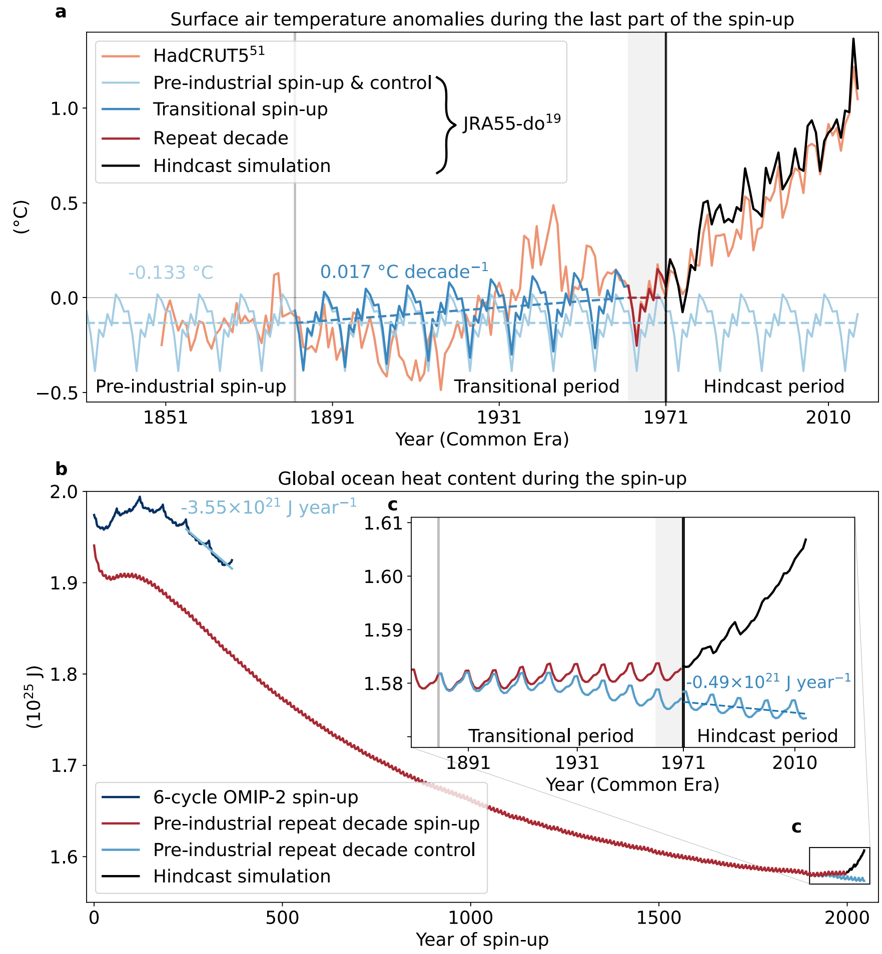

Fig. 1 | Experimental design of the spin-up. a Time series of global mean surface ocean air temperature anomalies from JRA55-do[19] during the last part of the ocean-sea ice model spin-up. The initial 1900 years of the spin-up are performed by applying repeat cycles of 1962–1971 atmospheric reanalysis forcing, from which a pre-industrial offset of 0.133 °C has been removed (light blue line and value). In orange the same anomalies from the observational data set HadCRUT5.1[51] which has a mean offset of 0.133 °C over 1850–1879 relative to the 1960s. During the transitional spin-up period, the offset increases by 0.017 °C decade^{-1} (light blue value and linear trend) back to the 1960s level. This is to simulate the transition from the equilibrated pre-industrial to the warmer 1960s oceanic state. The 1962–1971 decade is shown as the grey shaded period. From 1972 onward, inter-annual hindcast simulations are then branched off (e.g., the full forcing simulation in black where all atmospheric forcing fields evolve over time). The parallel control simulation is obtained by continuing the modified pre-industrial spin-up (light blue line) unchanged through the transitional period past 1972. **b** Time series of global ocean heat content during the five-cycle OMIP-2 spin-up (dark blue line, 10^{25} J, and linear trend over the last two cycles, -3.55×10^{21} J year^{-1}) and the pre-industrial spin-up (red line, 10^{25} J). The offset between the two time series at year 1 of the spin-up is due to the use of updated temperature fields and bathymetric changes in the repeat decade spin-up. **c** Inset of the last part of the spin-up, showing the transitional and hindcast periods with the 1960s period shaded in grey. The control simulation is given in light blue with its linear trend of -0.49×10^{21} J year^{-1} over 1972–2017. The black line is the ocean heat content in the full forcing simulation initialised in 1971.

illustrate its benefits using the ACCESS-OM2 ocean-sea ice model[20]. The spin-up is performed using repeat decadal cycles of the JRA55-do reanalysis forcing from 1962–1971, corrected for pre-industrial times, to equilibrate the model to a state prior to the recent rapid acceleration in OHU (Fig. 1 and Methods). There are no longer large initial shocks at the beginning of each spin-up cycle and we can account for model drift by subtracting the linear trend from a parallel control repeat decade simulation (Fig. 1b, c). Using this approach in an observationally constrained model gives us an estimate of the actual trajectory of OHC, including the multi-decadal internal variability since the 1970s. By decomposing the atmospheric trends into processes and regions (Methods), we can attribute the global heat uptake by drivers and basins over this period.

Results

Global ocean heat uptake

The observations of upper 2000 m global OHC[3] reach 2.40×10^{23} J in 2017 relative to the 1972–1981 baseline (dashed red line, Fig. 2a). We choose this baseline as it ends before the volcanic eruption of El Chichón in mid-1982 and the OMIP-2 models prior to 1972 undergo a very strong global cooling period (Supplementary Fig. 2a). The multi-model mean from the fully coupled CMIP6 model suite (light blue line in Fig. 2a) tracks the observed OHC estimate closely, however with an increasingly large spread among ensemble members. The full forcing ACCESS-OM2 hindcast (where all atmospheric forcing evolves over time) simulates a global OHC increase of 1.73×10^{23} J in the upper 2000 m (capturing 72% of the observational estimate).

This simulation improves considerably on the ACCESS-OM2 simulation that used the OMIP-2 spin-up approach, which lies at the bottom of the OMIP-2 ensemble (cf. black and dark blue lines in Fig. 2a). The hindcast also improves on most of the other 11 OMIP-2 models[18], whose multi-model-mean reaches 0.94×10^{23} J in 2017, and captures a more realistic rise in OHC without the rapid spurious global cooling adjustment prior to 1972 (Supplementary Fig. 2a). There is no control simulation available to use for de-drifting in the OMIP-2 protocol, and we have attempted to de-drift the global OHC by fitting and removing a linear trend over the last two OMIP-2 cycles (e.g., black lines, Supplementary Fig. 1a). Without this de-drifting, the

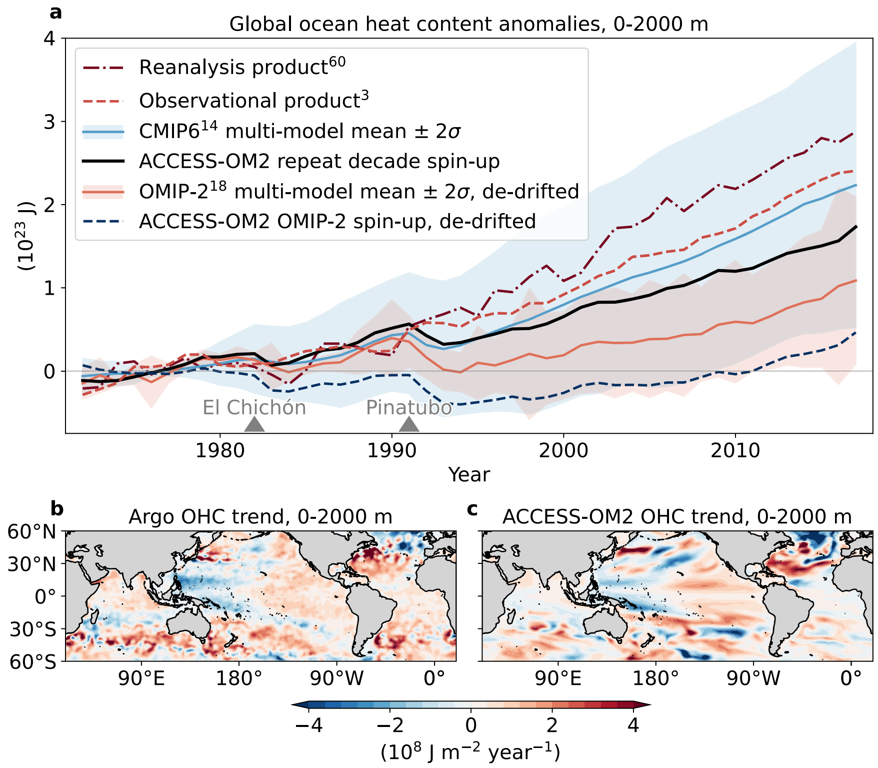

Fig. 2 | Recent global ocean heat content (OHC) anomalies in observations and hindcast model simulations. a Global ocean heat content anomalies (10^{23} J) in the upper 2000 m from ocean reanalysis[60], observations[3], 25 fully coupled historical CMIP6 model runs[14] (including their multi-model mean and 2σ variance), the full forcing ocean-sea ice simulation (ACCESS-OM2 repeat decade spin-up, where all atmospheric forcing fields evolve over time), 11 de-drifted OMIP-2 ocean-sea ice model simulations[18] (including their multi-model mean, and 2σ variance) and the de-drifted ACCESS-OM2 OMIP-2-based simulation. For the individual time series of each CMIP6 and OMIP-2 ensemble member, see Supplementary Fig. 2. The two triangle markers highlight the volcanic eruptions of El Chichón in 1982 and Mount Pinatubo in 1991. The baseline period for all time series is 1972–1981. **b**, **c** Spatial distribution of anomalous upper 2000 m ocean heat content trends over 2006–2017 in the Argo observations and in the full forcing ACCESS-OM2 simulation (10^8 J m^{-2} year^{-1}).

positive trend in OHC in the OMIP-2 models would be even weaker (see also Fig. 24e in Tsujino et al.[18]). If a similar additive improvement, that we see in ACCESS-OM2, were applied to the other models in the OMIP-2 ensemble, then the multi-model mean of an ensemble using our alternative spin-up approach would reach an upper 2000 m OHC anomaly of 2.31×10^{23} J in 2017, within four percentage points of the observations[3].

The spatial trend of the upper 2000 m OHC in the full forcing simulation corresponds well with Argo observations[21] (Fig. 2b, c and CMIP5 models over 2005–2015[22]), especially in the tropical Pacific and the Northern Atlantic. However, accumulation of anomalous heat in the model is reduced in the South Atlantic compared to Argo, and is likely caused by reduced ocean heat convergence in this region (see below). Most of the excess heat absorbed during this period is stored in the Southern Hemisphere (66.0% of the globally integrated trend relative to 72.7% in Argo). Over this shorter 2006-2017 period, the hemispheric OHC asymmetry has been linked to decadal climate variability[22], the asymmetry in anthropogenic forcing[23], the greater area of the Southern Hemisphere ocean[24] as well as anomalous ocean heat transport[12].

Heat uptake, transport and storage rates

In order to quantify the spatial distribution of OHC trends, we consider the vertically integrated heat budget which expresses the OHC tendency (termed here heat storage) as the sum of the anomalous net surface heat flux (heat uptake) and the convergence of the anomalous vertically integrated ocean heat transport (Eq. (2), Methods). Globally integrated, the full-depth heat uptake/storage rate over the last half century in the full forcing simulation is 5.4×10^{21} J year^{-1} (Fig. 3a). While trends have accelerated over the last 20 years, the spatial pattern of heat uptake has remained robust (cf., Fig. 3a and Supplementary Fig. 3a). The Southern Ocean dominates heat uptake with a rate of 6.9×10^{21} J year^{-1}. The dominant role of this region is a consequence of the strong heat fluxes into the ocean where sea surface temperatures (SSTs) are colder than the overlying atmosphere. These cold SSTs are maintained by strong westerly winds that drive upwelling of cold water to the surface, insulating the Southern Ocean from forced changes, and driving efficient heat uptake from the atmosphere[17,25–27]. In this simulation, heat uptake occurs predominantly in the Indian and Pacific sectors of the Southern Ocean. Northward Ekman transport subsequently subducts these water masses along isopycnals into mode and intermediate water layers[27]. Heat storage is also significant in the Atlantic sector of the Southern Ocean where it arises primarily from the convergence of oceanic heat transport rather than from local atmospheric heat uptake (Fig. 3a, b).

Patterns of heat uptake outside of the Southern Ocean are more variable. Heat loss is dominant in the Atlantic basin (-1.9×10^{21} J year^{-1}), especially north of 45°N. The Atlantic heat loss arises from its connection to the Southern Ocean via the Atlantic Meridional Overturning Circulation (AMOC). The AMOC transports 42% ($2.9 \pm 0.2 \times 10^{21}$ J year^{-1}) of the additional heat taken up in the Southern Ocean northward into the Atlantic (red arrow in Fig. 3b), where two-thirds thereof is lost to the atmosphere via ocean-air heat fluxes. Compared to observations, the model's AMOC maximum at 26.5°N is weak (9.1 Sv relative to the observed estimate of 17 Sv over 2004–2012[28], 1 Sv = 10^6 m^3 s^{-1}, Supplementary Fig. 4a), lower than most other OMIP-2 models[18], and may thus lead to weaker anomalous Southern Ocean heat export into the Atlantic. However, the changes in the AMOC strength in the full forcing simulation of ~1 Sv are small compared to the decadal variability of ± 2 Sv (black line, Supplementary Fig. 4a).

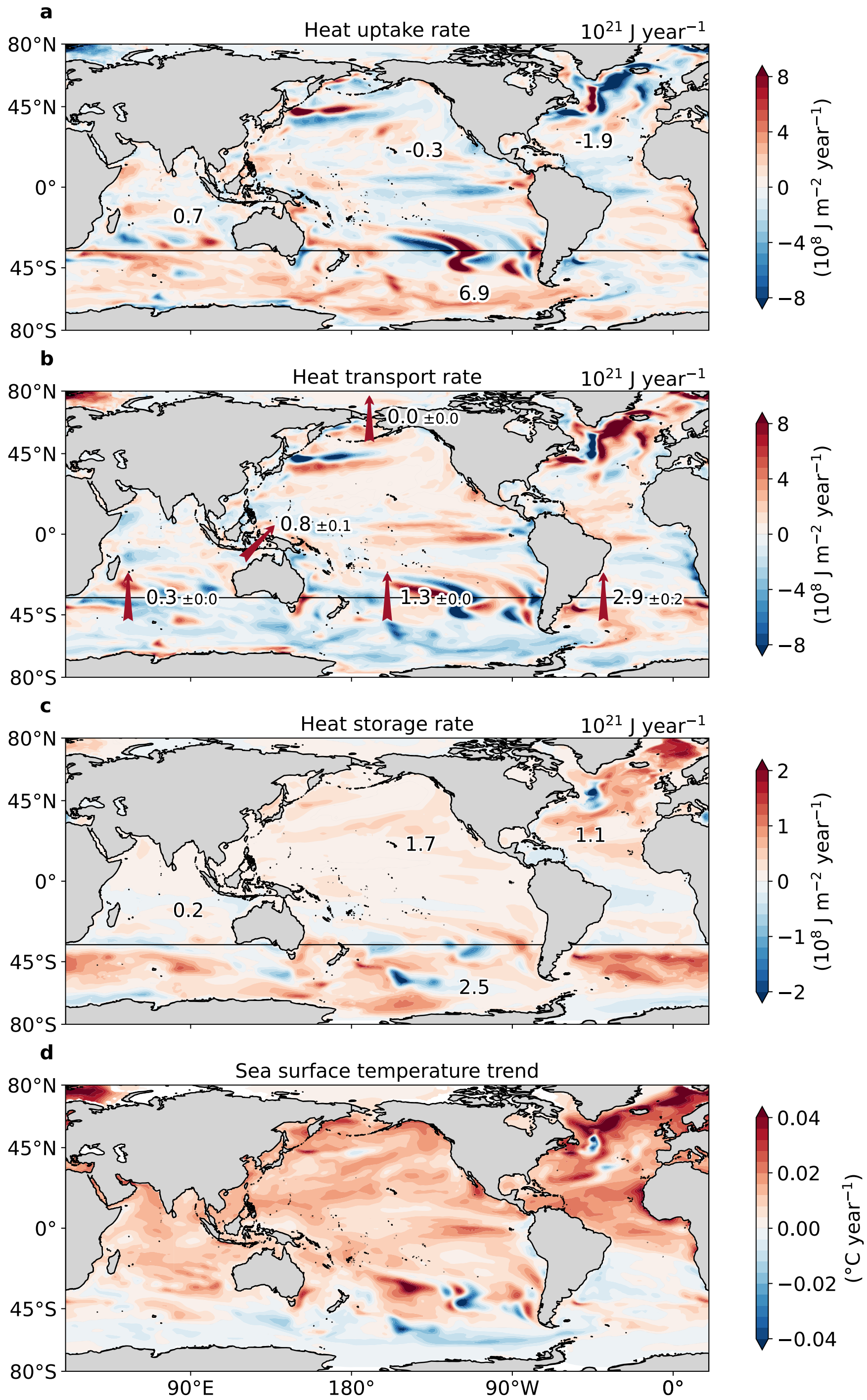

Fig. 3 | Spatial distribution of ocean heat uptake, transport, storage and sea surface temperature trends over 1972–2017 in the full forcing simulation (where all atmospheric forcing fields evolve over time). **a** Time integrated net surface heat flux anomalies (10^8 J m^{-2} year^{-1}) with positive heat uptake defined as into the ocean. The basin-wide values (10^{21} J year^{-1}) show the total area integrated trends over a particular ocean basin with the boundaries set by the black lines across the Southern Ocean, the Indonesian Throughflow, the Bering Strait and the continental land masses. The Southern Ocean ends at 36°S, the Bering Strait is at 65°N and the Indonesian Throughflow is defined between Java, New Guinea (105°W to 134°W) at 3°S and the Australian continent (20°S to 6°S) at 137°E. The Atlantic Ocean contributions include the Arctic Ocean north of 65°N and the marginal Hudson Bay, Baltic and Mediterranean basins. The Indian Ocean component also includes the Red Sea. The basin-wide values are rounded to one-decimal point accuracy. **b** Anomalous heat transport convergence calculated as a residual from the **a** heat uptake and **c** heat storage (10^8 J m^{-2} year^{-1}). The anomalous heat transport rates and their uncertainties across transects (10^{21} J m^{-2} year^{-1}) are calculated from anomalous heat and volume transports (Methods). **d** Simulated sea surface temperature trends (°C year^{-1}). Grid cells in **d** that have a climatological sea ice coverage above 85% have been removed and are shaded white.

Heat uptake in the Indian and Pacific subtropical and tropical basins plays only a minor role on the global scale (Fig. 3a). This is likely because the Indian and Pacific basins lack a convection-driven deep circulation[29,30] that would efficiently take up heat over multi-decadal time scales. In addition, heat uptake in the tropics is inhibited by the warming response of the SST (Fig. 3d). In contrast, at the high latitudes of the Southern Ocean, the SST increases at a rate that keeps pace with local atmospheric warming (due to wind-driven

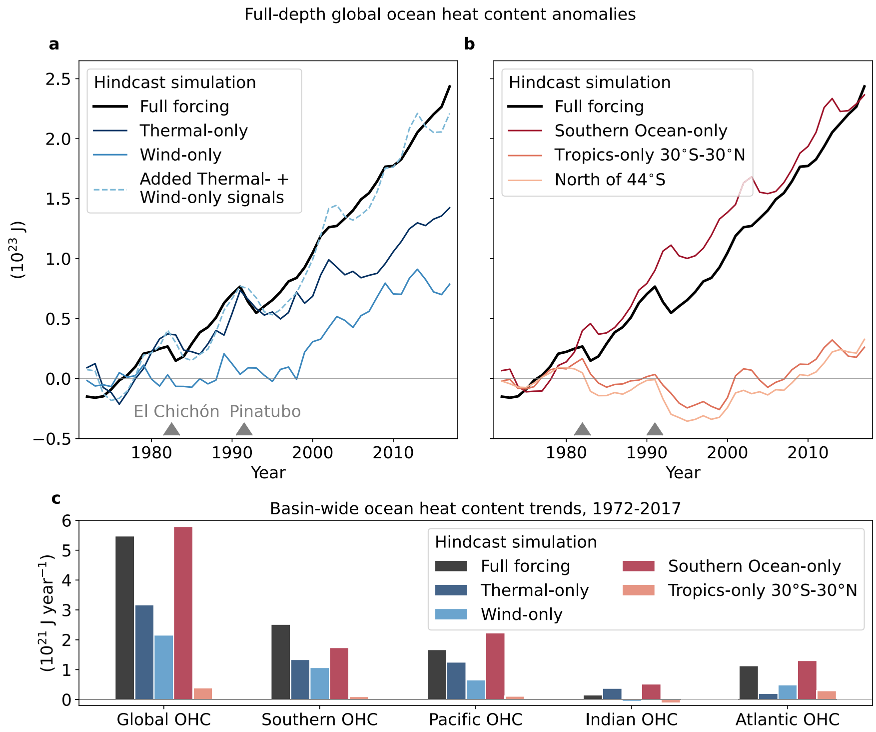

Fig. 4 | Simulated global and regional ocean heat content (OHC) changes due to thermal/wind trends and due to regionally-constrained atmospheric trends. **a** Time series of full-depth global ocean heat content anomalies (10^{23} J) in the full forcing simulation (black line), when only prescribing surface wind trends (i.e., Wind-only) and when only prescribing thermodynamic trends (i.e., Thermal-only, Methods). The dashed blue line shows the anomalies in both wind- and thermal-only hindcast simulations added together. The two triangle markers highlight the volcanic eruptions of El Chich ón in 1982 and Mount Pinatubo in 1991. The baseline period for all time series is 1972–1981. **b** Time series for the hindcast simulations where combined interannual wind and thermal forcing is applied only over the Southern Ocean (south of 44°S), the mid- and high northern latitudes (north of 44°S) and only over the tropics (30°S–30°N) with the remaining ocean area forced by the control repeat decade forcing. **c** Basin integrated ocean heat content trends (10^{21} J year^{-1}) in the hindcast simulations of **a** and **b**.

Ekman effects) creating favourable conditions for continuous ocean heat uptake (Fig. 3d).

Wind versus thermal effects

We next consider a set of hindcast simulations that isolate the impact of thermodynamic- (including air temperature, humidity and downward radiation) and wind-driven atmospheric changes over the global ocean and specific regions to better understand the drivers of recent OHU (Methods). In the wind-only simulation, zonal and meridional surface winds evolve over time while the other forcing fields are held fixed in the 1960s (and vice versa for the thermal experiment). The approach here differs from coupled and flux-anomaly forced ocean-sea ice model simulations that also aim to isolate contributions from winds and other changes[15,31] in that our experiments are forced by atmospheric trends from reanalysis instead of, for example, doubled atmospheric CO_2 concentrations, and thus they capture the observed trajectory of internal climate variability. The strong decadal variability in our simulations arises from the portion of the atmospheric forcing (whether thermal or wind forcing) that cycles through the repeat decade (Fig. 4a, b).

The two simulations that include only either thermal or surface wind trends explain 57% and 40% of the global OHC trend of 5.4×10^{23} J (Fig. 4a, c). As in the full forcing simulation, heat uptake in both thermal- and wind-only experiments is dominated by the Southern Ocean (3.1 and 3.9×10^{21} J year^{-1}, Supplementary Fig. 5a, e). In the wind-only simulation, Southern Ocean heat uptake is large because the SST cools as a result of enhanced northward Ekman transport of cool fresh Antarctic surface waters (Fig. 5a, b). This heat uptake is driven by sensible and upward longwave heat losses associated with the negative SST anomalies (Fig. 5c,d). Some compensation by latent and upward shortwave heat flux anomalies, due to increases in sea ice, are associated with cooling in this region[32] (Supplementary Table 1). It is important to note that wind changes also have a direct impact on sensible and latent heat fluxes through their dependence on wind speed in the model's bulk formulae. As opposed to the wind-only experiment, heat uptake in the thermal-only experiment is associated mainly with changes in downward longwave radiation (Fig. 5c), which appear more important than air temperature changes (as the sensible heat flux anomalies are reduced). Integrated over the Southern Ocean, the sensible heat flux drives almost double the heat uptake than the longwave radiative flux in the wind-only simulation (3.7 vs. 1.9×10^{21} J year^{-1}), while in the thermal-only simulation heat uptake through downward longwave radiation is more dominant (3.0 vs. 2.4×10^{21} J year^{-1}, Supplementary Table 1).

Both changes in surface winds and atmospheric thermodynamic properties can affect the export of anomalous heat from the Southern Ocean into the Pacific, Indian and Atlantic basins via the meridional overturning circulation. In particular, in the wind-only simulation, anomalous heat export northward is stronger than in the thermal-only simulation, due to the stronger westerlies which in turn increase the Ekman transport and thus the Southern Ocean's overturning circulation (Supplementary Fig. 5b, f). In contrast, the parameterised submesoscale eddy mixing, eddy advection and diffusion schemes play a minor role in contributing to ocean heat transport changes into the Atlantic and Indo-Pacific. In a fully coupled framework, Liu et al.[33] showed that in response to quadrupled atmospheric CO_2 concentrations, the poleward-strengthened westerlies displace and intensify the Southern Ocean's meridional overturning circulation which results in anomalous heat transport divergence at 60°S and increased surface heat fluxes while the opposite was shown for 45°S. In our wind-only simulation, we see strong heat transport divergence at almost all latitudes of the Indian and Pacific sectors of the Southern Ocean, while

https://doi.org/10.1038/s41467-022-32540-5

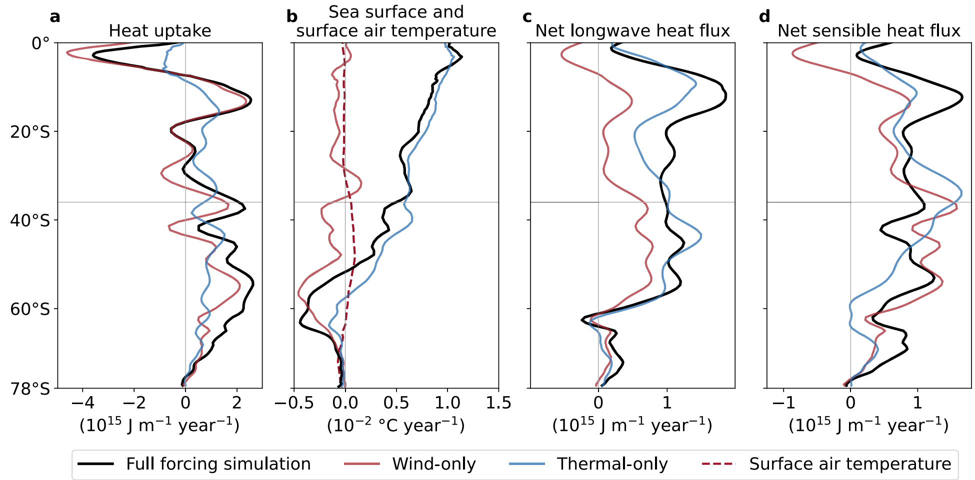

Fig. 5 | Southern Hemisphere ocean heat uptake, sea surface temperature and surface air temperature, net longwave and net sensible heat flux trends over 1972–2017. a Zonally integrated heat uptake in the simulations with full, wind-only and thermal-only forcing (10^{15} J year^{-1}), equal to the zonal integral of the spatial structure shown in Fig. 2a and Supplementary Fig. 5a, e. **b** Zonal mean sea surface temperature and surface air temperature trends (°C year^{-1}). **c**, **d** The contribution of net longwave and sensible heat fluxes to the total ocean heat uptake shown in **a** (10^{15} J year^{-1}). The horizontal lines at 36°S indicate the northern boundary of the Southern Ocean in our analysis. A 5-grid cell rolling mean has been applied in **a**, **c** and **d**.

heat converges in the Atlantic sector between 60°S-45°S (Supplementary Fig. 5b), likely because the Southern Ocean surface wind trends in JRA55-do are strongest in the Indian and Pacific sectors. We agree with Liu et al.[33], that wind stress changes are likely the primary drivers of ocean heat content change in the wind-only simulation (through their induced SST changes), rather than the direct wind-speed related turbulent heat flux change.

Regional contributions

On the global scale, the OHC trend can be reproduced when atmospheric trends in both winds and thermodynamic properties are applied only over the Southern Ocean south of 44°S (with repeat decade forcing applied north of this latitude, Fig. 4b). However, an important regional difference between the full forcing and Southern Ocean-only forced simulation is that in the latter, heat storage is larger in the Pacific, Indian and Atlantic Oceans and smaller in the Southern Ocean (cf., black and dark red bars in Fig. 4c). This is likely caused by enhanced northward heat transport in the Southern Ocean-only experiment across 36°S, despite similar Southern Ocean heat uptake rates in both simulations (6.98 vs. 6.97×10^{21} J year^{-1}, Fig. 3a, b and Supplementary Fig. 6a, b). However, the heat transport rates in the Southern Ocean-only experiment are influenced by the tapering zones between the repeat decade and interannual forcing. In addition, the Pacific and Atlantic basins experience weak heat loss across the surface due to these basins being forced by the cooler 1960s atmosphere (Supplementary Fig. 6a).

Performing an experiment with interannual trends applied only north of 44°S or just over the tropics 30°S–30°N, shows a global OHC trend of 0.3–0.4 × 10^{21} J year^{-1} (Fig. 4c). A positive trend, distinct from the repeat decade forcing oscillation, emerges only in the mid–1990s (light pink line, Fig. 4a), and is likely linked to the observed shift of the Interdecadal Pacific Oscillation into a negative phase. This favours La Niña-like conditions with increased trade winds and enhanced tropical heat uptake[34,35]. OHC trends over the 1992–2011 period from the tropical 30°S–30°N experiment appear mainly centred on the Equator in the western Pacific at 150 m depth (Supplementary Fig. 7), and are consistent with the observed trends over the same period[34]. A rapid increase in Indian Ocean heat content since the year 2000 has also been shown in observations[36] and occurs in a simulation with interannual trends restricted to only the Indian Ocean (not shown). This signal has been linked to the enhanced trade winds that strengthened warm water transport across the Indonesian Throughflow since the early 2000s[36,37]. However, over the 50-year time period, Interdecadal Pacific Oscillation-related trade wind and OHC changes for the most part cancel each other out as this climate mode underwent a full oscillation[34,38]. Additional model experiments with the interannual atmospheric trend forcing only applied over individual ocean basins north of 44°S/35°S (Pacific-only/Indian- and Atlantic-only experiments, Methods) reveal only minor OHC trends (Supplementary Figs. 8, 9). This further emphasises the key role of the Southern Ocean in driving global ocean heat content trends over the past half century.

Discussion

We have documented the evolution of ocean heat uptake, transport and storage over the last 50 years in a global ocean-sea ice model following a spin-up approach that improves on past simulations of OHC trends using the standard OMIP-2 protocol. The full forcing hindcast simulation considerably improves on the simulation with the same model but using the OMIP-2 spin-up, and reproduces the estimated trajectory of OHC in observations better than most OMIP-2 ensemble members. If the OMIP-2 project would follow the spin-up approach presented here, it is likely that both the multi-model mean and ensemble spread in Fig. 2a would shift upwards and better capture the observed trends.

Changes in surface winds and thermodynamic properties over the Southern Ocean each drive about half of the global heat uptake signal over the last half century (Fig. 6). These heat changes have important consequences for the zonal transport of the Antarctic Circumpolar Current with continued warming likely further accelerating the zonal flow[13]. As in the simulations with full or basin-wide forcing, heat uptake in the wind- and thermal-only experiments in the Indian and Pacific basins is minor, while the Atlantic Ocean is consistently losing heat across its surface (blue arrows, Fig. 6). In the full forcing as well as the wind- and thermal-only simulations, northward heat export from the Southern Ocean into the Atlantic dominates over export into the Indian and Pacific basins. While the Indo-Pacific plays only a minor role in multi-decadal heat uptake and storage, it can substantially impact global OHC trends over shorter periods through enhanced ocean heat uptake and reduced SST warming associated with the Interdecadal Pacific Oscillation[39] (e.g., during global warming hiatus periods such as from 2000–2009).

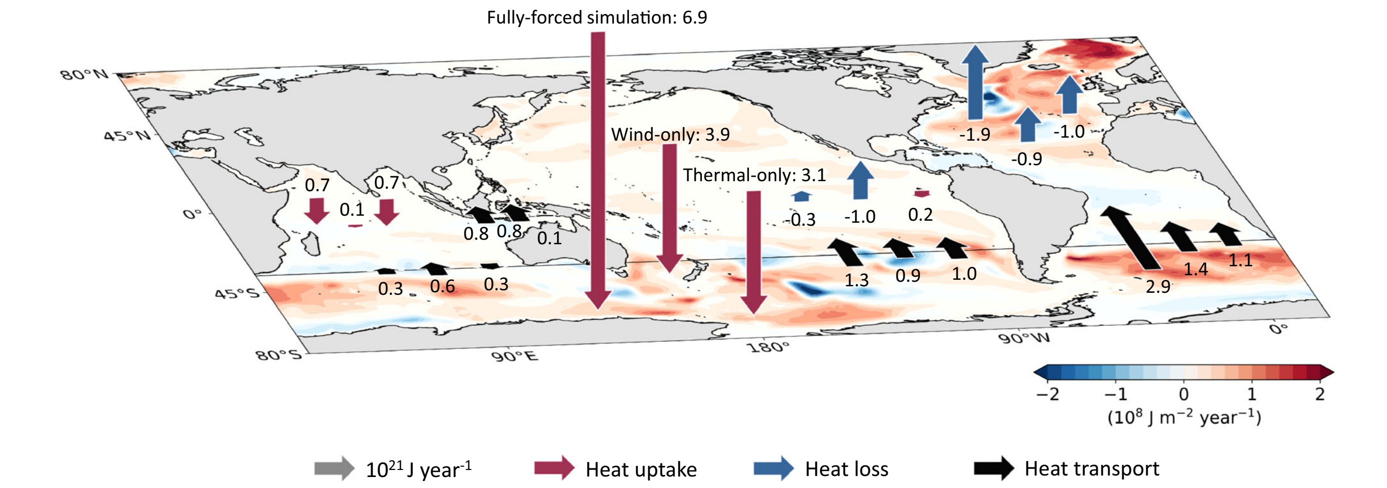

Fig. 6 | Schematic summarising anomalous global ocean heat uptake, heat loss and heat transport over the last half century in different historical simulations. The spatial pattern shows ocean heat storage rates in the full forcing simulation where all atmospheric forcing fields evolve over time (10^8 J m^{-2} year^{-1}). The global ocean is divided into the Southern Ocean and the Indian, Pacific and Atlantic basins as in Fig. 3. The red and blue vertical arrows into and out of the plane show the basin integrated heat uptake and heat loss rates in the full forcing (left arrow), wind-only (middle arrow) and thermal-only (right arrow) simulations (10^{21} J year^{-1}). The black arrows show the heat transport rates in the same simulations (from left to right: full, wind-only and thermal-only forcing) across the transects that separate the basins (10^{21} J year^{-1}). The arrows are to scale, and values are rounded to one-decimal point accuracy. The transport rates across the Bering Strait are one magnitude smaller and not shown.

Over the last twenty years of the full forcing simulation, the weakening AMOC in the North Atlantic (Supplementary Fig. 4) may be linked to positive redistribution feedbacks that have been previously described in a coupled climate model[40]. In this feedback, a weakened AMOC decreases meridional heat transport in the North Atlantic, leading to a divergence of heat, cooler SSTs and increased heat uptake in the subpolar gyre, which in turn further weakens the AMOC[40,41]. It is unclear if this feedback mechanism is contributing to the North Atlantic changes in the full forcing simulation, as heat uptake north of the Equator decreases (-0.6×10^{21} J year^{-1}) and heat transport increases ($+0.6 \times 10^{21}$ J year^{-1}) over the last twenty years of the run, compared to the full period.

Limitations in our results arise from the use of a single model with a 1° horizontal resolution, the biases related to errors in the model's representation of physical processes and uncertainties in reconstructing past atmospheric forcing. Uncertainties also arise from inherent uncertainties in the reanalysis product used, including the reliability of the implied radiative heat flux trends due to both greenhouse gases and aerosols, which remain poorly constrained in observations. Heat transport and heat loss across the surface can be dependent on the model resolution[42] with biases expected to decrease in a finer grid[18]. However, the model configuration used here matches the typical resolution of most OMIP-2 and CMIP6 ensemble members, and heat content anomalies following the OMIP-2 protocol are similar when using the higher resolution configurations of the model (Supplementary Fig. 1b). The low computational cost of the model we employ also allowed us to minimise deep ocean model drift with a long spin-up and permitted a suite of multi-decadal simulations that would otherwise be too expensive to explore using higher-resolution models.

In summary, our experiments emphasise that recent trends in Southern Ocean surface winds, surface air temperature and radiation have driven almost all of the globally integrated ocean warming of the past half century. Increased observational coverage over the Southern Ocean is therefore key to reconcile global surface heat fluxes, ocean heat uptake and heat content changes, as well as building increased confidence in climate models and climate change projections for the coming decades.

Methods

Model, forcing and spin-up

We use the global ocean-sea ice model ACCESS-OM2[20] in a 1° horizontal resolution configuration with 50 z* vertical levels. ACCESS-OM2 consists of the Geophysical Fluid Dynamics Laboratory MOM5.1 ocean model[43] coupled to the Los Alamos CICE5.1.2 sea ice model[44] via OASIS3-MCT[45]. Atmospheric forcing for the model is derived from a prescribed atmospheric state using the Japanese Reanalysis product JRA55-do-1-3[19] which covers the period 1958–2018. The forcing fields are zonal and meridional wind speed, air temperature and specific humidity at 10 m as well as downward short- and longwave radiation, rain- and snowfall, river and ice-related runoff and sea level pressure at the ocean's surface. These fields are used to calculate zonal and meridional wind stress, surface heat and freshwater fluxes using bulk formulae[46]. More details on the model setup and performance can be found in Kiss et al.[20].

We perform a 2000-year spin up of the model initiated from World Ocean Atlas 2013 v2 conditions[47] using modified repeat cycles of the JRA55-do 1962–1971 decade. We choose this decade as it has no extreme El Niño-Southern Oscillation events or tendencies[48] and has close to neutral conditions in the Interdecadal Pacific Oscillation (IPO index: −0.1)[49]. However, it has a positive Southern Annular Mode and three positive Indian Ocean Dipole events occurred in this period[50]. The choice of this decade is a compromise between an early period with limited observations where our confidence in the atmospheric forcing is low, and later periods where the anthropogenic signal is larger and the hindcast experiments would be shorter.

For the first 1910 years of the spin-up, we subtract from the repeat 1962–1971 forcing a pre-industrial offset of 0.133 °C from the surface air temperature and 0.7 W m^{-2} from the downward longwave radiation fields. This is to equilibrate the model to an estimate of the pre-industrial climate instead of a 1960s climate that already incorporates an anthropogenic footprint. Additionally, we modify the specific humidity in order to keep the relative humidity constant and avoid overly impacting evaporation and the latent heat flux. The surface air temperature offset is calculated from the difference between the JRA55-do mean during the 1962–1971 period and the years 1850–1879 in the HadCRUT5[51] data set (light blue and orange lines, Fig. 1a). The offset in downward longwave radiation is consistent with values presented in the fifth Assessment Report of the Intergovernmental Panel for Climate Change (IPCC AR5, Fig. SPM.5)[4]. The overall ratio of surface air temperature to downward longwave radiation offsets is the same as in the study by Stewart and Hogg[52] where they used offsets derived from the CMIP5 historical and moderate greenhouse gas emission scenario (RCP4.5) to run idealised climate change hindcast experiments. As in IPCC AR5 Fig. SPM.5[4], the uncertainty in the pre-industrial offset of downward longwave radiation (and surface air temperature) is likely as large as the value itself, but it is a reasonable approach given the limited data available from pre-industrial times.

The period 1910–2000 of the spin-up (i.e., 1882–1971 Current Era) is the transitional period where we linearly reduce the offsets in the forcing fields back to 1962–1971 levels (dark blue and dark red lines, Fig. 1a). This represents the developing anthropogenic impact on the ocean between the pre-industrial state and the warmer 1960s climate. In year 2000 of the spin-up (i.e., year 1972 Current Era), the interannually-forced hindcast simulations begin. The control simulation is a continuation of the pre-industrial spin-up with modified repeat decade forcing beyond 1972 (light blue line, Fig. 1a).

Hindcast experiments

We run a set of simulations that combine both climatological (1962–1971) and interannual (1971–2017) forcing to investigate the contribution of changing surface winds, thermodynamic properties and the role of individual oceanic regions to anomalous heat uptake since the 1970s.

The wind and thermal simulations include forcing the model over 1972–2017 with interannual zonal and meridional surface wind trends (the wind-only experiment) or combined surface air temperature, humidity, radiation, freshwater and sea level pressure trends (the thermal-only experiment), while repeat decade forcing is used for the other forcing fields. The hindcast experiments here do not allow a complete separation between buoyancy effects (including heating) and wind effects because buoyancy and heat fluxes both change in each of the wind- and thermal-only experiments; for example, the winds can force an SST change that will feed back and alter the sensible heat flux fields. Likewise the thermally-forced experiment can include changes in wind stress wherever ocean circulation changes are simulated, because the wind stress is controlled by the difference between wind speed and ocean current speed, although this effect is generally second order. While surface air temperature and radiation variations dominate the signal in the thermal-only simulation, freshwater fluxes can also contribute to changes in ocean circulation and thus ocean heat uptake and redistribution via changes in, for example, the meridional overturning circulation in the Atlantic and Southern Oceans[15,53].

The regional simulations (hereafter Southern Ocean-only, North of 44°S, Tropics-only 30°S–30°S, Pacific-, Indian- and Atlantic-only forcing simulations) include applying interannual trending atmospheric fields over a specific region of the global ocean while repeat decade forcing is applied over the remaining ocean area (e.g., blue contours in Supplementary Fig. 9). For these simulations, a linear smoothing boundary region of 4° latitude/longitude is used to combine the two forcing fields. For the Southern- and Pacific Ocean-only simulations, we choose the boundaries at 44°S as this latitude marks the poleward extent of the shallow subtropical cells. For the Indian and Atlantic Ocean simulations, we set the southern interannual forcing/repeat decade forcing boundary to 35°S at the southern tip of Africa.

Ocean heat content calculations

Heat content,

$$H = \iiint \rho_0 C_p \Theta \, \mathrm{d}V, \tag{1}$$

is calculated using a reference density $\rho_0 = 1035$ kg m^{-3}, a specific heat capacity $C_p = 3992.1$ J kg^{-1} K^{-1}, the model's prognostic temperature variable Conservative Temperature Θ[54,55] (K) and the (time-variable) grid cell volume dV (m^3).

The vertically integrated Eulerian heat budget can be expressed as

$$\frac{\partial}{\partial t}\int_z^0 H dt = Q_{net} - \nabla_h \cdot \boldsymbol{F}, \tag{2}$$

where the left-hand side is the depth integrated heat content tendency at a given location (J m^{-2} year^{-1}) between depth z and the surface, Q_{net} is the net surface heat flux and $\nabla_h \cdot \boldsymbol{F}$ is the divergence of the vertically integrated ocean heat transport. Changes in heat content arise from changes in heat exchange with the atmosphere (heat uptake) and/or from changes in the convergence of horizontal ocean heat transport. The anomalous heat uptake rate is calculated by first time integrating the net surface heat flux tendencies, including the turbulent (latent and sensible), radiative (short- and longwave), surface volume flux-associated and sea ice exchange components, before removing the linear trend in the time integrated tendencies of the control simulation, and finally fitting a linear trend to the result. The heat storage rate is calculated similarly. The heat transport convergences are calculated as the residual between heat uptake and storage (Eq. (2)). These calculations would be more difficult without a parallel-running control simulation (not available as part of OMIP-2) that can be used to remove drift as well as the steady-state pattern of heat input at low-latitudes and heat loss at high-latitudes connected by meridional ocean heat transport.

Ocean heat transport (OHT) rates across individual transects are calculated from the vertical integral of horizontal advective and parameterised diffusive, mesoscale- and submesoscale heat fluxes accumulated online. Uncertainties in these heat transport rates arise from the presence of non-zero net volume fluxes, which result in a dependence of the cross-transect heat transport on the arbitrary reference temperature[56,57]. We estimate the uncertainty in the anomalous heat transport rate based on the change in the volume transport across the transect $\Delta\Psi$ (m^3 s^{-1}) and a maximum possible range for the temperature $(\Delta\Theta)^{\max}$ at which that net volume transport could be assumed to return:

$$\Delta\mathrm{OHT} = \pm \rho_0 C_p \frac{(\Delta\Theta)^{\max}}{2} \Delta\Psi. \tag{3}$$

We define $(\Delta\Theta)^{\max}$ to be 30°C, an estimate of the maximum temperature range of the model. For example, if the maximum temperature of water transported through the Indonesian Throughflow is 30 °C, then the maximum ambiguity in the change in heat transport is estimated by assuming that this water returns back into the Pacific via the Southern Ocean at 0°C. This issue is discussed in more detail in Section S3 in the Supporting Information of Holmes et al.[56] and in Forget and Ferreira[57].

CMIP6 products

To compare the simulations in this study to atmosphere-ocean general circulation models, we analyse 16 ensemble members from CMIP6 as shown in the Supplementary Table 2. The choice of the models and anomaly calculation is based on Irving et al.[58] and includes first taking a cubic fit of the globally integrated 0–2000 m OHC over the length of the pre-industrial control simulation in each model. The length of this control simulation can be between 500–6000 years depending on the model. This fit is then subtracted from the historical simulation (ending in 2014) and SSP5-8.5 (2014–2017) projection simulation before the removal of the baseline 1972–1981 period.

Data availability

The model data to recreate the figures in this study have been deposited online in the Zenodo database under https://doi.org/10.5281/zenodo.6873094[59]. The full model output is stored on the National Computational Infrastructure and available upon contact to the first author. The Argo data were collected and made freely available by the International Argo Program and the national programs that contribute to it (http://www.argo.ucsd.edu, http://argo.jcommops.org). The Argo Program is part of the Global Ocean Observing System (https://doi.org/10.17882/42182). The product we used here was produced at the China Argo Real-time Data Center and available at http://www.argo.org.cn/english/. The CMIP6 data is available at the Earth System Grid Federation: https://esgf-node.llnl.gov/projects/cmip6/.

Code availability

The analysis scripts to create the forcing for the JRA55-do-1-3 repeat decade spin-up and to reproduce the figures are published online in the Zenodo database under https://doi.org/10.5281/zenodo.6873094[59].

References

1. Schuckmann, K. et al. Heat stored in the Earth system: where does the energy go? *Earth Syst. Sci. Data* **12**, 2013–2041 (2020).
2. Rhein, M. et al. Observations: Ocean. In *Climate Change 2013: The Physical Science Basis. Contribution of Working Group I to the Fifth Assessment Report of the Intergovernmental Panel on Climate Change. Fifth Assessment Report Of The Intergovernmental Panel On Climate Change*. pp. 255–315 (IPCC, Cambridge Univ. Press, Cambridge, United Kingdom, 2013).
3. Levitus, S. et al. World ocean heat content and thermosteric sea level change (0-2000 m), 1955–2010. *Geophys. Res. Lett.* **39**, L10603 (2012).
4. IPCC Summary for Policymakers. *Climate Change 2013: The Physical Science Basis Contribution Of Working Group I To The Fifth Assessment Report Of The Intergovernmental Panel On Climate Change* (eds Stocker, T. F. et al.) (Cambridge Univ. Press, Cambridge, United Kingdom and New York, NY, USA, 2013).
5. Meyssignac, B. et al. Measuring Global Ocean Heat Content to Estimate the Earth Energy Imbalance. *Front. Mar. Sci.* **6**, 432 (2019).
6. IPCC Summary for Policymakers. *IPCC Special Report On The Ocean And Cryosphere In A Changing Climate* (eds Pörtner, H. -O. et al.) (Cambridge Univ. Press, Cambridge, United Kingsom, 2019).
7. Durack, P., Gleckler, P., Landerer, F. & Taylor, K. Quantifying underestimates of long-term upper-ocean warming. *Nat. Clim. Change* **4**, 999–1005 (2014).
8. Gould, J. et al. Argo profiling floats bring new era of in situ ocean observations. Eos Trans. AGU **85**, 185–191 (2004).
9. Abraham, J. et al. A review of global ocean temperature observations: Implications for ocean heat content estimates and climate change. *Rev. Geophysics* **51**, 450–483 (2013).
10. Purkey, S. & Johnson, G. Warming of Global Abyssal and Deep Southern Ocean Waters between the 1990s and 2000s: Contributions to Global Heat and Sea Level Rise Budgets. *J. Clim.* **23**, 6336–6351 (2010).
11. Desbruyères, D., Purkey, S., McDonagh, E., Johnson, G. & King, B. Deep and abyssal ocean warming from 35 years of repeat hydrography. *Geophys. Res. Lett.* **43**, 356–10,365 (2016).
12. Roemmich, D. et al. Unabated planetary warming and its ocean structure since 2006. *Nat. Clim. Change* **5**, 240–245 (2015).
13. Shi, J., Talley, L., Xie, S., Peng, Q. & Liu, W. Ocean warming and accelerating Southern Ocean zonal flow. *Nat. Clim. Change* **11**, 1090–1097 (2021).
14. Eyring, V. et al. Overview of the Coupled Model Intercomparison Project Phase 6 (CMIP6) experimental design and organization. *Geosci. Model Dev.* **9**, 1937–1958 (2016).
15. Gregory, J. et al. The Flux-Anomaly-Forced Model Intercomparison Project (FAFMIP) contribution to CMIP6: investigation of sea-level and ocean climate change in response to CO_2 forcing. *Geosci. Model Dev.* **9**, 3993–4017 (2016).
16. Dias, F. et al. Ocean Heat Storage in Response to Changing Ocean Circulation Processes. *J. Clim.* **33**, 9065–9082 (2020).
17. Frölicher, T. et al. Dominance of the Southern Ocean in Anthropogenic Carbon and Heat Uptake in CMIP5 Models. *J. Clim.* **28**, 862–886 (2015).
18. Tsujino, H. et al. Evaluation of global ocean-sea-ice model simulations based on the experimental protocols of the Ocean Model Intercomparison Project phase 2 (OMIP-2). *Geosci. Model Dev.* **13**, 3643–3708 (2020).
19. Tsujino, H. et al. JRA-55 based surface dataset for driving ocean-sea-ice models (JRA55-do). *Ocean Model.* **130**, 79–139 (2018).
20. Kiss, A. et al. ACCESS-OM2: A Global Ocean-Sea Ice Model at Three Resolutions. *Geosci. Model Dev. Discuss.* **13**, 401–442 (2020).
21. Li, H. et al. Development of a global gridded Argo data set with Barnes successive corrections. *J. Geophys. Res.: Oceans* **122**, 866–889 (2017).
22. Rathore, S., Bindoff, N., Phillips, H. & Feng, M. Recent hemispheric asymmetry in global ocean warming induced by climate change and internal variability. *Nat. Commun.* **11**, 2008 (2020).
23. Irving, D., Wijffels, S. & Church, J. Anthropogenic Aerosols, Greenhouse Gases, and the Uptake, Transport, and Storage of Excess Heat in the Climate System. *Geophys. Res. Lett.* **46**, 4894–4903 (2019).
24. Wijffels, S., Roemmich, D., Monselesan, D., Church, J. & Gilson, J. Ocean temperatures chronicle the ongoing warming of Earth. *Nat. Clim. Change* **6**, 116–118 (2016).
25. Armour, K., Marshall, J., Scott, J., Donohoe, A. & Newsom, E. Southern Ocean warming delayed by circumpolar upwelling and equatorward transport. *Nat. Geosci.* **9**, 549–554 (2016).
26. Marshall, J. et al. The ocean's role in the transient response of climate to abrupt greenhouse gas forcing. *Clim. Dyn.* **44**, 2287–2299 (2015).
27. Morrison, A., Griffies, S., Winton, M., Anderson, W. & Sarmiento, J. Mechanisms of Southern Ocean Heat Uptake and Transport in a Global Eddying Climate Model. *J. Clim.* **29**, 2059–2075 (2016).
28. McCarthy, G. et al. Measuring the Atlantic Meridional Overturning Circulation at 26°N. *Prog. Oceanogr.* **130**, 91–111 (2015).
29. Godfrey, J., Johnson, G. C., McPhaden, M., Reverdin, G. & Wijffels, S. et al. Chapter 4.3 The tropical ocean circulation. *Ocean Circulation Clim.* **77**, 215–246 (2001).
30. Talley, L., Pickard, G., Emery, W. & Swift, J. Descriptive Physical Oceanography—An Introduction. (ELSEVIER,2011,7)
31. Todd, A. et al. Ocean-Only FAFMIP: Understanding Regional Patterns of Ocean Heat Content and Dynamic Sea Level Change. *J. Adv. Modeling Earth Syst.* **12**, e2019MS002027 (2020).
32. Wendler, G., Adolphs, U., Hauser, A. & Moore, B. On the surface energy budget of sea ice. *J. Glaciol.* **43**, 122–130 (1997).
33. Liu, W., Lu, J., Xie, S. & Fedorov, A. Southern Ocean Heat Uptake, Redistribution, and Storage in a Warming Climate: The Role of Meridional Overturning Circulation. *J. Clim.* **31**, 4727–4743 (2018).
34. England, M. et al. Recent intensification of wind-driven circulation in the Pacific and the ongoing warming hiatus. *Nat. Clim. Change* **4**, 222–227 (2014).
35. Henley, B. & King, A. Trajectories toward the 1.5° C Paris target: Modulation by the Interdecadal Pacific Oscillation. *Geophys. Res. Lett.* **44**, 4256–4262 (2017).

36. Lee, S. et al. Pacific origin of the abrupt increase in Indian Ocean heat content during the warming hiatus. *Nat. Geosci.* **8**, 445–449 (2015).
37. Maher, N., England, M., Gupta, A. & Spence, P. Role of Pacific trade winds in driving ocean temperatures during the recent slowdown and projections under a wind trend reversal. *Clim. Dynam.* **51**, 321–336 (2017).
38. Meehl, G., Hu, A. & Teng, H. Initialized decadal prediction for transition to positive phase of the Interdecadal Pacific Oscillation. *Nat. Commun.* **7**, 11718 (2016).
39. Meehl, G., Arblaster, J., Fasullo, J., Hu, A. & Trenberth, K. Model-based evidence of deep-ocean heat uptake during surface-temperature hiatus periods. *Nat. Clim. Change* **1**, 360–364 (2011).
40. Liu, W., Fedorov, A., Xie, S. & Hu, S. Climate impacts of a weakened Atlantic meridional overturning circulation in a warming climate. *Sci. Adv.* **6**, 1–8 (2020).
41. Couldrey, M. et al. What causes the spread of model projections of ocean dynamic sea-level change in response to greenhouse gas forcing? *Clim. Dyn.* **56**, 155–187 (2021).
42. Grist, J. et al. Increasing Atlantic Ocean Heat Transport in the Latest Generation Coupled Ocean-Atmosphere Models: The Role of Air-Sea Interaction. *J. Geophys. Res.: Oceans* **123**, 8624–8637 (2018).
43. Griffies, S. Elements of the modular ocean model (MOM). *GFDL Ocean Group Tech. Rep.* **7**, 620 (2012).
44. Hunke, E. C., Lipscomb, W. H., Turner, A. K., Jeffrey, N. & Elliot, S. CICE: The Los Alamos Sea Ice Model, Documentation and Software User's Manual, Version 5.0. Tech. Rep. LA-CC-06-012, Los Alamos National Laboratory. (2013).
45. Craig, A., Valcke, S. & Coquart, L. Development and performance of a new version of the OASIS coupler, OASIS3-MCT_3.0. *Geosci. Model Dev.* **10**, 3297–3308 (2017).
46. Fairall, C., Bradley, E., Rogers, D., Edson, J. & Young, G. Bulk parameterization of air-sea fluxes for tropical ocean-global atmosphere coupled-ocean atmosphere response experiment. *J. Geophys. Res.: Oceans* **101**, 3747–3764 (1996).
47. Locarnini, R. A. et al. World Ocean Atlas 2013, Volume 1: Temperature (NOAA Atlas NESDIS 73, 2013).
48. Huang, B. et al. Extended reconstructed sea surface temperature version 4 (ERSST. v4). Part I: upgrades and intercomparisons. *J. Clim.* **28**, 911–930 (2015).
49. Power, S., Casey, T., Folland, C., Colman, A. & Mehta, V. Inter-decadal modulation of the impact of ENSO on Australia. *Clim. Dyn.* **15**, 319–324 (1999).
50. Saji, N., Goswami, B., Vinayachandran, P. & Yamagata, T. A dipole mode in the tropical Indian Ocean. *Nature* **401**, 360–363 (1999).
51. Morice, C. et al. An Updated Assessment of Near-Surface Temperature Change From 1850: The HadCRUT5 Data Set. *J. Geophys. Res.: Atmospheres* **126**, e2019JD032361 (2021).
52. Stewart, K. & Hogg, A. Southern Ocean heat and momentum uptake are sensitive to the vertical resolution at the ocean surface. *Ocean Model.* **143**, 101456 (2019).
53. Winton, M., Griffies, S., Samuels, B., Sarmiento, J. & Frölicher, T. Connecting Changing Ocean Circulation with Changing Climate. *J. Clim.* **26**, 2268–2278 (2013).
54. McDougall, T. Potential Enthalpy: A Conservative Oceanic Variable for Evaluating Heat Content and Heat Fluxes. *J. Phys. Oceanogr.* **33**, 945–963 (2003).
55. McDougall, T. & Barker, P. Getting started with TEOS-10 and the Gibbs Seawater (GSW) oceanographic toolbox. *SCOR/IAPSO WG* **127**, 1–28 (2011).
56. Holmes, R., Zika, J., Ferrari, R., Thompson, A., Newsom, E. & England, M. Atlantic Ocean Heat Transport Enabled by Indo-Pacific Heat Uptake and Mixing. *Geophys. Res. Lett.* **46**, 13939–13949 (2019).
57. Forget, G. & Ferreira, D. Global ocean heat transport dominated by heat export from the tropical Pacific. *Nat. Geosci.* **12**, 351–354 (2019).
58. Irving, D., Hobbs, W., Church, J. & Zika, J. A Mass and Energy Conservation Analysis of Drift in the CMIP6 Ensemble. *J. Clim.* **34**, 3157–3170 (2021).
59. Huguenin, M., Holmes, R. & England, M. Data and analysis scripts for: Drivers and distribution of global ocean heat content over the last half century (Zenodo, 2022).
60. Cheng, L. et al. Evolution of Ocean Heat Content Related to ENSO. *J. Clim.* **32**, 3529–3556 (2019).

Acknowledgements

We thank Hiroyuki Tsujino and Hakase Hayashida for providing access to the OMIP-2 model output, Damien Irving and Taimoor Sohail for calculating the CMIP6 time series and we thank the CMIP and Argo projects for providing access to their data sets. We thank the Consortium for Ocean-Sea Ice Modelling in Australia (COSIMA; www.cosima.org.au) for their technical help, continued development and for making the ACCESS-OM2 model available at https://github.com/COSIMA/access-om2. The simulations in this project were conducted with resources and services from the National Computational Infrastructure which is supported by the Australian Government. M.F.H. is supported by a Scientia PhD scholarship from the University of New South Wales (Program code 1476), R.M.H. is supported by the Australian Research Council (ARC) grant DE21010004 and M.H.E. is supported by the ARC Australian Centre for Excellence in Antarctic Science and is also supported by the Centre for Southern Hemisphere Oceans Research (CSHOR), a joint research centre between QNLM, CSIRO, UNSW and UTAS. Additionally, this work was supported by both the ARC Australian Centre for Excellence in Antarctic Science (ACEAS; ARC Grant No. SR200100008) and the ARC Centre of Excellence for Climate Extremes (CLEX; ARC Grant No. CE170100023).

Author contributions

M.F.H. performed the analyses and wrote the intial draft of the paper in discussion with R.M.H. and M.H.E. All authors formulated the experimental design, contributed to interpreting the results and refinement of the paper.

Competing interests

The authors declare no competing interests.

Additional information

Supplementary information The online version contains

supplementary material available at https://doi.org/10.1038/s41467-022-32540-5.

Correspondence and requests for materials should be addressed to Maurice F. Huguenin.

Peer review information *Nature Communications* thanks the anonymous reviewer(s) for their contribution to the peer review of this work. Peer reviewer reports are available.

Reprints and permission information is available at http://www.nature.com/reprints

B

Appendix to Part 2

A copy of the published article that constitutes the material in Part 2 is included hereafter:

Huguenin, M. F.[1, 2, 3], Holmes R. M.[2,3, 4] & England M. H.[2,3] *Journal of Climate*. (2020b). **33**:9945–9964. https://doi.org/10.1175/JCLI-D-20-0198.1

1. Institute for Atmospheric and Climate Science, ETH Zürich, Zürich, Switzerland 2. Climate Change Research Centre, University of New South Wales, Sydney, NSW, Australia 3. ARC Centre of Excellence in Climate Extremes, University of New South Wales, Sydney, NSW, Australia 4. School of Mathematics and Statistics, University of New South Wales, Sydney, NSW, Australia

Key Role of Diabatic Processes in Regulating Warm Water Volume Variability over ENSO Events

MAURICE F. HUGUENIN,[a,b] RYAN M. HOLMES,[b,c] AND MATTHEW H. ENGLAND[b]

[a] *Institute for Atmospheric and Climate Science, ETH Zurich, Zurich, Switzerland;* [b] *Climate Change Research Centre, and ARC Centre of Excellence for Climate System Science, University of New South Wales, Sydney, New South Wales, Australia;* [c] *School of Mathematics and Statistics, University of New South Wales, Sydney, New South Wales, Australia*

(Manuscript received 19 March 2020, in final form 5 August 2020)

ABSTRACT: The equatorial Pacific warm water volume (WWV), defined as the volume of water warmer than 20°C near the equator, is a key predictor for El Niño–Southern Oscillation (ENSO), and yet much about the individual processes that influence it remains unknown. In this study, we conduct idealized ENSO simulations forced with symmetric El Niño– and La Niña–associated atmospheric anomalies as well as a historical 1979–2016 hindcast simulation. We use the water mass transformation framework to examine the individual contributions of diabatic and adiabatic processes to changes in WWV. We find that in both sets of simulations, El Niño's discharge and La Niña's recharge periods are initiated by diabatic fluxes of volume across the 20°C isotherm associated with changes in surface forcing and vertical mixing. Changes in adiabatic horizontal volume transport above 20°C between the equator and subtropical latitudes dominate at a later stage. While surface forcing and vertical mixing deplete WWV during El Niño, surface forcing during La Niña drives a large increase partially compensated for by a decrease driven by vertical mixing. On average, the ratio of diabatic to adiabatic contributions to changes in WWV during El Niño is about 40% to 60%; during La Niña this ratio changes to 75% to 25%. The increased importance of the diabatic processes during La Niña, especially the surface heat fluxes, is linked to the shoaling of the 20°C isotherm in the eastern equatorial Pacific and is a major source of asymmetry between the two ENSO phases, even in the idealized simulations where the wind forcing and adiabatic fluxes are symmetric.

KEYWORDS: Dynamics; ENSO; Ocean circulation; Diabatic heating; Climate models; Interannual variability

1. Introduction

El Niño–Southern Oscillation (ENSO) is a coupled ocean–atmosphere phenomenon in the equatorial Pacific that dominates variability in Earth's climate system on the interannual time scale. Although ENSO's key dynamics are found in the tropical Pacific, its impacts occur on a global scale. The instrumental record of global surface air temperature (SAT) shows the dominant role of ENSO during recent periods of warming and cooling (Trenberth et al. 2007; Hartmann et al. 2013). High sea surface temperature (SST) values in the equatorial Pacific during the 1997/98 El Niño increased global SAT by 0.2°–0.64°C (depending on the data product; Reynolds et al. 2007; Morice et al. 2012), while global SAT decreases during La Niña events (Reynolds et al. 2007; Meehl et al. 2011; Roemmich and Gilson 2011).

As a result of its profound socioeconomic and environmental impacts (e.g., see Diaz et al. 2001; Collins et al. 2010; Timmermann et al. 2018), an increased understanding of ENSO's underlying dynamics and key metrics is necessary. Warm water volume (WWV; defined as the volume of water above the 20°C isotherm in the equatorial region 120°E−80°W, 5°N–5°S) is one such metric, and is commonly used to forecast ENSO events as it leads eastern Pacific SST anomalies by 6–8 months (Bosc and Delcroix 2008; McPhaden 2012; Neske and McGregor 2018). Since its suggestion as a key ingredient in ENSO dynamics by Wyrtki (1975, 1985), the warm water volume has played a key role in many conceptual theories of ENSO, such as the discharge/recharge oscillator theory (Suarez and Schopf 1988; Jin 1997a,b; Burgers et al. 2005). In recent decades, WWV has been established as an integral component of many analyses, models, and statistical forecast schemes for ENSO (e.g., Meinen and McPhaden 2000; Izumo et al. 2018; Timmermann et al. 2018). However, knowledge of the precise mechanisms influencing WWV remains limited. The goal of this study is to analyze the relative importance of the various processes leading to changes in WWV.

Over a typical ENSO cycle, WWV undergoes discharge and recharge phases resulting from both adiabatic and diabatic volume fluxes. Adiabatic volume fluxes change WWV through horizontal transport (above the 20°C isotherm) into or out of the WWV region, or through surface volume fluxes due to precipitation, evaporation, and river runoff (Lengaigne et al. 2012). Diabatic processes induce WWV changes via water mass transformation (WMT) with heating/cooling of water near 20°C leading to a change in the temperature of that water, and thus a movement of volume across the 20°C isotherm (Walin 1982; Large and Nurser 2001; Groeskamp et al. 2019; Holmes et al. 2019a).

There are two main diabatic processes that alter WWV; first, the surface heat flux, comprising the radiative, sensible, and latent heat fluxes, changes the temperature of water masses in the surface layers resulting in across-isotherm volume fluxes. The surface heat flux is strongly dependent on SST, with enhanced heat loss occurring over warm SSTs. During the build-up phase of El Niño the equatorial Pacific accumulates heat, which following the peak of the event is subsequently discharged to extratropical latitudes, from where it is radiated back into the atmosphere or into space (Trenberth et al. 2002)

Corresponding author: Maurice F. Huguenin, m.huguenin-virchaux@unsw.edu.au

DOI: 10.1175/JCLI-D-20-0198.1

and also discharged into deeper ocean layers (Roemmich and Gilson 2011; Johnson and Birnbaum 2017; Wu et al. 2019). The other important diabatic process relates to small-scale turbulent mixing, which can also drive significant across-isotherm volume fluxes. Turbulent mixing is an important component of the cold tongue SST budget and contributes to changes in SST over a range of time scales (Moum et al. 2013; Bernie et al. 2005). Strong turbulence in the equatorial Pacific associated with the large vertical shear above the eastward flowing Equatorial Undercurrent (EUC) mixes the warmer surface waters with cold upwelled waters (Smyth and Moum 2013) and, depending on depth, leads to diabatic volume exchanges across the 20°C isotherm. This turbulence also plays an important role in the global ocean's heat budget by moving heat into deeper, colder layers that connect with the deep ocean's overturning circulation (Holmes et al. 2019b). The dynamics of upper equatorial turbulence are complex, being influenced by processes such as the diurnal cycle, tropical instability waves, the seasonal cycle, equatorial Kelvin waves, and ENSO events themselves (Gregg et al. 1985; Lien et al. 1995; Smyth and Moum 2013; Holmes and Thomas 2015; Pham et al. 2017; Warner and Moum 2019). Additionally, a third diabatic volume flux arises in numerical climate models: numerical mixing, emerging from truncation errors in the model's advection scheme (Holmes et al. 2019a).

While the role of adiabatic fluxes during discharge and recharge periods is relatively well understood based on data from the Tropical Atmosphere and Ocean Array (see, e.g., Meinen and McPhaden 2000, 2001) and modeling studies (see, e.g., McGregor et al. 2013, 2014), much about the diabatic processes remains unknown and will be the focus here. While studies by Meinen and McPhaden (2000), Clarke et al. (2007), and Lengaigne et al. (2012) agree that diabatic processes are important contributors to WWV changes, the observation-based study by Bosc and Delcroix (2008) and the modeling study by Brown and Fedorov (2010) suggest that diabatic volume changes on ENSO-related time scales are negligible, thus highlighting the importance for further analyses with other models and datasets. Lengaigne et al. (2012) suggests that diabatic fluxes may also explain some of the asymmetries and nonlinearities in ENSO's underlying dynamics, highlighting the need for a more in-depth analysis of the WWV budget in an idealized setting where asymmetries are controlled. In most studies so far, either vertical (and in modeling studies additionally numerical) mixing or both surface forcing and vertical mixing fluxes were inferred by using a residual. Here, we use the WMT framework (Walin 1982; Large and Nurser 2001; Holmes et al. 2019a; Groeskamp et al. 2019) in temperature space applied online within a global ocean model to diagnose the diabatic terms directly during idealized, symmetric ENSO events as well as during a hindcast simulation over the 1979–2016 period.

The rest of this paper is organized as follows: in section 2, the ocean model, atmospheric forcing, and experimental design are described. To simulate idealized ENSO events and examine asymmetries, an approach using empirical orthogonal functions (EOFs) similar to McGregor et al. (2014) is used. In section 3 we discuss ocean-sourced asymmetries in standard ENSO metrics arising from these idealized simulations where the atmospheric forcing is symmetric. Section 4 introduces the theoretical aspects of the WWV budget and how it is diagnosed within the models. After investigating the climatological WWV budget in section 5, we take a closer look at the anomalies during the idealized discharge and recharge phases of ENSO (section 6). We then compare the WWV budget terms from the idealized simulations to the event-to-event variability over the 1979–2016 period (section 8) before summarizing our results and their implications (section 9).

2. Model, data, and methods

a. The ocean–sea ice model

In this study, we use a 1/4° global ocean model with 50 $z*$ vertical levels based on the ocean component of the Geophysical Fluid Dynamics Laboratory (GFDL) CM2.5 coupled climate model (Delworth et al. 2012; Griffies 2012). Atmospheric forcing for the model is derived from a prescribed atmospheric state (sections 2b and 2c) using eight fields to calculate zonal and meridional wind stress, and surface heat and freshwater fluxes using bulk formulas (Fairall et al. 1996). The eight atmospheric fields are zonal and meridional wind speed, air temperature, and specific humidity at 10 m, and downward longwave and shortwave radiation, precipitation, and sea level pressure at the ocean's surface. Vertical diffusion is parameterized using the K-profile parameterization scheme (KPP; Large et al. 1994). The model can be considered eddy-resolving in the tropics (Hallberg 2013; Jochum et al. 2008). In the baseline model, there is no explicit horizontal diffusion of tracer gradients and thus sharp lateral tracer gradients are smoothed by the numerical advection scheme. The associated diffusion is termed "numerical mixing" as discussed further in section 4 and in Holmes et al. (2019a). More information and discussion on the model details, diffusive mixing parameterizations, and the model performance can be found in Spence et al. (2017), Stewart et al. (2017), and Holmes et al. (2019a).

b. Forcing for the idealized, symmetric simulations

For the idealized simulations, the model was spun up over a 500-yr period using the climatological Coordinated Ocean-ice Reference Experiment Normal Year Forcing (CORE-NYF; Large and Yeager 2004). For our idealized simulations, we add ENSO-related perturbations derived from the European Centre for Medium-Range Weather Forecasts' (ECMWF's) ERA-Interim product for 1979–2016 (Dee et al. 2011) to the base CORE-NYF fields.

Our perturbation experiments are constructed to isolate the most important aspects of ENSO variability in the atmospheric forcing (as quantified by the leading two EOFs of monthly tropical Pacific wind stress variability) to isolate oceanic-sourced asymmetries. Following the approach by McGregor et al. (2013, 2014), we first regress NOAA's ERSST v4 Niño-3.4 (N34) index (Smith and Reynolds (2003), calculated as the SST deviation in the equatorial region 170°–120°W, 5°N–5°S onto the ERA-Interim wind stress anomalies from 1979 to 2016. This regression yields the spatial pattern of wind stress anomalies that are linearly associated with El Niño ($X_{1,\tau}$;

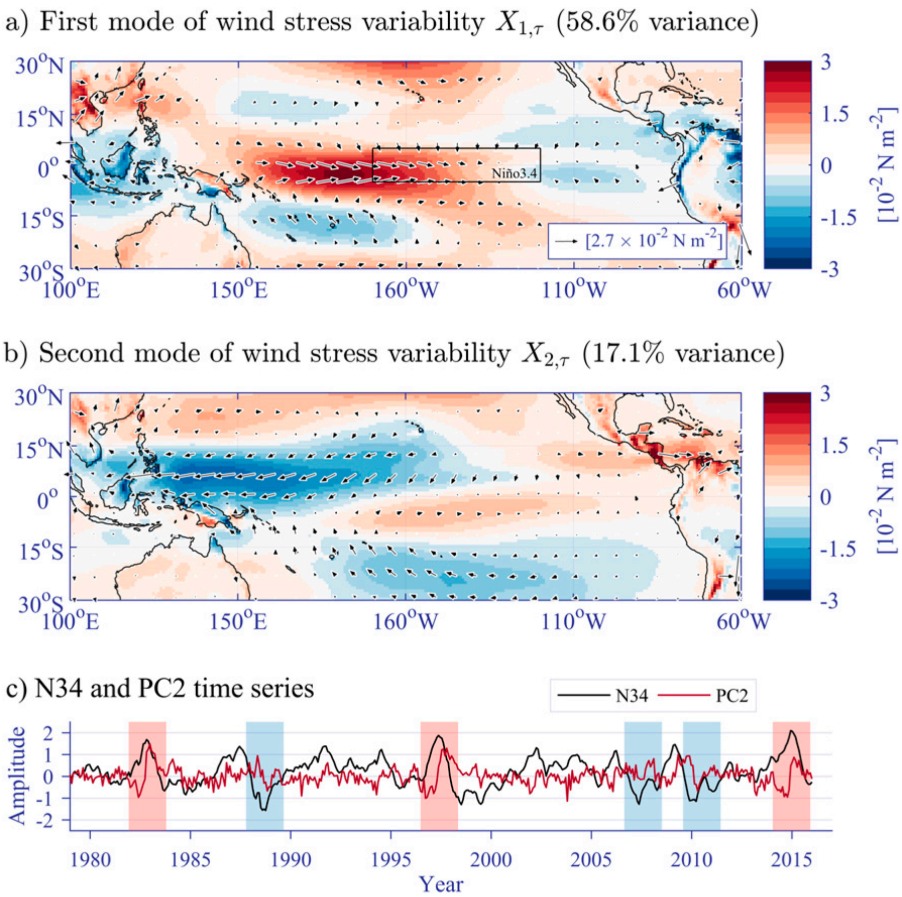

FIG. 1. The (a) first and (b) second mode of wind stress variability related to ENSO from the ERA-Interim product (10^{-2} N m^{-2}). The zonal wind stress component is shaded. The Niño-3.4 area (170°–120°W and 5°N–5°S) is indicated as the framed area in (a). (c) The associated time series with the observed N34 (Reynolds et al. 2007) in black and PC2 in red. The red and blue shaded areas in (c) indicate the three strongest El Niño and La Niña events, each covering a 24-month period centered around the peak N34 anomalies.

Fig. 1a). This pattern captures the weakening of the Walker circulation during an El Niño event and is characterized by westerly wind stress anomalies in the western tropical Pacific, with slightly larger values in the Southern Hemisphere. Calculating the first EOF of equatorial wind stress anomalies instead of regressing N34 gives a time series that is highly correlated with N34 (correlation coefficient $r = 0.76$). As in McGregor et al. (2014) we use the smoother N34 time series here. This first mode captures 58.6% of the wind stress variability in the equatorial region.

To calculate the second pattern, the anomalies associated with $X_{1,\tau}$ and N34 are removed from the wind stress anomaly time series at each spatial location and the first EOF of the residual wind stress over the tropical Pacific region 100°E−60°W, 10°N–10°S is calculated [as in McGregor et al. (2014)]. The resulting wind stress pattern ($X_{2,\tau}$; Fig. 1b) and its associated principal component time series (PC2; Fig. 1c) capture a strong meridional gradient of zonal wind anomalies across the equator and play a crucial role in the winds' nonlinearity related to ENSO (Zeller et al. 2019). This mode gains importance when it changes sign during the peak of El Niño and initiates a southward shift of the westerly wind anomalies (Fig. 1c, McGregor et al. 2013; Stuecker et al. 2013). The resulting Ekman-induced transport is much higher in the Northern than in the Southern Hemisphere, leading to an equatorial divergence of water masses (McGregor et al. 2014; Stuecker et al. 2015; Timmermann et al. 2018). This second mode drives 17.1% of the variability within the residual wind stress anomalies; combined, the first two EOF patterns explain 75.7% of the total wind stress variability within the ERA-Interim dataset.

McGregor et al. (2014) used the two time series N34 and PC2 (Fig. 1c) from observations to simulate the variability of the tropical Pacific over the time period 1979–2011. Instead of using the full time series, we construct idealized synthetic time series for N34 and PC2 from the three strongest El Niño events as a basis to simulate isolated symmetric El Niño and La Niña events (i.e., we only use the time series during the red shaded periods in Fig. 1c). For our first experiments, the evolution of N34 and PC2 during the three strongest El Niño events for 1979–2016 are composited and centered at their peak in December (i.e., month 12; Fig. 2). Fourth-order polynomials are fitted to the mean of these three events and slowly evolve

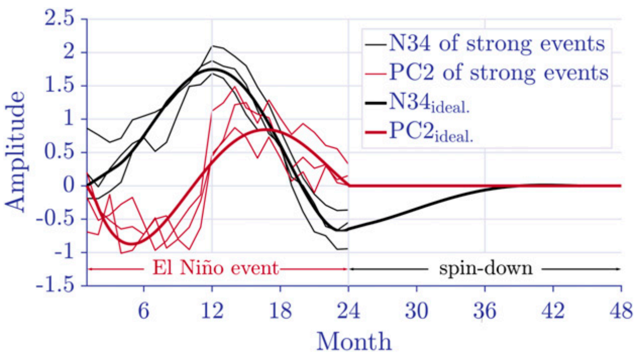

FIG. 2. The idealized synthetic time series in bold for N34 (black) and PC2 (red) during the 2-yr-long El Niño event followed by a 2-yr-long spindown period. The thin lines show the observed N34 values (black) and the calculated PC2 time series (red) during the three strongest El Niño events in Fig. 1c, namely 1982/83, 1997/98, and 2014–16, centered in December.

in a way that approximates the mean of the three strong ENSO events (bold lines in Fig. 2). The polynomials are constrained to start close to zero, thereby requiring minimal adjustment at the beginning in order to achieve a smooth event onset. In addition, the N34 time series is adjusted to slowly return to zero during a spindown period of two years following the event (months 24–48), while the PC2 time series is zero during the full spindown period (Fig. 2). We also simulate a symmetric ''La Niña'' event, where the time series are simply set to negative amplitude with respect to the El Niño case. This allows us to investigate any asymmetric responses resulting from ocean-sourced nonlinearities in the presence of symmetric atmospheric forcing.

The atmospheric fields that force the model are then derived using regressions of the N34 index and PC2 time series as described in the appendix. To increase the signal-to-noise ratio, ensemble simulations were also performed. However we found that differences between the ensemble members are more than two orders of magnitude smaller than the variability in the ensemble mean, and so we only present results from one ensemble member. We calculate the anomalies relative to the time-mean fields of eight years in the control simulation, except for ocean heat content where we subtract the time-varying control simulation to better account for the drift in the 200–2000-m layers.

c. Interannual model simulation

We follow up our idealized, symmetric ENSO simulations with an interannual hindcast simulation for the period 1979–2016 with an updated configuration of the model (Kiss et al. 2020). The forcing for this configuration is from the JRA55-do v1.3 reanalysis for 1958–2018 (Tsujino et al. 2018) and the spinup was performed by using five repeat cycles of JRA55-do (Kiss et al. 2020). The resolution and model physics in this configuration are identical to the base model, except that it uses an updated 50-level vertical grid and it includes the Gent and McWilliams (1990) parameterization for mesoscale eddies as well as explicit Redi (1982) along-isopycnal diffusion. However, these parameterizations are scaled with latitude and neither plays an important role in the tropics. For our analysis, we analyze the 1979–2016 period of the last cycle where the online WMT diagnostics are output.

3. ENSO's ocean-sourced anomalies during idealized events

In this section, we first discuss the ocean-sourced anomalies and asymmetries in our idealized symmetrically forced El Niño and La Niña simulation before following up with an in-depth analysis of the WWV budget.

Although ENSO's anomalies are strongest in the Pacific, they have impacts on a global scale (e.g., Roemmich and Gilson 2011; Wu et al. 2019; Cheng et al. 2019). Global mean sea surface temperature (GMSST) anomalies during the strong El Niño 1997–98 exceeded 0.2°C in NOAA's OI SST V2 dataset (Reynolds et al. 2007; Roemmich and Gilson 2011). This is mostly caused by the warm eastern equatorial Pacific during El Niño. In our idealized El Niño simulation, maximum GMSST anomalies are reached in December, with a value of 0.092°C (blue line, Fig. 3a). These anomalies are lower than the 0.2°C in NOAA's OI SST v2 product, but expected as our idealized simulation is based on composite events.

The N34 index explains a large part of the increase in GMSST (light blue line in Fig. 3c). The maximum value of the N34 index (1.57°C), is slightly lower than given by the idealized time series (dashed line Fig. 3c), which is not unexpected since SST is determined dynamically within the model. In the last four months of the El Niño event (months 20–24), both the idealized and modeled N34 anomalies are negative, indicating a change to developing La Niña–like conditions. This represents the discharged state of the tropical Pacific at the end of the El Niño event. To first order, the anomalies in the La Niña simulation (Figs. 3b,d) are opposite to the El Niño event. In particular, the N34 index and GMSST anomalies are close to the exact opposite during La Niña, with only a slightly increased amplitude (Fig. 3).

The rate of change of the ocean's heat content (OHC) is highest when both GMSST and the N34 index peak at month 12 (orange line, Fig. 3a). As expected, this suggests that the warmest equatorial Pacific SST values coincide with the highest anomalous surface heat fluxes into the atmosphere during El Niño [and opposite for month 12 during La Niña in Fig. 4, as in Meinen and McPhaden (2001); Johnson and Birnbaum 2017; Cheng et al. 2019]. The global ocean's heat release continues until month 20 of the simulation when equatorial SSTs and surface heat fluxes return to neutral conditions. The WWV anomalies as a proxy for the upper equatorial OHC show a similar behavior as the global OHC anomalies, with discharge during El Niño lasting 15 months and recharge occurring over a period of 14 months during La Niña (red line, Figs. 3c,d). Unlike OHC, the anomalous WWV time series shows a considerable positive and negative peak prior to the peak of El Niño and La Niña. This behavior is caused by the first EOF mode of wind stress anomalies initiating an equatorward surface Ekman transport during El Niño, while causing a poleward transport during La Niña (McGregor et al. 2014). The surface Ekman transport during this stage is more dominant than the subsurface geostrophic transport of the opposing sign,

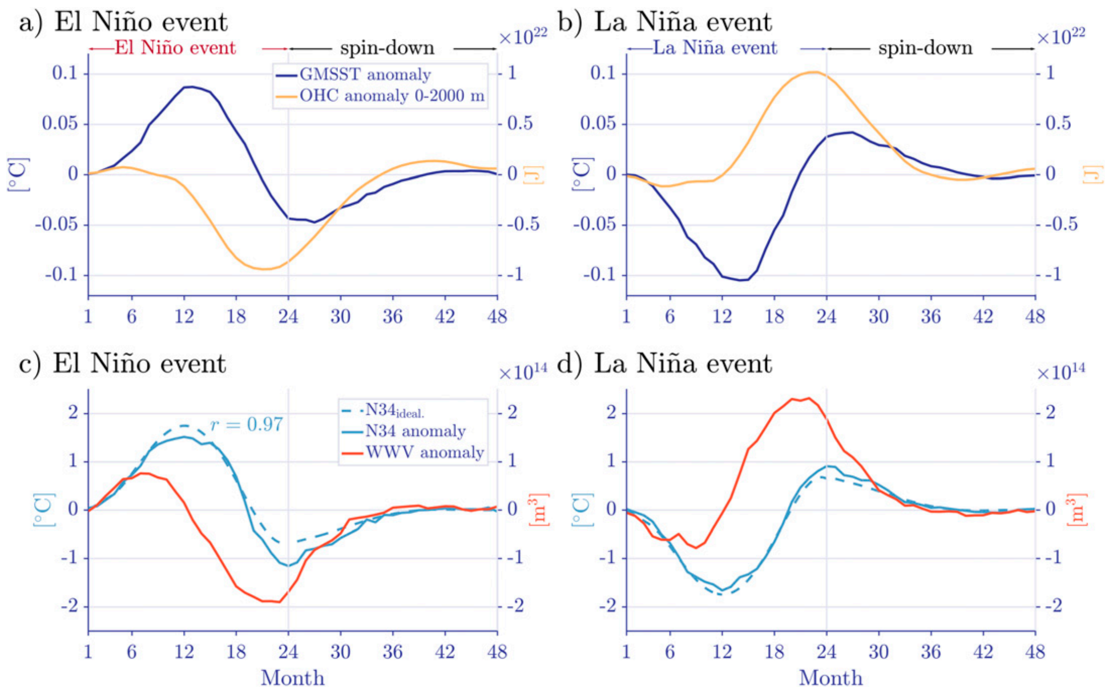

FIG. 3. Anomalous time series for the (a),(b) global mean sea surface temperature (GMSST; °C) and globally integrated ocean heat content (OHC; J) as well as (c),(d) the idealized N34 index, the simulated N34 index (°C), and the WWV anomalies (m^3) during the idealized and symmetric El Niño and La Niña events. In (c) the correlation coefficient (r) between the observed and simulated N34 index is shown in blue. The vertical lines at month 24 represent the end of the event and the subsequent start of the 2-yr-long spindown period with climatological forcing.

effectively causing a recharge and discharge of WWV (McGregor et al. 2014). The global OHC anomalies do not show this distinct increase or decrease prior to the peak of the events. The WWV anomalies before the discharge phase (Fig. 3c) are lower compared to those in Meinen and McPhaden (2000) and likely caused by the weaker build-up prior to the event due to the transition from climatological forcing.

Additionally, our idealized experimental design also contains the following simplifications that could each contribute to deviations from observed events. 1) We use NOAA's ERSST

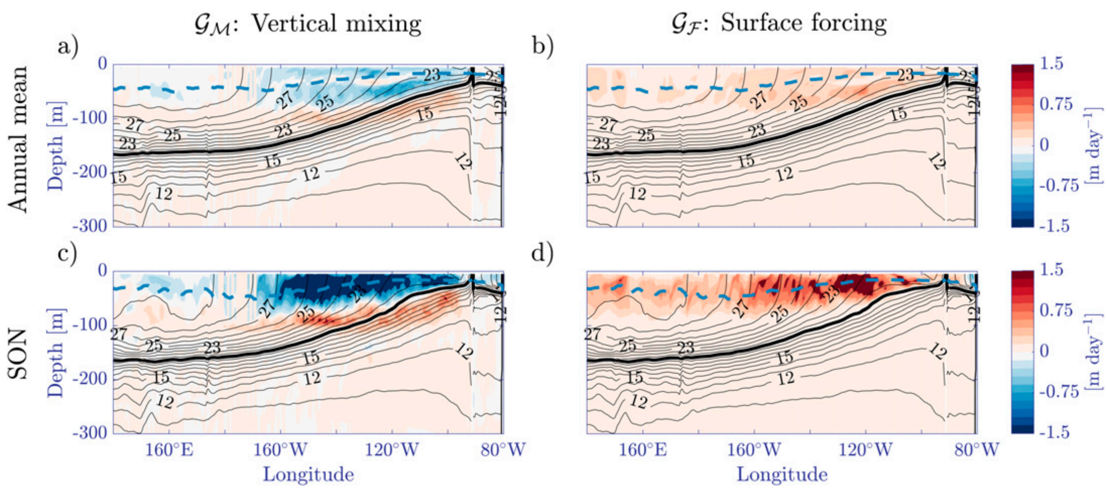

FIG. 4. Depth–longitude transects across the equatorial Pacific of the water mass transformation velocities [Eqs. (3) and (2)] for (a),(c) vertical mixing $\mathcal{G}_{\mathcal{M}}$ and (b),(d) surface forcing $\mathcal{G}_{\mathcal{F}}$ (m day^{-1}) in the CORE-NYF control simulation. The WMT velocities are accumulated in temperature space and remapped to depth using the mean isotherm depths. The upper two panels show the annual mean and the lower panels the mean over the September–November (SON) period when the diabatic fluxes are seasonally intense (Fig. 5b). The contours show the distribution of the equatorial isotherms with the 20°C isotherm in bold. The dashed blue line in the uppermost layers indicates the mixed layer depth defined as a 0.032 kg m^{-3} density difference from the surface. The discontinuity at 90°W is caused by the model's bathymetry near the Galápagos Islands.

v4 N34 index as in McGregor et al. (2014) to derive the atmospheric forcing. This index, in particular during strong El Niño events, is weaker than the same index in the ERA-Interim reanalysis (Dee et al. 2011) and HadISST (Rayner et al. 2003) products as it has larger parametric uncertainties at smaller spatial and shorter time scales (including for ENSO events, Liu et al. 2015; McGregor et al. 2017). 2) We force the model in these simulation with an interpolated atmospheric field from monthly-averaged anomalies and a grid resolution of 220 km, and thus do not fully capture high-frequency variability such as westerly wind events, which are known to impact WWV anomalies (Menkes et al. 2014). 3) In our simulations, we use only the first two EOF modes of equatorial wind stress anomalies associated with El Niño, which account for 75% of the total variance. Despite these approximations, the idealized simulations are able to reproduce the key physical processes throughout ENSO.

4. The warm water volume budget

In this section we give a brief theoretical introduction into the WWV budget and how it is constructed within the model experiments. We define WWV as the volume of water above the 20°C isotherm in the area between Borneo (116°30′E), the South American coastline (78°W) and 5°N–5°S. This WWV definition has been previously used in studies by Meinen and McPhaden (2000), Lengaigne et al. (2012), McGregor et al. (2014), and others. We define the Indonesian Throughflow (ITF) as the transport between Borneo (116°30′E) and New Guinea (133°45′E) at 2°S.

To understand and diagnose the WWV budget, we not only evaluate horizontal adiabatic volume fluxes, but also evaluate how volume is exchanged vertically across the 20°C isotherm. Across-isotherm volume fluxes can be studied by using the WMT framework, first introduced by Walin (1982). It describes the processes that lead to a given water parcel's change in temperature and subsequent movement across isotherms.

Changes in WWV over time are dependent on both adiabatic and diabatic processes:

$$\frac{d\mathrm{WWV}}{dt} = \underbrace{\mathcal{T}_{5°\mathrm{N}+5°\mathrm{S}} + \mathcal{T}_{\mathrm{ITF}} + \mathcal{J}}_{\text{Adiabatic processes}} + \underbrace{\mathcal{G}_{\mathcal{F}} + \mathcal{G}_{\mathcal{M}} + \mathcal{G}_{\mathcal{I}}}_{\text{Diabatic processes}}, \quad (1)$$

where $d\mathrm{WWV}/dt$ is the WWV tendency ($\mathrm{m^3\,s^{-1}}$), calculated by using snapshots of the temperature field at the beginning and end of each month [the period over which the right-hand side diagnostics in Eq. (1) are accumulated online]. The adiabatic processes include the lateral transport of water masses above 20°C into and out of the WWV region across the three transects 5°N, 5°S ($\mathcal{T}_{5°\mathrm{N}+5°\mathrm{S}}$), and the ITF ($\mathcal{T}_{\mathrm{ITF}}$; $\mathrm{m^3\,s^{-1}}$). In addition, the surface volume flux $\mathcal{J}$ ($\mathrm{m^3\,s^{-1}}$) accounts for small adiabatic volume changes due to river runoff, precipitation, and evaporation of water above 20°C when freshwater enters or leaves the ocean at the sea surface. The surface volume fluxes in the model enter and exit the ocean at the sea surface temperature (Holmes et al. 2019a). Thus, there is no additional sensible heat flux into the ocean associated with differences in temperature between the freshwater and the surface seawater. Therefore, in the model, these fluxes are considered adiabatic. These adiabatic variables are diagnosed by summing the associated transports over all temperature classes warmer than 20°C. The calculations (i.e., the binning into temperature classes) take place online at every time step of the model simulation. Here we show the monthly accumulated averages of these online diagnostics.

The three diabatic WMT volume fluxes include surface forcing $\mathcal{G}_{\mathcal{F}}$, vertical mixing $\mathcal{G}_{\mathcal{M}}$, and numerical mixing $\mathcal{G}_{\mathcal{I}}$, each expressed in units of meters cubed per second ($\mathrm{m^3\,s^{-1}}$). The surface forcing volume flux $\mathcal{G}_{\mathcal{F}}$ across the 20°C isotherm is driven by the surface heat flux and its different components (shortwave, longwave, sensible, and latent heat fluxes). The term $\mathcal{G}_{\mathcal{F}}$ is the convergence of these heat fluxes within a given temperature class, which indicates fluid warming and therefore crossing isotherms toward warmer or colder fluid. Likewise, $\mathcal{G}_{\mathcal{M}}$ is the WMT volume flux arising from parameterized diffusive vertical mixing processes. Through heating and cooling fluid, diffusive mixing likewise moves water across temperatures classes. These two WMT fluxes are calculated as diagnostics from the heat budget binned into temperature space (Holmes et al. 2019a), and depend on the across-isotherm heat fluxes through

$$\mathcal{G}_{\mathcal{F}} = \frac{1}{\rho_0 C_p} \iint \left.\frac{\partial \mathcal{F}}{\partial \Theta}\right|_{20°\mathrm{C}} dA, \quad (2)$$

$$\mathcal{G}_{\mathcal{M}} = \frac{1}{\rho_0 C_p} \iint \left.\frac{\partial \mathcal{M}}{\partial \Theta}\right|_{20°\mathrm{C}} dA. \quad (3)$$

Here, ρ_0 is the reference density of seawater ($1035\,\mathrm{kg\,m^{-3}}$), C_p is the specific heat capacity of seawater at constant pressure ($3992.1\,\mathrm{J\,kg^{-1}\,K^{-1}}$), and $\mathcal{F}$ is the total surface heat flux ($\mathrm{W\,m^{-2}}$) into all fluid warmer than a given potential temperature Θ at each horizontal location (taking into account the penetration of shortwave radiation into the interior). Similarly, $\mathcal{M}$ is the total heat flux into all fluid warmer than Θ at each horizontal location due to vertical diffusion and the nonlocal heat flux component of the KPP boundary layer mixing scheme ($\mathrm{W\,m^{-2}}$) of Large and Yeager (2004), although this nonlocal term plays a minor role. Both $\mathcal{F}$ and $\mathcal{M}$ are diagnosed online by binning the corresponding Eulerian heat budget diagnostics into temperature classes at every time step. The temperature bin size is 0.5°C. We evaluate the WWV budget at 20°C and the area integral is performed over the WWV region (116°30′E−78°W, 5°N–5°S). More details on the numerical implementation of these WMT diagnostics are presented in Holmes et al. (2019a).

Last, the WMT flux $\mathcal{G}_{\mathcal{I}}$ arises from numerical diffusion associated with truncation errors in the model's tracer advection scheme (i.e., numerical mixing). The advection scheme is three-dimensional and acts to smooth both vertical and horizontal tracer gradients at the grid scale (Colella and Woodward 1984). Due to choices made to minimize sources of explicit diffusion (namely, zero explicit lateral diffusion or background vertical diffusivity), numerical diffusion makes a nonnegligible contribution to the global climatological heat budget (Holmes

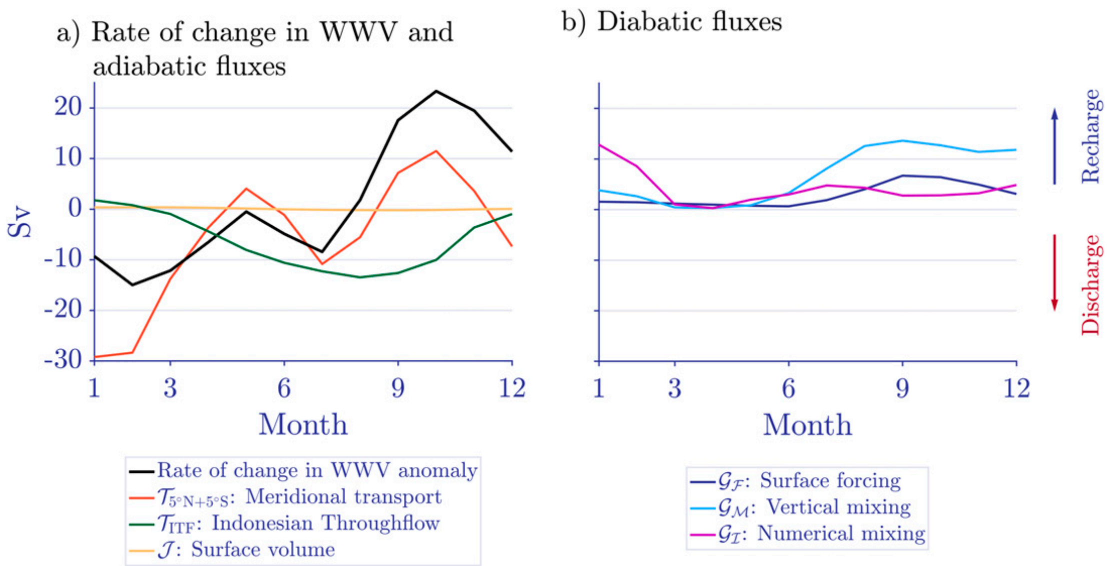

FIG. 5. Annual cycle of the climatological (a) adiabatic and (b) diabatic WWV budget terms (Sv) in the CORE-NYF control simulation. The change in WWV as the sum of the other fluxes is shown as the black line in (a). Positive values indicate a volume flux into the WWV region (i.e., a recharge) and negative values indicate a volume flux out of the region (i.e., a discharge). A 3-month running mean has been applied.

et al. (2019a); their Fig. 3) and the WWV budget. We calculate $\mathcal{G}_{\mathcal{I}}$ as the residual of Eq. (1).

The WWV budget additionally includes terms associated with the parameterization of submesoscale eddies (Fox-Kemper et al. 2008) and, in the 1979–2016 hindcast simulation, mesoscale eddies (Redi 1982; Gent and McWilliams 1990). These fluxes make negligible contributions to the WWV budget but are included in our calculation as $\mathcal{G}_{\mathcal{E}}$ (eddy mixing) in order to accurately calculate numerical mixing as the residual.

5. The climatological warm water volume budget

Before our analysis of the anomalous WWV budget terms during ENSO, we first investigate its climatology as the anomalous fluxes are tightly linked to the seasonal cycle.

The climatological WWV in the control simulation exhibits a small long-term spinup trend of $9.1 \times 10^{12}\,m^3\,yr^{-1}$ (equivalent to 0.28 Sv; 1 Sv $\equiv 10^6\,m^3\,s^{-1}$). It is closely linked to the equatorial overturning circulation and comprises a balance between the adiabatic and diabatic fluxes. Vertical mixing in the annual mean cools surface water masses and simultaneously warms deeper layers, represented by the negative (blue) and positive (red) across-isotherm (or diathermal) velocity regions in Fig. 4a. Surface forcing is consistently warming the surface region (Fig. 4b). The annual mean 20°C isotherm is positioned on average in the warming region of both diabatic fluxes, indicating a net upward volume flux across the isotherm into the WWV above. Thus, vertical mixing (+6.7 Sv) and surface forcing (+2.7 Sv) both show positive contributions to the annual mean budget. Numerical mixing plays only a minor role. The convergent diathermal transport is balanced by negative contributions from the predominantly eastward trade winds driving a divergent Ekman transport across 5°N and 5°S (−6.1 Sv) and transport through the ITF (−6.2 Sv; Schott et al. 2004). The impact of the surface volume flux is negligible compared to the other terms (as in Meinen and McPhaden 2001; Lengaigne et al. 2012; Brown and Fedorov 2010) and will not be discussed further.

These processes (both adiabatic and diabatic) have a seasonal cycle linked to the strength of the equatorial trade winds (Horel 1982). The WWV peaks near the end of the year, increasing in the second half of the year, and decreasing in the first half (black line Fig. 5a). While meridional transport explains part of the WWV recharge in the second half of the year, most of this increase stems from the enhanced diabatic fluxes (Fig. 5b). The stronger trade winds in the second half of the year increase upwelling of cold water masses, shoaling of the 20°C isotherm and heat absorption from the atmosphere (Fig. 4d). At the same time, shear- and wind-driven turbulence in the upper EUC intensifies, driving stronger diabatic upwelling via vertical mixing across the shallower 20°C isotherm (Fig. 4c; Moum et al. 2013; Liu et al. 2016). Combined, the two diabatic fluxes result in positive diathermal velocities across the 20°C isotherm in the eastern equatorial Pacific and an increase in WWV (i.e., the sum of Figs. 4c and 4d results in an overall positive, red spatial pattern). Further, the stronger trade winds also cause an increased sea surface height (SSH) difference between the Indian and Pacific Ocean leading to an increased strength of the ITF, which partially offsets the two diabatic fluxes in the second half of the year (green line, Fig. 5a; Shinoda et al. 2012).

6. The warm water volume budget during idealized ENSO events

We now examine the anomalous WWV budget terms and asymmetries during the idealized, symmetric events before comparing them to events in the hindcast simulation. Over the

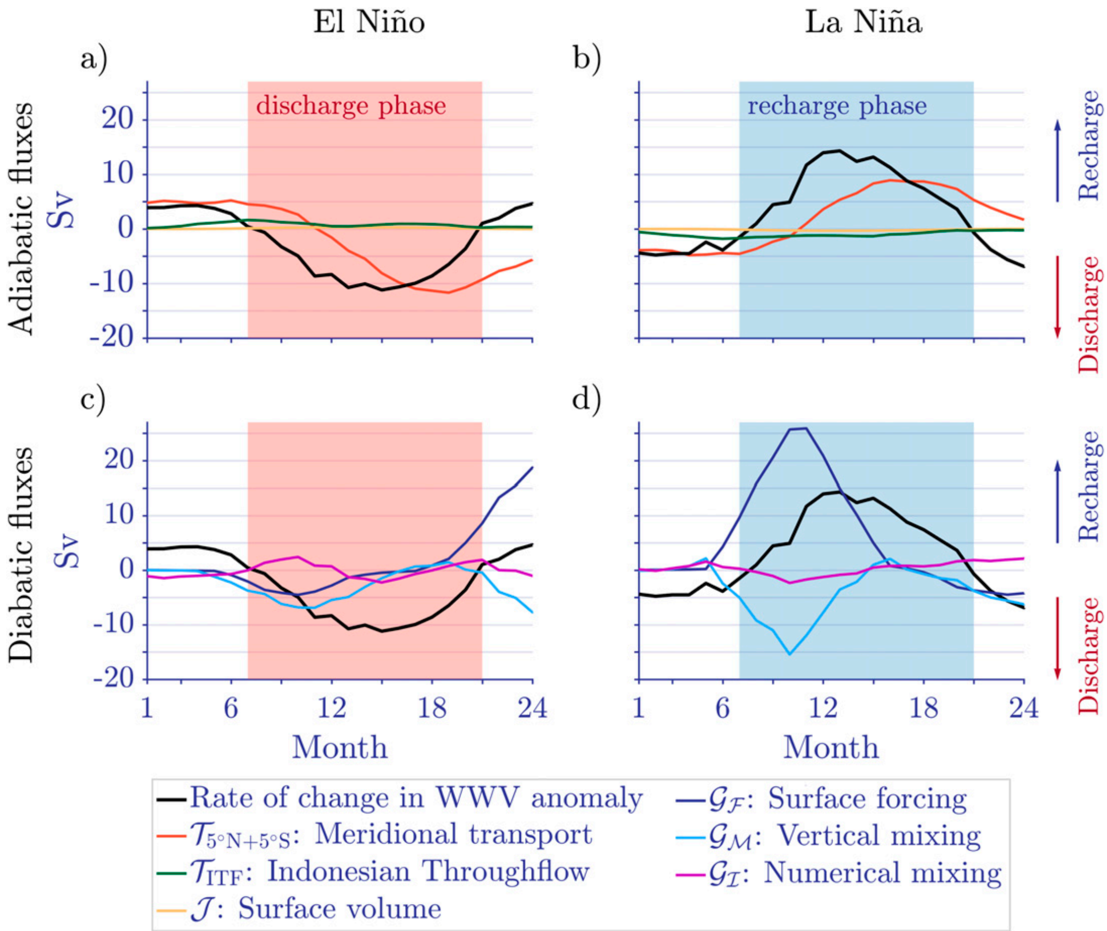

FIG. 6. The (a),(b) adiabatic and (c),(d) diabatic WWV budget terms (Sv) as anomalies throughout the idealized, symmetric El Niño and La Niña simulations. A 5-month running mean as in Meinen and McPhaden (2000) has been applied. The discharge phase [red shaded period in (a)] is defined as the period when the change in WWV is negative from months 7–21. To ensure a symmetric analysis during La Niña, the recharge phase (blue shaded period) covers the same period. Positive values indicate volume transport into the WWV region (i.e., a recharge), negative values represent transport out of the WWV region (i.e., a discharge).

ENSO cycle, WWV undergoes changes associated with the recharge and discharge of heat. We define the discharge phase during the idealized El Niño as the period when the WWV anomaly is decreasing; that is, the rate of change in WWV is negative (red shaded period from months 7 to 21; Figs. 6a,c). To ensure a symmetric analysis, we define the recharge phase during La Niña as the same time period (blue shading, Figs. 6b,d). The anomalies are calculated by subtracting off the climatological budget discussed in the previous section.

a. The idealized symmetric El Niño discharge

The discharge phase during El Niño is initiated in July when the rate of change in the WWV anomaly becomes negative (Fig. 6a). WWV depletion in this simulation thus starts five months ahead of the peak of El Niño and leads over the 15-month period to a total volume decrease of $2.5 \times 10^{14}\,\mathrm{m}^3$ (corresponding to 6.3 Sv or a shoaling of the 20°C isotherm by 12.8 m when averaged over the WWV region). Depletion of WWV occurs in two phases, with an initial decrease driven mainly by diabatic fluxes across the 20°C isotherm (approximately months 7–14) followed by a period with dominant horizontal adiabatic transport out of the equatorial region (approximately months 12–21; red area, Figs. 6a,c).

Changes in surface forcing and vertical mixing drive the initial phase of WWV decrease (blue lines, Fig. 6c). This is consistent with the observation-based study by Meinen and McPhaden (2001) where there are suggestions that the WWV discharge due to diabatic processes (inferred as the residual of the WWV change minus the lateral transport) is dominant in the early part of the 1997 El Niño (e.g., Fig. 13 of Meinen and McPhaden 2001). However, uncertainties in their calculations are large (estimated as ±6 Sv). This highlights the need for future observation-based studies to better reconcile the role of the observed diabatic, vertical fluxes. The weaker trade winds during El Niño reduce upwelling of cold water masses to the surface, decrease shear- and wind-driven mixing and deepen the 20°C isotherm. These effects combined result in an overall reduced/anomalous surface forcing and vertical mixing flux across the 20°C isotherm compared to climatological conditions (cf. Figs. 7a and 4c).

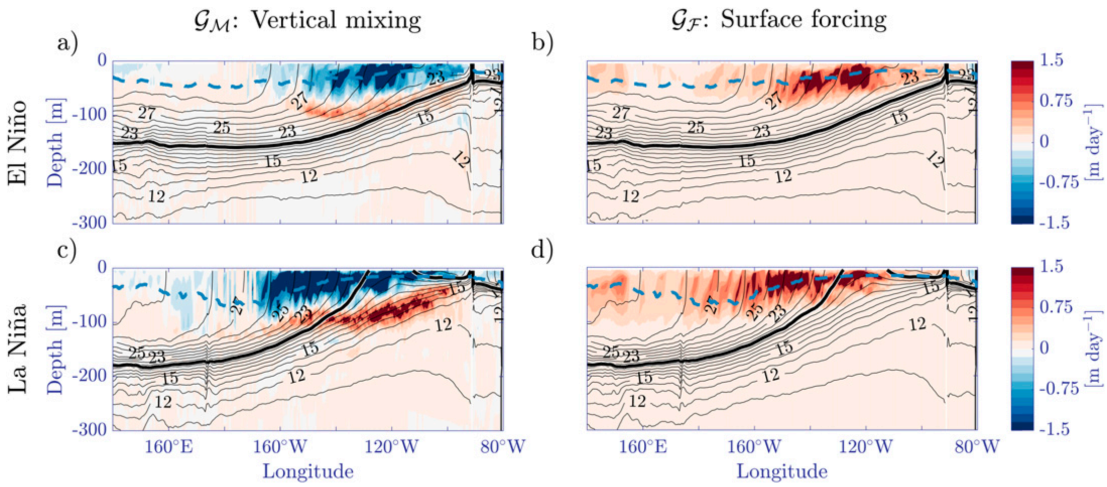

FIG. 7. Mean depth–longitude transects for September–November across the equatorial Pacific of the water mass transformation velocities for (a),(c) vertical mixing $\mathcal{G}_{\mathcal{M}}$ and (b),(d) surface forcing $\mathcal{G}_{\mathcal{F}}$ (m day^{-1}) during the idealized, symmetric El Niño and La Niña events. The contours show the distribution of the equatorial isotherms with the 20°C isotherm in bold. The dashed blue line in the uppermost layers indicates the mixed layer depth as defined in Fig. 4.

The reduced surface forcing and vertical mixing fluxes until the peak of El Niño agree well with the observational study by Warner and Moum (2019). Numerical mixing anomalies play a minor role throughout the discharge phase contributing only 4% to the overall changes in WWV (Fig. 8a). Together, the total diabatic volume flux throughout the discharge phase amounts to a volume change of -1.1×10^{14} m^3, contributing ~45% to the total change (Fig. 8a), and is comparable to the average estimate over the 1976–2004 time period in Lengaigne et al. (2012).

The second phase of WWV discharge occurs about six months later, with meridional transport as the dominant driver (red line in Fig. 6a). During the initial discharge phase (months 7–11), anomalous adiabatic transport through 5°N and 5°S opposes WWV depletion by off-equatorial westerly wind bursts, moving more warm water into the equatorial band (McGregor et al. 2016). The high amplitude of the first EOF mode (Fig. 1a) combined with the positive amplitude of the second EOF mode (Fig. 1b) of wind stress anomalies during the second year of the simulation drive a strong Ekman divergence and geostrophic transport of warm water masses across 20°C to higher latitudes (McGregor et al. 2012, 2014; Zeller et al. 2019).

While the large-scale horizontal transport through 5°N and 5°S during the second phase of discharge is high, the strength of the ITF is decreased throughout the full discharge phase (green line in Fig. 6a, which is slightly positive throughout the time period). This is the result of the reduced SSH gradient between the Indian and the Pacific Ocean during El Niño (Sprintall and Révelard 2014; Feng et al. 2018). Including the ITF, the total adiabatic transport during the discharge period contributes 1.4×10^{14} m^3, or about 55%, to the total WWV changes (Fig. 8a). During this second phase (months 11–21), the diabatic volume fluxes play only a minor role.

The change to La Niña–like conditions at the end of the discharge phase concurrent with the negative amplitude of the idealized N34 index (black line, Fig. 2) is also evident here in the increase in WWV (months 20–24, Fig. 3a). This is caused by the shallower 20°C isotherm and colder SST values in the eastern Pacific, leading to increased ocean heat absorption around the 20°C isotherm as indicated by an increase in the surface forcing term (dark blue line, Fig. 3a).

b. The idealized symmetric La Niña recharge

As during El Niño, the change in WWV during La Niña occurs over two stages. The initial phase is dominated by diabatic volume fluxes and the latter half of the recharge phase is mainly controlled by meridional transport (Figs. 6b,d). During La Niña's recharge, the total change in WWV (i.e., blue region in Figs. 6b,d) is 2.9×10^{14} m^3, slightly higher than the change in volume during El Niño's discharge phase (Fig. 8b) despite the symmetric atmospheric forcing (this is equivalent to a discharge of 7.4 Sv or a deepening of the 20°C isotherm by about 15 m when averaged over the WWV region). It is likely caused by the ocean being able to absorb more heat when conditions are cool in contrast to El Niño's heat loss.

Compared to El Niño's discharge phase, not all volume fluxes are opposite and of the same magnitude. The most striking differences lie in the vertical mixing and surface forcing fluxes (cf. blue curves in Figs. 6c,d). The strengthened trade winds during La Niña drive increased vertical mixing in the upper ocean (Fig. 7c; Warner and Moum 2019), yet counterintuitively, the vertical mixing volume flux does not increase but decreases WWV (i.e., in the same sense as during El Niño events). This remarkable asymmetry is a result of the strong nonlinearity associated with shifts in the 20°C isotherm position. Specifically, the shoaling of the 20°C isotherm in the eastern equatorial Pacific moves the isotherm from the subsurface, where mixing warms water, toward the surface where mixing cools water masses (Figs. 7c and 8b). This leads to a downward volume flux across the 20°C isotherm due to mixing throughout much of the eastern Pacific toward cooler and deeper layers, and thus a decrease of WWV.

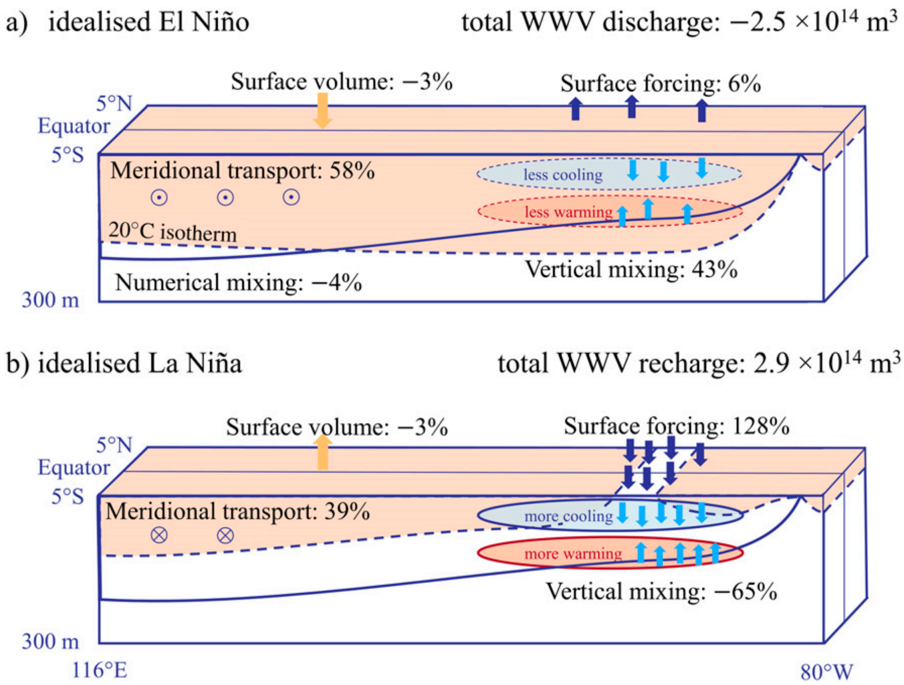

FIG. 8. Snapshots of the warm water volume during the peak of the idealized, symmetric (a) El Niño discharge and (b) La Niña recharge phases alongside the time-integrated contribution of the WWV budget terms over the full discharge/recharge period. The solid line between 116°E and 80°W displays the climatological 20°C isotherm depth and the dashed line its anomalous position during the event. Before the El Niño event, WWV is anomalously large (hence a deep isotherm) and the integrated WWV budget terms over the event result in the net discharge of WWV. The blue and red shaded areas in the eastern equatorial Pacific indicate where vertical mixing is cooling and warming water masses that lead to buoyancy-driven vertical heat and volume fluxes across isotherms indicated by the light blue arrows. The dark blue arrows show how anomalous surface forcing leads to depletion in (a) and build-up in (b) of WWV across the 20°C isotherm. The two symbols ⊙ and ⊗ illustrate meridional WWV transport out of and into the equatorial region, respectively. Meridional transport here combines the horizontal transport across 5°N, 5°S and the ITF.

In contrast, the surface forcing volume flux clearly dominates WWV build-up, with a much stronger response compared to El Niño's discharge period. The increased trade wind strength, the shallower 20°C isotherm (where it is more strongly influenced by surface forcing) and the cold SST values lead to a high anomalous heat absorption in the eastern equatorial Pacific. This warm water is then subsequently advected westward and accumulates in the western Pacific warm pool, deepening the 20°C isotherm there (Fig. 7d). The total contribution of the surface forcing volume flux to the WWV increase is $3.7 \times 10^{14}\,\mathrm{m}^3$ (128% of the total change in WWV). However, as the vertical mixing contribution opposes this surface forcing volume flux, the overall diabatic volume transport accounts for ~62% (Fig. 8b). This interplay between strong vertical mixing and strong surface forcing fluxes during the transition to the peak of La Niña is also supported in the observational study by Warner and Moum (2019). Numerical mixing during La Niña's recharge phase, as during El Niño's discharge of heat, again plays only a minor role (purple line in Figs. 6c,d). It contributes only ~1% to the changes in WWV (Fig. 8b).

Contrary to the vertical fluxes, meridional transport into the WWV region during the recharge phase is largely symmetric with respect to El Niño's discharge. This is caused by the prescribed symmetric wind stress perturbations, which drive most of the adiabatic transport (see, e.g., McGregor et al. 2012, 2014; Zeller et al. 2019). The small asymmetry in the adiabatic transport relative to the idealized El Niño may be related to differences in the 20°C isotherm depth capturing a different fraction of the geostrophic return flow despite symmetric wind stress forcing. Consistent with the recharge oscillator theory, Meinen et al. (2001) and McGregor et al. (2014), horizontal transport lags the peak SST/wind stress anomalies (roughly when the WWV changes are largest) by about four months. The ITF is consistently stronger than normal throughout the full recharge period (green line in Fig. 6b), as strong trade winds increase the SSH in the western equatorial Pacific and drive a larger WWV transport into the Indian Ocean. In total, the adiabatic horizontal transport (and surface volume flux) is responsible for ~38% of the total recharge as compared to the ~55% contribution during El Niño's discharge (Fig. 8b).

In summary, we see that the meridional, adiabatic transport of WWV between the two symmetrically forced ENSO phases is largely symmetric. The diabatic processes however are a considerable source of asymmetry arising from the dependence

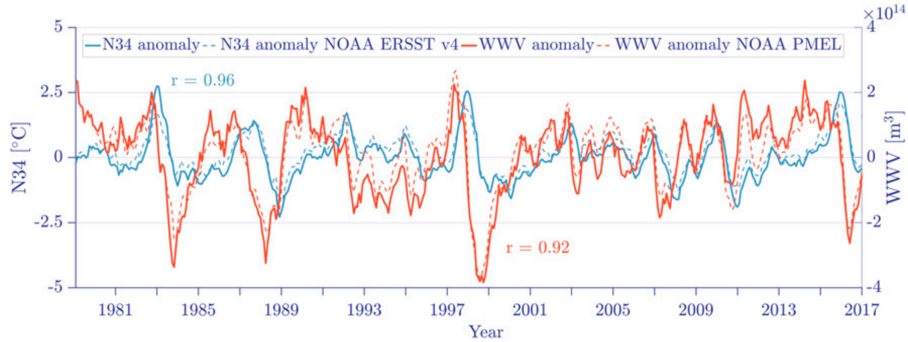

FIG. 9. Time series of the simulated N34 index (°C) and anomalous WWV (m^3) during the 1979–2016 hindcast simulation compared to observations in Reynolds et al. (2007) and Meinen and McPhaden (2000). The observed indices are given as dashed blue and red lines and the correlation coefficients (r) between the simulated and observed time series are indicated with blue and red values.

of the heat fluxes on SST and the vertical movement of the 20°C isotherm coupled with mixing changes.

La Niña events typically last longer and have a reduced amplitude relative to their corresponding El Niño events as they often reintensify during the following winter (Okumura and Deser 2010). Our idealized forcing based on the exact opposite of a composite of El Niño events therefore overestimates the magnitude of La Niña. Additionally, La Niña events do not include a clear shift from negative to positive values in the PC2 time series (red line during red periods, Fig. 1c). It is therefore important to compare our idealized symmetric simulations to ENSO events and their event-to-event variability in a simulation with atmospheric forcing more closely following observations. The next section first validates the 1979–2016 hindcast simulation against observations before an in-depth analysis of the variability in the WWV budget between events.

7. ENSO's ocean-sourced anomalies during 1979–2016

The simulated N34 index over the 1979–2016 period captures the observed variations in NOAA's ERSST v4 N34 index (Smith and Reynolds 2003) reasonably well (blue lines, Fig. 9). The three strong El Niño events in 1982/83, 1997/98, and 2015/16, on which our analysis focuses on, are slightly overestimated in the simulation compared to the observational time series. As expected, the anomalous WWV time series leads the N34 index by 3–6 months (red lines, Fig. 9). While the correlation between the simulated and observed WWV time series is high ($r = 0.92$), the magnitude is somewhat underestimated during the El Niño in 1997/98 and the La Niña event 2010/11.

As the position of the 20°C isotherm is a key factor influencing WWV, it is important to validate it against observations during El Niño and La Niña events. As mentioned above, a shallow position increases diabatic WWV transport through enhanced vertical mixing and the penetrating solar heat fluxes while a deep 20°C isotherm leads to a reduced effect. The climatological position of the 20°C isotherm compares reasonably well to observations (black lines, Fig. 10; Kiss et al. 2020), although it is slightly shallower west of 140°W (by ~20 m) and deeper (by ~15 m) east of 140°W. During the 1997/98 El Niño, as warm water reaches the eastern equatorial Pacific, the 20°C isotherm in the east deepens by about 120 m in ECMWF's Ocean Reanalysis 5 product (ORA-S5; Zuo et al. 2018; Fig. 10). The hindcast simulation captures this downward shift of the isotherm, although with a negative bias of ~30 m around 140°W and a positive bias of ~30 m at 80°W near the South American coastline. The isotherm position shown in Fig. 10 is the mean over the September–November period. During the following La Niña in 1998/99, the simulation exhibits a somewhat too shallow 20°C isotherm in the central Pacific and a negative bias of about 20–25 m in the surface region at 110°W compared to ORA-S5 (blue lines, Fig. 10). These tilt differences in the isotherm position also occur during other events and likely explain most of the offset between the simulated and observed anomalous WWV time series in Fig. 9.

8. The warm water volume budget during 1979–2016

Over the 38-yr period between 1979 and 2016, the equatorial Pacific undergoes multiple discharge and recharge phases of WWV (red shaded and blue shaded periods, Fig. 11). While there are more than three El Niño and La Niña events during this period, our analysis here will focus on three strong events each. We define these discharge and recharge events as when the rate of change in WWV anomalies (black line in Fig. 11a) is negative and positive respectively.

During El Niño, discharge peaks between 22 and 27 Sv and is much stronger than the 11 Sv in the idealized simulation (Fig. 6a). As a consequence, the overall total change in WWV associated with these events is much larger ($3.5–5.5 \times 10^{14}\,m^3$ compared to the $2.5 \times 10^{14}\,m^3$ in Fig. 8a). The length of the discharge phases (red shaded period in Fig. 11) is largely constant between events and consistent with the length in the idealized El Niño simulation. La Niña events on the other hand show a larger event-to-event variability in the total change in WWV ($2.5–4.2 \times 10^{14}\,m^3$) as well as the length of the recharge period (8–15 months, blue shaded period in Fig. 11).

a. First phase: Diabatic fluxes

As in the idealized simulation, the initial discharge phase during El Niño is dominated by the diabatic volume fluxes. Over all three strong El Niño events, both surface forcing and

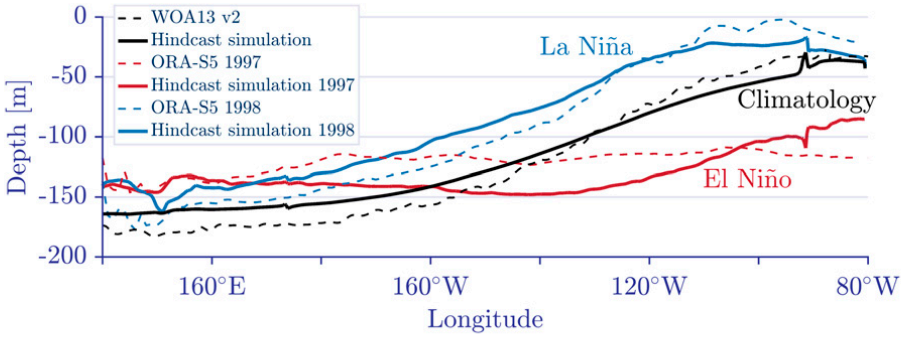

FIG. 10. Depth–longitude transect of the 20°C isotherm for September–November across the equatorial Pacific during the El Niño event in 1997 (blue lines) and La Niña event in 1998 (red lines) in the 1979–2016 hindcast simulation. The dashed blue and red lines show the isotherm distribution during the same time period in the ORA-S5 ocean reanalysis product (Zuo et al. 2018). In black the climatological position of the 20°C isotherm compared to the observations in the *World Ocean Atlas* (*WOA13* v2; Locarnini et al. 2013).

vertical mixing deplete WWV (light and dark blue lines during the red periods, Fig. 11b). The contribution of the diabatic fluxes to the total change in WWV over the discharge periods in 1982/83 and 1997/98 is 23% and 38%. For the 1997/98 El Niño event, this value is lower compared to the 50% in both Lengaigne et al. (2012) and Meinen and McPhaden (2001). However, we expect differences compared to Lengaigne et al. (2012) arising from the temporal filtering [Lengaigne et al. (2012) use a 16-month to 8-yr bandpass filter while we employ a 5-month running mean] as well as model and forcing differences (parameterizations, numerical mixing and surface forcing products). Compared to the observations in Meinen and McPhaden (2001), the lower diabatic contribution may be caused by the fact that the 20°C isotherm is biased deep. A too deep isotherm in the eastern equatorial Pacific likely results in a lower contribution of the diabatic fluxes to changes in warm water volume, as these fluxes are strongest near the surface. However, the observational estimates also include

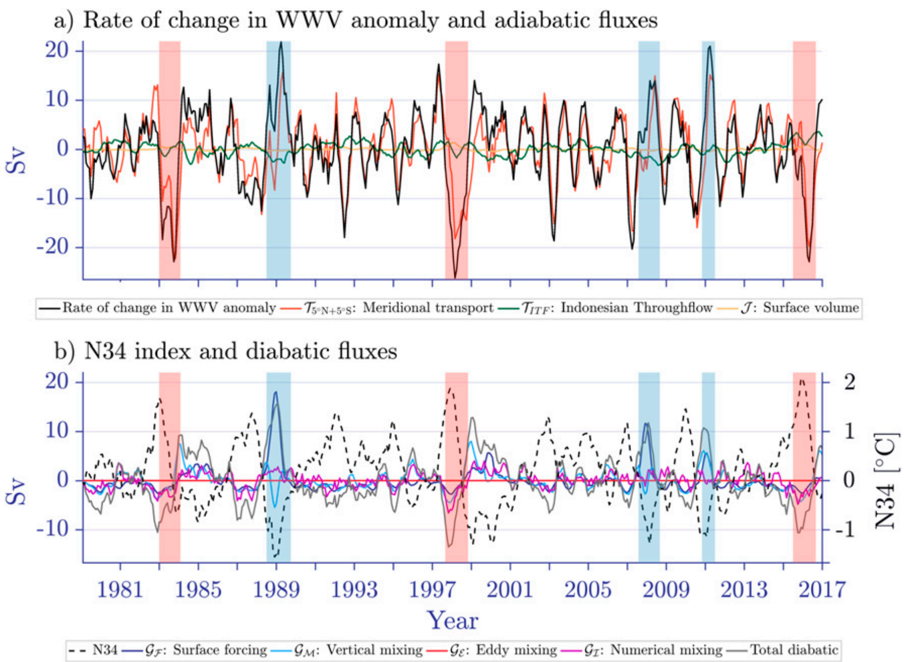

FIG. 11. (a) The change in the WWV anomaly as well as the adiabatic and (b) diabatic volume fluxes (Sv) during the 1979–2016 hindcast simulation. A 5-month running mean as in Meinen and McPhaden (2000) has been applied. The red discharge and blue recharge periods for the three strongest El Niño and La Niña events are defined as when the rate of change in the WWV anomaly [black line in (a)] is negative and positive, respectively. In (b) we also show the N34 index (°C) as a dashed black line and the total diabatic volume fluxes in gray. Positive and negative values indicate a contribution to the recharge and discharge of WWV, respectively.

large uncertainties due to missing data [e.g., Meinen and McPhaden (2001) mention that their error bars are generally as large as their signal].

In the three strong El Niño events the timing and behavior of the diabatic fluxes correspond well with the idealized simulation (cf. Figs. 11b and 6c). One notable exception is that numerical mixing plays a somewhat larger role.

The diabatic fluxes during the 1988/89 and 2007/08 La Niña events also share a strong similarity with the idealized event (despite the symmetric nature of the idealized La Niña): strong surface forcing at the peak of the event increases WWV while at the same time its increase is compensated by a negative vertical mixing flux (blue shaded periods, Fig. 11b). During the 1988/89 event, mixing undergoes changes associated with positive and negative contributions that mostly cancel out over the full recharge period (light blue line, Fig. 11b). In July 1988, the 20°C isotherm is largely within the warming region of vertical mixing, effectively causing a net positive volume flux into the WWV (Fig. 12a). Six months later, as the isotherm outcrops in the far eastern equatorial Pacific, the cooling via mixing near the surface exceeds the warming further west where the isotherm is deeper (Fig. 12b). Finally, as the isotherm returns to its deeper position in May 1989, it moves back into the region where mixing warms water masses (Fig. 12c). The results in Lengaigne et al. (2012) do not show these compensating fluxes throughout different phases of WWV recharge, possibly due to their low-pass temporal filter. During the strong La Niña event in 2010/11, surface forcing exhibits a reduced amplitude compared to the previous La Niña events, and vertical mixing is increasing WWV. This behavior of the diabatic fluxes is caused by the 20°C isotherm being positioned much deeper than during the previous events in the region where vertical mixing warms waters.

The consistent behavior of the diabatic fluxes during the three strong El Niño events is revealed when all three events are composited (Fig. 13a). The depletion of WWV by the diabatic fluxes leads the peak of the event (i.e., the peak of the N34 index) by three to six months, similar to the idealized simulation (Fig. 6c). Vertical mixing in all three El Niño events increases from September the following year (i.e., month 20; Fig. 13a), indicating the shift to La Niña–like conditions after El Niño. During La Niña, the composite time series reveal the strong effect of surface forcing, mainly caused by the high amplitude during the 1988/89 event, and highlight the compensating stages of vertical mixing (Fig. 13c). While the behavior of the diabatic fluxes is similar in strong and moderate El Niño events (although with a lower magnitude, not shown), moderate La Niña events do not show a strong surface forcing flux, but rather an increase in vertical mixing (Fig. 13e). These effects arise from the reduced upward shift of the 20°C isotherm, its prolonged position in the vertical mixing–warming (i.e., recharging) region, and the enhanced turbulence in the eastern equatorial Pacific.

b. Second phase: Adiabatic fluxes

The second phase of WWV changes during all discharge and recharge periods is linked to increased adiabatic transport across 5°N and 5°S, and is strongly in phase with the overall

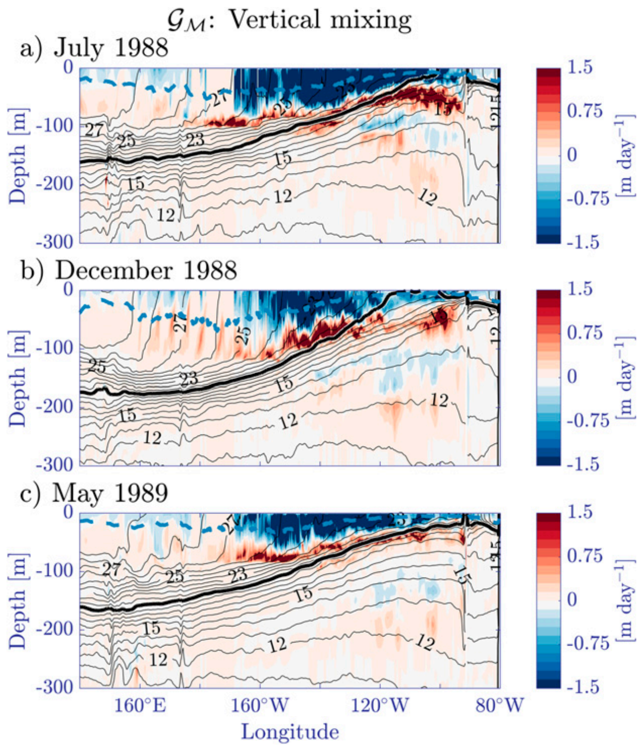

FIG. 12. Depth–longitude transects across the equatorial Pacific of the vertical mixing water mass transformation velocities $\mathcal{G}_{\mathcal{M}}$ during the 1988/89 La Niña event in the hindcast simulation. The contours show the distribution of the equatorial isotherms with the 20°C isotherm in bold. The dashed blue line in the uppermost layers indicates the mixed layer depth as defined in Fig. 4. As La Niña develops, the 20°C isotherm shifts upward into the surface region where enhanced vertical mixing cools water masses (blue region) and leads to strong downward volume flux across the isotherm into deeper layers. After the peak of the event, vertical mixing decreases and the isotherms return to their original position below the region where vertical mixing warms water masses (red region).

changes in WWV (Figs. 13b,d). The positive transport anomalies before the peak of the event are consistent across the three strong El Niño events, as in the idealized simulation (red line, Fig. 13b). Peak adiabatic transport during El Niño events ranges between −22.2 and −18.2 Sv, and is about 25% larger than the transport during La Niña events (14.9–15.1 Sv). This highlights, as in the idealized simulations, the increased importance of the adiabatic fluxes during El Niño. The volume flux across 5°N during all three El Niño events in Fig. 11 is more dominant than the one across 5°S (not shown), agreeing with the studies of McGregor et al. (2013, 2014) and Zeller et al. (2019). This results from the interplay between the two EOF modes of wind stress anomalies and Ekman-induced surface transport (McGregor et al. 2014). The Indonesian Throughflow (green line, Fig. 11a) is opposing changes in the adiabatic transport across 5°N and 5°S during all ENSO events, caused by a reduced volume transport during El Niño and increased transport during La Niña as discussed above. The contributions of meridional transport and the ITF to changes in WWV over the 1982/83 and 1997/98 El Niño events (79% and 67%) are

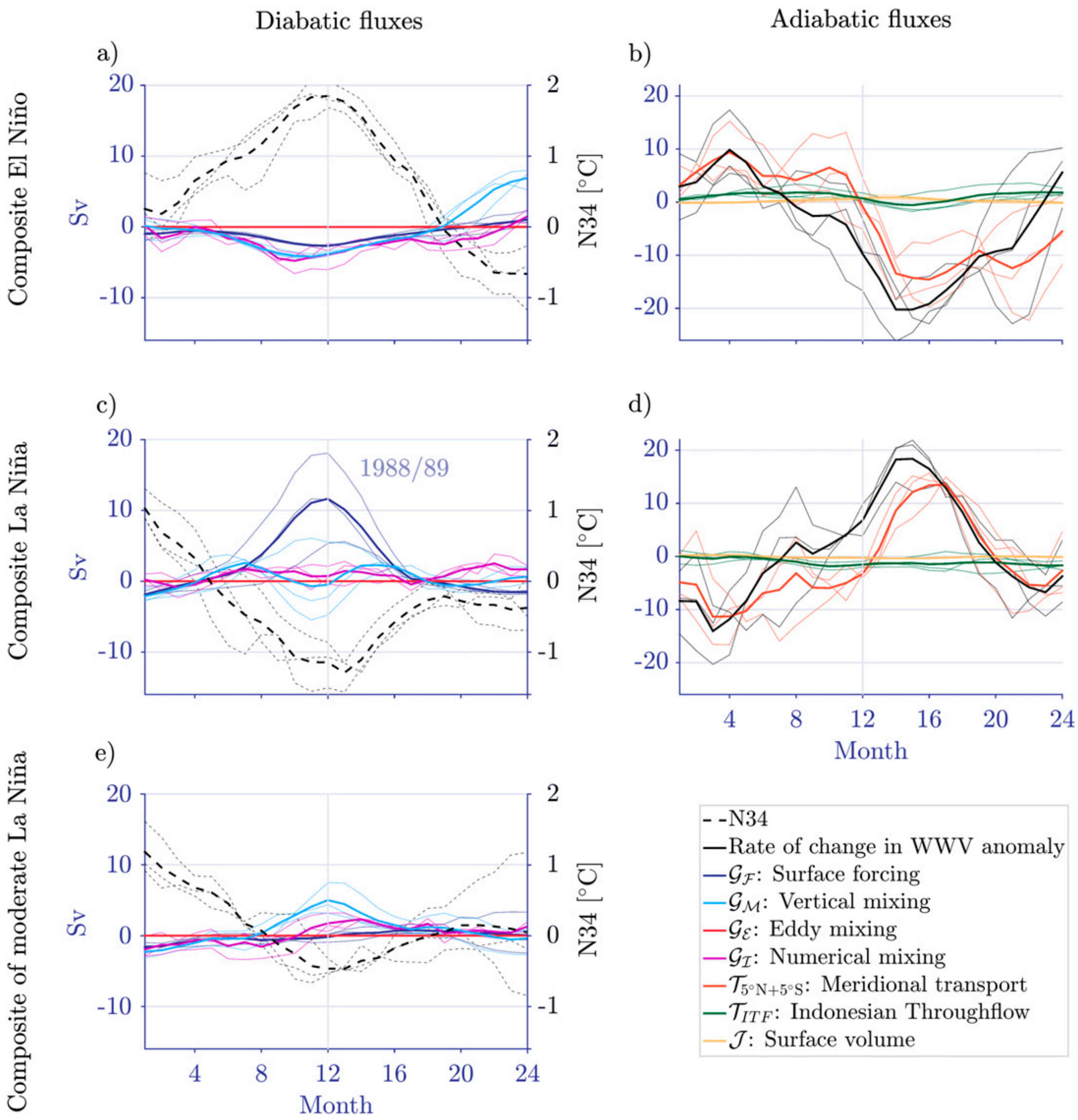

FIG. 13. Composite time series centered in December (month 12) of the (a),(c) diabatic WWV budget terms as well as (b),(d) the rate of change in WWV and the adiabatic terms (Sv) during the three strong El Niño and La Niña events shaded in red and blue in Fig. 11. The label 1988/89 in (c) shows the time series of the surface forcing term during the 1988/89 La Niña event. (e) The composite diabatic time series for three moderate La Niña events in 1984/85, 1995/96, 2006/07. In the left panels we also show the time series for the N34 index (°C) (dashed black line). The faint lines are the time series corresponding to the three events while the solid lines are the composites.

higher compared to the values for the same events (63% and 45%) in Lengaigne et al. (2012). The differences during these events, as well as during the 1988/89 La Niña, may arise from their 16-month to 8-yr low-pass temporal filter reducing the contribution of meridional transport.

9. Conclusions

In this study, we analyzed the diabatic and adiabatic volume fluxes and associated nonlinear ocean processes that contribute to WWV variability during ENSO events. To this end, we constructed idealized, symmetric ENSO-related atmospheric fields to force a global high-resolution ocean–sea ice model and compared these simulations with the event-to-event variability from a 1979–2016 hindcast simulation. The use of the WMT framework made it possible to individually calculate all fluxes that contribute to changes in WWV.

Changes to the WWV during El Niño's discharge were initiated by the diabatic volume fluxes associated with surface forcing and vertical mixing, both strongly linked to the 20°C isotherm position and the strength of the trade winds. Weaker trade winds during El Niño reduce upwelling of cold water moving the 20°C isotherm away from the surface while also increasing eastern equatorial SSTs and driving an anomalous surface heat flux into the atmosphere. This results in an anomalous decrease of WWV due to surface forcing (dark blue sections, Fig. 14a). At the same time, the deepening 20°C

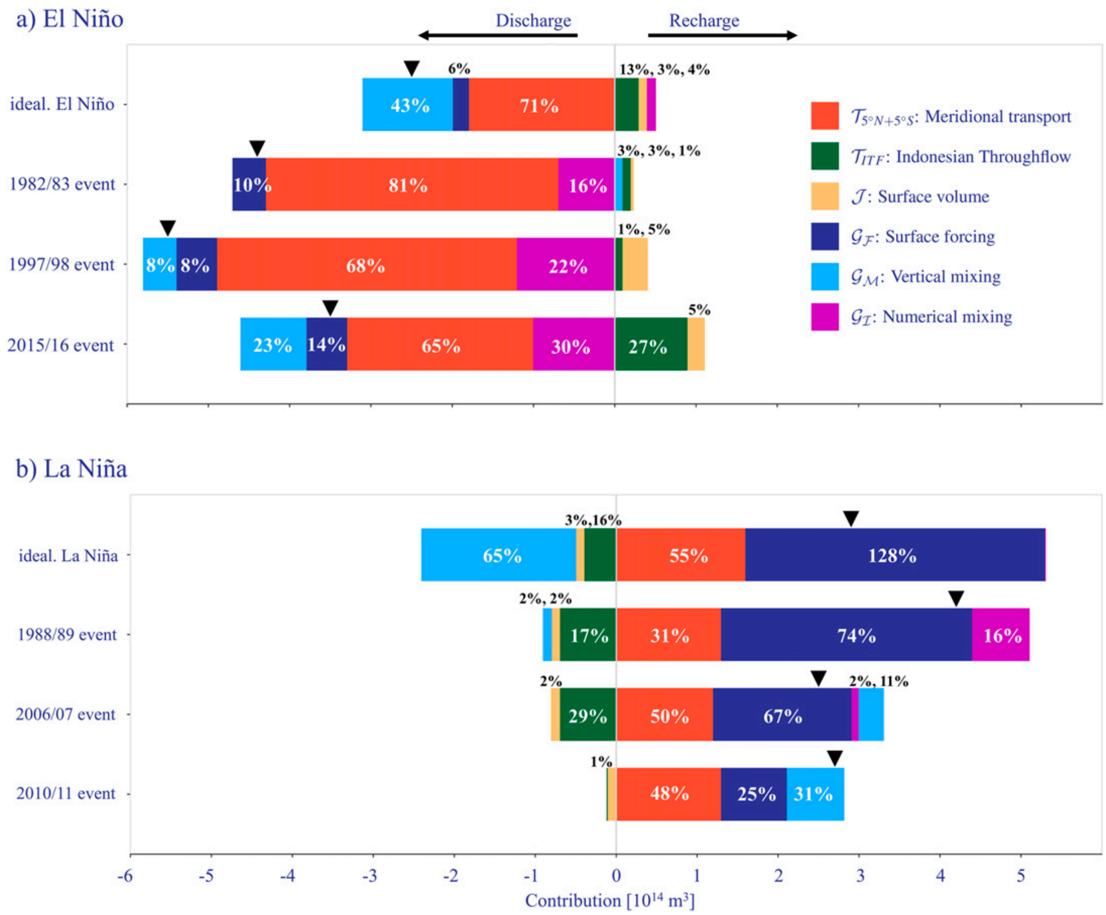

FIG. 14. The total time-integrated contribution of each anomalous WWV budget term (10^{14} m^3) during (a) El Niño and (b) La Niña periods as defined by the red and blue shaded periods in Fig. 6 (idealized) and Fig. 11 (hindcast). A negative value of a given flux indicates its role in discharging WWV and a positive value indicates a recharge respectively. The percentage values in each section show the time-integrated contribution to the total change in WWV and are calculated from values rounded to one-digit accuracy. The triangular markers show the total change in WWV over a particular event.

isotherm moves away from the region of strong wind- and shear-driven mixing, whose intensity also reduces (light blue sections, Fig. 14a). The second phase of WWV discharge, occurring about six months later, was controlled by meridional adiabatic transport across 5°N and 5°S with the ITF always acting to oppose changes in WWV (red and green sections, Fig. 14a).

During La Niña, the stronger trade winds increase upwelling of cold water masses and the 20°C isotherm shoals, sometimes outcropping in the eastern Pacific. Exposure of the 20°C isotherm to increased heat uptake by surface forcing in this region creates a strong across-isotherm volume flux responsible for most of the WWV recharge (dark blue sections, Fig. 14b). While turbulence is enhanced during La Niña, the shoaling of the isotherm into the surface layers, where mixing drives cooling of water rather than warming, means that vertical mixing can drive an anomalous decrease in WWV (light blue sections, Fig. 14b). This key asymmetry, that mixing drives anomalous discharge in both El Niño and La Niña events, arises from the strong dependence of the diabatic fluxes on the position of the 20°C isotherm. However, in the hindcast simulation (as opposed to the idealized simulations) the contribution of vertical mixing to the overall discharge during La Niña is concealed by opposing volume fluxes occurring at different times as the 20°C isotherm transitions through regions of vertical mixing–driven warming and cooling. In contrast, the idealized simulations, which are forced with symmetric atmospheric forcing, highlight the key role of the diabatic fluxes in driving ocean-sourced asymmetries in the WWV budget. On average, the ratio of the diabatic to adiabatic contributions to WWV changes during El Niño is about 40% to 60% while for La Niña this ratio changes to 75% to 25%.

While the diabatic fluxes in the observed WWV budget in Meinen and McPhaden (2001) could only be derived as the residual from the horizontal transport, the model study by Brown and Fedorov (2010) showed that errors in the calculation of horizontal fluxes can be of the same magnitude as the vertical fluxes. They further present evidence that the vertical fluxes on ENSO-related time scales in the eastern Pacific are small, contradicting the observational studies by Meinen and

McPhaden (2000, 2001) and the modeling study by Lengaigne et al. (2012). By revisiting the WWV budget with a precise online calculation of the individual fluxes, we were able to further minimize errors associated with the closure of this budget and thereby highlight the dominant role of the diabatic fluxes during La Niña. Despite differences to Meinen and McPhaden (2000) and Lengaigne et al. (2012) in the methods used to calculate the WWV budget terms (limited observations versus the use of different models, parameterization schemes and atmospheric forcing) our study supports the main finding that diabatic volume fluxes are as important as adiabatic volume fluxes in driving WWV changes on ENSO time scales. Our results are at odds with the conclusions of Brown and Fedorov (2010). The differences may arise because their short 6-yr simulation over 1992–98 does not capture a strong La Niña where diabatic fluxes play a larger role. They also define the WWV as the volume of water above the 25 kg m^{-3} isopycnal that is up to 25 m shallower than the 20°C isotherm in the EUC (see their Fig. 1b) and use a 30-day running mean for their diapycnal transport.

The results in this study highlight the key role of diabatic processes in the eastern equatorial Pacific on ENSO time scales. A good representation of diffusive mixing and turbulence in models is therefore needed in order to correctly simulate these processes. The large event-to-event variability of ENSO in the hindcast simulation motivates future research into the evolution, spatial extent and amplitude of different events. Furthermore, it will be of value to investigate the decadal to multidecadal variability of WWV and ocean heat content to gain insight into the role of the equatorial Pacific in long-term heat uptake and redistribution, especially in light of current climate change.

Acknowledgments. The authors are supported by the Australian Research Council, including the ARC Centre of Excellence for Climate Extremes, through Grant FL150100090 and MHE is additionally supported by the Centre for Southern Hemisphere Oceans Research (CSHOR). We thank P. Spence for the 500-yr CORE-NYF spinup of the model and A. Kiss for the 300-yr JRA55-do spin-up of the hindcast simulation. We thank I. Medhaug, R. Knutti, N. Maher, and S. McGregor for valuable discussions and input during this project. We also thank the two anonymous reviewers for comments and suggestions that helped improve the quality of the paper. The simulations in this project were conducted with resources and services from the National Computational Infrastructure which is supported by the Australian Government. We thank NOAA's GFDL, ESRL, NODC, and the TAO Project Office of NOAA/PMEL as well as the Japanese Meteorological Agency for free access to their CORE-NYF, SST, WWV, *World Ocean Atlas*, and the Japanese Ocean Reanalysis data. We thank the ECMWF for providing free access to the complete ERA-Interim and ORA-S5 products. We also thank the Consortium for Ocean-Sea Ice Modelling in Australia (COSIMA; www.cosima.org.au) for their technical help, continued development and for making the ACCESS-OM2 suite of models available at https://github.com/COSIMA/access-om2. The model output is available upon request to the authors and the analysis scripts are publicly available at https://github.com/mauricehuguenin/enso_diabatic_fluxes.

APPENDIX

Derivation of Atmospheric Forcing for the Idealized Model Simulations

The regression analysis and the idealized time series in section 2b provide the spatial evolution for wind stress perturbations related to ENSO. The patterns of the atmospheric variables used in the idealized model simulations are obtained by regressing the full 38-yr-long N34 and PC2 time series onto each ERA-Interim anomaly field, resulting in two spatial patterns for each variable (examples are shown in Fig. A1).

The time evolution for the total atmospheric forcing is then calculated by multiplying the X_1 and X_2 spatial patterns with their associated idealized time series and adding them to the CORE-NYF climatological forcing:

$$\underbrace{F_{\text{ideal.}}(x, y, t)}_{\text{Forcing}} = \underbrace{\overline{F(x, y, t)}}_{\text{Climatology}} + \underbrace{X_{1,F}(x, y)\text{N34}_{\text{ideal.}}(t)}_{\text{Perturbation}} + \underbrace{X_{2,F}(x,y)\text{PC2}_{\text{ideal.}}(t)}_{\text{Perturbation}}, \tag{A1}$$

where $F_{\text{ideal.}}(x, y, t)$ is one of the six idealized forcing anomaly fields dependent on time, $\overline{F(x, y, t)}$ is the base forcing field without any interannual variability from the CORE-NYF dataset, $X_{1,F}(x, y)$, $X_{2,F}(x, y)$ are the two regression patterns of a given field F derived from the ERA-Interim product (Fig. 1), and $\text{N34}_{\text{ideal.}}(t)$ and $\text{PC2}_{\text{ideal.}}(t)$ are the associated idealized time series (Fig. 2). Put most simply, the ENSO perturbation forcing fields are derived from regressions of the $\text{N34}_{\text{ideal.}}(t)$ and $\text{PC2}_{\text{ideal.}}(t)$ time series onto the respective atmospheric fields required to construct the bulk formulas for heat and freshwater forcing.

For the remaining two input variables (zonal and meridional wind speed) we use a different method to derive the symmetric fields. In the model, wind speed is converted to wind stress by the wind stress law (Fairall et al. 1996):

$$\tau = (\tau_x, \tau_y) = \rho_a C_D \underbrace{\sqrt{u_{10}^2 + v_{10}^2}}_{U_{10}} (u_{10}, v_{10}), \tag{A2}$$

where $\boldsymbol{\tau}$ is the wind stress vector with its zonal (τ_x) and meridional (τ_y) components (N m^{-2}), ρ_a is the density of air at sea level (1.25 kg m^{-3}), C_D is the unitless drag coefficient, u_{10} and v_{10} are the zonal and meridional wind speeds (m s^{-1}), and U_{10} is the wind speed magnitude (m s^{-1}). For the derivation of the atmospheric forcing, we use a constant drag coefficient of 1.5×10^{-3} (Kara et al. 2007) for simplicity. Differences relative to the wind speed-dependent drag coefficient are negligible.

Due to the quadratic dependence of this equation on wind speed, the resulting wind stress anomalies if given symmetric ENSO-related wind speed anomalies are asymmetric. As we aimed for symmetric wind stress anomalies during our El Niño and La Niña simulations, we therefore solved this equation in

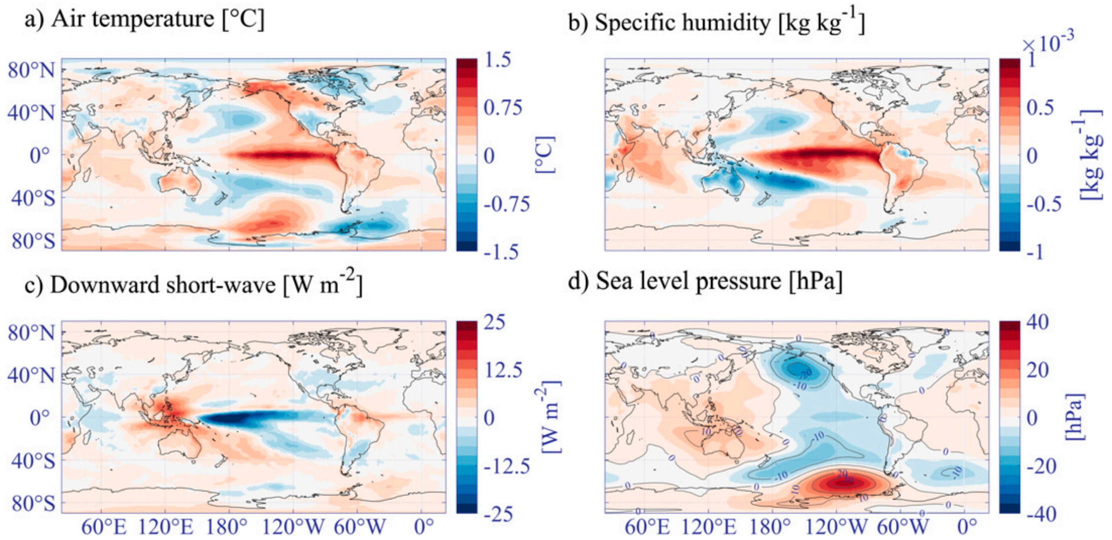

FIG. A1. Examples of four out of the eight atmospheric regression patterns X_1 associated with ENSO used in the atmospheric forcing for the idealized symmetric events. These spatial patterns are calculated by regressing the observed N34 index (Reynolds et al. 2007) onto anomalous spatial maps from the ERA-Interim reanalysis product for 1979–2016 (Dee et al. 2011) and taking the time mean. (a) Air temperature (°C), (b) specific humidity (kg kg^{-1}), (c) downward shortwave radiation (W m^{-2}), and (d) sea level pressure (Pa).

an inverse manner for the two unknowns u_{10} and v_{10}. To solve Eq. (A2) for wind speed, we first obtained the wind stress anomaly fields τ'_x and τ'_y from the EOF analysis described in section 2, that is, from $\tau'_x = X_{1,\tau'_x}\mathrm{N34}_{\mathrm{ideal.}} + X_{2,\tau'_x}\mathrm{PC2}_{\mathrm{ideal.}}$ for the zonal component during El Niño (Figs. 1a,b, 2). The following section sets out how we then used the wind stress law to solve for the two unknowns u_{10} and v_{10}.

First, the zonal component of the wind stress law is rewritten as a Reynolds decomposition:

$$\underbrace{\overline{\tau_x}+\tau'_x}_{l} = \underbrace{\rho_a C_D}_{k}\underbrace{\sqrt{(\overline{u_{10}}+u'_{10})^2+(\overline{v_{10}}+v'_{10})^2}}_{U_{10}}\,(\overline{u_{10}}+u'_{10}),$$

$$\Rightarrow l = kU_{10}(\overline{u_{10}}+u'_{10}), \tag{A3}$$

where $\overline{u_{10}}$ and $\overline{v_{10}}$ are the climatological values from the CORE-NYF dataset, $\overline{\tau_x}$ is calculated from $\overline{u_{10}}$ and $\overline{v_{10}}$ by Eq. (A2), τ'_x, u'_{10} and v'_{10} are the perturbation values, l is the total zonal wind stress forcing including climatological and perturbation values, and k contains the two constants for the density of air and the drag coefficient. Solving the second line of Eq. (A3) for u'_{10} results in

$$u'_{10} = \frac{l}{kU_{10}} - \overline{u_{10}}. \tag{A4}$$

The same procedure as in Eq. (A3) is applied to the meridional component and yields

$$v'_{10} = \frac{m}{kU_{10}} - \overline{v_{10}}, \tag{A5}$$

where $m = kU_{10}(\overline{v_{10}}+v'_{10})$ is the total meridional wind stress forcing including climatological and perturbation values.

As a next step we combine l and m, resulting in the expression

$$l^2 + m^2 = k^2U_{10}^2[(\overline{u_{10}}+u'_{10})^2 + (\overline{v_{10}}+v'_{10})^2] = k^2U_{10}^4, \tag{A6}$$

and solve for the positive wind speed magnitude U_{10}:

$$U_{10} = \left|\frac{\sqrt[4]{l^2+m^2}}{\sqrt{k}}\right|. \tag{A7}$$

Inserting Eq. (A7) into Eqs. (A4) and (A5) allows us to solve for the two unknowns u'_{10} and v'_{10}:

$$u'_{10} = \pm\frac{l\sqrt{k}}{k\sqrt[4]{l^2+m^2}} - \overline{u_{10}}, \tag{A8}$$

$$v'_{10} = \pm\frac{m\sqrt{k}}{k\sqrt[4]{l^2+m^2}} - \overline{v_{10}}, \tag{A9}$$

where the correct sign is determined using the wind stress anomaly spatial patterns.

By using this approach, it is ensured that desired symmetric wind stress anomalies are applied to the model. However, wind speed values from Eqs. (A8) and (A9) are also used to calculate the wind speed magnitude in the bulk formulas of sensible and latent heat fluxes [Eqs. (2a), (2b), and (3) in Fairall et al. (1996)]. Using the asymmetric wind speed values thus leads to asymmetric sensible and latent heat fluxes and furthermore also results in an 18% higher mean wind speed magnitude during La Niña than El Niño. While this asymmetry in sensible and latent heat fluxes as well as in wind speed magnitude is not ideal, it is of less importance than applying the correct symmetric wind stress values.

REFERENCES

Bernie, D. J., S. J. Woolnough, J. M. Slingo, and E. Guilyardi, 2005: Modeling diurnal and intraseasonal variability of the ocean mixed layer. *J. Climate*, **18**, 1190–1202, https://doi.org/10.1175/JCLI3319.1.

Bosc, C., and T. Delcroix, 2008: Observed equatorial Rossby waves and ENSO-related warm water volume changes in the equatorial Pacific Ocean. *J. Geophys. Res.*, **113**, C06003, https://doi.org/10.1029/2007JC004613.

Brown, J. N., and A. V. Fedorov, 2010: Estimating the diapycnal transport contribution to warm water volume variations in the tropical Pacific Ocean. *J. Climate*, **23**, 221–237, https://doi.org/10.1175/2009JCLI2347.1.

Burgers, G., F.-F. Jin, and G. J. van Oldenborgh, 2005: The simplest ENSO recharge oscillator. *Geophys. Res. Lett.*, **32**, L13706, https://doi.org/10.1029/2005GL022951.

Cheng, L., K. E. Trenberth, J. T. Fasullo, M. Mayer, M. Balmaseda, and J. Zhu, 2019: Evolution of ocean heat content related to ENSO. *J. Climate*, **32**, 3529–3556, https://doi.org/10.1175/JCLI-D-18-0607.1.

Clarke, A. J., S. Van Gorder, and G. Colantuono, 2007: Wind stress curl and ENSO discharge/recharge in the equatorial Pacific. *J. Phys. Oceanogr.*, **37**, 1077–1091, https://doi.org/10.1175/JPO3035.1.

Colella, P., and P. R. Woodward, 1984: The piecewise parabolic method (PPM) for gas-dynamical simulations. *J. Comput. Phys.*, **54**, 174–201, https://doi.org/10.1016/0021-9991(84)90143-8.

Collins, M., and Coauthors, 2010: The impact of global warming on the tropical Pacific Ocean and El Niño. *Nat. Geosci.*, **3**, 391–397, https://doi.org/10.1038/ngeo868.

Dee, D. P., and Coauthors, 2011: The ERA-Interim reanalysis: Configuration and performance of the data assimilation system. *Quart. J. Roy. Meteor. Soc.*, **137**, 553–597, https://doi.org/10.1002/qj.828.

Delworth, T. L., and Coauthors, 2012: Simulated climate and climate change in the GFDL CM2.5 high-resolution coupled climate model. *J. Climate*, **25**, 2755–2781, https://doi.org/10.1175/JCLI-D-11-00316.1.

Diaz, H. F., M. P. Hoerling, and J. K. Eischeid, 2001: ENSO variability, teleconnections and climate change. *Int. J. Climatol.*, **21**, 1845–1862, https://doi.org/10.1002/joc.631.

Fairall, C. W., E. F. Bradley, D. P. Rogers, J. B. Edson, and G. S. Young, 1996: Bulk parameterization of air–sea fluxes for Tropical Ocean–Global Atmosphere Coupled Ocean–Atmosphere Response Experiment. *J. Geophys. Res.*, **101**, 3747–3764, https://doi.org/10.1029/95JC03205.

Feng, M., N. Zhang, Q. Liu, and S. Wijffels, 2018: The Indonesian throughflow, its variability and centennial change. *Geosci. Lett.*, **5**, 3, https://doi.org/10.1186/s40562-018-0102-2.

Fox-Kemper, B., R. Ferrari, and R. Hallberg, 2008: Parameterization of mixed layer eddies. Part I: Theory and diagnosis. *J. Phys. Oceanogr.*, **38**, 1145–1165, https://doi.org/10.1175/2007JPO3792.1.

Gent, P. R., and J. C. McWilliams, 1990: Isopycnal mixing in ocean circulation models. *J. Phys. Oceanogr.*, **20**, 150–155, https://doi.org/10.1175/1520-0485(1990)020<0150:IMIOCM>2.0.CO;2.

Gregg, M. C., H. Peters, J. C. Wesson, N. S. Oakey, and T. J. Shay, 1985: Intensive measurements of turbulence and shear in the Equatorial Undercurrent. *Nature*, **318**, 140–144, https://doi.org/10.1038/318140a0.

Griffies, S. M., 2012: Elements of the Modular Ocean Model (MOM). GFDL Ocean Group Tech. Rep. 7, NOAA/GFDL, 645 pp., https://mom-ocean.github.io/assets/pdfs/MOM5_manual.pdf.

Groeskamp, S., S. M. Griffies, D. Iudicone, R. Marsh, A. G. Nurser, and J. D. Zika, 2019: The water mass transformation framework for ocean physics and biogeochemistry. *Annu. Rev. Mar. Sci.*, **11**, 271–305, https://doi.org/10.1146/annurev-marine-010318-095421.

Hallberg, R., 2013: Using a resolution function to regulate parameterizations of oceanic mesoscale eddy effects. *Ocean Modell.*, **72**, 92–103, https://doi.org/10.1016/j.ocemod.2013.08.007.

Hartmann, D. L., and Coauthors, 2013: Observations: Atmosphere and surface. *Climate Change 2013: The Physical Science Basis*, T. F. Stocker et al., Eds., Cambridge University Press, 159–254.

Holmes, R. M., and L. N. Thomas, 2015: The modulation of equatorial turbulence by tropical instability waves in a regional ocean model. *J. Phys. Oceanogr.*, **45**, 1155–1173, https://doi.org/10.1175/JPO-D-14-0209.1.

——, J. D. Zika, and M. H. England, 2019a: Diathermal heat transport in a global ocean model. *J. Phys. Oceanogr.*, **49**, 141–161, https://doi.org/10.1175/JPO-D-18-0098.1.

——, ——, R. Ferrari, A. F. Thompson, E. R. Newsom, and M. H. England, 2019b: Atlantic Ocean heat transport enabled by Indo-Pacific heat uptake and mixing. *Geophys. Res. Lett.*, **46**, 13 939–13 949, https://doi.org/10.1029/2019GL085160.

Horel, J. D., 1982: On the annual cycle of the tropical Pacific atmosphere and ocean. *Mon. Wea. Rev.*, **110**, 1863–1878, https://doi.org/10.1175/1520-0493(1982)110<1863:OTACOT>2.0.CO;2.

Izumo, T., M. Lengaigne, J. Vialard, I. Suresh, and Y. Planton, 2018: On the physical interpretation of the lead relation between warm water volume and the El Niño southern oscillation. *Climate Dyn.*, **52**, 2923–2942, https://doi.org/10.1007/S00382-018-4313-1.

Jin, F.-F., 1997a: An equatorial ocean recharge paradigm for ENSO. Part I: Conceptual model. *J. Atmos. Sci.*, **54**, 811–829, https://doi.org/10.1175/1520-0469(1997)054<0811:AEORPF>2.0.CO;2.

——, 1997b: An equatorial ocean recharge paradigm for ENSO. Part II: A stripped-down coupled model. *J. Atmos. Sci.*, **54**, 830–847, https://doi.org/10.1175/1520-0469(1997)054<0830:AEORPF>2.0.CO;2.

Jochum, M., G. Danabasoglu, M. Holland, Y.-O. Kwon, and W. G. Large, 2008: Ocean viscosity and climate. *J. Geophys. Res.*, **113**, C06017, https://doi.org/10.1029/2007JC004515.

Johnson, G. C., and A. N. Birnbaum, 2017: As El Niño builds, Pacific warm pool expands, ocean gains more heat. *Geophys. Res. Lett.*, **44**, 438–445, https://doi.org/10.1002/2016GL071767.

Kara, A. B., A. J. Wallcraft, E. J. Metzger, H. E. Hurlburt, and C. W. Fairall, 2007: Wind stress drag coefficient over the global ocean. *J. Climate*, **20**, 5856–5864, https://doi.org/10.1175/2007JCLI1825.1.

Kiss, A. E., and Coauthors, 2020: ACCESS-OM2: A global ocean–sea ice model at three resolutions. *Geosci. Model Dev.*, **13**, 401–442, https://doi.org/10.5194/gmd-13-401-2020.

Large, W. G., and A. G. Nurser, 2001: Ocean surface water mass transformation. *Ocean Circulation and Climate*, G. Siedler, J. Church, and J. Gould, Eds., International Geophysics Series, Vol. 77, Academic Press, 317–336, https://doi.org/10.1016/S0074-6142(01)80126-1.

——, and S. G. Yeager, 2004: Diurnal to decadal global forcing for ocean and sea-ice models: The data sets and flux climatologies. NCAR Tech. Note NCAR/TN-460+STR, 105 pp., https://doi.org/10.5065/D6KK98Q6.

——, J. C. McWilliams, and S. C. Doney, 1994: Oceanic vertical mixing: A review and a model with a non-local boundary layer parameterization. *Rev. Geophys.*, **32**, 363–403, https://doi.org/10.1029/94RG01872.

Lengaigne, M., U. Hausmann, G. Madec, C. Menkes, J. Vialard, and J.-M. Molines, 2012: Mechanisms controlling warm water volume interannual variations in the equatorial Pacific: Diabatic versus adiabatic processes. *Climate Dyn.*, **38**, 1031–1046, https://doi.org/10.1007/s00382-011-1051-z.

Lien, R.-C., D. R. Caldwell, M. C. Gregg, and J. N. Moum, 1995: Turbulence variability at the equator in the central Pacific at the beginning of the 1991–1993 El Niño. *J. Geophys. Res.*, **100**, 6881–6898, https://doi.org/10.1029/94JC03312.

Liu, C., A. Köhl, Z. Liu, F. Wang, and D. Stammer, 2016: Deep-reaching thermocline mixing in the equatorial Pacific cold tongue. *Nat. Commun.*, **7**, 11576, https://doi.org/10.1038/ncomms11576.

Liu, W., and Coauthors, 2015: Extended Reconstructed Sea Surface Temperature version 4 (ERSST.v4): Part II. Parametric and structural uncertainty estimations. *J. Climate*, **28**, 931–951, https://doi.org/10.1175/JCLI-D-14-00007.1.

Locarnini, R. A., and Coauthors, 2013: *Temperature*. Vol. 1, *World Ocean Atlas 2013*, NOAA Atlas NESDIS 73, 40 pp., http://data.nodc.noaa.gov/woa/WOA13/DOC/woa13_vol1.pdf.

McGregor, S., A. Timmermann, N. Schneider, M. F. Stuecker, and M. H. England, 2012: The effect of the South Pacific convergence zone on the termination of El Niño events and the meridional asymmetry of ENSO. *J. Climate*, **25**, 5566–5586, https://doi.org/10.1175/JCLI-D-11-00332.1.

——, N. Ramesh, P. Spence, M. H. England, M. J. McPhaden, and A. Santoso, 2013: Meridional movement of wind anomalies during ENSO events and their role in event termination. *Geophys. Res. Lett.*, **40**, 749–754, https://doi.org/10.1002/grl.50136.

——, P. Spence, F. U. Schwarzkopf, M. H. England, A. Santoso, W. S. Kessler, A. Timmermann, and C. W. Böning, 2014: ENSO-driven interhemispheric Pacific mass transports. *J. Geophys. Res. Oceans*, **119**, 6221–6237, https://doi.org/10.1002/2014JC010286.

——, A. Timmermann, F.-F. Jin, and W. S. Kessler, 2016: Charging El Niño with off-equatorial westerly wind events. *Climate Dyn.*, **47**, 1111–1125, https://doi.org/10.1007/s00382-015-2891-8.

——, A. Sen Gupta, D. Dommenget, T. Lee, M. J. McPhaden, and W. S. Kessler, 2017: Factors influencing the skill of synthesized satellite wind products in the tropical Pacific. *J. Geophys. Res. Oceans*, **122**, 1072–1089, https://doi.org/10.1002/2016JC012340.

McPhaden, M. J., 2012: A 21st century shift in the relationship between ENSO SST and warm water volume anomalies. *Geophys. Res. Lett.*, **39**, L09706, https://doi.org/10.1029/2012GL051826.

Meehl, G. A., J. M. Arblaster, J. T. Fasullo, A. Hu, and K. E. Trenberth, 2011: Model-based evidence of deep-ocean heat uptake during surface-temperature hiatus periods. *Nat. Climate Change*, **1**, 360–364, https://doi.org/10.1038/nclimate1229.

Meinen, C. S., and M. J. McPhaden, 2000: Observations of warm water volume changes in the equatorial Pacific and their relationship to El Niño and La Niña. *J. Climate*, **13**, 3551–3559, https://doi.org/10.1175/1520-0442(2000)013<3551:OOWWVC>2.0.CO;2.

——, and ——, 2001: Interannual variability in warm water volume transports in the equatorial Pacific during 1993–99. *J. Phys. Oceanogr.*, **31**, 1324–1345, https://doi.org/10.1175/1520-0485(2001)031<1324:IVIWWV>2.0.CO;2.

——, ——, and G. C. Johnson, 2001: Vertical velocities and transports in the equatorial Pacific during 1993–99. *J. Phys. Oceanogr.*, **31**, 3230–3248, https://doi.org/10.1175/1520-0485(2001)031<3230:VVATIT>2.0.CO;2.

Menkes, C. E., M. Lengaigne, J. Vialard, M. Puy, P. Marchesiello, S. Cravatte, and G. Cambon, 2014: About the role of westerly wind events in the possible development of an El Niño in 2014. *Geophys. Res. Lett.*, **41**, 6476–6483, https://doi.org/10.1002/2014GL061186.

Morice, C. P., J. J. Kennedy, N. A. Rayner, and P. D. Jones, 2012: Quantifying uncertainties in global and regional temperature change using an ensemble of observational estimates: The HadCRUT4 data set. *J. Geophys. Res.*, **117**, D08101, https://doi.org/10.1029/2011JD017187.

Moum, J. N., A. Perlin, J. D. Nash, and M. J. McPhaden, 2013: Seasonal sea surface cooling in the equatorial Pacific cold tongue controlled by ocean mixing. *Nature*, **500**, 64–67, https://doi.org/10.1038/nature12363.

Neske, S., and S. McGregor, 2018: Understanding the warm water volume precursor of ENSO events and its interdecadal variation. *Geophys. Res. Lett.*, **45**, 1577–1585, https://doi.org/10.1002/2017GL076439.

Okumura, Y. M., and C. Deser, 2010: Asymmetry in the duration of El Niño and La Niña. *J. Climate*, **23**, 5826–5843, https://doi.org/10.1175/2010JCLI3592.1.

Pham, H. T., W. D. Smyth, S. Sarkar, and J. N. Moum, 2017: Seasonality of deep cycle turbulence in the eastern equatorial Pacific. *J. Phys. Oceanogr.*, **47**, 2189–2209, https://doi.org/10.1175/JPO-D-17-0008.1.

Rayner, N., D. E. Parker, E. Horton, C. Folland, L. Alexander, D. Rowell, E. Kent, and A. Kaplan, 2003: Global analyses of sea surface temperature, sea ice, and night marine air temperature since the late nineteenth century. *J. Geophys. Res.*, **108**, 4407, https://doi.org/10.1029/2002JD002670.

Redi, M. H., 1982: Oceanic isopycnal mixing by coordinate rotation. *J. Phys. Oceanogr.*, **12**, 1154–1158, https://doi.org/10.1175/1520-0485(1982)012<1154:OIMBCR>2.0.CO;2.

Reynolds, R. W., T. M. Smith, C. Liu, D. B. Chelton, K. S. Casey, and M. G. Schlax, 2007: Daily high-resolution-blended analyses for sea surface temperature. *J. Climate*, **20**, 5473–5496, https://doi.org/10.1175/2007JCLI1824.1.

Roemmich, D., and J. Gilson, 2011: The global ocean imprint of ENSO. *Geophys. Res. Lett.*, **38**, L13606, https://doi.org/10.1029/2011GL047992.

Schott, F. A., J. P. McCreary Jr., and G. C. Johnson, 2004: Shallow overturning circulations of the tropical-subtropical oceans. *Earth's Climate*, **147**, 261–304, https://doi.org/10.1029/147GM15.

Shinoda, T., W. Han, E. J. Metzger, and H. E. Hurlburt, 2012: Seasonal variation of the Indonesian Throughflow in Makassar Strait. *J. Phys. Oceanogr.*, **42**, 1099–1123, https://doi.org/10.1175/JPO-D-11-0120.1.

Smith, T. M., and R. W. Reynolds, 2003: Extended reconstruction of global sea surface temperatures based on COADS data (1854–1997). *J. Climate*, **16**, 1495–1510, https://doi.org/10.1175/1520-0442-16.10.1495.

Smyth, W. D., and J. N. Moum, 2013: Marginal instability and deep cycle turbulence in the eastern equatorial Pacific Ocean. *Geophys. Res. Lett.*, **40**, 6181–6185, https://doi.org/10.1002/2013GL058403.

Spence, P., R. M. Holmes, A. M. Hogg, S. M. Griffies, K. D. Stewart, and M. H. England, 2017: Localized rapid warming of West Antarctic subsurface waters by remote winds. *Nat. Climate Change*, **7**, 595–603, https://doi.org/10.1038/nclimate3335.

Sprintall, J., and A. Révelard, 2014: The Indonesian Throughflow response to Indo-Pacific climate variability. *J. Geophys. Res. Oceans*, **119**, 1161–1175, https://doi.org/10.1002/2013JC009533.

Stewart, K., A. M. Hogg, S. Griffies, A. Heerdegen, M. Ward, P. Spence, and M. England, 2017: Vertical resolution of baroclinic modes in global ocean models. *Ocean Modell.*, **113**, 50–65, https://doi.org/10.1016/j.ocemod.2017.03.012.

Stuecker, M. F., A. Timmermann, F.-F. Jin, S. McGregor, and H.-L. Ren, 2013: A combination mode of the annual cycle and the El Niño/Southern Oscillation. *Nat. Geosci.*, **6**, 540–544, https://doi.org/10.1038/ngeo1826.

——, F.-F. Jin, A. Timmermann, and S. McGregor, 2015: Combination mode dynamics of the anomalous northwest Pacific anticyclone. *J. Climate*, **28**, 1093–1111, https://doi.org/10.1175/JCLI-D-14-00225.1.

Suarez, M. J., and P. S. Schopf, 1988: A delayed action oscillator for ENSO. *J. Atmos. Sci.*, **45**, 3283–3287, https://doi.org/10.1175/1520-0469(1988)045<3283:ADAOFE>2.0.CO;2.

Timmermann, A., and Coauthors, 2018: El Niño–Southern Oscillation complexity. *Nature*, **559**, 535–545, https://doi.org/10.1038/s41586-018-0252-6.

Trenberth, K. E., J. M. Caron, D. P. Stepaniak, and S. Worley, 2002: Evolution of El Niño–Southern Oscillation and global atmospheric surface temperatures. *J. Geophys. Res.*, **107**, 4065, https://doi.org/10.1029/2000JD000298.

——, and Coauthors, 2007: Observations: Surface and atmospheric climate change. *Climate Change 2007: The Physical Science Basis*, S. Solomon et al., Eds., Cambridge University Press, 235–336.

Tsujino, H., and Coauthors, 2018: JRA-55 based surface dataset for driving ocean–sea-ice models (JRA55-do). *Ocean Modell.*, **130**, 79–139, https://doi.org/10.1016/j.ocemod.2018.07.002.

Walin, G., 1982: On the relation between sea-surface heat flow and thermal circulation in the ocean. *Tellus*, **34**, 187–195, https://doi.org/10.3402/tellusa.v34i2.10801.

Warner, S. J., and J. N. Moum, 2019: Feedback of mixing to ENSO phase change. *Geophys. Res. Lett.*, **46**, 13 920–13 927, https://doi.org/10.1029/2019GL085415.

Wu, Q., X. Zhang, J. A. Church, and J. Hu, 2019: ENSO-related global ocean heat content variations. *J. Climate*, **32**, 45–68, https://doi.org/10.1175/JCLI-D-17-0861.1.

Wyrtki, K., 1975: El Niño—The dynamic response of the equatorial Pacific Ocean to atmospheric forcing. *J. Phys. Oceanogr.*, **5**, 572–584, https://doi.org/10.1175/1520-0485(1975)005<0572:ENTDRO>2.0.CO;2.

——, 1985: Water displacements in the Pacific and the genesis of El Niño cycles. *J. Geophys. Res.*, **90**, 7129–7132, https://doi.org/10.1029/JC090iC04p07129.

Zeller, M., S. McGregor, and P. Spence, 2019: Hemispheric asymmetry of the Pacific shallow meridional overturning circulation. *J. Geophys. Res. Oceans*, **124**, 5765–5786, https://doi.org/10.1029/2018JC014840.

Zuo, H., M. Balmaseda, K. Mogensen, and S. Tietsche, 2018: OCEAN5: The ECMWF Ocean Reanalysis System and its real-time analysis component. European Centre for Medium-Range Weather Forecasts, 44 pp.

C

Additional Peer-Reviewed Study

A copy of the additional published article as a first author during the PhD candidature and the author's contribution is included hereafter. This article is published under the CC BY-NC-ND licence (see page xxxv for the copyright statement).

Huguenin, M. F. [1, 2, 3, 4], Fischer, E. M.[1], Kotlarski, S.[4], Scherrer, S. C.[4], Schwierz, C.[4], & Knutti, R.[1] (2020a). Lack of Change in the Projected Frequency and Persistence of Atmospheric Circulation Types Over Central Europe. *Geophysical Research Letters*. **47**. https://doi.org/10.1029/2019GL086132

R. K. had the initial idea for the persistence measure. M. F. H. performed the analyses and wrote the initial draft of the paper in discussion with the other co-authors. All authors formulated the experimental design, contributed to interpreting the results and refinement of the paper.

1. Institute for Atmospheric and Climate Science, ETH Zürich, Zürich, Switzerland 2. Climate Change Research Centre, University of New South Wales, Sydney, NSW, Australia 3. ARC Centre of Excellence in Climate Extremes, University of New South Wales, Sydney, NSW, Australia 4. Federal Office of Meteorology and Climatology, MeteoSwiss, Zürich, Switzerland

Geophysical Research Letters

RESEARCH LETTER
10.1029/2019GL086132

Key Points:
- Climate models project warmer and drier Central European summer conditions under strong global warming independent of the circulation type
- For most circulation types, the models do not agree on the sign and/or magnitude of the projected change in the frequency and persistence
- Current global climate models do not support a general trend towards more persistent weather in Central Europe

Supporting Information:
- Supporting Information S1

Correspondence to:
M. F. Huguenin,
m.huguenin-virchaux@unsw.edu.au

Citation:
Huguenin, M. F., Fischer, E. M., Kotlarski, S., Scherrer, S. C., Schwierz, C., & Knutti, R. (2020). Lack of change in the projected frequency and persistence of atmospheric circulation types over Central Europe. *Geophysical Research Letters*, *47*. https://doi.org/10.1029/2019GL086132

Received 6 NOV 2019
Accepted 24 MAR 2020

Lack of Change in the Projected Frequency and Persistence of Atmospheric Circulation Types Over Central Europe

Maurice F. Huguenin[1,2,3], Erich M. Fischer[1], Sven Kotlarski[2], Simon C. Scherrer[2], Cornelia Schwierz[2], and Reto Knutti[1]

[1]Institute for Atmospheric and Climate Science, ETH Zurich, Zurich, Switzerland, [2]Federal Office of Meteorology and Climatology, MeteoSwiss, Zurich, Switzerland, [3]Climate Change Research Centre and ARC Centre of Excellence for Climate Extremes, University of New South Wales, Sydney, New South Wales, Australia

Abstract In recent summers, Europe experienced record-breaking heatwaves, wildfires (in Northern Europe), and large-scale water scarcity. Apart from anthropogenic warming, one contribution leading to such exceptionally hot weather was a weaker jet stream allowing a quasi-stationary high-pressure system to persist for many days. Here, we quantify changes in the frequency and persistence of the Central European large-scale circulation types using various climate models. Independent of the circulation type, the models project warmer and drier future summer conditions in Central Europe, but no consistent shift to a more persistent summer or winter circulation. Most of the frequency and persistence changes are small and either within the internal variability or inconsistent across models. The model projections in this study do not support the claim of more persistent weather over Central Europe. Reconciling the results of different approaches and classifications is therefore critical to understand and predict changes in extreme weather over Europe.

Plain Language Summary The atmospheric flow over Central Europe is a key component of both its weather and climate. Recent studies have suggested that the Central European weather patterns are becoming more persistent due to our influence on the climate system. Persistent conditions can lead to record-breaking droughts and heatwaves. It is therefore important to know how the flow conditions (also called circulation types) may change in the future. Here, we use a wide range of global climate models and classify a circulation type for each day. We distinguish between the eight main wind directions and a high- and low-pressure type. Then, we quantify changes in the frequency and length of these circulation types under a strong global warming scenario at the end of the 21st century. In summer, we find a shift to warmer and drier conditions. Our models also show somewhat more persistent summer westerlies. In winter, the changes are not clear. Most of the changes in the circulation are small and likely within the range expected from natural random weather fluctuations. Our study highlights the importance of using many different climate models and other methods to investigate the highly variable Central European circulation today and under a future climate.

1. Introduction

The Central European weather and climate is controlled by the large-scale extratropical atmospheric flow of which the midlatitude westerly jet streams are key components (Woollings et al., 2010). There are two physical processes that give rise to the strength and position of the subtropical and eddy-driven jets: the westerly acceleration of poleward moving air consistent with the local vorticity balance as well as the momentum and heat forcing arising from transient eddies (Peña-Ortiz et al., 2013; Woollings et al., 2010). Most often, there is no spatial separation between individual jet streams (Woollings et al., 2010). As a result of human-induced climate change, the hemispheric lower-tropospheric temperature gradient is projected to weaken, and may thus impact on the jet streams and the atmospheric circulation over the European continent downstream (Blackport & Screen, 2019; Coumou et al., 2018; Coumou & Rahmstorf, 2012; Intergovernmental Panel on Climate Change [IPCC], 2014; Jézéquel et al., 2018; Mori et al., 2019; Steirou et al., 2017).

To study the regional impacts and long-term changes in the atmospheric circulation over Central Europe, the large-scale flow is commonly classified into different circulation types (Demuzere et al., 2011;

Kučerová et al., 2017), each with a characteristic temperature and precipitation signal on the continent. Persistent circulation types are often associated with the occurrence of extreme events resulting in drought and heatwaves in summer (Perkins, 2015; Pfleiderer & Coumou, 2018; Röthlisberger et al., 2016) or heavy snowfall events in winter (Cattiaux et al., 2010; Pfahl & Wernli, 2012). However, the impacts of circulation types on the weather and extreme events are expected to change in a warmer climate (e.g., a future circulation type may bring stronger storm activity due to warmer air being able to hold a higher moisture content; Molnar et al., 2015).

Evidence from observational and modeling studies is now emerging that accelerated warming in the Arctic may affect the Central European circulation by increasing its persistence (Cohen et al., 2014; Coumou et al., 2018; Francis et al., 2018; Pfleiderer et al., 2019; Vavrus, 2018). The increased sea ice loss and subsequent Arctic warming affects the planetary waves, the midlatitude jet streams, and the strength of the storm tracks (Cohen et al., 2012; Coumou et al., 2018). This consequently favors more extreme weather over Europe (Barnes & Screen, 2015; Francis & Vavrus, 2012; Pfleiderer & Coumou, 2018). However, there is currently low confidence in the linkage between Arctic and mid-latitude weather (Barnes & Polvani, 2015; Francis et al., 2018). While Blackport et al. (2019) and Fyfe (2019) present compelling evidence that Arctic warming impacts on the circulation over Eurasia are not responsible for recent severe midlatitude winters, Dai and Song (2020) state that climatic impacts of Arctic warming are probably small outside the high latitudes.

The inherent complexities to simulate changes in the atmospheric circulation caused by sea ice loss and accelerated warming in the Arctic together with changes in the water cycle and land-atmosphere interactions under global warming hinder the scientific consensus in many modeling studies (Barnes & Screen, 2015; Vavrus, 2018). To some degree, this might be caused by the current climate models not robustly supporting the links between sea ice loss, increased heat transfer from the ocean to the atmosphere and the corresponding impact on the atmospheric circulation that carries air from the Arctic into the mid-latitudes (Fyfe, 2019). Difficulties in assessing the impact of Arctic amplification also arise from the short observational time series and the high degree of internal synoptic-scale variability in the midlatitude circulation. Therefore, many questions on changes to the atmospheric circulation over Central Europe remain unanswered.

By classifying the atmospheric flow over Central Europe into different circulation types using a wide range of global general circulation models (GCMs), we can investigate their future changes and surface impacts under global warming scenarios. The different models enable us to capture the high degree of variability in the circulation as well as uncertainties in future changes.

2. Data, Classification Software, and Methods

2.1. Model and Reference Data

To best capture the complex, nonlinear interactions on a global scale, we use coupled ocean–atmosphere GCMs in our analysis. We use daily output from the global Community Earth System Model version 1.2 (CESM12-LE, hereafter CESM; Hurrell et al., 2013) in the large ensemble setup with 84 realizations and a grid spacing of $2.5° \times 1.9°$. To explore model structural uncertainty in our analysis, we additionally use data from 18 models of the Coupled Model Intercomparison Project Phase 5 (CMIP5) with a total of 23 realizations bilinearly regridded to a resolution of 1° (for more information on the CMIP5 models, see Supporting Information Table S1). For both model setups, we use data from the historical period (1960–2005) and from the representative concentration pathway 8.5 forcing scenario (2006–2099). While the GCM's grid resolution over Central Europe is a limiting factor in our analysis, the available data enables us to investigate both current and future Central European climate variability within a large number of ensemble members. Future climate change signals are analyzed for the period 2070–2099 with respect to the historical reference period 1988–2017.

As a reference data set, we use the combined ERA-40/-Interim reanalysis product for the time period 1960–2017 with a spatial resolution of 1° (Dee et al., 2011; Uppala et al., 2005). ERA-40 covers the time period from the 1 January 1960 until the 31 August 2002, while ERA-Interim extends the data set until the 31 December 2017.

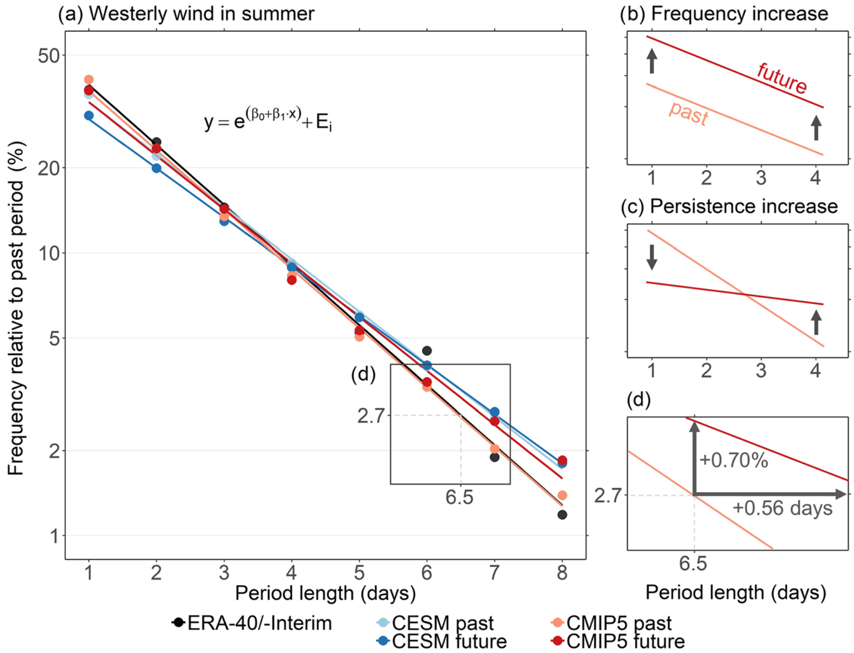

Figure 1. (a) Frequency and length of uninterrupted summer westerly wind periods for the reanalysis (black) and the ensemble mean CESM (blue) and CMIP5 (red) data sets with a logarithmic fit. The equation in black represents the logarithmic regression model $y = e^{\beta_0+\beta_1 \cdot x} + E_i$, where β_0 is the intercept, β_1 is the slope that we define as our persistence measure, and E_i is the error term. (b, c) Schematics of changes to the fit in only the frequency or persistence. (d) Inset for the CMIP5 data showing changes to the persistence fit and its impacts on a continuous 6.5-day long period as an example of the interpretation. Subfigures (b, c, and d) are not to scale.

2.2. The COST733class Classification Software

Following Weusthoff (2011) and Rohrer et al. (2017), we classify the main synoptic-scale circulation types over Central Europe (3°E to 20°E and 41°N to 52°N; Figure S1) with the COST733class software from Demuzere et al. (2011) using daily geopotential height fields on 500 hPa. We use these midtropospheric flow fields as they are more robust compared to ground-based variables over the Alpine region in lower resolution models.

From the COST733class software, we use the Grosswetter-types classification method (cf. also Beck et al., 2007) that determines circulation types according to their correlation with a strict zonal, meridional, or anticyclonic/cyclonic flow pattern with a pressure maximum/minimum in the center of the domain (Weusthoff, 2011). We use the following 10 circulation types: the eight main wind directions west (W), southwest (SW), northwest (NW), north (N), northeast (NE), east (E), and south (S) as well as cyclonic (C) and anticyclonic (A) flow patterns. Our analysis focuses on the summer (June–August) and winter (December–February) seasons.

2.3. A Measure for Persistence

A persistent circulation type is defined as one that prevails over an uninterrupted time period. Figure 1 serves as an example how we construct the persistence measure for all circulation types. The length of a continuous circulation type period and its seasonal frequency (e.g., here for westerly wind in summer; Figure 1a) are well described by a logarithmic regression, implying that the transition probability to another type is largely independent of the length of the period. A 1-day period of westerly wind in summer is nearly twice as frequent as a 2-day period. A logarithmic regression model thus allows us to estimate the decrease in the frequency with increasing duration of a given circulation type. Changes in the slope between past and future time periods are thus equivalent to changes in the persistence. Note that our approach is limited by the data availability for a given circulation type. For example, it cannot be applied to easterly wind as this circulation type only occurs on 1 to 2 days each season (Figures 2a and 2b and S2f). We also require uninterrupted

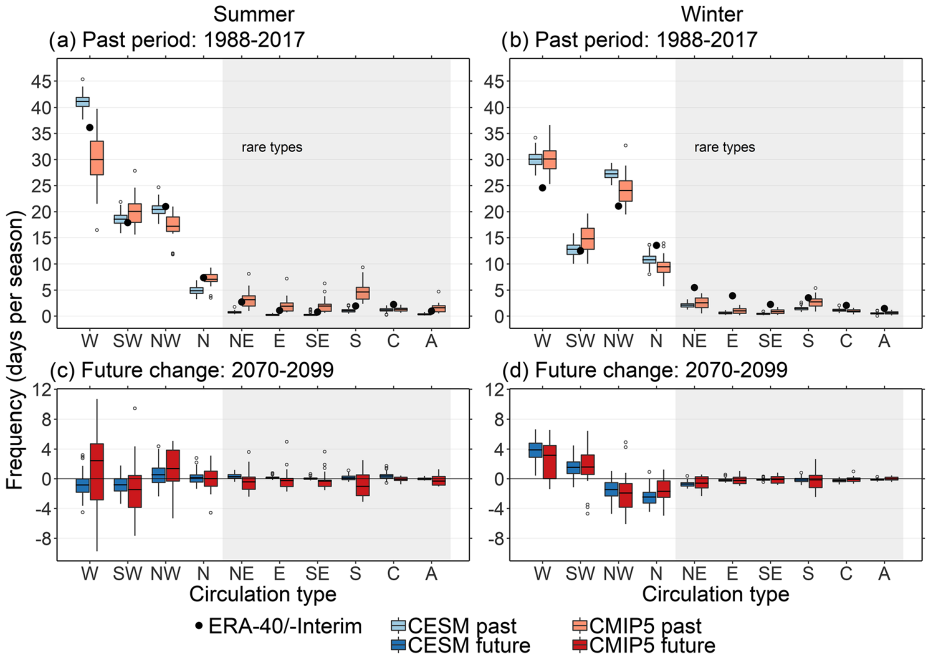

Figure 2. Frequency of the 10 circulation types (days per season) during (a) summer and (b) winter for the period 1988–2017 in both CESM (blue) and the CMIP5 models (red). The frequency in the reanalysis data is given as the black dot. In (c) and (d), the projected changes (days per season) in the models for the future period 2070–2099 are shown relative to the past period. The horizontal line in each boxplot represents the ensemble mean. The gray shaded area indicates the rare circulation types. See section 2.2 for a definition of the circulation types.

periods of the same circulation type for our persistence measure. We analyze all circulation types but focus our interpretation on the four main types.

To calculate a consistent regression model across the reanalysis, the CESM and the CMIP5 data sets for both the past and future time periods, we first remove continuous time periods occurring less than 1% each season and also ensure that we calculate the regression over the same period length for all three data sets. This means that if the reanalysis includes period lengths of up to 5 days and the CESM model has longer periods, we calculate the regression model including up to 5-day periods. We then define the slope parameter of the logarithmic fit β_1 as our persistence measure.

Changes to the regression fit arise from the two combined changes in the frequency and in the persistence: (1) a change in the intercept of the fit β_0 represents a frequency change of a given circulation type (Figure 1b); and (2) a change in the slope results in a frequency change towards short periods and a simultaneous change to longer-term periods, that is, a change in the persistence (Figure 1c). As a change in persistence of a given circulation type is dependent on the frequency, we consider as suggested by Kyselý (2008), changes in the frequency in our calculation of the future persistence. This means that we account for a higher probability of persistence given a future frequency increase of a circulation type (and vice versa). As an illustration of the two effects, Figure 1d shows the changes to a 6.5-day westerly wind period in the CMIP5 ensemble mean. This period is as frequent today as a 7-day period in the future (horizontal arrow), and a 6.5-day period today will be 0.7% more frequent in the future (vertical arrow).

3. Results and Discussion

3.1. Changes in the Frequency of Circulation Types

The large-scale atmospheric flow field over Central Europe is dominated by the four wind directions west, northwest, southwest, and north, which contribute 75% to 80% to the seasonal variability (Figures 2a and 2b). The models reproduce the seasonal frequencies in the reanalysis data set reasonably well (Figures 2a and 2b). For both summer and winter seasons, the results are very similar to those in Rohrer et al. (2017).

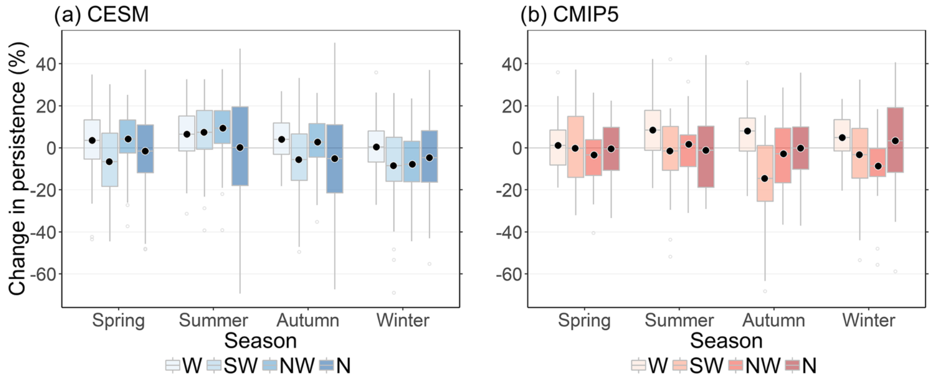

Figure 3. Seasonal future persistence change (%) for the four main circulation types in (a) CESM and (b) CMIP5 relative to the past period as boxplots representing the spread within the ensemble members. The ensemble mean for each circulation type is given as a black dot.

The variability within the CESM ensemble members (blue boxplots) is small compared to the CMIP5 members (red boxplots). While the CESM data only account for internal variability, the CMIP5 models additionally include model uncertainty explaining the larger spread found in this data set.

CESM and CMIP5 also differ in their biases with respect to the reanalysis. In summer, the frequency of westerlies over Central Europe relative to the reanalysis is overestimated in CESM (Figure 2a), likely caused by the too zonal flow in this model (Kwon et al., 2018). The increased frequency of westerlies in CESM is compensated by an underestimation of the northerly flow and the rarer circulation types. In the CMIP5 models, the mean frequencies in summer are reproduced reasonably well, except for an underestimation of westerlies. During the winter season, westerlies and north westerlies are overestimated in both model data sets at the expense of northerly flow and the rarer circulation types (Figure 2b). In winter, all models consistently underestimate the rare circulation types (Figure 2b). This is unfortunate as some of these circulation types (e.g., the anticyclonic circulation) may be conducive to temperature extremes (Black & Sutton, 2006; Pfahl & Wernli, 2012; Brunner et al., 2018).

The observed trends in the frequency of the circulation types over the 1960–2017 period are not significant on the 95% confidence level (Figures S3 and S4) and lie within the variability of the modeled trends (Figure S5). The significance level is in some cases exceeded when considering only a 30-year period (e.g., the frequency of north westerlies significantly decreases with -3.2 days decade^{-1} in summer for 1988–2017). However, these trends turn out to be not robust when considering longer periods. Consequently, we urge cautiousness in assessing trends in the atmospheric circulation over short time intervals.

Projected future changes in circulation frequencies are consistently small and within the range of ± 4 days per season (Figures 2c and 2d). The spread in the frequency changes for the main circulation types within CMIP5, owing to model variability, is considerably larger than in CESM. The only significant change occurring in the future period is an increase in westerlies in winter in the CESM model (Figure 2d). However, this change may in part be overestimated in this model due to the zonal flow bias mentioned above.

3.2. Changes in the Persistence of Circulation Types

The future changes in the persistence measure show a large spread in both CESM and CMIP5, are small, and not significant (Figure 3). In part, this may be caused by the large natural variability within the Central European circulation and the models' difficulties in linking dynamic and thermodynamic changes. This was for instance recognized considering Arctic sea ice loss and its relation to the midlatitude dynamics (Fyfe, 2019). The CESM results indicate an increase in persistence in summer and a decrease in winter (Figure 3a). In CMIP5, potential future seasonal changes are not as clear. Only the westerly circulation type shows an increased persistence over all four seasons in both CESM and CMIP5 with a maximum in summer. In CESM, north-westerly persistence is also projected to increase throughout spring, summer, and autumn (Figure 3a).

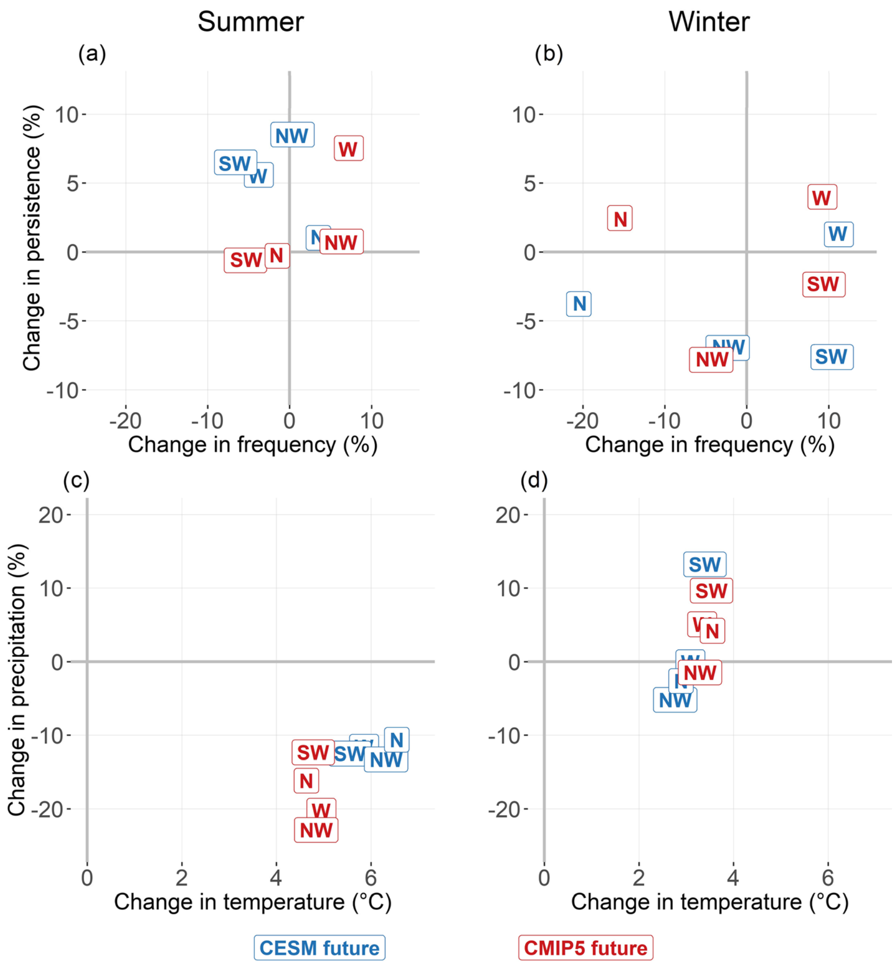

Figure 4. Summary of future 2070–2099 summer and winter (a, b) frequency and persistence (%) as well as (c, d) temperature (°C) and precipitation (%) changes of the main Central European circulation types relative to 1988–2017. Shown here is the ensemble mean for CESM (blue) and CMIP5 (red). For more information on the variability between the ensemble members, see Figures 3 and S6.

3.3. Summary of Frequency and Persistence Changes

The relative future frequency and persistence changes are summarized by way of the ensemble means in Figures 4a and 4b. As introduced above, the models project a small change towards more persistent summer westerlies but generally disagree on the sign and magnitude of the changes for the other circulation types. In winter, evidence for higher persistence is even weaker; persistence can either increase or decrease depending on the circulation type. Considering the large variability across the ensemble members, we argue that projected changes in the frequency and persistence are likely within the range of internal variability or not consistent across models (Figures 3, S6a, S6b, and S7).

The overall small changes in the frequency and persistence might in part arise from the models' current limitations in simulating future changes in the atmospheric circulation. It has been suggested that they underestimate or even miss links between Arctic sea ice loss and the midlatitude circulation (Fyfe, 2019; Mori et al., 2019), that the models might be underestimating changes in the water cycle caused by enhanced evapotranspiration in a warming climate (Pfleiderer et al., 2019), or that they might encounter difficulties in simulating land-atmosphere feedback mechanisms (Hirschi et al., 2011).

In addition to the frequency and persistence changes, we also evaluate future changes in near-surface temperature and precipitation during the occurrence of each circulation type (see Figures S9–S20 for spatial maps). We find an average shift to warmer and drier conditions in Central Europe across all circulation types in summer (Figure 4c), consistent with IPCC (2014), Coumou et al. (2018), and Li et al. (2018). The projected warming signal for the winter season is about 50% smaller than in summer. In part, this increased summer warming signal can be explained by the positive feedback mechanisms between the surface air temperature, soil moisture, evapotranspiration, and clouds in a warmer climate (Seneviratne et al., 2010) and by the influence of lapse rate changes linked to an extending Hadley circulation (Brogli et al., 2019; Kröner et al., 2017). Our results here agree with the statement of more dry-warm summers in Pfleiderer et al. (2019) and the projections of the Swiss Climate Scenarios CH2018 (CH2018, 2018).

4. Conclusions and Outlook

In this study, we classified daily geopotential height at 500 hPa between 1960 and 2100 from a CESM initial condition large ensemble setup and models from the CMIP5 project into 10 circulation types over Central Europe. As a validation data set, we used the ERA-40/-Interim reanalysis product for the time period 1960–2017. Our Grosswetter-types classification method categorized 10 circulation types according to a correlation coefficient with a strictly zonal, meridional, or anticyclonic/cyclonic flow in the COST733class software. We analyzed observed and projected changes in their frequency and expanded from Demuzere et al. (2011), Kučerová et al. (2017), and Rohrer et al. (2017) by considering a larger set of models, allowing for a better assessment of model uncertainty, and by introducing a new persistence measure to assess projected changes in the length of a continuous circulation type for the future time period 2070–2099. We also evaluated the future effects of each individual circulation type on temperature and precipitation impacts.

The projected changes in the frequency and persistence are small across models and circulation types, and the large variability in the signals arises either from internal climate fluctuations or model disagreement. Where simulated changes are stronger, they are usually not consistent across models. The clearest signal is towards somewhat more persistent westerlies in summer. Our results therefore, at least based on the currently available climate models, the chosen weather classification and for Central Europe, do not support the claim that anthropogenic influence on the jet streams makes the weather more persistent (as in Rohrer et al., 2017; Coumou et al., 2018; Francis et al., 2018; Mann et al., 2018; Pfleiderer et al., 2019) and are more in line with studies showing no clear change (Chen et al., 2016; Schaller et al., 2018). Some of these studies that see changes in fact only see a small change that needs many model simulations to become significant. A rigorous intercomparison of different methodological approaches, weather classifications, and model experiments is needed to reconcile the apparent discrepancies in the interpretation of the findings. Before these discrepancies are resolved, the interpretation of past trends and single-weather events as well as explicit or implied extrapolations into the future is speculative at best. Also note that the relation between jet waviness and extreme events is complex and depends on the region (Röthlisberger et al., 2016). We do not conclude from our findings that there is no effect but that current climate models do not agree on changes in the atmospheric circulation.

Future changes in both temperature and precipitation are clearer. The models project a future change towards more hot-and-dry Central European summers independent of the circulation and in winter a shift to warmer conditions with precipitation changes dependent on the circulation type.

Our results show that assessing future changes in the Central European circulation remains a challenging topic, which is best undertaken by using both single and multimodel ensemble setups to capture the large variability and model spread. Complications in arriving at clear signals may also partially arise from the models' limited capacity to correctly simulate interactions between the ocean, sea ice, and atmosphere and its large-scale impacts on the European weather. Some of these deficiencies may be similar in most models (Mori et al., 2019).

We advocate for future research expanding upon our persistence measure to investigate high-impact changes in very rare long-term persistent events. It would be beneficial to evaluate the transitional probabilities for each circulation type and whether they differ for different models. Additionally, it would be helpful to further examine the isolated impact of Arctic sea ice loss and the resulting changes in the temperature gradient on the atmospheric circulation (Gerber et al., 2012; Screen & Blackport, 2019), its implications on the extratropical jet stream, and future Central European weather persistence with the latest model configurations in the CMIP6 project.

Acknowledgments

We thank U. Beyerle for assistance in setting up the COST733class software and his technical support throughout this project. We thank the editor, Alessandra Giannini, and two anonymous reviewers for their constructive suggestions that have improved the manuscript. We thank the University of Augsburg for free access to the classification software and documentation. In addition, we thank the European Center for Mid-Range Weather Forecast (ECMWF) for providing access to the ERA-40/-Interim reanalysis product, and we thank the National Center for Atmospheric Research (NCAR) for the development of the CESM. We acknowledge the World Climate Research Program's Working Group on Coupled Modeling, which is responsible for CMIP, and we thank the climate modeling groups (listed in Table S1) for producing and making available their model output. The COST733class output files and analysis scripts are publicly available at https://github.com/mauricehuguenin/europe_circulation_types.

References

Barnes, E. A., & Screen, J. A. (2015). The impact of Arctic warming on the midlatitude jet-stream: Can it? Has it? Will it? *WIREs Climate Change*, *6*, 277–286. https://doi.org/10.1002/wcc.337

Barnes, E. A., & Polvani, L. M. (2015). CMIP5 Projections of Arctic Amplification, of the North American/North Atlantic Circulation, and of Their Relationship. *Journal of Climate*, *28*(13), 5254–5271. https://doi.org/10.1175/JCLI-D-14-00589.1

Beck, C., Jacobeit, J., & Jones, P. D. (2007). Frequency and within-type variations of large-scale circulation types and their effects on low-frequency climate variability in Central Europe since 1780. *International Journal of Climatology*, *27*, 473–491. http://doi.org/10.1002/joc.1410

Black, E., & Sutton, R. (2006). The influence of oceanic conditions on the hot European summer of 2003. *Climate Dynamics*, *28*, 53–66. https://doi.org/10.1007/s00382-006-0179-8

Blackport, R., Screen, J. A., van der Wiel, K., & Bintanja, R. (2019). Minimal influence of reduced Arctic sea ice on coincident cold winters in midlatitudes. *Nature Climate Change*, *9*(9), 697–704. https://doi.org/10.1038/s41558-019-0551-4

Blackport, R., Screen, J. A., van der Wiel, K., & Bintanja, R. (2019). Coincident cold winters in mid-latitudes. *Nature Climate Change*, *9*(9), 697–704. https://doi.org/10.1038/s41558-019-0551-4

Brogli, R., Kröner, N., Sørland, S. L., Lüthi, D., & Schär, C. (2019). The role of Hadley circulation and lapse-rate changes for the future European summer climate. *Journal of Climate*, *32*, 385–404. https://doi.org/10.1175/JCLI-D-18-0431.1

Brunner, L., Schaller, N., Anstey, J., Sillmann, J., & Steiner, A. K. (2018). Dependence of present and future European temperature extremes on the location of atmospheric blocking. *Geophysical Research Letters*, *45*, 6311–6320. https://doi.org/10.1029/2018GL077837

Cattiaux, J., Vautard, R., Cassou, C., Yiou, P., Masson-Delmotte, V., & Codron, F. (2010). Winter 2010 in Europe: A cold extreme in a warming climate. *Geophysical Research Letters*, *37*, L20704. https://doi.org/10.1029/2010GL044613

CH2018 (2018). CH2018-Climate scenarios for Switzerland, Technical Report, National Centre for Climate Services, Zurich, 271 pp. ISBN: 978–3–9525031-4-0

Chen, H. W., Zhang, F., & Alley, R. B. (2016). The robustness of midlatitude weather pattern changes due to Arctic sea ice loss. *Journal of Climate*, *29*, 7831–7849. https://doi.org/10.1175/JCLI-D-16-0167.1

Cohen, J., Screen, J. A., Furtado, J. C., Barlow, M., Whittleston, D., Coumou, D., et al. (2014). Recent Arctic amplification and extreme mid-latitude weather. *Nature Geoscience*, *7*(9), 627–637. https://doi.org/10.1038/ngeo2234

Cohen, J. L., Furtado, J. C., Barlow, M. A., Alexeev, V. A., & Cherry, J. E. (2012). Arctic warming, increasing snow cover and widespread boreal winter cooling. *Environmental Research Letters*, *7*(1). https://doi.org/10.1088/1748-9326/7/1/014007

Coumou, D., Di Capua, G., Vavrus, S., Wang, L., & Wang, S. (2018). The influence of Arctic amplification on mid-latitude summer circulation. *Nature Communications*, *9*(1), 1–12. https://doi.org/10.1038/s41467-018-05256-8

Coumou, D., & Rahmstorf, S. (2012). A decade of weather extremes. *Nature Climate Change*, *2*(7), 491–496. https://doi.org/10.1038/nclimate1452

Dai, A., & Song, M. (2020). Little influence of Arctic amplification on mid-latitude climate. *Nature Climate Change*, *10*(3), 231–237. https://doi.org/10.1038/s41558-020-0694-3

Dee, D. P., Uppala, S. M., Simmons, A. J., Berrisford, P., Poli, P., Kobayashi, S., et al. (2011). The ERA-Interim Reanalysis: Configuration and performance of the data assimilation system. *Quarterly Journal of the Royal Meteorological Society*, *137*(656), 553–597. https://doi.org/10.1002/qj.828

Demuzere, M., Kassomenos, P., & Philipp, A. (2011). The COST733 circulation type classification software: An example for surface ozone concentrations in Central Europe. *Theoretical and Applied Climatology*, *105*(1), 143–166.

Francis, J. A., Skific, N., & Vavrus, S. J. (2018). North American weather regimes are becoming more persistent: Is Arctic amplification a factor? *Geophysical Research Letters*, *45*, 11,414–11,422. https://doi.org/10.1029/2018GL080252

Francis, J. A., & Vavrus, S. J. (2012). Evidence linking Arctic amplification to extreme weather in mid-latitudes. *Geophysical Research Letters*, *39*, L06801. https://doi.org/10.1029/2012GL051000

Fyfe, J. C. (2019). Midlatitudes unaffected by sea ice loss. *Nature Climate Change*, *9*(9), 649–650. https://doi.org/10.1038/s41558-019-0560-3

Gerber, E. P., Butler, A., Calvo, N., Charlton-Perez, A., Giorgetta, M., Manzini, E., et al. (2012). Assessing and Understanding the Impact of Stratospheric Dynamics and Variability on the Earth System. *Bulletin of the American Meteorological Society*, *93*, 845–859. https://doi.org/10.1175/BAMS-D-11-00145.1

Hirschi, M., Seneviratne, S. I., Alexandrov, V., Boberg, F., Boroneant, C., Christensen, O. B., et al. (2011). Observational evidence for soil-moisture impact on hot extremes in southeastern Europe. *Nature Geoscience*, *4*, 17. https://doi.org/10.1038/ngeo1032

Hurrell, J. W., Holland, M. M., Gent, P. R., Ghan, S., Kay, J. E., Kushner, P. J., et al. (2013). The Community Earth System Model: A framework for collaborative research. *Bulletin of the American Meteorological Society*, *94*(9). https://doi.org/10.1175/bams-d-12-00121

IPCC (2014). In Core Writing Team, R. K. Pachauri, & L. A. Meyer (Eds.), *Climate change 2014: Synthesis report. Contribution of Working Groups I, II and III to the Fifth Assessment Report of the Intergovernmental Panel on Climate Change*, (p. 151). Geneva, Switzerland: IPCC.

Jézéquel, A., Cattiaux, J., Naveau, P., Radanovics, S., Ribes, A., Vautard, R., et al. (2018). Trends of atmospheric circulation during singular hot days in Europe. *Environmental Research Letters*, *13*(5). https://doi.org/10.1088/1748-9326/aab5da

Kröner, N., Kotlarski, S., Fischer, E., Lüthi, D., Zubler, E., & Schär, C. (2017). Separating climate change signals into thermodynamic, lapse-rate and circulation effects: Theory and application to the European summer climate. *Climate Dynamics*, *48*, 3425. https://doi.org/10.1007/s00382-016-3276-3

Kučerová, M., Beck, C., Philipp, A., & Huth, R. (2017). Trends in frequency and persistence of atmospheric circulation types over Europe derived from a multitude of classifications. *International Journal of Climatology*, *37*, 2502–2521. https://doi.org/10.1002/joc.4861

Kwon, Y. O., Camacho, A., Martinez, C., & Hyodae, S. (2018). North Atlantic winter eddy-driven jet and atmospheric blocking variability in the Community Earth System Model Version 1 large ensemble simulations. *Climate Dynamics*, *51*(9-10), 3275–3289. https://doi.org/10.1007/s00382-018-4078-6

Kyselý, J. (2008). Influence of the persistence of circulation patterns on warm and cold temperature anomalies in Europe: Analysis over the 20th century. *Global and Planetary Change*, *62*(1–2), 147–163. https://doi.org/10.1016/j.gloplacha.2008.01.003

Li, C., Michel, C., Graff, L. S., Bethke, I., Zappa, G., Bracegirdle, T. J., et al. (2018). Midlatitude atmospheric circulation responses under 1.5 and 2.0 °C warming and implications for regional impacts. *Earth System Dynamics*, *9*(2), 359–382. https://doi.org/10.5194/esd-9-359-2018

Mann, M. E., Rahmstorf, S., Kornhuber, K., Steinman, B. A., Miller, S., Petri, S., & Coumou, D. (2018). Projected changes in persistent extreme summer weather events: The role of quasi-resonant amplification. *Science Advances*, *4*(10). https://doi.org/10.1126/sciadv.aat3272

Molnar, P., Fatichi, S., Gaál, L., Szolgay, J., & Burlando, P. (2015). Storm type effects on super Clausius–Clapeyron scaling of intense rainstorm properties with air temperature. *Hydrology and Earth System Science*, *19*, 1753–1766. https://doi.org/10.5194/hess-19-1753-2015

Mori, M., Kosaka, Y., Watanabe, M., Nakamura, H., & Kimoto, M. (2019). A reconciled estimate of the influence of Arctic Sea-ice loss on recent Eurasian cooling. *Nature Climate Change*, *9*(2), 123–129. https://doi.org/10.1038/s41558-018-0379-3

Peña-Ortiz, C., Gallego, D., Ribera, P., Ordonez, P., & Alvarez-Castro, M. D. C. (2013). Observed trends in the global jet stream characteristics during the second half of the 20th century. *Journal of Geophysical Research: Atmosphere*, *118*, 2702–2713. http://doi.org/10.1002/jgrd.50305

Perkins, S. E. (2015). A review on the scientific understanding of heatwaves-their measurement, driving mechanisms, and changes at the global scale. *Atmospheric Research*, *164–165*, 242–267. https://doi.org/10.1016/j.atmosres.2015.05.014

Pfahl, S., & Wernli, H. (2012). Spatial coherency of extreme weather events in Germany and Switzerland. *International Journal of Climatology*, *32*, 1863–1874. http://doi.org/10.1002/joc.2401

Pfleiderer, P., & Coumou, D. (2018). Quantification of temperature persistence over the northern hemisphere land-area. *Climate Dynamics*, *51*(1–2), 627–637. https://doi.org/10.1007/s00382-017-3945-x

Pfleiderer, P., Schleussner, C. F., Kornhuber, K., & Coumou, D. (2019). Summer weather becomes more persistent in a 2° C world. *Nature Climate Change*, *9*(9), 666–671. https://doi.org/10.1038/s41558-019-0555-0

Rohrer, M., Croci-Maspoli, M., & Appenzeller, C. (2017). Climate change and circulation types in the Alpine region. *Meteorologische Zeitschrift*, *26*(1), 83–92.

Röthlisberger, M., Pfahl, S., & Martius, O. (2016). Regional-scale jet waviness modulates the occurrence of midlatitude weather extremes. *Geophysical Research Letters*, *43*, 10,989–10,997. https://doi.org/10.1002/2016GL070944

Schaller, N., Sillmann, J., Anstey, J., Fischer, E. M., Grams, C. M., & Russo, S. (2018). Influence of blocking on Northern European and Western Russian heatwaves in large climate model ensembles. *Environmental Research Letters*, *13*, 054015. https://doi.org/10.1088/1748-9326/aaba55

Screen, J. A., & Blackport, R. (2019). How robust is the atmospheric response to projected Arctic sea ice loss across climate models? *Geophysical Research Letters*, *46*, 11,406–11,415. https://doi.org/10.1029/2019GL084936

Seneviratne, S. I., Corti, T., Davin, E., Hirschi, M., Jaeger, E. B., Lehner, I., et al. (2010). Investigating soil moisture–climate interactions in a changing climate: A review. *Earth-Science Reviews*, *99*(3–4), 125–161. https://doi.org/10.1016/j.earscirev.2010.02.004

Steirou, E., Gerlitz, L., Apel, H., & Merz, B. (2017). Links between large-scale circulation patterns and streamflow in Central Europe: A review. *Journal of Hydrology*, *549*, 484–500. https://doi.org/10.1016/j.jhydrol.2017.04.003

Uppala, S. M., Kållberg, P. W., Simmons, A. J., Andrae, U., Bechtold, V. D. C., Fiorino, M., et al. (2005). The ERA-40 re-analysis. *Quarterly Journal of the Royal Meteorological Society*, *131*(612), 2961–3012. https://doi.org/10.1256/qj.04.176

Vavrus, S. J. (2018). The influence of Arctic amplification on mid-latitude weather and climate. *Current Climate Change Reports*, *4*(3), 238–249. https://doi.org/10.1007/s40641-018-0105-2

Weusthoff, T. (2011). Weather type classification at MeteoSwiss–Introduction of new automatic classification schemes. *Arbeitsberichte der MeteoSchweiz, 235*.

Woollings, T., Hannachi, A., & Hoskins, B. (2010). Variability of the North Atlantic eddy-driven jet stream. *Quarterly Journal of the Royal Meteorological Society*, *136*, 856–868. https://doi.org/10.1002/qj.625

Globi, a Swiss cartoon character, can be found on page 27.